

AD-A100 043

POLITECNICO DI MILANO (ITALY) IST DI MACCHINE  
THE DYNAMICS OF SOLID PROPELLANT COMBUSTION. (U)  
DEC 80 L DE LUCA, A COGHE, A REGGIORI

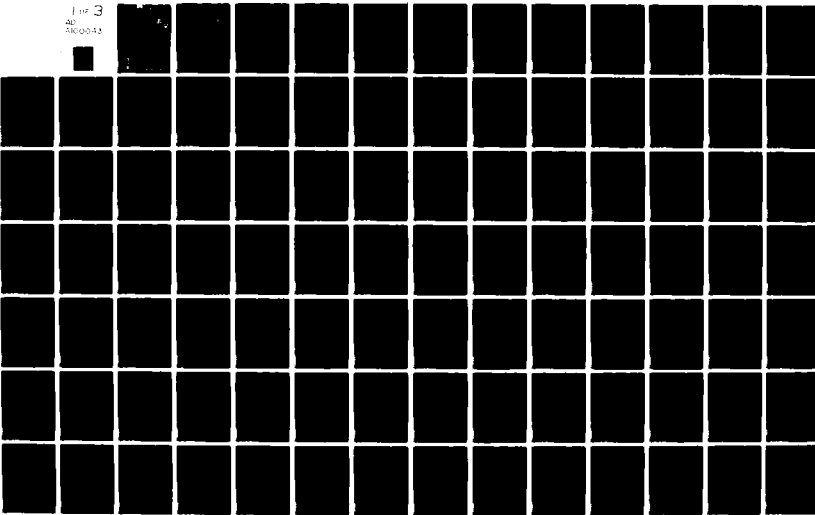
F/G 21/9.2

DA-ERO-78-6-029

NL

UNCLASSIFIED

Line 3  
20  
AD-A100 043



107278  
ADA100043

THE DYNAMICS OF SOLID PROPULSION COMBUSTION

Final Technical Report  
October 1977 - December 1980

by

Luigi De Luca (Principal Investigator)  
Aldo Coghe (Co-Investigator)  
Adolfo Raggioli (Co-Investigator)

31 December 1980

EUROPEAN RESEARCH OFFICE  
United States Army  
London England

GRANT NUMBER DA-ERO No. 78-G-029

GRANTEE : Prof. Corrado Casci, Director  
CNPM - Istituto di Macchine  
Politecnico di Milano  
20133 Milano, Italy.

Approved for Public Release; distribution unlimited

FILE COPY

81611052

## THE DYNAMICS OF SOLID PROPELLANT COMBUSTION

Final Technical Report  
October 1977 - December 1980

by

Luigi De Luca (Principal Investigator)  
Aldo Coghe (Co-Investigator)  
Adolfo Reggiori (Co-Investigator)

31 December 1980

EUROPEAN RESEARCH OFFICE  
United States Army  
London England

GRANT NUMBER DA-ERO No. 78-G-029

GRANTEE : Prof. Corrado Casci, Director  
CNPM - Istituto di Macchine  
Politecnico di Milano  
20133 Milano, Italy.

Approved for Public Release; distribution unlimited

2  
DTIC  
SELECTED  
JUN 11 1981

## UNCLASSIFIED

SECURITY CLASSIFICATION OF THIS PAGE (When Data Entered)

R&amp;D 2401-AN

REPORT DOCUMENTATION PAGE		READ INSTRUCTIONS BEFORE COMPLETING FORM
1. REPORT NUMBER 6	2. GOVT ACCESSION NO. A100043	3. RECIPIENT'S CATALOG NUMBER
4. TITLE (and subtitle) The Dynamics of Solid Propellant Combustion.		5. TYPE OF REPORT & PERIOD COVERED Final Technical Report Nov 77 - Dec 80
6. AUTHOR(s) Luigi De Luca; Aldo Coghe; Adolfo Reggiori		7. PERFORMING ORG. REPORT NUMBER DA-ERO-78-G-029
8. CONTRACT OR GRANT NUMBER(s)		9. PERFORMING ORGANIZATION NAME AND ADDRESS CNPM - Istituto di Macchine Politecnico di Milano 20133 Milano, Italy
10. PROGRAM ELEMENT, PROJECT, TASK AREA & WORK UNIT NUMBERS 6.11.02A IT161102BH57-06		11. CONTROLLING OFFICE NAME AND ADDRESS USARDSG-UK Box 65 FPO NY 09510
12. REPORT DATE 31 December 1980		13. NUMBER OF PAGES 243
14. MONITORING AGENCY NAME & ADDRESS (if different from Controlling Office)		15. SECURITY CLASS. (of this report) Unclassified
16. DISTRIBUTION STATEMENT (of this Report) Approved for Public Release; distribution unlimited		17. DISTRIBUTION STATEMENT (of the abstract entered in Block 20, if different from Report)
18. SUPPLEMENTARY NOTES		
19. KEY WORDS (Continue on reverse side if necessary and identify by block number) Solid Propellant Combustion; Combustion Stability; Static and Dynamic Stability; Extinction; Ignition Dynamics.		
20. ABSTRACT (Continue on reverse side if necessary and identify by block number) A nonlinear stability analysis of solid rocket propellant burning was carried out, within the framework of a thermal theory for thin (quasi-steady gas phase) heterogeneous flames. This required an integral method in reducing the partial differential equation for the condensed phase heat conduction to an approximate ordinary differential equation. A nonlinear algebraic function, called static restoring function, was found that contains all basic properties of equilibrium and stability of burning solid propellants. This function depends on the nature of the solid propellant (including its		

UNCLASSIFIED

SECURITY CLASSIFICATION OF THIS PAGE(When Data Entered)

20. Contd.

flame) and the operating conditions. Analysis of the static restoring function reveals the existence of lower and upper burning stabilities. Nonlinear static and dynamic burning stability boundaries were determined and stability properties of several unsteady flame models were compared. Domains of stationary reacting solutions, damped oscillatory burning, self-sustained oscillatory burning, non sustained burning were singled out. Pressure deflagration limit was evaluated. Validity and plausible extensions of this theory are discussed.

Most of the analytical predictions were verified by computer simulated burning tests. Experimental results obtained in shock tube apparatus, depressurization strand burner, laser doppler velocimetry rig are presented.

Accession for

NTIS GRA&I	<input type="checkbox"/>
DTIC TAB	<input type="checkbox"/>
Unannounced	<input type="checkbox"/>
Justification	<input type="checkbox"/>
By	<input type="checkbox"/>
Distribution	<input type="checkbox"/>
Availability	<input type="checkbox"/>
Analyst	<input type="checkbox"/>
Dist	<input type="checkbox"/>
Sp	<input type="checkbox"/>

A

UNCLASSIFIED

SECURITY CLASSIFICATION OF THIS PAGE(When Data Entered)

TABLE OF CONTENTS

Title Page	page
ABSTRACT	ii
TABLE OF CONTENTS	iv
<u>CHAPTER 1 - SCOPE, OBJECTIVES, AND BACKGROUND</u>	1
Sec. 1.1 - SCOPE OF THIS WORK	1
Sec. 1.2 - OBJECTIVES AND PLAN OF PRESENTATION	2
Sec. 1.3 - LITERATURE SURVEY	3
§ 1.3.1 - Nonlinear dynamic extinction by fast depressurization	3
§ 1.3.2 - Nonlinear dynamic extinction by fast deradiation	9
§ 1.3.3 - Nonlinear oscillating combustion	12
<u>CHAPTER 2 - NONLINAR THEORY OF SOLID PROPELLANT COMBUSTION STABILITY</u>	15
Sec. 2.1 - BACKGROUND AND NOMENCLATURE	16
Sec. 2.2 - FORMULATION OF THE GENERAL QUASI-STEADY GAS PHASE TRANSIENT PROBLEM	18
Sec. 2.3 - QUASI-STEADY FLAME MODELS	24
§ 2.3.1 - MTS flame	24
§ 2.3.2 - KTSS flame	26
§ 2.3.3 - KZ flame	28
§ 2.3.4 - LC flame	29
§ 2.3.5 - Working map for quasi-steady gas phase	30
§ 2.3.6 - Final comments on quasi-steady gas phase	31
Sec. 2.4 - AN ORDINARY DIFFERENTIAL EQUATION FORMULATION OF THE PROBLEM	33
Sec. 2.5 - NATURE OF THE STATIC RESTORING FUNCTION	41
§ 2.5.1 - Qualitative remarks	41
§ 2.5.2 - Effect of operating conditions	43
§ 2.5.3 - Effect of flame models	44
§ 2.5.4 - Effect of the polynomial order	45
§ 2.5.5 - Effect of $C_g/C_c \neq 1$	45
§ 2.5.6 - Effect of $\epsilon \neq 0$	45
Sec. 2.6 - NONLINEAR STATIC STABILITY ANALYSIS	47
§ 2.6.1 - Number and nature of the allowed static solutions	47
§ 2.6.2 - Static stability boundary	48
§ 2.6.3 - Measurement of static stability strength	49
§ 2.6.4 - Pressure deflagration limit	50

Sec. 2.7 - NONLINEAR DYNAMIC STABILITY ANALYSIS	51
§ 2.7.1 - Dynamic extinction of solid propellants	51
§ 2.7.2 - Lower and upper dynamic combustion stability	56
§ 2.7.3 - Self-sustained oscillatory burning of solid propellants	57
§ 2.7.4 - Ignition of solid propellants	60
§ 2.7.5 - Final remarks on dynamic combustion stability	61
§ 2.7.6 - Important remark on the static boundaries	62
Sec. 2.8 - NUMERICAL COMPUTATIONS	63
§ 2.8.1 - Numerical approach	63
§ 2.8.2 - Dynamic extinction of solid propellants	68
§ 2.8.3 - Upper dynamic combustion stability	68
§ 2.8.4 - Self-sustained oscillatory burning of solid propellants	69
§ 2.8.5 - Effect of $C_g/C_c \neq 1$	70
§ 2.8.6 - Ignition of solid propellants	71
§ 2.8.7 - Further computer runs on dynamic combustion stability	72
Sec. 2.9 - STATE OF THE ART OF THE NONLINEAR APPROACH	73
<u>CHAPTER 3 - EXPERIMENTAL UNSTEADY BURNING RESULTS</u>	76
Sec. 3.1 - SHOCK TUBE EXPERIMENTS	76
Sec. 3.2 - DEPRESSURIZATION EXPERIMENTS	79
REFERENCES	81
NOMENCLATURE	89
LIST OF TABLES	93
Tables 1 - 11	
LIST OF FIGURES	109
Figures 1 - 96	
<u>CHAPTER 4 - LASER-OPTICAL TECHNIQUES</u>	213
Sec. 4.1 - INTRODUCTION	213
Sec. 4.2 - LASER DOPPLER VELOCIMETRY	213
Sec. 4.3 - PARTICLE SIZING	216
Sec. 4.4 - EXPERIMENTAL APPARATUS	219
Sec. 4.5 - EXPERIMENTAL RESULTS	221
Sec. 4.6 - CONCLUSIONS	224
REFERENCES	225
LIST OF TABLES	227
LIST OF FIGURES	227
Tables 4.1 - 4.2	
Figures 4.1 - 4.12	
<u>CHAPTER 5 - CONCLUSIONS AND FUTURE WORK</u>	
Sec. 5.1 - CONCLUSIONS	240
Sec. 5.2 - FUTURE WORK	240

## CHAPTER 1 - SCOPE, OBJECTIVES, AND BACKGROUND

### Sec. 1.1 - SCOPE OF THIS WORK

Purpose of this work is to formulate, within the framework of a thermal theory, basic laws governing the nonlinear dynamics of solid propellant burning. This implies that:

- (1) findings should be readily extended to other cases of heterogeneous combustion; in particular the results are not dependent on the nature of solid propellant.
- (2) new flame models are not being proposed, rather a method is offered to judge how good any unsteady flame model is.
- (3) information regarding steady state solutions is found as a particular case.
- (4) interactions combustion/fluid-dynamics (e.g., in a rocket combustion chamber) are not considered.

By making the usual set of assumptions (see Sec. 2.1), one is reduced to study the stability properties of the nonlinear heat conduction equation in the condensed phase (the standard Fourier partial differential equation with time-varying boundary conditions). This is done by an approximate analytical technique, but keeping the nonlinearity of the problem. It will be shown that a nonlinear algebraic function, called static restoring function, can be determined defining nonlinear static and dynamic burning stability boundaries for finite size disturbances. These boundaries are valid for any kind of transient burning (e.g., depressurization or deradiation).

No attempt is made to explain or predict the steady flame structure of burning propellants. This is supposed to be assigned in terms of burning rate vs pressure (experimental data) and flame temperature vs pressure (thermochemical equilibrium computations). This information, in addition to a proper flame model, is enough to define the fundamental nonlinear burning stability properties of solid propellants.

This stability analysis can be applied to any flame model and solid propellant composition, but the actual numerical values do depend on the specific flame model and solid propellant composition chosen. The results can be verified by computer simulation (i.e., by numerical integration of the basic set of governing equations) and/or experiments. While plenty of computer results are already available, the experimental part of this work starts just now to provide results.

This final technical report comprehends and supersedes the previous annual technical reports. The opportunity is taken to review the theory and summarize most of the numerical and experimental findings by our research group. The complete literature so far published by this group is listed as Refs. 1-19.

### Sec. 1.2 - OBJECTIVES AND PLAN OF PRESENTATION

Consider the physical system of Fig. 1a representing a strand of solid propellant, subjected to a radiant flux impinging with instantaneous intensity  $(1-r) \cdot I_0(t)$  on its surface, burning with instantaneous rate  $\dot{R}(t)$  in a semi-closed vessel at instantaneous pressure  $P(t)$  and ambient temperature  $T_\infty$ . The overall problem of transient solid propellant combustion consists of predicting the burning rate history in time.

Specific objectives of this study are:

- (1) distinguish between static and dynamic burning regimes.
- (2) define and evaluate nonlinear static stability boundaries.
- (3) define and evaluate nonlinear dynamic stability boundaries.
- (4) define and evaluate nonlinear pressure deflagration limit.
- (5) predict number and nature of static solutions.
- (6) predict dynamic extinction, including overstability, by fast depressurization and/or deradiation.
- (7) predict self-sustained oscillating burning regime.
- (8) is there a univocally defined ignition boundary?
- (9) what is the influence of the implemented flame model on the above predictions?
- (10) what is the influence of the implemented integral method on the above predictions?
- (11) numerical and experimental verifications of the above predictions.

First, a literature survey of the problem is offered in Sec. 1.3. Then, the basic set of assumptions and equations is illustrated in Secs. 2.1 - 2.3; the transformation of the PDE into an approximately equivalent ODE is performed in Sec. 2.4; properties of the resulting nonlinear algebraic restoring function are discussed in Sec. 2.5. Static and dynamic burning stability are respectively treated in Sec. 2.6 and Sec. 2.7; the self-sustained oscillating regime is illustrated in § 2.7.3. The point on the status of the theory is made in Sec. 2.9. Numerical computations verifying the analytical predictions are reported in Sec. 2.8. Experimental results are summarized in Ch. 3 (ballistic experiments) and Ch. 4 (laser based optical techniques). Conclusions and suggestions for future work are collected in Ch. 5.

References, nomenclature, tables and figures are given at the end of Ch. 3 (ballistic studies) and Ch. 4 (laser techniques).

### Sec. 1.3 - LITERATURE SURVEY

The question of solid propellant burning stability in general and dynamic extinction in particular has been well debated in the relevant literature (Refs. 20-77), but few works have been really constructive. The erroneous application of the quasi-steady gas phase assumption, the strong limitations of linearized theories, and the empirical nature of most of the proposed extinction criteria are the most serious drawbacks in this area.

In this work, quantitative criteria for nonlinear static and dynamic stability of burning propellants are defined by means of flame models. The integral method of Goodman (Ref. 78) is implemented in order to apply known mathematical methods to the resulting approximate ODE formulation of the problem. The same method has already been applied (Ref. 76) to particle burning; somewhat simpler use has been made at Princeton (Refs. 79-80) on solid propellant rocket engines. The concept of using the simpler ODE formulation of the problem, instead of the ODE one, is relatively common in Soviet literature. However, the method of transformation is rather different; an interesting review of the mathematical problem was made by Gostintsev (Ref. 81). The approach has been applied mainly to ignition, unsteady burning, and stability problems. Remark that the Soviet approach differs not only in the mathematical details, but especially in the structure of the physical model. Instead of using a flame model, the Soviet investigators resort to the Zeldovich method (e.g., see Ref. 47), consisting of constructing the instantaneous thermal gradient at the condensed phase side of the burning surface from experimental steady state data. However, this method is useful in establishing intrinsic stability boundaries, but in principle cannot be extended to obtain stability boundaries.

#### § 1.3.1 - Nonlinear Dynamic Extinction by Fast Depressurization

At Politecnico di Milano several years of efforts (Refs. 1-19) were dedicated to the question of dynamic extinction driven by fast changes both of pressure and/or radiation. Following a line of research initiated at Princeton (Ref. 3), an original approach, based on a nonlinear burning stability analysis, was developed within the framework of a thermal model of thin (quasi-steady) heterogeneous flames (Refs. 1-3). This analysis was applied to the specific problem, among others, of predicting the minimum burning rate (lower dynamic stability point), in function of pressure, under which extinction of the burning solid propellant necessarily occurs independently on its past history (Ref. 4). The limiting burning rate is a property strictly dependent on the nature of the reacting substance; but it is affected by the operating conditions, such as pressure, ambient temperature, and

heat exchange with the environment. This extinction criterion, suggested in 1975, is valid instantaneously for any monotonic decrease in time of both pressure and/or radiation. Improvements and extensions of the proposed theory, including numerical and experimental checks, are under progress (Refs. 9-19).

Although dynamic extinction might occur under a variety of conditions, due to the pioneering work of Ciepluch (Refs. 20-22) in 1961, only dynamic extinction by depressurization appears largely analyzed both experimentally and theoretically (Refs. 20-57). Unfortunately, the understanding of this phenomenon is still little satisfactory. No criterion whatsoever is found in the literature for the case of dynamic extinction by fast deradiation reported by the Princeton group (Refs. 58-59). Ciepluch (Refs. 20-22) conducted one of the first systematic experimental studies of depressurization transients in a laboratory combustion chamber closely simulating conditions of an actual motor. Fast depressurization was obtained by suddenly opening a chamber vent hole. Initial chamber pressure in the range 34 to 82 atm and ambient pressures down to 3.5 mm of mercury were explored. The burning transient was followed by measuring simultaneously combustion luminosity (primarily in the visible range) and chamber pressure. Several AP-based composite propellants were tested; few data on double-base compositions were also reported. The following conclusions were reached:

- (1) a critical depressurization rate exists below which burning continues and above which extinction occurs.
- (2) the critical depressurization rate increases linearly as the chamber pressure prior to venting increases.
- (3) the critical depressurization rate is substantially affected by the propellant composition.
- (4) reignition may follow extinction if the depressurization is not too fast and/or nozzle back pressure is not too low.

For a critical review of papers on dynamic extinction by depressurization offered until 1969, the reader might consult Merkle (Ref. 29). Papers dealing mainly with rocket engine extinguishment, rather than just a semi-closed volume (no combustion/fluid-dynamics coupling), are neglected in this review. The papers by Von Elbe (Refs. 23-24) should be noted; an analytical expression given by Von Elbe for the critical depressurization rate has been rather widely used. Although later proved wrong by Merkle (Ref. 29) and Krier (Ref. 42) on different arguments, this expression for dynamic burning rate

$$(1.3.1.) \quad \dot{R}(t) = \bar{R} \left[ 1 + 2 \frac{n}{P(t)} \frac{\alpha_c}{\bar{R}^2} \frac{dP(t)}{dt} \right]$$

and others of the same nature are still being used, mostly for practical applications. In particular, the critical de-pressurization rate is given by

$$(1.3.2) \quad \left[ - \frac{dP(t)}{dt} \right]_{cr} = \frac{1}{2} \frac{P(t)}{n} \frac{\bar{R}^2}{\alpha_c}$$

being  $\bar{R}$  the steady, unperturbed burning rate. This and similar expressions are meaningless from our point of view. A detailed critical review of this type of oversimplified transient burning models was given by Krier (Ref. 42), who generalized the previous expression for dynamic burning rate

$$(1.3.3) \quad \dot{R}(t) = \bar{R} \left[ 1 + \psi \frac{n}{P(t)} \frac{\alpha_c}{\bar{R}^2} \frac{dP(t)}{dt} \right]$$

being  $\psi = \text{const}$  for several investigators (e.g.  $\psi = 2$  in Refs. 23-24). Krier analytically showed that actually  $\psi$  is a function of burning surface properties and pressure jump, and that this function can be computed a priori for each propellant. However, relationships of the type of Eq. 1.3.3 are restricted to small values of  $dP(t)/dt$  and small excursion of  $\dot{R}(t)$  with respect to  $\bar{R}$ . Therefore, they are of no use for dynamic extinction problems.

Two excellent contributions should explicitly be mentioned. Merkle (Ref. 29) pointed out several mistakes crept in the literature, furnished a new quasi-steady flame model and recognized that dynamic extinction depends on the entire  $P(t)$  curve. However, he did not formulate an extinction criterion, since a critical value of surface temperature ( $T_s = 600$  K corresponding to  $\Theta_s = 0.43$  for the propellant AP/PBAA No. 941 taken as datum case in this study) was empirically picked up below which chemical reactions are considered too weak to sustain the deflagration wave. A paper by T'ien (Ref. 38), in 1974, is the only one aimed directly at establishing an extinction criterion for fast depressurization. T'ien argues that heat losses are the mechanism for both static and dynamic extinction of solid propellants; this view is not fully shared in this instance. However, T'ien concludes (Refs. 38-40) that for depressurization transients, if the instantaneous burning rate drops below the unstable burning rate solution at the final pressure, extinction will occur. T'ien derives his quantitative criterion from another study by him of flammability limits of premixed flames under the influence of environmental disturbances (Ref. 39). A somewhat similar result has been found in this investigation (Refs. 1-19), but by a completely different approach.

The line of research evolved within the framework of Zeldovich method (Refs. 43-44) is of limited value. Istratov et al. (Ref. 45), in 1964, used an integral method in order to determine

an approximate solution to the unsteady nonlinear energy equation in the condensed phase of a propellant burning with constant surface temperature. Extinction was assumed to occur when the surface thermal gradient on the condensed side exceeds a critical value corresponding to the static stability line. This is mistaken, since nothing can be said a priori about dynamic burning in a range of burning rate that is statically unstable. Novozhilov (Ref. 46), in 1967, improved the previous model by considering a variable surface temperature and recognizing that dynamic burning is allowed also in the range of parameters where statically stable solutions are not found. Extinction was then assumed to occur when the burning rate at the final pressure drops below a limiting value experimentally established in nonstationary burning conditions. This "ad hoc" criterion, if feasible, would rely on very delicate experimental results.

The question of a possible early warning of extinction during a depressurization transient evaluated via the Zeldovich method was examined in a paper by the Princeton group (Ref. 47) in 1971. The possibility was checked that the crossing of the static stability boundary is sufficient to subsequently produce dynamic extinction. No clear answer to this question was given. In our opinion the static stability boundary has only secondary relevance in a dynamic situation. Indeed, according to the same Princeton reference, "the dynamic conditions of extinguishment tend to shift the stability line" (pag. 257 of Ref. 47). Further extensive work in this area (Ref. 48) failed to reach more significant conclusions. Finally Novozhilov (p. 216 of Ref. 49), in 1973, observed that this "question requires certain information about the properties of the system outside the area of smooth burning. Such information cannot be obtained from experiments on steady state combustion. For the calculation of unsteady conditions in the unstable region it is necessary to draw on certain schemes of combustion, which make it possible to predict the properties of propellants beyond the static stability limit". Further work by Soviet investigators (Refs. 50-56) offered fresh experimental information and theoretical considerations, but failed to define a physically sound extinction criterion.

Experimentally, the results reported in Refs. 24 and 29 (go/no-go boundaries), Ref. 32 (flame structure during depressurization), Ref. 34 (flame temperature and emission spectra during depressurization), Ref. 54 (condensed phase temperature during depressurization) are the most interesting. They allow detailed and reliable comparison with analytical and numerical results. Obviously, the most wanted result is the burning rate history during depressurization transients. Unfortunately, no reliable data exist yet in this particularly difficult area of investigation, although a large number of contributions have been offered. For a good summary of the results so far obtained and a critical discussion of the techniques implemented, the reader might consult the excellent review given in Ref. 57.

Experimental results are often ambiguous to interpret due to the interplay and overlapping of several factors; attention is preferably focused on data collected from laboratory burners (ranging from depressurization strand burners to simulated rocket combustion chambers) rather than actual rocket motors where fluiddynamic effects may be dominant. However, even results from laboratory burners are not easy to compare due to: implementation of different extinction criteria, diagnostic techniques, and operating conditions; scattering of results; confused theoretical guidelines in data handling.

In the pioneering work by Ciepluch (Refs. 20-22) the critical boundary between (permanent) extinction and continued burning was found, with a go/no-go technique, to be a straight line in the  $dP/dt$  vs  $P_i$  (initial pressure) linear plot. Further data were provided, among others, by Von Elbe and McHale (Ref. 24) in an effort to substantiate Von Elbe's theoretical predictions (Ref. 23). They tested three AP-based composite propellants in a depressurization strand burner (300  $\text{cm}^3$  internal volume) furnished by frangible diaphragm (ruptured by a solenoid driven plunger) and orifice plate to control the depressurization rate. Flame luminosity in time was monitored with a photodiode simultaneously to pressure decay; initial pressures from 33 to 5 atm were used. Von Elbe and McHale plotted  $dP/dt$  vs  $P$  at extinction (as determined by zero luminosity); the critical boundary was found to be straight in a  $\lg/\lg$  plot.

Merkle and Summerfield (Ref. 29) produced a rather complete set of data by systematically testing several AP composite and one catalyzed DB propellants. A special laboratory combustor was designed to minimize erosive burning effects and to cause monodimensional "cigarette" burning of the sample. Fast pressure decay was obtained by rupturing a double diaphragm system. The exhaust gases initially pass through both a primary (large) nozzle and a secondary (small) nozzle; the small nozzle controls the chamber pressure as long as the diaphragms remain in place. When the diaphragms are removed, the small nozzle also is removed (being located in the double diaphragm apparatus). By properly combining nozzles of different diameters, the initial pressure level as well as the depressurization rate could be varied. Pressure and light emission (as seen by a photomultiplier in the visible) were simultaneously recorded. Extinction was considered to occur when zero light emission from the flame could be observed. Initial pressures in the range 75 to 14 atm were explored. Venting was always to atmospheric pressure; because of this, reignition was nearly always observed. The following conclusions were reached:

- (1) the critical boundary between extinction (permanent or temporary) and continued burning was found, with a go/no-go technique, to be always straight in the  $dP/dt$  vs  $P$  linear plot.

- (2) increasing AP loading from 75% to 82.5% makes the propellant more than twice as difficult to extinguish (in terms of initial, i.e. maximum,  $dP/dt$ ).
- (3) increasing AP particle size from 45 to 180  $\mu\text{m}$  (unimodal distributions) makes the propellant easier to extinguish (for a fixed loading of 75% AP).
- (4) little difference was observed when PBAA, PBCT, and PU binders (for a fixed loading of 80% AP) were tested.
- (5) aluminum (16  $\mu\text{m}$  particles) addition up to 15% makes the propellant slightly more difficult to extinguish (for a fixed composition of AP 77.5%/binder 22.5%); but the opposite is true for  $P_i < 27 \text{ atm}$ .

It should be remarked that some of these conclusions (AP particle size and binder type effects) may be in conflict with other experimental studies in which, however, permanent extinction was recorded. Merkle and Summerfield adopted the permanent extinction criterion only for the catalyzed DB test, since no visible radiation can be detected from DB burning at low pressures. They found that:

- (6) the tested catalyzed DB propellant (N-5 composition) is much easier to extinguish than any of the tested AP composite propellants.

Interesting and detailed observations on the flame structure of composite propellants during depressurization were reported by Selzer and Steinz in a series of papers (Refs. 32-33). They showed that, regardless of the depressurization rate, the flame intensity (as seen by spectral emission from OH, NH, CN, Na lines and carbon continuum) falls to zero soon after the impact of the first rarefaction wave on the burning surface. This is possibly followed by the appearance of an incipient flame, after a time span of the order of the condensed phase thermal wave relaxation time, if the depressurization rate is not too fast. Marked pressure oscillations are observed when this secondary flame develops, the flame decay being otherwise exponential. The authors further claimed that the adiabatic expansion of the flame quenches the active gaseous chemical reactions; this would explain why the first zero intensity of flame radiation is noticed when the instantaneous pressure has dropped only to about 70% of the initial pressure. The average O/F mixture ratio was observed to be higher during some part of the transient burning than during steady state, due to preferential consumption of AP particles exposed on the propellant surface; the binder surface looked molten and not thicker than a few microns (for depressurization tests from 45 to 1 atm with AP 76%/PBCT 24% composition). The implication is that the binder gasification is the first to suffer the effects of a pressure expansion. It was stressed that during depressurizations AP may undergo important postreactions in the condensed phase, which would distort the O/F mixture ratio with respect to steady state and cause 3-D effects. However, it was later concluded that more important

steps are the easiness of gas reactions and the decomposition mechanism of binder. It was finally confirmed, in agreement with Ciepluch (Refs. 20-22) and Merkle (Ref. 29), that conditions at the end of the depressurization process, i.e. the final shape of the pressure history and the exhaust pressure, can be determining in extinction.

#### § 1.3.2 - Nonlinear dynamic extinction by fast deradiation

Studies on dynamic extinction by fast deradiation overlap with those on radiative ignition. Ohlemiller, at Princeton University in 1970, first observed dynamic extinction by fast deradiation while constructing ignition map of uncatalyzed DB (a NC composition) by a CO<sub>2</sub> laser source, providing up to 120 cal/cm<sup>2</sup>s at the target, in the range 3 to 34 atm of nitrogen. It seems that, independently, the discovery was made in USSR by Mikheev in his Candidate's Dissertation appeared about at the same time (1970), but unavailable to this writer. From successive work published in the open literature, one would guess that Mikheev's data concerned uncatalyzed DB propellants tested in a furnace at low radiant flux (few cal/cm<sup>2</sup>s) at 1 atm of air or nitrogen. Supporting evidence for the dynamic character of this phenomenon and further experimental data were successively offered mainly at Princeton University (Refs. 3,58-59) and in USSR (Refs. 60-63 and pp.173-187 of Ref. 64). The radiative pulse experiment on steadily burning propellants, reported in Ref. 58, was suggested by Yu. A. Gostintsev during a stay at Princeton University.

Theoretical considerations (Refs. 58,60,62-63) were offered mainly in the framework of Zeldovich approach. However, just as in the case of dynamic extinction by fast depressurization, the Zeldovich stability boundary is not meant to apply to transient burning stability. The dynamic stability boundary for fast deradiation was shown to coincide with that for fast depressurization in Ref. 1; details will be given later in § 2.7.1. No other attempt to evaluate the dynamic stability boundary for fast deradiation is known to this author.

All successful experimental results collected at Princeton University concern radiation by a 100 W continuous wave, multimode CO<sub>2</sub> laser emitting at 10.6 μm in the far infrared. Cylindrical samples of propellant were tested in a strand burner with two optical windows for high speed cinematography and light emission recording (both visible and infrared photodetectors were available). Two mechanical shutters (of iris leaf type) provided a trapezoidal radiation pulse, the action time of the shutters could be regulated from 1 to 10 ms. Dynamic extinction of steadily burning samples (ignited by hot wire) subjected to laser pulse was observed for two DB uncatalyzed compositions, but it could not be seen for the tested DB catalyzed propellant

(Ref. 58). Experiments were made up to 11 atm of nitrogen; the minimum pulse length required for extinction, determined by a go/no-go technique, was found to increase with pressure but decrease with radiant flux intensity; the radiation cut-off time was 2 ms for all tests; experiments in air were not conducted; composite propellants were not tried.

Ignition tests were performed, in the range 5 to 21 (sometimes up to 34) atm of nitrogen or air, for 12 propellants representative of several classes (uncatalyzed and catalyzed DB, unmetallized and metallized AP composite, HMX composite) both with laser and arc image furnaces. Dynamic extinction associated with ignition was again observed only for several uncatalyzed DB compositions with 0, 0.2, and 1% carbon addition (Refs. 3 and 59). Ignition boundaries, determined by a go/no-go technique, revealed an ignition corridor bounded essentially by two parallel straight lines in the  $\lg$  radiant heating time vs  $\lg$  radiant flux intensity plot. The lower boundary defines the minimum exposure time for self-sustained flame propagation; it is not affected by ambient atmosphere (air or nitrogen) and radiation cut-off time. The upper boundary defines the critical (i.e. maximum) exposure time above which a radiation overdriven flame extinguishes when the external radiant beam is removed; this boundary is strongly affected by the ambient atmosphere (extinction occurs in air but not in nitrogen), pressure (increasing pressure widens the ignition corridor), radiation cut-off time (slow cut-off widens the ignition corridor). For pressures less than 11 atm the ignition corridor was totally wiped out. All this was confirmed by high speed movies and photodetectors. However, the same propellant extinguishable at the laser apparatus could not be extinguished when tested, in similar operating conditions, at an arc image apparatus. This used as source a 2.5 kW high pressure xenon arc lamp with spectral emission in the visible (similar to sunlight, peak near  $0.55 \mu\text{m}$ ), except for some nonequilibrium high intensity bands in the near infrared. Tests at the arc image apparatus were conducted only for ignition runs. The different results obtained with uncatalyzed DB propellants with the two radiative sources were mainly attributed to different optical properties (volumetric absorption and scattering are strongly wavelength dependent; uncatalyzed DB propellants are much more opaque in the far infrared than in the visible) and larger radiant flux cut-off time with the arc image apparatus (about twice with respect to the laser apparatus). Other minor differences were also operative: spatial structure of the radiant beams (less sharp with the arc image source), sample positioning (protruding from a metallic holder at the laser apparatus but flush at the arc image; this may cause heat sink effects), different beam geometry (collimated and perpendicular for laser but

converging and oblique for arc image). The different results between noncatalyzed DB vs catalyzed DB and AP composite propellants, observed at both laser and arc image apparatus, were attributed to different flame structure (both catalyzed DB and AP composite propellants feature large heat feedback from the gas phase with respect to heat release at the burning surface; this will be shown to be stabilizing) and different radiation interaction with the combustion products (radiation is gently terminated and effectively decreased by carbonaceous filaments and particulate generated by the burning samples; this is specially true for catalyzed DB propellants). However, it is expected, in principle, that all propellants should manifest dynamic extinction by fast deradiation if tested in the appropriate range of operating conditions.

To the best of the author's knowledge, the only easily available Soviet paper with detailed experimental data on dynamic extinction by fast deradiation is the one by Mikheev and Levashov (Ref. 61). Data reported concern a DB composition, without and with carbon addition (1%), at 1 atm of nitrogen subjected to low (< 10 cal/cm<sup>2</sup>s) radiant flux from an electrically heated incandescent graphite plate. Mechanical shutters, with about 30 ms action time, were used to control the pulse length. Three types of experiments were performed: ignition, radiation pulse of parametrically varied duration on steadily burning samples, radiation pulse of parametrically varied intensity on steadily burning samples. Ignition runs showed the familiar ignition corridor just discussed (cf. Refs. 3 and 59). The second experiment showed a decrease of critical (minimum value leading to extinction) duration of radiant pulse for increasing flux intensity. The third experiment showed critical (minimum value leading to extinction) radiant flux intensity increasing for increasing initial temperature (20°C or 100°C) and for increasing transparency of the sample.

Interesting experimental data on transient burning and surface structure during and after deradiation were provided by Mikheev et al. in a successive paper (pp. 173-187 of Ref. 64). They used an arc image furnace (the source was a xenon lamp of 10 kW) capable of a radiant flux from 1 to 10 cal/cm<sup>2</sup>s. Experiments on a DB propellant and pressed nitrocellulose samples, both without and with 1% carbon addition, were carried out at 1 atm of air or nitrogen. Mechanical shutters with an action time < 2 ms were used to send trapezoidal (square as seen by samples with large thermal and reacting layers relaxation times in the condensed phase) radiation pulses on target. Ignition, fast deradiation, and fast irradiation experiments were performed. A capacitive transducer system was set up to record the instantaneous strand weight and, by inference, the unsteady

mass burning rate; the frequency passband of the system was 0 to 250 Hz. With the DB + 1% C propellant ( $a=100 \text{ cm}^{-1}$ ), dynamic extinction was observed for tests in nitrogen; reignition would occur for tests in air; reignition would not occur for tests in air with restricted samples; self-sustained burning was oscillatory in character (16-20 Hz). For the DB propellant without carbon addition ( $a=10 \text{ cm}^{-1}$ ) dynamic extinction could not be obtained (recall: maximum radiant flux way 10 cal/ cm<sup>2</sup>s); self-sustained burning was again oscillatory (10 Hz). For both propellants, when deradiation occurred, the burning surface was immediately covered with a dense distribution (100% for DB + 1% C and 50% for DB without carbon) of bubbles (0.1 mm diameter). The authors suggested that this may be associated with gas evolution breach, in the subsurface layer, caused by the sharp burning rate decrease. The authors further emphasized the multidimensional nature of phenomena occurring at and near the burning surface; unsteady and nonuniform character of burning surface, on microscale level, even for steady combustion; low frequency (10-20 Hz) burning associated with condensed thermal wave relaxation time, higher frequency (50 to 100 Hz) being probably associated with local small scales of burning surface.

#### § 1.3.3 - Nonlinear oscillating combustion

The original work of Huffington (Refs. 65-66) on chuffing and oscillatory burning of cordite goes back to the beginning of the '50. Experimental results and a theoretical interpretation, in terms of condensed phase thermal explosion, were given for both phenomena. The proposed mechanism for oscillatory burning of cordite is the successive explosion, assisted by gas phase heat feedback, of discrete surface layers of decreasing thickness with increasing pressure. The Frank-Kamenetskii thermal explosion theory (Ref. 67) was extended to consider a monodimensional slab of decomposing explosive, enclosed between two parallel walls, with one surface (hot boundary) subjected to a constant rate of heat transfer while the other (cold boundary) is maintained at a constant temperature. For cordite this temperature was taken as the melting temperature (460 K); for other cases it was just the ambient temperature. The solution determines, for a given heat transfer rate to the burning surface, the critical slab thickness and surface temperature above which the volumetric decomposition develops to explosive rates. These critical values were found to depend on the dimensionless parameter  $E_c^{\circ}/\alpha T_{\infty}$ , being  $E_c^{\circ}$  the activation energy of the distributed exothermic reaction (assumed of Arrhenius type) in the condensed phase and  $T_{\infty}$  the cold boundary temperature. The theory was quite successful in predicting, at 20 atm, a thickness of layer burnt off in a single explosion of about 50  $\mu\text{m}$  and a frequency of about 40

Hz. This theoretical approach, remarkable 25 years ago, suffers today the known limitations of the Frank-Kamenetskii type of theory.

A relatively large amount of work on oscillatory burning of several reactive materials, including DB and AP-based composite propellant, was performed by Soviet investigators. A good review, mostly focused on the theoretical aspects of this question, is contained in Novozhilov's monograph on solid propellant burning (Ref. 49). In particular, a numerical solution for the unsteady propagation of an exothermic reaction front in a gasless system (condensed phase energy equation coupled with a distributed chemical reaction rate term of Arrhenius type) was given in 1971 (Ref. 68). The rather vague mechanism invoked by the authors, to explain the oscillating combustion observed under a wide combination of the relevant parameters, relies on the "excess enthalpy" of the steadily propagating combustion front as compared with the enthalpy of the initial material. Librovich and Makhviladze (Ref. 69) took up this problem in 1974; they simplified the gasless system by considering a collapsed chemical layer separating the initial material from the combustion products. An analytical solution was found via an integral method (Fourier transform) and successfully compared with the previous numerical solution of Ref. 68. In both cases an increase of the activation energy was found to increase the period of the oscillating combustion rate and the amount of movement of the reaction front during one oscillation, but decrease the mean velocity. Frequencies were of the order of several 10 Hz. The oscillating mechanism, according to Librovich and Makhviladze, consists of a succession of fast burn-up of unreacted but heated layers, each requiring a prolonged thermal time lag for the ignition to occur.

Experimental results on self-sustained oscillatory combustion of pure and metallized DB propellants, both in a strand burner and rocket combustion chamber, were published by Svetlichny et al. (Ref. 70) in 1971. In the pressure range 1-140 atm, combustion oscillations (revealed by radiation emission and electrical conductivity of the burning zone) up to several 10 Hz were detected. The authors qualitatively ascribed these oscillations to unstable thermal relaxation of the condensed phase heated layer.

However, according to the same authors (Ref. 70), self-sustained oscillatory burning of the same DB propellants at pressure less than 70 atm is due to incomplete combustion. This and other oscillating mechanisms related to burning peculiarities (e.g., incomplete burning invoked in Ref. 70 and inhomogeneities of the combustion wave in Refs. 71-72) are out of the scope of this work. Oscillatory burning due to combustion/fluid-dynamics coupling (e.g., see Ref. 73) is also out of the scope of this work. In this work self-sustained oscillatory burning of exclusively thermokinetic character is considered for the wide class of heterogeneous combustion systems. It will be shown that this type of oscillatory burning is mainly related to the presence of a strongly exothermic chemical reaction in the condensed phase (collapsed at the burning surface). Pressure will be seen to favor stability. The combustion frequency, of the order of few 10-100 Hz, will be found to increase with pressure. The charac-

teristic burning rate spikes associated with these oscillations intuitively confirm the physical mechanism suggested by Librovich and Makhviladze (Ref. 69).

First detailed analytical predictions and numerical results, for a model explicitly considering the heterogeneous burning of a solid propellant (quasi-steady MTS flame), were offered by De Luca (Refs. 2-3) in 1976. Other results and an interpretation in terms of bifurcation diagrams were given by De Luca (Refs. 12, 18) later. Kooker and Nelson (Ref. 74) numerically confirmed the existence of a self-sustained oscillatory burning regime for solid propellants (the quasi-steady KTSS linearized flame model was adopted), but without making any attempt to predict the existence and the properties of such a special regime. The assumption of quasi-steady gas phase in these developments might be open to criticism, as rightly pointed out by T'ien (Ref. 75). Peters (Ref. 76) numerically observed self-sustained oscillations of hybrid burning of porous spherical particles of combustible material immersed in an infinite stagnant oxidizing atmosphere by solving, via an integral method (polynomial space dependence of the relevant variables), the governing set of 5 ODE's. A rigorous analytical treatment of the oscillating combustion associated with gasless burning of condensed systems discussed in Refs. 68-69 was recently offered by Matkowsky and Sivashinski (Ref. 77). They showed that a periodically pulsating solution arises as a Hopf bifurcation from the uniformly propagating solution, the bifurcation parameter being the product of a nondimensional activation energy and a factor measuring the difference between nondimensionalized temperatures of unburned reacting material and the combustion products. The amplitude, frequency, and velocity of the propagating pulsating front were also computed (within the framework of a nonlinear treatment).

CHAPTER 2 - NONLINEAR THEORY OF SOLID PROPELLANT COMBUSTION STABILITY

In this chapter an overview of the theoretical developments, both analytical and numerical, concerning nonlinear burning stability of solid propellants is offered. First the basic assumptions and equations are revised, then the transformation of the governing PDE into an ODE is performed. This allows us to define static and dynamic stability properties of burning solid propellants. For the first time with respect to previous reports by this research group:

- (a) results obtained by using MTS, KTSS (both linearized and nonlinear versions), KZ, and LC flame models are compared.
- (b) the validity of the nonlinear dynamic stability boundary is extended to complicated forcing functions such as simultaneous deradiation and depressurization, consecutive deradiation and depressurization, radiation pulses.
- (c) the nonlinear stability theory includes now the case of specific heat ratio not necessarily unity ( $C_g/C_c \neq 1$ ) and the case of radiative heat loss from the burning surface not necessarily zero ( $\epsilon \neq 0$ ).
- (d) the range of self-sustained oscillatory burning is investigated in detail both at large and low pressure.
- (e) new concepts about the pressure deflagration limit are illustrated in detail.
- (f) further results on ignition transients are presented.

Moreover, some detailed analyses of the MTS, KTSS (both linearized and nonlinear versions), KZ, and LC flame models are offered. Numerical computations verifying most of the analytical predictions are shown. A section on the state of the art of the nonlinear burning stability theory ends this chapter. Experimental results from shock tube and depressurization strand burner are reported in Ch. 3; experimental results by laser techniques are reported in Ch. 4.

### Sec. 2.1 - BACKGROUND AND NOMENCLATURE

The physical system dealt with is presented in its most general form in the schematic of Fig. 1a. The pressure of the vessel, the radiant flux impinging on the surface of the strand (originating exclusively from some external energy source), the ambient temperature measured at the cold boundary of the propellant sample (supposed to be infinitely long), and any other parameter which can be controlled in a known way from the outside of the vessel are designated as controlling parameters. A change of one or more of these controlling parameters will affect, in some way, the state of the physical system and, consequently, they are also called external perturbations.

On the other side, we designate as intrinsic perturbations sources all those "small" (in a sense to be specified) irregularities and imperfections always present in the real world but which are nevertheless neglected in the idealized picture of Fig. 1a. For example, nonuniform composition of the strand, impurities variously scattered in the condensed phase, complicated geometry of the burning surface, etc., all contribute to hopefully small but persistent differences of the actual phenomena from those described by mathematical models.

Whether the perturbation sources are external or intrinsic, the prior, supposedly unperturbed steady state profile of temperature in the combustion wave will be modified to some new perturbed unsteady profile. Let us define the disturbance temperature profile as the profile of the point-by-point difference between the perturbed profile and the original, unperturbed profile. The general problem of static stability may be stated as follows: given a stationary state of the physical system, the system is forced to a close but nonstationary state and it is asked whether the system, after a long enough period of time, will go back to its initial state or will move away from it. In the specific physical configuration considered in this study, it is asked whether the disturbance temperature profile will die out in time or not. Mathematically, the problem is an initial value problem and is usually described by a parabolic type of partial differential equation.

It is of concern to distinguish between static and dynamic stability. The general problem of dynamic stability may be stated as follows: given an initial stationary state of the physical system, the system is forced to a different (final) stationary state by means of appropriate changes in time of pressure and/or radiant flux and it is asked whether the system, after a long enough period of time, will reach the wanted final state or another(if existing)final state. In other words, the stability of a system where intrinsic perturbation sources exclusively are considered to be acting (stability of a state) is called static. Conversely, the sta-

bility of a system in which the external controlling parameters are changing in time and multiple final states exist (stability of a transition) is called dynamic. It will be shown that in the latter case the rate of change in time of the pressure, for example, is of fundamental importance and this explains the expression "dynamic stability".

In this research program, the ultimate objective is to establish boundaries separating regions of stability from those of instability on some convenient graphical plot. It will be shown that static and dynamic stability boundaries are different in nature.

Since the mathematical problem is formidable, no general method has been found so far for solving the stability problem in its various aspects. Historically, a large amount of work has been devoted to stability problems in fluid dynamics. A standard treatment in this and related fields is the linearized approach, which is based on two essential assumptions: disturbance quantities infinitesimally small and a mathematical model (differential equations, boundary conditions, and any other relationship) containing only disturbance quantities of first order. Under these hypotheses, the problem reduces to an eigenvalue formulation whose mathematical theory is very well developed. Besides this standard approach, several other approximate and often ad hoc methods have been set up in various fields of applied sciences. The reason for such a confusing state of affairs is essentially one: the behavior of most physical systems is described by nonlinear equations and nowadays not only a mathematical theory encompassing all types of nonlinearities, but even analytical methods capable of dealing with specific types of nonlinearities, are not yet available.

In this study, in order to avoid the serious drawbacks of any linearized treatment, a nonlinear combustion stability analysis by means of an approximate approach is offered. Basically, the problem will be transformed from a PDE into an ODE formulation via an integral method. Notice that the proposed approach requires the implementation of a flame model, since Zeldovich method is of no help (see Sec. 1.3). However, any flame model capable to describe quantitatively the heat feedback from the gas phase to the burning surface is in principle acceptable. The choice of the flame model is at the option of the investigator. Obviously, the proposed stability theory can only extract the stability properties (both static and dynamic) implicitly buried in any flame model. This fact, in turn, might help in the choice of the best flame model for a given combustion problem.

A composite, ammonium perchlorate based solid rocket propellant, denoted as AP/PBAA No. 941, is taken as datum case throughout this report. However, this by no means is meant to imply that the approach is restricted to some specific class of solid propellants. The physical and chemical properties of the propellant AP/PBAA No. 941 are listed in Tab.1.

**SEC. 2.2 - FORMULATION OF THE GENERAL QUASI-STEADY GAS  
PHASE TRANSIENT PROBLEM**

Except where explicitly excluded, the following set of assumptions is valid throughout this work. With reference to Fig. 1:

a) Entire Strand.

1. Monodimensional.
2. Constant thermal, physical, and chemical properties.
3. At cold boundary, in thermal equilibrium with ambient.
4. Subjected to no external forces (acceleration, gravity, electromagnetism).
5. No emission of radiation (only external radiation sources).

b) Condensed Phase.

1. Semi-infinite slab.
2. Uniform and isotropic composition.
3. Adiabatic, except at the burning surface.
4. No chemical activity.
5. No radiation scattering.
6. No photochemical effects.

c) Interface.

1. Infinitesimally thin plane surface (collapsed condensed phase reacting layer).
2. One-step, irreversible gasification process (pyrolysis).

d) Gas Phase.

1. Semi-infinite column of gas.
2. Mixture of thermally perfect gases of average molecular weight  $\bar{M}$ .
3. One-phase, laminar, nonviscous, strongly subsonic flow.
4. Adiabatic, except at the burning surface.
5. No interaction with (external) radiation.
6. Lewis number = 1, each chemical species has the same specific heat  $C_p$ , mass diffusion is expressed by Fick's law; therefore the gas phase can be described by a simple thermal model (see Sec. 2.3).
7. Quasi-steady behavior, with finite reacting layer thickness.

The following set of reference parameters is used for nondimensionalizing (with specific reference to the propellant AP/PBAA No. 941 taken as datum case; see also Tab. 1):

$P_{ref}$	$\equiv 68$	atm
$T_{ref}$	$\equiv 300$	K
$\mathcal{R}_{ref}$	$\equiv \mathcal{R}(P_{ref}) = 0.837$	cm/s
$T_{s,ref}$	$\equiv T_s(P_{ref}) = 1000$	K
$T_{f,ref}$	$\equiv T_f(P_{ref}) = 2430$	K
$x_{ref}$	$\equiv a_c/\mathcal{R}_{ref} = 1.673 \times 10^{-3}$	cm
$t_{ref}$	$\equiv a_c/\mathcal{R}_{ref}^2 = 1.998 \times 10^{-3}$	s
$Q_{ref}$	$\equiv C_c(T_{s,ref} - T_{ref}) = 231$	cal/g
$I_{ref}$	$\equiv \rho_c C_c \mathcal{R}_{ref} (T_{s,ref} - T_{ref}) = 297.8$	cal/cm <sup>2</sup> s

from which one gets the following nondimensional variables:

$\Psi$	$= P/P_{ref}$	nondim. pressure
$R$	$= \mathcal{R}/\mathcal{R}_{ref}$	nondim. burning rate
$X$	$= x/x_{ref}$	nondim. distance
$\delta$	$= d/x_{ref}$	nondim. thickness
$\delta_a$	$= (1/a_c)/x_{ref}$	nondim. absorption layer thickness
$\tau$	$= t/t_{ref}$	nondim. time
$H$	$= Q_s/Q_{ref}$	nondim. surface heat release
$Q$	$= Q_f/Q_{ref}$	nondim. gas heat release
$F_o$	$= I_o/I_{ref}$	nondim. radiant flux intensity
$q$	$= \psi/I_{ref}$	nondim. conductive heat flux.

Notice that for the temperature, both of the following definitions are used according to need:

$$(2.2.1a) \quad \theta(\ ) = \frac{T(\ ) - T_{ref}}{T_{s,ref} - T_{ref}}, \text{ e.g. } \theta_f = \frac{T_f - T_{ref}}{T_{s,ref} - T_{ref}}$$

$$(2.2.1b) \quad T(\ ) = \frac{T(\ )}{T(\ ),ref}, \text{ e.g. } T_f = \frac{T_f}{T_{f,ref}}$$

where the choice of the particular definition depends on the specific physical phenomenon being considered.

The general nondimensional quasi-steady gas phase transient formulation includes the unsteady condensed phase problem (Eq. 2.2.2), relationships accounting for the surface mass production (Eqs. 2.2.3), the quasi-steady gas phase problem (Eqs. 2.2.4 - 2.2.8), some auxiliary relationships assigning the gas phase and burning surface heat release (Eqs. 2.2.9 - 2.2.10) and the time history of the controlling parameters (Eqs. 2.2.11 - 2.2.12). Obviously, the gas phase treatment is not complete without the energy equation whose first integral gives the heat feedback law; this is discussed in Sec. 2.3. For details about the writing of the equations, the reader is referred to Ref. 3.

$$(2.2.2) \left\{ \begin{array}{l} \frac{\partial \theta}{\partial \tau} + R \frac{\partial \theta}{\partial X} = \frac{\partial^2 \theta}{\partial X^2} + N_t F_o f(X, \lambda) \quad \text{II PDE } \tau \geq 0, X \leq 0 \\ \theta(X, \tau = 0) = \text{assigned} \quad \text{IC} \\ \theta(X \rightarrow -\infty, \tau) = \theta_{-\infty} \quad \text{BC2} \\ \left( \frac{\partial \theta}{\partial X} \right)_{C,S} = \frac{\lambda_g}{\lambda_c} \left( \frac{\partial \theta}{\partial X} \right)_{g,S} + (1 - N_t)(1 - r_\lambda) F_o - q_1(\theta_s) \\ \quad - R \left[ H_{ref} + \frac{C_g - C_c}{C_c} (1 - \theta_s) \right] \quad \text{BC1} \end{array} \right.$$

where the boundary condition BC1 at  $X=0$  merely states the energy conservation at the burning surface (see Fig. 1b).

The specific form of the function  $f(X, \lambda)$  depends on the optical model of the condensed phase (absorbing vs absorbing-scattering) and nature of the external radiation source (monochromatic vs polychromatic and collimated vs uncollimated). If the impinging radiation is polychromatic, the burning surface reflectivity  $r(\lambda)$  in the boundary condition BC1 at  $X = 0$  shall be wavelength averaged; if the burning surface composition is not uniform,  $r(\lambda)$  shall also be surface averaged; if the burning surface is not a diffuse reflector, the angular dependence of  $r(\lambda)$  shall be taken into account. Details about the radiation distribution in the condensed phase and, more generally, about the derivation of Eq. 2.2.2 can be found in Ref. 7, for example. For the common case of an optically transparent condensed phase, assumed absorbing but not scattering, the familiar Beer's law is obtained

$$f(X, \lambda) = \frac{1 - r_\lambda}{\delta_a} \exp(X/\delta_a) \quad X \leq 0$$

to be evaluated at the particular operating wavelength if radiation is monochromatic.

In the boundary condition BC1 at  $x = 0$ :

$q_{g,s}(\Psi, R) = \frac{\lambda_g}{\lambda_c} \left( \frac{d\theta}{dx} \right)_{g,s}$  is the nondimensional heat feedback to be defined by a flame model;

$q_1(\theta_s)$  is the nondimensional heat loss from the burning surface to be explicitly given;

$H_{ref}$  is conventionally supposed positive if endothermic;  
 $N_t$  is a transparency factor ( $N_t = 0$  for opaque condensed phase and  $N_t = 1$  for transparent condensed phase).

The last point deserves some comment. The hypothesis of a collapsed reacting layer might imply in some cases that a certain thickness of condensed phase is shrunken to an infinitesimally small value. For consistency, the (external) radiant flux should be separated in a portion deposited directly at the surface (as if the propellant were opaque) and in a (remaining) portion distributed volumetrically in the condensed phase according to the proper extinction coefficient. The transparency factor  $N_t$ , therefore, should be set equal to the fraction of radiant flux absorbed in the reacting layer when it is thought of as extended. However, the extent and the very existence of a condensed phase reacting layer is an extremely controversial question. In this study  $N_t$  is taken either as 0 or 1, although this is not a necessity.

Heat losses from the burning surface typically occur by radiative emission:

$$q_1(\theta_s) = \epsilon \sigma \frac{\left[ \theta_s(T_{s,ref} - T_{ref}) + T_{ref} \right]^4 - \left[ \theta_a(T_{s,ref} - T_{ref}) + T_{ref} \right]^4}{\rho_c C_c k_{ref} (T_{s,ref} - T_{ref})}$$

being  $\epsilon$  the burning surface emissivity and  $\sigma$  the Boltzmann constant.

As to the surface mass production, the following combined pyrolysis is used according to need both for steady and unsteady states:

$$(2.2.3a) \quad R = \exp \left[ \frac{-E_s / \mathcal{R}}{T_{s,ref}} \left( \frac{1}{T_s} - 1 \right) \right] \quad \text{Arrhenius, } \theta_s \geq \theta_k$$

$$(2.2.3b) \quad R = (\theta_s - \theta_m)^w \quad \text{KTSS, } \theta_k \geq \theta_s \geq \theta_m$$

$$(2.2.3c) \quad R = 0 \quad \theta_s \leq \theta_m$$

where  $\theta_m$  is some empirically defined minimum temperature under which the solid propellant undergoes no chemical activity. The power  $w$  is determined by matching the two pyrolysis laws at a given surface temperature, say  $\theta_s = \theta_k$ , near the ambient temperature. This formulation of the pyrolysis law allows us to avoid the "cold boundary difficulty" of the Arrhenius expression.

Relationships for the quasi-steady gas phase include the mass continuity

$$(2.2.4) \quad U(x, \tau) = \frac{\rho_c}{\rho_g(x, \tau)} R(\tau) ;$$

the momentum equation describing a trivial pressure distribution (possibly changing in time)

$$(2.2.5) \quad \Psi(x, \tau) = \Psi(\tau) ;$$

the state equation (in dimensional terms)

$$(2.2.6) \quad P(t) = \rho_g(x, t) \frac{\rho}{m} T(x, t) ;$$

the integral energy balance assigning the quasi-steady flame temperature

$$(2.2.7) \quad \theta_f(\tau) = \theta_s + \frac{C_c}{C_g} (Q - \frac{q_{g,s}}{R}) ;$$

an estimate of the (average) characteristic flame thickness given by

$$(2.2.8) \quad x_f = R \tau_{re} \rho_c / \bar{\rho}_g = R \tau'_{re} (\lambda_g / \lambda_c) (C_c / C_g) = \bar{U} \tau_{re}$$

where  $\tau_{re}$  is a characteristic reaction time to be defined by a flame model.

The heat release in the gas phase can be assumed dependent on pressure only

$$(2.2.9) \quad Q(\Psi) = \bar{\theta}_s(\Psi) + \frac{C_g}{C_c} \left[ \bar{\theta}_f(\Psi) - \bar{\theta}_s(\Psi) \right] + \bar{H}(\Psi)$$

being the pressure dependent portion of the steady net heat release at the burning surface defined by

$$\bar{H}(\Psi) = H_{ref} + \frac{C_g - C_c}{C_c} \left[ 1 - \bar{\theta}_s(\Psi) \right]$$

The quantity  $H_{ref}$  has to be assigned independently and strictly depends on the original condensed phase composition only. For example, for the broad class of nonmetallized, AP composite propellants (Ref. 82c)

$$(2.2.10) \quad H_{ref} = \frac{p(+Q_{cr,AP} + Q_{v,AP} - Q_{NH_3/HClO_4}) + (1-p) Q_{v,Binder}}{C_C (T_{s,ref} - T_{ref})}$$

taking into account the:

- (1) endothermic processes of AP crystalline transition from orthorombic to cubic at  $240^0C$  and AP dissociative sublimation of zeroth order with respect to pressure.
- (2) exothermic reactions of the premixed  $NH_3/HClO_4$  flame due to AP decomposition (this flame is so thin down to 1 atm that it can be collapsed at the burning surface).
- (3) endothermic binder gasification.

The steady dependence of burning rate on pressure

$$\bar{R} = \bar{R} (\Psi)$$

at standard conditions (300 K ambient temperature and adiabatic combustion) is assumed experimentally known. The steady dependence of adiabatic flame temperature on pressure

$$\bar{\theta}_f = \bar{\theta}_f (\Psi)$$

is assumed known from standard equilibrium thermochemistry. For example, for the datum case considered (see Tab. 1), the following relationship was found to hold up to 100 atm: in dimensional terms

$$T_f(P) = T_{f,ref} - \frac{50}{68} (P_{ref} - P)$$

where  $T_{f,ref} = 2430$  K and  $P_{ref} = 68$  atm (Ref. 29b). The steady flame temperature in the presence of an external radiant flux can be obtained by the following integral energy balance in the gas phase

$$\bar{\theta}_f(\Psi, F_O) = \bar{\theta}_f(\Psi) + \frac{C_g - C_C}{C_g} \left[ \bar{\theta}_s(\Psi, F_O) - \bar{\theta}_s(\Psi) \right] + \frac{(1-\lambda)F_O - \dot{q}_1}{\bar{R}(\Psi, F_O)}$$

Finally, it is understood that:

$$(2.2.11) \quad \Psi(\tau) = \text{externally assigned}$$

$$(2.2.12) \quad F_O(\tau) = \text{externally assigned}$$

according to the wanted transient burning.

### Sec. 2.3 - QUASI-STEADY FLAME MODELS

In order to define explicitly the function  $q_{gas}(\Psi, R)$  required for the BC1 of the PDE describing the transient thermal profile in the condensed phase (Eq. 2.2.2), a flame model has to be chosen. It is emphasized that any flame model can be picked up. For the composite propellant AP/PBAA No. 941 taken as a datum case, several flame models were tested: MTS, KTSS (both developed by Summerfield and coworkers), KZ and LC. These flame models are all thermal in nature and invoke the assumptions mentioned in Sec. 2.2.

#### § 2.3.1 - MTS flame

The model worked out by Merkle, Turk, and Summerfield (MTS, Ref. 29) is basically a judicious combination, based on experimental data, of the diffusive and kinetic aspects of the gas phase reactions. The model worked out by Krier, T'ien, Sirignano, and Summerfield (KTSS, Ref. 83) can be seen as a particular case of the previous one when the flame is purely diffusion controlled. The MTS model will be used for most of the theoretical developments of this report. For a detailed knowledge of how the model is derived, the reader is referred to the original Ref. 29b and also to Refs. 82, 84-85 treating the GDF theory from which the MTS flame model has evolved. Only qualitative comments will be offered here.

Any pattern of chemical reactions, no matter how complicated, involves the two physically distinct phenomena of mass diffusion and chemical kinetics. It is known from homogeneous combustion theory that quite often diffusion processes dominate the kinetic processes in the sense that

$$\tau_{di}/\tau_{ki} \gg 1$$

or, conversely, the opposite extreme may be true. These two limiting configurations are respectively known as diffusion and premixed flames. For heterogeneous combustion, in particular of solid propellants, there are instances in which the gas phase portions of the deflagration wave may be treated according to one of the above limiting configurations. But, in principle, especially for transients connected to large excursions of the controlling parameters, the gas phase treatment of a heterogeneous combustion wave has to account for both processes. This was originally done by Summerfield in his GDF theory for the AP steady flame model. Later, an extension was made for the AP quasi-steady flame model accounting for variable flame and surface temperatures. Although derived for the specific case of the AP class of propellants, the formulation of the MTS flame model is quite general and may be adapted to other cases of heterogeneous combustion.

For the specific case of AP composite propellants, the MTS flame model accounts not only for the granular diffusion flame (GDF) of the oxidizer with the binder (Ref. 29), but also for a distended premixed flame corresponding to the AP decomposition products burning. In this study, the simplified version with the premixed flame collapsed at the burning surface has been adopted. This assumption is acceptable (p. 28 of Ref. 29b) for pressure values not lower than say, 1 atm. The most important parameter characterizing the gas phase during a quasi-steady transient is the heat feedback to the burning surface. According to the (collapsed) MTS flame model, the nondimensional heat feedback is

$$(2.3.1) \quad q_{g,s} = QR \left[ \frac{\sqrt{\tau'_{ki}}}{\sqrt{\tau'_{re}}} \exp(-R^2\tau'_{re}) + \frac{\sqrt{\tau'_{di}}}{\sqrt{\tau'_{re}}} \frac{1-\exp(-R^2\tau'_{re})}{R^2\tau'_{re}} \right]$$

where  $\tau'_{ki}$  is a nondimensional kinetic time parameter;  
 $\tau'_{di}$  is a nondimensional diffusion time parameter;  
 $\tau'_{re}$  is a nondimensional reaction time parameter;  
 $R$  is given by an Arrhenius-type pyrolysis law, typically.

Following the MTS flame model development, we put

$$(2.3.2) \quad \sqrt{\tau'_{ki}} = A_M \frac{T_f}{\Psi} \exp \left[ \frac{E_f/\mathcal{R}}{2T_{f,ref}} \left( \frac{1}{T_f} - 1 \right) \right]$$

where a second order gas phase reaction has been postulated to occur wholly at the highest temperature  $T_f$  (p. 29 of Ref. 82a) and

$$(2.3.3) \quad \sqrt{\tau'_{di}} = B_M \frac{(T_f)^{5/6}}{(\Psi)^{1/3} (T_s)^{7/8}}$$

where the diffusional mixing rate of fuel pockets with the surrounding atmosphere of oxygen-rich gases is assumed to depend on the surface temperature  $T_s$  (p. 31 of Ref. 82a).

The two constants  $A_M$  and  $B_M$  are determined for each propellant by the best fit of the steady state burning rate theory to the measured burning rate data (p. 38 of Ref. 29b). An application is shown in Fig. 2 for the propellant AP/PBAA No. 941. In the spirit of the GDF theory, it is further assumed (e.g., see p. 33 of Ref. 29b) that the overall solid

propellant reaction time parameter can be expressed as the following simple combination of the two above limiting cases:

$$(2.3.4) \quad \sqrt{\tau'_{re}} = \sqrt{\tau'_{di}} + \sqrt{\tau'_{ki}}$$

This relationship was shown to represent the pressure dependence of the burning rate quite accurately for a wide range of composite propellants (Ref. 82) and also to describe the depressurization extinction correctly for composite and, to some extent, double base propellants (Ref. 29). However, it should be recognized that the whole MTS approach depends on the arbitrary assumption of Eq. 2.3.4 and the choice of the  $A_M$  and  $M_B$  constants. How this choice is affected by the fitting procedure mentioned above is illustrated in Fig. 2 (different pressure interval) and Fig. 3 (different low end of the pressure interval).

### § 2.3.2 - KTSS flame

According to KTSS flame model, the nondimensional heat feedback to the burning surface (Ref. 83) is

$$(2.3.5) \quad \dot{q}_{g,s} = \frac{Q}{R} \frac{1 - \exp(-R^2 \bar{\tau}'_{di})}{\bar{\tau}'_{di}}$$

where  $\bar{\tau}'_{di}$  is an average nondimensional diffusion time parameter;

$R$  is given by a power pyrolysis law, typically.

Notice that the above KTSS heat feedback law, derived for a diffusionally controlled AP flame, is a particular case of the MTS heat feedback law where

$$\sqrt{\tau'_{re}} \approx \sqrt{\tau'_{di}} \gg \sqrt{\tau'_{ki}}$$

$$(2.3.6) \quad \tau'_{di} = \frac{B_M^2}{(\Psi)^{2/3}} \frac{(T_f)^{5/3}}{(T_s)^{7/4}} \approx \frac{\text{const}}{(\Psi)^{2/3}} = \bar{\tau}_{di}$$

that is, when the diffusion time parameter is much larger than the kinetic time parameter and is temperature independent. Extensive experimental investigation (Ref. 82) shows that for AP propellant flames the diffusional mixing is, indeed, sensibly slower than the chemical kinetics as long as the pressure is larger than say, 1 atm. It is also expected (Ref. 29) that flame temperature undershoots during decelerated transients slow down the chemical kinetics much more effectively than the diffusional mixing (compare Eq. 2.3.2 vs Eq. 2.3.3).

In its linearized version, the nondimensional KTSS heat feedback law is given by

$$(2.3.7) \quad \dot{q}_{g,s}(\Psi, R) = \frac{Q}{R\bar{\tau}'_{di}}$$

which is a particular case of the full expression (Eq. 2.3.5), when the further assumption is made that

$$(2.3.8) \quad \exp(-R^2\bar{\tau}'_{di}) \ll 1$$

corresponding to  $\bar{\tau}'_{di}$  very large but finite burning rate. The constraint of Eq. 2.3.8 is usually valid for steady burning, but is not acceptable in extinction transients, since under this circumstance  $R \rightarrow 0$  while  $\bar{\tau}'_{di}$  remains finite and, therefore,

$$\exp(-R^2\bar{\tau}'_{di}) \rightarrow 1.0$$

Note: in the linearized version commonly used, the nondimensional KTSS heat feedback law is written as

$$(2.3.9) \quad \dot{q}_{g,s}(\Psi, R) = \frac{\Psi^{2n}}{R} \left[ \Psi^{n/w} + \bar{H}(\Psi) \right]$$

Then, by comparing Eq. 2.3.7 with Eq. 2.3.9, the average non-dimensional diffusion time parameter can be evaluated

$$(2.3.10) \quad \bar{\tau}'_{di} = \frac{Q}{\Psi^{2n}} \frac{1}{\Psi^{n/w} + \bar{H}(\Psi)}$$

An essential ingredient for both MTS and KTSS flame models is the experimental stationary  $R(\Psi)$  curve. The steady state structure of the MTS and KTSS models are respectively shown in Fig. 4 and Fig. 5 for the propellant AP/PBAA No. 941. It is worthwhile to remark that even the linearized version of the KTSS model can accurately reproduce the experimental stationary  $R(\Psi)$ . A comparison of the two plots shows no strong difference as to the steady state behavior of the flame models under examination. Consider now the quasi-steady behavior as plotted in Fig. 6 (MTS model) and Fig. 7 (KTSS model). It is obvious that the linearized KTSS model is physically unrealistic for low burning rate.

In summary:

- (a) stationary or small perturbation solutions of the MTS and KTSS (even linearized) flame model are similar at high pressure, since in these instances only small changes in temperature and burning rate are considered;
- (b) at low pressure and/or low burning rate, AP flame is kinetically controlled and therefore should not be described by the KTSS (even nonlinearized) model;

(c) the KTSS linearized model can never predict extinction because the heat feedback law is found to be inversely proportional to the burning rate.

§ 2.3.3 - KZ flame

According to KZ flame model, the nondimensional heat feedback to the burning surface (Ref. 86) is

$$(2.3.11) \quad \dot{q}_{g,s} = \frac{Q}{R} \frac{C_c}{C_g} \frac{\alpha_c}{\rho_c} \frac{\dot{\omega}(\tau)}{\dot{\omega}_{ref}^2} \left[ 1 - \exp(-R \frac{\lambda_c}{\lambda_g} \frac{C_g}{C_c} x_f) \right]$$

where

$$(2.3.12) \quad \frac{\alpha_c}{\rho_c} \frac{\dot{\omega}(\tau)}{\dot{\omega}_{ref}^2} = \text{const.} \Psi^\beta(\tau) \cdot \exp\left(-\frac{E_f/Q}{T_{f,ref}} \frac{1}{\tau_f}\right)$$

is a nondimensional mass reaction rate per unit volume ( $\dot{\omega}$  is measured in  $\text{g/cm}^3\text{s}$ ). The power  $\beta$  is the reaction order of the overall, one-step, irreversible kinetics controlling the gas phase heat release. Taking into account the quasi-steady mass continuity, one can write

$$(2.3.13) \quad \frac{\lambda_c}{\lambda_g} \frac{C_g}{C_c} x_f = \frac{\lambda_c}{\lambda_g} \frac{C_g}{C_c} \frac{\rho_c}{\rho_g} R(\tau) \bar{\tau}_{ki} = R(\tau) \bar{\tau}'_{ki}$$

where  $\bar{\tau}'_{ki}$  is an average nondimensional kinetic time parameter. The heat feedback is more concisely given by

$$(2.3.14) \quad \dot{q}_{g,s} = Z \frac{\Psi^\beta}{R} \left[ 1 - \exp(-R^2 \bar{\tau}'_{ki}) \right]$$

where  $R$  is assigned by an Arrhenius pyrolysis law and  $Z$  is a constant to be evaluated for each propellant.

The further assumption of linearized behavior, i.e.

$$(2.3.15) \quad \exp(-R^2 \bar{\tau}'_{ki}) \ll 1$$

requiring  $\bar{\tau}'_{ki}$  very large but finite burning rate, was invoked by the authors (Ref. 86). In the version commonly used, the heat feedback is

$$(2.3.16) \quad \dot{q}_{g,s}(\Psi, R) = Z \frac{\Psi^\beta(\tau)}{R(\tau)}$$

Obviously, the same comments made above with reference to KTSS linearized flame are now in order. The authors suggest

to evaluate the constant  $Z$  from the initial (steady) condition of the burning transient as

$$(2.3.17) \quad Z = \bar{R}_i^2 \frac{\bar{\theta}_{i,s} + \bar{H}_i}{\psi_i^\beta}$$

Remark that in this way the flame model is not able to recover the steady state results. Although the authors state that the difference is not important, this is embarrassing. In this work, a different approach was taken: the constant is evaluated at each pressure in such a way that the experimental curve  $\bar{R}(\psi)$  is reproduced

$$(2.3.18) \quad Z(\psi) = \bar{R}^2(\psi) \frac{\bar{\theta}_s(\psi) + \bar{H}}{\psi^\beta}$$

Under these circumstances, KZ and KTSS linearized flame model are found to be identical from the point of view both of heat feedback and burning stability.

The KZ heat feedback, derived for a kinetically controlled AP flame, is conceptually a particular case of the MTS heat feedback when

$$\sqrt{\tau'_{re}} \approx \sqrt{\tau'_{ki}} \gg \sqrt{\tau'_{di}}$$

However, from a physical point of view this limiting condition seems more typical of DB rather than AP-based solid propellants. In any event, KZ formalism is similar to KTSS since both models assume a distributed heat release of uniform value over the flame thickness  $X_f$  (in both cases the flame is supposed attached to the burning surface).

#### § 2.3.4 - LC flame

According to LC flame model, the nondimensional heat feedback to the burning surface (Ref. 87) is

$$(2.3.19) \quad q_{q,s} = \frac{\bar{R}'}{\bar{R}(\tau)} \left[ \frac{C_q}{C_c} \frac{E}{\Lambda} \left( \frac{1}{1 + \frac{n_s - n}{E} \ln \psi} - 1 \right) + 1 + H_{ref} \right]$$

where  $E \equiv \frac{E_s / \tau}{T_{s,ref}}$

$$\Lambda \equiv E \left( 1 - \frac{T_{\infty}}{T_{s,ref}} \right)$$

The pyrolysis law used by LC is a generalized version of Arrhenius expression including a pressure dependence through the power  $n_s$  (usually  $n_s = 0$ ). With the nomenclature used in

Ref. 87, one finds for Eq. 2.2.3a

$$(2.3.20) \quad R(\tau) = \psi^n_s \exp \left[ \frac{A(\theta_s - 1)}{1 + \frac{A}{E}(\theta_s - 1)} \right]$$

The pressure dependent portion of the heat feedback law, assumed the same as in the steady state, is embodied in Eq. 2.3.19 without ever specifying what the dependency is. KTSS and KZ also assumed the pressure dependent portion of the heat feedback law to be the same as in the steady state, but enforced respectively a diffusion and a kinetics controlled burning mechanism.

Both KZ and LC flame models were derived under the same constraint (large characteristic times) as the linearized KTSS; they are subjected to the same limitations of applicability as well. While KTSS and LC recover the steady state burning rate dependence on pressure when transient effects vanish, KZ does not. Although differences at steady state can be small if an appropriate choice of  $\beta$  is made, this is a weakness of KZ flame.

#### § 2.3.5 - Working Map for Quasi-Steady Gas Phase

A useful comparison for what follows is shown in Fig. 8, where the MTS heat feedback (often used in this study) and the linearized KTSS heat feedback (commonly used in the literature) are plotted together in the range 10 to 50 atm ( $\dot{q}_{g,s}$  curves). From this graphical plot one observes that, for a given set of external conditions, two steady solutions (reacting configuration A and unreacting configuration C) are found for the MTS model, but only one for the linearized KTSS model (reacting configuration A).

It is instructive at this point to consider the working map of Fig. 9. This is a  $R$  vs  $\dot{q}_{g,s}(\Psi, R)$  plot applicable to any flame model. In Fig. 9 MTS flame was implemented under the indicated conditions. Isobaric curves describe the heat feedback at the corresponding pressure; remark that  $\dot{q}_{g,s}(\Psi, R=0) = 0$ . Lines at constant ambient temperature (for adiabatic burning) or at constant radiant flux (for  $\theta_{\infty}=0$ ) describe the steady heat flux absorbed in the condensed phase

$$\left( \frac{d\bar{\theta}}{dx} \right)_{g,s} \equiv \bar{q}_{g,s}(\Psi, F_o, \theta_{\infty}) = \bar{R}(\bar{\theta}_s - \theta_{\infty}) + \bar{R}\bar{H} - (1-r_{\lambda})F_o$$

At the crossing of  $\dot{q}_{g,s}(\Psi, R)$  with  $\bar{q}_{g,s}(\Psi, F_o, \theta_{\infty})$ , steady solutions  $R(\Psi, F_o, \theta_{\infty})$  vs  $\dot{q}_{g,s}$  are singled out. Curves  $\dot{q}_{g,s}(\Psi, R)$  depend on the flame modeling, curves  $\bar{q}_{g,s}(\Psi, F_o, \theta_{\infty})$  depend on external parameters only. Two steady solutions are found for each set of external parameters: the trivial  $R = 0$  (unreact-

ing state) and some  $\bar{R} \neq 0$  (reacting state). For quasi-steady gas phase transients driven by decradiation for example, the instantaneous solution in time runs on the isobaric curve of interest; only when a steady burning configuration is reached, the solution will stop at the crossing with the relevant  $Q_g$ 's curve. Similar remarks hold true for any flame model, except that the unreacting or extinguished state  $\bar{R} = 0$  is not allowed for linearized (in the sense of Eq. 2.3.8) models.

By decreasing ambient temperature and/or external radiant flux (negative values of  $P_g$  imply heat loss from burning surface), the corresponding  $\bar{R}(\Psi, F_0, 0_\infty)$  are seen in Fig. 9 to become lower and lower at any pressure. The question arises: are there minimum values of  $\Psi, F$ , and  $0_\infty$  below which  $\bar{R} \neq 0$  is not allowed or, if allowed, is unstable? This would assign static limits to burning domain of the flame model under consideration. The answer for decreasing heat loss is shown in Figs. 31-33 (to be discussed later): the point of maximum heat feedback roughly corresponds to the minimum allowed steady burning rate at any given pressure. For  $0_\infty \rightarrow 0.429$  (zero Kelvin), it is found in Fig. 10 that the steady solution does not reach this minimum (steady) burning rate; but obviously other effects would come into play at low ambient temperature. For decreasing pressure (with adiabatic burning at  $0_\infty = 0$ ), a steady solution is always found. However, it will be seen in this report that burning instability shows up defining a pressure deflagration limit  $P_{DL}$ ; this will require further analysis. Remark that so far no constraint whatsoever has been placed on unsteady burning.

Burning stability properties will be shown to be strongly affected by the value of the surface heat release. For our datum case (see Tab. 1), the best value computed from the literature is  $Q_s = -158.2$  cal/g (the exothermicity is due to the primary premixed ammonia/perchloric acid flame occurring when ammonium perchlorate decomposes). For the MTS flame, parametric changes of  $Q_s$ , while  $T_f(P)$  is kept fixed, imply to evaluate the appropriate set of  $A_M$  and  $B_M$  constants for each value of  $Q_s$  in order to maintain the same (experimental) burning rate law  $\bar{R}(P)$ . Alternatively, one can use just one set of  $A_M$  and  $B_M$  constants (for example, that corresponding to the standard value of  $Q_s = -158.2$  cal/g) and consider a family of solid propellants whose burning rate  $\bar{R}(P)$  depends on  $Q_s$  according to the graphical plot of Fig. 11 (see also Tab. 2). This second point of view was adopted in this report. For the KTSS flame such a problem does not arise, since no fitting is required.

#### §2.3.6 - Final Comments on Quasi-Steady Gas Phase

The modelling approach discussed in this report, being of rather general formulation, can be specialized to any transient burning problem within the basic limitation of

nondimensional thin flames of thermal character. In particular, dynamic burning associated with fast depressurization and/or deradiation can be studied. The range of validity is essentially established by that of the flame model. Among the flame models reported in this chapter, the most general is MTS whose range of validity, with the formulation given in Eqns. 2.3.1 - 2.3.4, covers 1 to 100 atm (p. 27 of Ref. 29c). For pressures above 100 atm, the assumptions of monodimensionality (condensed and gaseous thermal waves much larger than burning surface roughness) and condensed phase homogeneity (condensed phase thermal wave much larger than mean particle size) fail for MTS as well as all other flame models considered in this chapter. For pressures less than 1 atm, a distended  $\text{NH}_3/\text{HClO}_4$  premixed flame should be considered in MTS flame; this was done by Merkle (pp. 49-53 of Ref. 29c) but is not reported here.

Even within these validity limits, from a rigorous point of view extinction (and ignition) transients cannot be described by quasi-steady gas phase models. Indeed, these phenomena are intrinsically unsteady. However, error due to applying quasi-steady gas phase assumption is estimated negligible to the extent in which the gas phase characteristic times are small with respect to the condensed phase thermal wave characteristic time.

With these restrictions in mind, one can pick up its favorite pyrolysis law and flame model, assign the wanted external laws  $\Psi(\tau)$  and  $F_0(\tau)$ , select the appropriate optical model and thermal properties for the condensed phase, enforce the correct initial conditions, and finally numerically integrate the PDE of Eq. 2.2.2. What do we get? Trends and bounds, but no predictions. For static as well as dynamic burning, more sophisticated analyses are required. This is discussed in next section. Nevertheless, the importance of numerical approach cannot be overlooked; complete burning transients cannot be evaluated otherwise. Several transients obtained by numerical integration will be shown later.

Sec. 2.4 - AN ORDINARY DIFFERENTIAL EQUATION FORMULATION  
OF THE PROBLEM

Basically, the mathematical method is the one set up for the first time by Von Karman and Prandtl in the study of boundary layers and later generalized by Goodman, among others, to a large number of thermal problems. The method can be extended to any other problem described by nonlinear PDE of parabolic type. In our case, the approach consists in defining a parameter  $\xi(t)$ , called the penetration distance of the thermal wave in the condensed phase, "such that for  $x \geq \xi(t)$  the propellant slab, for all practical purposes, is at an equilibrium temperature and there is no heat transferred beyond this point" (p.53 of Ref. 78). The evolution in time of the thermal profile in the condensed phase is obtained by following the time history of the penetration distance propagating into an initially uniform temperature field. Within this penetration layer, progressing in time, the qualitative space distribution of temperature is assumed known *a priori*; but we make sure that, in so doing, the integral balance of thermal energy in the condensed phase is preserved. In other words, the price to be paid for making the transformation from PDE to ODE formulation is an approximate solution of the local space distribution of temperature; this is not such a serious drawback because the interest is in the time evolution of the surface temperature. In any event, several investigations found an error of only some percents for various cases in which both the exact and the integral solutions were evaluated. For example, see Fig. 5 on p. 89 of Ref. 78 showing the temperature time history at the surface of a semi-infinite slab with triangular surface heat flux.

In order to get a deeper understanding of questions related to the integral method as applied to thermal problems, the interested reader might wish to consult the excellent review by Goodman (Ref. 78) and the references given there. Before getting involved in mathematical details, the reader should be warned about the limits of the integral method. Any solution obtained by the integral method contains hopefully small but irrevocable errors in the final numerical results. The question of how to improve the accuracy then arises. It has been argued that "there is no *a priori* guarantee that increasing the order of the polynomial (used to represent the space distribution of the unsteady temperature profile) will improve the accuracy. Although the accuracy is frequently improved with this technique, it can be demonstrated, nonetheless, that there are cases for which it actually worsens" (p.96 of Ref. 78). In this same reference it is suggested that the method of weighted residuals provides a very efficient method for improving the accuracy of the results obtained by using the integral method.

The simple integral method implemented in this work can be considered a special case of the method of weighted residuals when just one parameter (the penetration distance  $\xi$ ) and one weighting function are considered. Under these circumstances, the only equation to be considered is the heat balance integral (see below). Since the integral method assumes a uniform initial distribution of temperature, a new nondimensional variable is defined:

$$(2.4.1) \quad u(x, \tau) \in \bar{O}(x) = O(x, \tau) \quad x \leq 0$$

where

$$(2.4.2) \quad \bar{O}(x) = O_{\infty} + (\bar{O}_s - O_{\infty}) e^{\frac{X\bar{R}}{x}} \quad x \leq 0$$

is the initial steady state distribution of temperature and  $O(x, \tau)$  is the temperature distribution following some perturbation. The new variable  $u(x, \tau)$  may therefore be conveniently interpreted as the finite temperature disturbance propagating inside the condensed phase and superimposed on the initial temperature distribution after the action of perturbation. At the initial instant  $\tau=0$ , by definition  $O(x, \tau) = \bar{O}(x)$  and  $u(x, \tau) = 0$ . Suppose now that, in the following instant, a perturbation starts acting on the system and makes  $u(x, \tau) \neq 0$ : the goal of the analysis is to determine the ultimate effect of such a temperature disturbance after waiting a period of time sufficiently long for the perturbation to disappear. No assumption whatsoever is made as to the size of the temperature disturbance.

The analysis will be restricted to the case of an optically opaque propellant, in the sense that

$$(a_c/\lambda) / (1/a_{\lambda}) \gg 1$$

at constant (not necessarily reference) ambient temperature  $O_{\infty}$ . The basic set of nondimensional equations for an optically opaque propellant ( $N_t=0$ ), initially burning with constant rate  $R$  at constant pressure  $\Psi$ , while subjected to a radiant flux of constant intensity  $F_o$ , is

$$(2.4.3) \quad \left\{ \begin{array}{l} \frac{\partial O}{\partial \tau} + R \frac{\partial O}{\partial X} = \frac{\partial^2 O}{\partial X^2} \quad \text{II PDE} \\ O(x, \tau=0) = \bar{O}(x) \quad \text{IC} \\ O(x=-\infty, \tau) = O_{\infty} \quad \text{BC2} \\ \left( \frac{\partial O}{\partial X} \right)_{C,S} = \frac{\lambda}{C} \left( \frac{\partial O}{\partial X} \right)_{G,S} - R \left[ H_{ref} + (C_g/C_c - 1)(1 - O_s) \right] + (1 - r_{\lambda}) F_o - \dot{q}_1(O_s) \quad \text{BC1} \end{array} \right.$$

where  $R(\tau)$  is the burning rate defined by any appropriate pyrolysis law and  $(\lambda_c/\lambda_g)(\partial\bar{\theta}/\partial X)_{g,s} \cdot \dot{q}_{g,s}(\bar{\theta}, R)$  is the heat feedback law defined by any appropriate flame model. In terms of the disturbance temperature  $u(X, \tau)$ , the set of equations is:

$$(2.4.4) \quad \left\{ \begin{array}{l} \frac{\partial u}{\partial \tau} = R \left( \frac{d\bar{\theta}}{dX} - \frac{\partial u}{\partial X} \right) + \frac{\partial u^2}{\partial X^2} - \frac{d^2 \bar{\theta}}{dX^2} \\ u(X, \tau=0) = 0 \\ u(X \rightarrow -\infty, \tau) = 0 \\ \left( \frac{\partial u}{\partial X} \right)_{c,s} = \frac{\lambda_g}{\lambda_c} \left( \frac{\partial u}{\partial X} \right)_{g,s} - \frac{\lambda_g}{\lambda_c} \left( \frac{d\bar{\theta}}{dX} \right)_{g,s} + R \left[ H_{ref} + \left( \frac{C_g}{C_c} - 1 \right) (1 - \bar{\theta}_s + u_s) \right] \\ \quad + \left( \frac{d\bar{\theta}}{dX} \right)_{c,s} - (1 - r_\lambda) \bar{F}_o + \dot{q}_1 (\bar{\theta}_s - u_s) \end{array} \right.$$

where

$$(2.4.5) \quad \left\{ \begin{array}{ll} R(\tau) = \exp \left[ \frac{-E_s/\varrho}{T_{s,ref}} \left( \frac{1}{(\bar{\theta}_s - u_s)(1 - \frac{T_{ref}}{T_{s,ref}}) + \frac{T_{ref}}{T_{s,ref}}} - 1 \right) \right] & \text{for } (\bar{\theta}_s - u_s) > \theta_k \\ R(\tau) = \left[ \bar{\theta}_s - u_s(\tau) \right]^w & \text{for } (\bar{\theta}_s - u_s) \leq \theta_k \end{array} \right.$$

Notice that at the initial instant  $\tau=0$ , the surface energy balance is

$$(2.4.6) \quad \left( \frac{d\bar{\theta}}{dX} \right)_{c,s} - \frac{\lambda_g}{\lambda_c} \left( \frac{d\bar{\theta}}{dX} \right)_{g,s} - (1 - r) \bar{F}_o + \dot{q}_1 (\bar{\theta}_s) = \bar{R} \left[ H_{ref} + \left( \frac{C_g}{C_c} - 1 \right) (1 - \bar{\theta}_s) \right]$$

where

$$(2.4.7) \quad \left\{ \begin{array}{ll} \bar{R} = \exp \left[ \frac{-E_s/\varrho}{T_{s,ref}} \left( \frac{1}{\bar{\theta}_s (1 - \frac{T_{ref}}{T_{s,ref}}) + \frac{T_{ref}}{T_{s,ref}}} - 1 \right) \right] & \text{for } \bar{\theta}_s > \theta_k \\ \bar{R} = \bar{\theta}_s^w & \text{for } \bar{\theta}_s \leq \theta_k \end{array} \right.$$

Therefore, BC1 of Eq. 2.4.4 can also be written as

$$(2.4.8) \quad \left( \frac{\partial u}{\partial x} \right)_{c,s} \equiv (u_x)_{c,s} = \frac{\lambda_g}{\lambda_c} \left( \frac{\partial u}{\partial x} \right)_{g,s} + (1-r_\lambda) (\bar{F}_o - \bar{r}_o) - \left[ \dot{q}_1 (\bar{0}_s) - \dot{q}_1 (\bar{0}_s - u_s) \right] \\ - \left[ \bar{R} \left[ H_{ref} + \left( \frac{C_g}{C_c} - 1 \right) (1 - \bar{0}_s) \right] - R \left[ H_{ref} + \left( \frac{C_g}{C_c} - 1 \right) (1 - \bar{0}_s + u_s) \right] \right].$$

The transformation into an ODE of the PDE of Eq. 2.4.4, with BC1 given by Eq. 2.4.8, can be performed by assuming a polynomial dependence of the disturbance temperature on the space variable:

$$(2.4.9) \quad u(x, \tau) \stackrel{\sim}{=} K_0(\tau) + K_1(\tau) x + K_2(\tau)x^2 + \dots + K_n(\tau)x^n.$$

Comments about the implications of this particular thermal profile are given below. The above  $n+1$  coefficients  $K_i(\tau)$  are to be determined from the boundary conditions which express no disturbance (up to the  $(n-1)$ -th derivative) at the cold end of the penetration depth and the energy balance at the hot boundary of the penetration depth. With our formulation this implies:

$$(2.4.10) \quad \left. \begin{array}{l} 1. \quad \frac{\partial u}{\partial x} (x = 0, \tau) = (u_x)_{c,s} \\ 2. \quad u(x = x_\xi, \tau) = 0 \\ 3. \quad \frac{\partial u}{\partial x} (x = x_\xi, \tau) = 0 \\ \vdots \\ n+1. \quad \frac{\partial^{n-1} u}{\partial x^{n-1}} (x = x_\xi, \tau) = 0 \end{array} \right.$$

where  $x_\xi = -\xi(\tau)$  is the penetration distance to be obtained below. After algebraic manipulations, one obtains for the unknown profile of the disturbance temperature

$$u(x, \tau) = (u_x)_{c,s} \frac{\xi}{n} (1 + \frac{x}{\xi})^n.$$

For  $x = 0$  one obtains at the burning surface

$$u(x = 0, \tau) \equiv u_s = (u_x)_{c,s} \frac{\xi}{n}$$

from which the unknown penetration depth can be expressed as

$$(2.4.11) \quad \xi(\tau) = n \frac{u_s}{(u_x)_{c,s}} \quad .$$

The disturbance temperature profile is then given by

$$(2.4.12) \quad u(x, \tau) = u_s \left(1 + \frac{x}{\xi}\right)^n \quad 0 < |x| < \xi(\tau)$$

where  $u_s(\tau)$  is the unknown surface temperature disturbance to be determined. It is obvious from the above relationship that the time history of the disturbance temperature is restricted to disturbance thermal profiles monotonically decaying in space. Indeed, there is no way for this polynomial profile to accommodate an inflection point. The difficulty may be overcome by "allowing a new penetration depth to begin propagating at each maximum or minimum" (p. 96 of Ref. 78) of the heat input into the condensed phase. However, this procedure will not prove necessary here, since testing both the static and dynamic stability does not require a detailed knowledge of the structure of the thermal profile.

A space integration can now be performed over  $x$  from 0 to  $-\xi(\tau)$  of the PDE:

$$(2.4.13) \quad \frac{d}{d\tau} \int_0^{-\xi(\tau)} u(x, \tau) dx = R u_s - (u_x)_{c,s} - R \Delta(\bar{u}) + \Delta(\frac{du}{dx})$$

where

$$(2.4.14) \quad \left\{ \begin{array}{l} \Delta(\bar{u}) = \bar{u}(x=0) - \bar{u}(x=-\xi) \\ \Delta(\frac{du}{dx}) = \frac{du}{dx}(x=0) - \frac{du}{dx}(x=-\xi) \end{array} \right.$$

being  $\xi(\tau)$  defined by Eq. 2.4.11. Upon substituting the approximate disturbance temperature profile described by Eq. 2.4.12, the following differential expression is obtained:

$$(2.4.15) \quad \frac{d}{d\tau} \frac{u_s^2}{(u_x)_{c,s}} = - \frac{n+1}{n} \left[ R u_s - (u_x)_{c,s} - R \Delta(\bar{u}) + \Delta(\frac{du}{dx}) \right]$$

Since  $(u_x)_{c,s} = f(u_s(\tau); \Psi(\tau), F_O(\tau))$ , one obtaines from Eq. 2.4.8

$$(2.4.16) \frac{d(u_x)_{c,s}}{d\tau} = \frac{du_s}{d\tau} \left[ \frac{\partial(u_x)_{c,s}}{\partial u_s} \right]_{\Psi, F_O} + \frac{d\Psi}{d\tau} \left[ \frac{\partial(u_x)_{c,s}}{\partial \Psi} \right]_{u_s} - (1-r_\lambda) \frac{dF_O}{d\tau} .$$

For example, the time derivative of the thermal gradient at the condensed phase side may be explicitly written as

$$(2.4.17) \frac{d(u_x)_{c,s}}{d\tau} = \frac{du_s}{d\tau} \left[ \frac{\lambda_q}{\lambda_c} \left( \frac{\partial(u_x)_{c,s}}{\partial u_s} \right)_{\Psi} + \frac{d(R \left[ R_{ref} + \frac{C_q}{C_c} (1 - \bar{U}_s + u_s) \right] + \dot{q}_1)}{du_s} \right] + \frac{\lambda_q}{\lambda_c} \frac{d\Psi}{d\tau} \left( \frac{\partial(u_x)_{c,s}}{\partial \Psi} \right)_{u_s} - (1-r_\lambda) \frac{dF_O}{d\tau}$$

which can be evaluated once a flame model has been chosen and the laws  $\Psi(\tau)$  and  $F_O(\tau)$  have been externally assigned. By deriving, one obtains from Eqs. 2.4.15 and 2.4.16

$$(2.4.18) \frac{1}{(u_x)_{c,s}^2} \left[ 2u_s \frac{du_s}{d\tau} (u_x)_{c,s} - u_s^2 \left[ \frac{du_s}{d\tau} \left[ \frac{\partial(u_x)_{c,s}}{\partial u_s} \right]_{\Psi, F_O} + \frac{d\Psi}{d\tau} \left[ \frac{\partial(u_x)_{c,s}}{\partial \Psi} \right]_{F_O, u_s} \right] - (1-r_\lambda) \frac{dF}{d\tau} \right] = - \frac{n+1}{n} \left[ R u_s - (u_x)_{c,s} - R \Delta(\bar{O}) + \Delta(\frac{d\bar{O}}{dX}) \right] .$$

Finally, the following nonlinear ODE for the time dependent surface temperature disturbance is obtained:

$$(2.4.19) \frac{du_s}{d\tau} = - \frac{n+1}{2n} \frac{(u_x)_{c,s}}{u_s} \frac{R u_s - (u_x)_{c,s} - R \Delta(\bar{O}) + \Delta(\frac{d\bar{O}}{dX})}{1 - \frac{1}{2} \frac{u_s}{(u_x)_{c,s}} \left[ \frac{\partial(u_x)_{c,s}}{\partial u_s} \right]_{\Psi, F_O}} + \frac{\frac{d\Psi}{d\tau} \left[ \frac{\partial(u_x)_{c,s}}{\partial \Psi} \right]_{F_O, u_s} - (1-r_\lambda) \frac{dF_O}{d\tau}}{2 \frac{(u_x)_{c,s}}{u_s} - \left[ \frac{\partial(u_x)_{c,s}}{\partial u_s} \right]_{\Psi, F_O}}$$

with  $u_s(\tau=0) = 0$

which is approximately equivalent to the initial PDE+boundary conditions formulation. Notice that in the above equation  $\bar{v}(x)$  is known (see Eq. 2.4.2) and that only the surface temperature appears.

The above nonlinear ODE in the unknown  $u_s(\tau)$  describes the response of the system to a finite size departure of the surface temperature from the stationary value due not only to intrinsic perturbation sources acting on the system (static stability), but also to any arbitrary but externally assigned monotonical change in time of controlling parameters such as pressure and radiant flux (dynamic stability). If one wishes to know the whole temperature profile, he has only to substitute  $u_s(\tau)$  in Eq. 2.4.12, evaluate  $\xi(\tau)$  from Eq. 2.4.11 with the help of Eq. 2.4.8, and then use the  $u_s(\tau)$  definition (Eq. 2.4.1) in order to determine the resultant temperature profile.

Considerations of a general character on the static stability of the system described by Eq. 2.4.19 can now be made. A given equilibrium configuration of the system is asymptotically stable if

$$\left. \begin{array}{l} u_s(\tau) \rightarrow 0 \\ \text{or} \\ 0(x, \tau) \rightarrow \bar{v}(x) \end{array} \right\} \text{for } \tau \rightarrow \infty$$

In other words, the system is (asymptotically) stable if the disturbance disappears at large time and the system returns to its initial steady configuration. Following Lyapunov (p. 216 of Ref. 88), Eq. 2.4.19 can be written, in a more concise way, as

$$(2.4.20) \left\{ \begin{array}{l} \frac{du_s}{d\tau} = - f(u_s) + g(\tau, u_s) \\ u_s(\tau=0) = 0 \end{array} \right.$$

where

$$(2.4.21) \quad f(u_s) \equiv \frac{n+1}{2n} \frac{(u_x)_{c,s}}{u_s} \frac{R u_s - (u_x)_{c,s} - R \Delta(\bar{v}) + \Delta(\frac{d\bar{v}}{dx})}{1 - \frac{1}{2} \frac{u_s}{(u_x)_{c,s}} \left[ \frac{\partial (u_x)_{c,s}}{\partial u_s} \right]_{\Psi, F_O}}$$

is the autonomous (i.e., time independent) contribution, and

$$(2.4.22) \quad g(\tau, u_s) \equiv \frac{\frac{d\Psi}{d\tau} \left[ \frac{\partial (u_x)_{c,s}}{\partial \Psi} \right]_{F_O, u_s} - (1-\chi_\lambda) \frac{dE}{d\tau}}{2 \frac{(u_x)_{c,s}}{u_s} - \left[ \frac{\partial (u_x)_{c,s}}{\partial u_s} \right]_{\Psi, F_O}}$$

is the nonautonomous (i.e., time dependent) contribution. If no forcing function is acting on the system, i.e.

$$\Psi = \text{cost} \quad \text{and} \quad F_o = \text{cost},$$

then Eq. 2.4.20 reduces to

$$(2.4.23) \quad \frac{du_s}{d\tau} = - f(u_s)$$

by which the autonomous contribution assumes the meaning of a static restoring function. Indeed, under these circumstances, one can think of the chemically reacting system comprised of the deflagrating condensed material as analogous to a mass-spring type of mechanical system which the non-linear characteristic  $f(u_s)$ . Considering the  $u_s(\tau)$  definition of Eq. 2.4.1, Eq. 2.4.20 can also be written as

$$(2.4.24) \quad \left\{ \begin{array}{l} \frac{d\theta_s}{d\tau} = f(\bar{\theta}_s - \theta_s) - g(\tau, \bar{\theta}_s - \theta_s) \\ \theta_s(\tau=0) = \bar{\theta}_s \end{array} \right.$$

The static restoring function  $f(\bar{\theta}_s - \theta_s)$  depends on the nature of the deflagrating substance but not on its burning history; however it is affected by the operating conditions (pressure, ambient temperature, and heat exchange with environment), flame model, and approximating polynomial order. The nonautonomous term  $g(\tau, \bar{\theta}_s - \theta_s)$  changes in time according to the first derivatives of the external controlling parameters (see Eq. 2.4.22); however it is not affected by the choice of the approximating polynomial order. The static restoring function, being a property of the deflagrating substance, can be examined a priori (see next section) independently on any specific burning process. On the contrary, nothing can be said a priori for the nonautonomous term. Nevertheless, the following important remark can be made immediately. The final outcome of a burning process is controlled only by the static restoring function when:

- (1) no forcing function is acting (static stability); see Sec. 2.6.
- (2) forcing functions monotonically change in time from some initial to some final value (dynamic stability); e.g., depressurization or deradiation; see Sec. 2.7.
- (3) forcing functions are of arbitrary shape but level off in time (dynamic stability; e.g., pressure or radiation pulses; see § 2.7.4).

## Sec. 2.5 - NATURE OF THE STATIC RESTORING FUNCTION

The static restoring function is an algebraic nonlinear function strictly dependent on the nature of the burning propellant (including the specific way its flame is described, i.e. the flame model implemented, and the order of the approximating polynomial used in Sec. 2.4) and the operating conditions. Before examining quantitative plots, consider the qualitative plots of Fig. 12a and Fig. 12b. This allows to extract the basic properties of the static restoring function independently of the flame description. It is anticipated that the heat release at the surface of the propellant is the most influential parameter on the shape of the static restoring function.

### § 2.5.1 - Qualitative Remarks

Consider the qualitative plot of Fig. 12a. According to Eq. 2.4.24, when no forcing function is acting on the system, all the points (algebraic roots) for which  $f(\bar{\theta}_S - \bar{\theta}_S) = 0$  define possible equilibrium configurations for the burning propellant, since they correspond to  $d\bar{\theta}_S/d\tau = 0$ . It is seen in Fig. 12a that, in addition to the trivial  $\bar{\theta}_S = 0$  (unburning propellant, root C), two more equilibrium solutions (roots A and B) are allowed, in general, for a given set of parameters. Let us consider the equilibrium configuration corresponding to root A. Suppose that, for some unspecified reason, the burning rate or the surface temperature increases a finite amount; then the burning propellant is no longer in a stationary configuration,  $d\bar{\theta}_S/d\tau = f(\bar{\theta}_S - \bar{\theta}_S)$  is negative, and the system reacts by decreasing its surface temperature. Conversely, if for a unspecified reason, the surface temperature of a propellant burning according to the configuration of root A decreases, the propellant reacts by increasing its surface temperature. These movements, around point A, are indicated by arrows in Fig. 12a. It is concluded that the equilibrium configuration corresponding to root A is stable because, when disturbed, the propellant always moves back toward A. By the same arguments, it is concluded that the equilibrium configuration corresponding to root B is unstable; any disturbance yields movement away from the point. Therefore, in steady state experiments, only solution A is observed.

If the set of parameters is changed, for example the pressure is increased from  $P$  to  $P_1$ , the initial condition of the ODE (see Eq. 2.4.2) is changed so that a new pair of roots,  $A_1$  and  $B_1$ , is found in addition to the trivial  $\bar{\theta}_S = 0$  of root C. Again, root  $A_1$  defines a stable equilibrium configuration, while root  $B_1$  defines an unstable equilibrium configuration corresponding to the new set of parameters. Likewise, a new pair of roots,  $A_2$  and  $B_2$ , in addition to the trivial  $\bar{\theta}_S = 0$  of root C, is found if the pressure is decreased from  $P$  to  $P_2$ . It follows that the  $\bar{\theta}_S$  axis in Fig. 12a includes, in addition to the trivial solution of nonburning propellant at the root C, a segment of stable solution  $A_1$  and a segment of associated unstable solution  $B_1$  (each pair of roots corresponds to a given set of parameters). Further effects noticeable in Fig. 12a will be discussed later.

It should be explicitly observed that the trivial  $\theta_s=0$  solution may be obtained only if the exponential Arrhenius-type pyrolysis law for mass production at the surface is dropped (see Eq. 2.2.1a). The trivial  $\theta_s=0$  solution implies that no external energy source (e.g., radiation) is acting on the solid propellant.

The qualitative picture of Fig. 12a illustrates the general behavior of the static restoring function when the pressure is varied parametrically at fixed ambient temperature and surface heat release. The behavior of the static restoring function when the surface heat release is varied parametrically, at fixed ambient temperature and pressure, is illustrated by the qualitative picture of Fig. 12b. Of course, all previous considerations hold true. For example, when the surface heat release is low enough (in a sense which will be better understood below), the propellant behaves again according to the static restoring function represented by curve CBA (Fig. 12b). However, for increasing values of the surface heat release, it is found that the static restoring function is represented by curve  $CB_1A_1D_1E_1$ . This is rather surprising; in principle, there are now five potential equilibrium configurations.

Based on the previous analysis, however, it is immediately recognized that C is the stable equilibrium solution for the unreacting state (trivial solution). Further discussion is required to understand the nature of the remaining four roots. This is easily accomplished by considering the steady state energy balance of the overall combustion wave. For example, the graphic plot of Fig. 9 shows that for each set of parameters only one solution exists for the reacting state. Conventionally, call A that particular root of Figs. 12a and 12b corresponding to the energy balance solution of Fig. 9. It follows that root  $E_1$ , although stable according to Lyapunov, is eliminated as being a reacting equilibrium solution. In other words, root  $E_1$  is a false equilibrium solution introduced by the approximate ODE formulation of the problem. The remaining roots  $B_1$  and  $D_1$  are, then, both unstable equilibrium solutions for the reacting state.

For further increase of the surface heat release, it is observed that A- and D-type roots respectively increase (moving to right) and decrease (moving to left) in the plot of Fig. 12b, until coalescence and then crossing over occur with exchange of stability character. This important point will be discussed in detail later (see Sec. 2.6). For further increasing of the surface heat release, B- and D-type roots disappear after coalescence, while both  $A_2$  and  $E_2$  roots, for different reasons, are eliminated as being stable reacting solutions (curve  $CA_2E_2$  in Fig. 12b). Under these circumstances, it follows that the only allowed solution is the trivial unreacting configurations represented by root C. Any attempt to produce a stationary combustion wave with a static restoring function of type  $CA_2E_2$  will inevitably result in extinction. This type of extinction, however, cannot be qualified as "dynamic". Similar behavior is observed in Fig. 12a for decreasing pressure at constant  $Q_s$ .

Quantitative plots of the static restoring function,  $f(\bar{\theta}_s - \theta_s)$  vs the nondimensional surface temperature  $\theta_s$  are given for the propellant AP/PBAA No. 941. A quantitative plot requires the choice of a specific flame model and a specific order of the approximating polynomial (see Sec. 2.4). By applying different flame models to the same propellant, different stability properties are predicted: this offers a criterium for discriminating potentially good from bad flame models. In this work MTS, KTSS (both linear and nonlinear), KZ, and LC flame models are implemented. As to the order of the approximating polynomial, a cubic law was chosen to represent the space distribution of the disturbance thermal profile. This choice was suggested by a large body of literature on heat transfer problems (e.g., Ref. 78) and by similar solid propellant rocket problems (Refs. 79 - 80). However, there is no a priori guarantee that is the best (and even, simply, a good) choice. The choice has to be verified, somehow. This is shown in Sec. 2.7.

#### § 2.5.2 - Effect of Operating Conditions

Plots obtained implementing MTS, KTSS nonlinear, KTSS linear (or, equivalently, LC or KZ with an appropriate choice of the associated constant as suggested in § 2.3.3) flame models, with a cubic disturbance thermal profile, are respectively shown in Figs. 13-18, Figs. 19-20, and Fig. 21. MTS flame was applied by assuming a combined exponential-power pyrolysis law at the burning surface (see Eqs. 2.2.3, with  $\theta_k=0.15$  and  $\theta_m=0$ ). KTSS flame was applied by assuming a power pyrolysis law (see Eq. 2.2.3b, with  $w=6$  and  $\theta_m=0$ ) over the whole range of surface temperature of interest. Comparative results are shown in Fig. 22, for some standard operating conditions, leading to the conclusion that MTS is perhaps the best flame model but KTSS nonlinear is strongly competitive; KTSS linear (or LC or KZ in the appropriate form) yield identical results. The effect of the order of the approximating polynomial for the disturbance thermal profile is shown in Figs. 23-26 for MTS flame only. The effect of the specific heat ratio  $C_g/C_{g1}$  is described in Fig. 27 (quasi-steady working map) and Fig. 28 (static restoring function).

The effect of ambient pressure on the static restoring function vs the nondimensional surface temperature is illustrated in Fig. 13 for the indicated set of parameters (MTS flame and  $n=3$ ); further effects due to the combined action of pressure and surface heat release will be discussed successively. An increase of pressure implies an increase of the stable equilibrium surface temperature, but a less pronounced increase of the unstable equilibrium surface temperature. The strength of the stability (see Sec. 2.6) is enhanced by an increase of pressure. Similar comments hold true as to the effect of external radiant

flux on the restoring function (Fig. 14). It is important, however, to note that an increase of external radiant flux decreases the unstable equilibrium surface temperature and above a certain value of radiant flux intensity (e.g., 40 cal/cm<sup>2</sup>-s for the set of parameters in Fig. 14) no more unstable solutions are found. This implies that, in principle (see Sec. 2.7), at each pressure a minimum value of external radiant flux intensity exists above which the dynamic boundary can no longer be defined.

The effects of surface heat release (Figs. 15a and 15b) are more involved. Note that, for increasing values of surface heat release, the behavior of the static restoring function shifts from a CBA-type (see Fig. 15a) curve for  $Q_S = -150$  and  $-158.2$  cal/g, to CBDAE (see Fig. 15b) for  $Q_S = -170$  and  $-180$  cal/g, and to CBDAE for  $Q_S = -200$  cal/g, with A-D roots coalescence occurring at  $Q_S = -190$  cal/g. This implies that at 30 atm the propellant will show not only dynamic stability effects in the low range of surface temperature (root B in Fig. 15a) but also dynamic and/or static stability effects in the large range (roots D and E in Fig. 15b). Similar behavior is observed at 10 atm (see Fig. 16), with A-D roots coalescence occurring at  $Q_S = -170$  cal/g. It is concluded that at each pressure a critical value of  $Q_S$  exists above which instability of the burning propellant will show up; the critical value of  $|Q_S|$  increases with pressure. This trend is confirmed in Fig. 17 showing that, for the standard value of  $Q_S = -158.2$  cal/g, A-D roots coalescence occurs at 6 atm. This combined effect of pressure and surface heat release is of major importance; more detailed analyses will be carried out in Sec. 2.7.

The effects of ambient temperature (Fig. 18) are of little interest in the range investigated.

#### § 2.5.3 - Effect of Flame Models

Similar trends are observed for the nonlinear KTSS flame model, again with  $n=3$ . The effect of ambient pressure in Fig. 19 is very close to that found with MTS (cf. with Fig. 13); minor differences are found in the region near the statically unstable root. The same comments hold true as to the effect of surface heat release (Fig. 20).

Drastically different results are observed for the linear KTSS (or KZ or LC) flame model, always with  $n=3$ . The effect of ambient pressure in Fig. 21 is virtually the same (as compared both to MTS and KTSS nonlinear) for surface temperature about or larger than the steady state value, but is physically meaningless for surface temperature less than about 90% of the steady state value (no zero solution and no unstable root).

The static restoring functions for the three flames are plotted simultaneously in Fig. 20, always with  $n=3$ ,

for the standard conditions specified in the figure ( $P=30$  atm,  $T_{\infty}=300$  K,  $Q_g=-158.2$  cal/g, adiabatic). The comparison graphically emphasizes the differences just mentioned. The linear KTSS (or LC or KZ) are discarded from being in principle acceptable flame models, the nonlinear KTSS is acceptable for most of the surface temperature range of values (except near extinction, since chemical kinetics is not considered), MTS flame is in principle acceptable over the whole range of surface temperature of interest.

#### § 2.5.4 - Effect of Polynomial Order

The effect of the order of the polynomial approximating the disturbance thermal profile on the static restoring function is illustrated in Fig. 23 ( $P=10$  atm), Fig. 24 ( $P=20$  atm), Fig. 25 ( $P=30$  atm) and Fig. 26 ( $P=40$  atm) for the MTS flame. The shape of the static restoring function is kept for  $n$  varying from 2 to 4; the steady state (or stable reacting) solution is always recovered (by construction); the trivial zero solution is also always recovered; the surface temperature associated with the unstable reacting solution slightly increases for  $n$  decreasing. Numerical values can be better appreciated in Tab. 3: typically, the surface temperature associated with the B root increases of less than 10% when  $n$  decreases from 3 to 2. However, upper dynamic stability (see § 2.7.3) is favored by  $n$  decreasing. This point will be further investigated.

#### § 2.5.5 - Effect of $C_g/C_c \neq 1$

The effect of specific heat ratio  $C_g/C_c$  not (necessarily) unity is illustrated in Figs. 27-28. The quasi-steady working map of Fig. 27 is plotted simultaneously for  $C_g/C_c=1.12$  and  $C_g/C_c=1.00$ ; KTSS nonlinear flame was adopted. Only minor differences can be detected due to H-H( $\phi_g$ ) when  $C_g/C_c \neq 1$ ; similar differences are found with other flame models as well. However, drastic differences arise as to the static restoring function in the region of upper (static and dynamic) instability. The plot of Fig. 28 concerns MTS flame with  $n=3$ ; the static restoring function is drawn simultaneously for  $C_g/C_c = 1.12$  and  $C_g/C_c=1.00$  at 10 atm and 30 atm of pressure. One can hardly detect any difference at 30 atm (no upper instability), whereas upper instability at 10 atm is strongly reduced by  $C_g/C_c = 1.12$ . Similar trends are found with other flame models as well.

Both effects (quasi-steady working map and static restoring function) are confirmed for  $C_g/C_c = 1.24$ .

#### § 2.5.6 - Effect of $\epsilon \neq 0$

The effect of radiative heat loss from the burning surface with emissivity  $\epsilon = 0.75$  was found negligible in all

respects (steady thermal profiles, quasi-steady flame models, burning stability, and unsteady burning transients). This is not surprising if one compares the little magnitude of the radiative energy loss with the remaining energy terms in the boundary condition of the governing PDE (see Eq.2.2.2).

## Sec. 2.6 - NONLINEAR STATIC STABILITY ANALYSIS

Static stability analysis of a burning propellant relates to the capability of the propellant to keep its burning equilibrium configuration in time. It was shown in Sec. 2.4 that this implies to study the properties of the nonlinear ODE

$$(2.6.1) \quad \frac{d\bar{\tau}_s}{d\tau} = + f(\bar{\tau}_s - \tau_s)$$

which in turn depends on the shape of the algebraic nonlinear static restoring function  $f(\bar{\tau}_s - \tau_s)$  examined in Sec. 2.5. The following problems are of relevance in the area of static stability:

1. prediction of number and nature of the allowed static solutions (see § 2.6.1).
2. prediction of static stability boundary (see § 2.6.2).
3. measurement of static stability strength (see § 2.6.3).
4. prediction of the pressure deflagration limit (see § 2.6.4).

### § 2.6.1 - Number and nature of the allowed static solutions

It is shown in § 2.7.2 and § 2.7.3 that three regions of interest can be distinguished, for increasing values of  $Q_s$  (see Tab. 4 and cf. Fig. 12b):

1. before  $\Lambda - D$  roots coalescence, the static reacting solution is the usual stationary combustion wave strictly defined by root  $\Lambda$ .
2. after  $\Lambda - D$  roots coalescence but before  $B - D$  roots coalescence, the static reacting solution is a self-sustained oscillating combustion wave around root  $\Lambda$ .
3. after  $B - D$  roots coalescence, no static reacting solution whatsoever is allowed.

Obviously, the trivial unreacting solution  $\bar{\tau}_s = \bar{R} = 0$  (when allowed) is always statically stable. Therefore, too much surface energy release excludes any steady reacting solution and under these circumstances the only possible configuration, even in a static environment, is the unreacting state. These predictions were verified by numerical integration of the governing PDE. Results concerning self-sustained oscillatory burning are discussed in § 2.8.4. Results concerning the static stability of the equilibrium reacting configuration are shown in Fig. 29.

Under the standard set of parameters indicated, numerical values for the allowed static solutions are given as an example in Tab. 4. In particular, the range of  $Q_s$  values for which self-sustained oscillating combustion waves are expected is given, in function of pressure, in Tab. 5. Both calculations were per-

formed for MTS flame with  $n=3$ . The above questions will be investigated in detail in § 2.7.2 and § 2.7.3, since they require further analysis.

### § 2.6.2 - Static stability boundary

An important piece of information in the static stability analysis of a burning propellant is the minimum value of surface temperature (or burning rate) above which stable steady burning is allowed. In order to evaluate this value, a most important feature common to all static restoring functions is emphasized. The specific surface temperature value,  $\epsilon_g^{ST}$ , at which the pair of solutions  $A_i^{ST}$  stable and  $B_i^{ST}$  unstable coalesces, at a given pressure (Fig. 12a) and for a given set of parameters,

$$A_i^{ST} = B_i^{ST} = \epsilon_s^{ST}$$

defines the branching or metastable point at that pressure (and for that set of parameters). Corresponding to this special value of the surface temperature a change of the character of stability occurs at the given pressure, in that for  $\epsilon_s < \epsilon_g^{ST}$  all the potential equilibrium solutions at the pressure (corresponding to different ambient temperature and/or heat loss from the burning propellant) are statically unstable (roots  $B_i$ ) while for  $\epsilon_s > \epsilon_g^{ST}$  all the equilibrium solutions at that pressure are statically stable (roots  $A_i$ ). Therefore, the branching point at a given pressure isolates the critical static stability value,  $\epsilon_g^{ST}$ , of the surface temperature at that pressure under which no steady reacting solution is allowed. Construction of the static stability boundary on the  $R$  vs  $\epsilon_g$ ,<sub>s</sub> plane, in a range of pressure, consists of connecting the critical static stability points defined for each pressure of interest in the wanted range (and for a given set of parameters). This implies the search of the branching point at any fixed pressure.

A general method (based on nonadiabaticity of the propellant) for solving this problem is discussed below. However, for the specific case of a solid composite propellant, the search for the branching point may be performed immediately, although not rigorously, based on observation of the physical processes. Consider the qualitative picture superimposed in Fig. 30 on a standard MTS flame plot. Recall that burning rate and surface temperature are univocally related by an appropriate pyrolysis law. Therefore, it is irrelevant to define the branching point in terms of burning rate or surface temperature. Now, as schematically indicated in Fig. 30, the branching point is determined at each pressure by the geometrical condition of vertical tangent, i.e. infinite slope or maximum heat feedback. Indeed, for  $\epsilon_s > \epsilon_g^{ST}$  a change of burning rate or surface temperature produces opposing effects on the thermal gradients at the surface from the condensed and the gas phase sides; for example, the former increases but the latter decreases when the burning rate is disturbed up-

ward. This competition is the stabilizing mechanism. For  $\bar{\phi}_s < \phi_s^{ST}$  a change of burning rate affects, in the same direction, both thermal gradients; this is destabilizing. Just at the point with vertical tangent, the two unstable and stable static roots  $\bar{\phi}_s < \phi_s$  coincide and an exchange of the stability character of the solutions occurs; therefore, we may identify this point as the neutral branching or metastable point  $\phi_s^{MB}$ . For  $\phi_s > \phi_s^{MB}$  the behavior of the system depends on the direction of the perturbation. Now, in order to construct a static stability boundary in the plane  $R_s$  vs  $\bar{\phi}_s$ , it is enough to connect the branching points  $\phi_s^{MB}$ ,  $\phi_s^{ST}$  associated with each parameter. This boundary separates the region where static solutions are allowed from the region where no static solution can be found.

This method, first suggested in Ref. 3, is not rigorous since the contribution from the surface reactions is neglected. Its advantage is simplicity. For accurate results, the procedure illustrated in Fig. 31 ( $\Omega_s = 120$  cal/g), Fig. 32 ( $\Omega_s = 158.2$  cal/g) and Fig. 33 ( $\Omega_s = 200$  cal/g) for a MTS flame has to be used. This consists in applying a larger and larger heat loss to the burning propellant until just one solution is found (coalescing from one statically stable and unstable root). Obviously, this search can be made directly for any flame model without knowledge of the static restoring function. However, the same results should be obtained by searching the coalescence of the corresponding A and B roots of the static restoring function. This is illustrated in Fig. 34 ( $P=20$  atm), Fig. 35 ( $P=20$  atm), Fig. 36 ( $P=40$  atm) and Fig. 37 ( $P=50$  atm) for the MTS flame with  $n=3$ . The closeness of the two sets of results confirms the validity of the ODE formulation of the problem. Obviously, this second approach is affected by the choice of the approximating polynomial order. The quantitative differences between the two sets of results may be appreciated by comparison of Tab. 6 (based on heat feedback) with Tab. 7 (based on static restoring function with  $n=3$ ).

#### § 2.6.3 - Measurement of static stability strength

The static stability analysis can be put on a quantitative basis by means of the "first" Lyapunov criterion (Ref. 88). According to this, the solution of the nonlinear autonomous ODE of Eq. 2.6.1 is stable in the neighborhood of a point  $\bar{\phi}_s^*$  if

$$\left[ \frac{d f(\bar{\phi}_s + \delta_s)}{d \bar{\phi}_s} \right]_{\bar{\phi}_s = \bar{\phi}_s^*} < 0$$

at the point of interest  $\bar{\phi}_s^*$ . The physical meaning of this criterion was explained in Sec. 2.5. In keeping with the spirit of this physical interpretation, the strength of the

stability of the solution at a point  $\alpha_g^S$  may be measured by the magnitude of the derivative  $d\dot{\alpha}/d\alpha_g$  evaluated at  $\alpha_g = \alpha_g^S$ . How this value is affected by typical parameters is shown in Tab. 8. In the exceptional case of a branching, or metastable, point in which the unstable and the stable solutions coalesce, the above first criterion is not valid. In the present situation, however, it is enough to say that the point  $\alpha_g^S$  is stable from one side ( $\alpha_g > \alpha_g^S + \epsilon$ ) while it is unstable on the other side ( $\alpha_g < \alpha_g^S - \epsilon$ ), so that, overall, the point  $\alpha_g^S$  is said to be *stable*. It should be clear that the first Lyapunov criterion (used for measuring the strength of the stability) is essentially a linearization criterion of the originally nonlinear ODE; however, it is plausible that both roots C and A are stable to "iritic" disturbances of an unknown size, atra. The extent of the stability region around the stable roots could be estimated by the Lyapunov "direct" method; but this is not a purpose of this analysis. Physically, it is expected that the range of stability of C root (always stable) is limited upward by B, while the range of stability of A root (if stable) is limited downward by  $\alpha$ . But dynamic effects may increase the range of stability of C root against the range of stability of A root.

Values of the static stability strength in various conditions are summarized in Tab. 8.

#### § 2.6.4 - pressure\_deflagration\_limit

It is experimentally known that, for a given set of operating conditions, a minimum pressure exists (for each solid propellant) under which no self-sustained combustion wave propagation is allowed. Surprisingly enough, this pressure deflagration limit is not as clear-cut as one might think. Results, obtained within the framework of the quasi-steady flame models considered in this work, will be discussed by the end of next section. As matter of fact, the tight coupling between pressure and surface heat release (e.g., revealed by Figs. 15-17) needs to be clarified in detail before attempting to understand the intimate nature of the pressure deflagration limit as emerging from this investigation.

## Sec. 2.7 - NONLINEAR DYNAMIC STABILITY ANALYSIS

It is wished to predict, under an appropriate set of assumptions, the behavior of an heterogeneous deflagration wave initially propagating steadily (including zero burning rate) under a given set of external parameters and then subjected to arbitrary but known changes in time of pressure and/or radiant flux. This is easily done if an ODE formulation of the problem is available.

Dynamic stability of a burning propellant relates to transition of the propellant, from a given initial, to some final set of operating conditions for which multiple adiabatic equilibrium configurations (statically stable) are allowed. A burning propellant is dynamically stable if the wanted transition is successful; if the transition leads to a final configuration different from the wanted one, the burning propellant is dynamically unstable.

The nonlinear ODE of Eq. 2.4.24 describes the instantaneous response of the system to a finite size departure of the surface temperature from the stationary value due not only to intrinsic perturbation sources (static stability), but also to any arbitrary but externally assigned monotonical change in time of controlling parameters such as pressure and/or radiant flux (dynamic stability). This can be of great advantage for describing time histories of ignition and/or extinction transients. However, a more important and fruitful point of view can be taken. Indeed, it was already emphasized in Sec. 2.4 that the surface temperature time derivative is governed by the static restoring  $(\bar{G}_S - \tau_0)$ , even for finite size disturbances, both for static and dynamic burning stability. It will be shown that this holds true asymptotically for forcing functions levelling off in time and instantaneously for forcing functions monotonically decreasing in time. Studying the nature of the algebraic static restoring function leads to a very general burning stability analysis without ever solving the nonlinear ODE of Eq. 2.4.24 or PDE of Eq. 2.2.2.

### § 2.7.1 - Dynamic extinction of solid propellants

In this subsection inquiry is made about the possibility of dynamic extinction of the solid propellant even though it may be capable of statically stable burning for the given final set of operating conditions. It is expected that this will be a function of the rate of decrease of the operating conditions from the initial set of values. Specific reference to this question will be made, but the overall line of attack is of a general nature. In order to apply the integral method without excessive difficulties, optical opacity of the condensed phase is assumed. This hypothesis is relevant to the case of radiant flux change, but it is not expected to affect the conclusions in any significant way, as it will be discussed at the end of this subsection.

The objective now is to predict when an allowed static transition (realized through a succession of exclusively steady state configurations) becomes forbidden if one attempts to realize it in a transient (quasi-steady gas phase) fashion. Let us consider a pure deradiation transient performed according to

$$(2.7.1) \quad F_o(\tau) = F_{o,i} + (F_{o,f} - F_{o,i}) \left[ 1 - \exp(-B_r \cdot \tau) \right]$$

on an opaque propellant with fixed pressure  $\Psi(\tau) = \Psi$ . Such a transient is represented by a dashed line in Fig. 38a. It is assumed that  $A_f$  and  $A_p$  are both statically stable roots. If an undershoot occurs, the transition will be dynamically stable only if a recovery point (defined in Fig. 38a as the point where  $dR/d\tau = 0$ ) occurs. Dynamic stability means than an inquiry is made about the possibility of the occurrence of a recovery point.

In order to determine the location of a dynamic stability boundary (if it exists) on the standard  $R$  vs  $\dot{q}_{e,s}$  plane used to define flame models, follow this approach. First, a definition is sought for a critical dynamic stability point at a given pressure and, second, a connection is made of all the dynamically critical points in the desired range of pressure. The critical dynamic stability point may now be identified with that special value  $\dot{q}_s^D$  of the surface temperature, if any, such that extinction necessarily follows when the surface temperature is even momentarily less than this special value. All points  $\dot{q}_s < \dot{q}_s^D$  (Fig. 39) are "no-return" points since they do not allow recovery, while all points  $\dot{q}_s > \dot{q}_s^D$  are possible "return" points since they do allow recovery. The critical dynamic stability point, if any, is isolated by the coalescence of the return with the no-return points.

In the case of deradiation only according to Eq. 2.7.1, the general expression of Eq. 2.4.24 may be specialized to

$$(2.7.2) \quad \frac{d\dot{q}_s}{d\tau} = f(\bar{\tau}_s - \dot{q}_s; \Psi, F) = g(\tau, \bar{\tau}_s - \dot{q}_s; B_r, F_{o,i}, F_{o,f})$$

where

$$(2.7.3) \quad \begin{cases} g(\tau > 0^+, \bar{\tau}_s - \dot{q}_s) = \frac{(1-r) B_r (F_{o,i} - F_{o,f}) \exp(-B_r \cdot \tau)}{\frac{2(u_x)_{c,s}}{u_s} - \left[ \frac{\delta(u_x)_{c,s}}{\delta u_s} \right]} \Psi, F_o \\ g(\tau < 0^-, \bar{\tau}_s - \dot{q}_s) = 0 \end{cases}$$

Dynamic stability analysis requires consideration of the nonlinear ODE of Eq. 2.7.2. The basic difference from the

static stability analysis is that the rate of return of the surface temperature toward the equilibrium value now depends explicitly on time, so that no a priori analysis is possible. However, Eq. 2.7.2 shows that the rate of the response of the system can be separated in two terms: of these,  $f(\bar{v}_s - v_s)$  is the autonomous contribution previously discussed while  $g(\tau, \bar{v}_s - v_s)$  is the nonautonomous contribution due to the finite disturbance subsequent to the given deradiation law.

The main interest is the asymptotic behavior of the system for  $\tau \rightarrow \infty$ : to predict whether the final stable equilibrium root  $A_f$  or the trivial solution  $v_s = 0$  (root C) will be reached (Figs. 38a - 38b). For the wide range of controlling parameters varying in time according to monotonically decreasing functions, the qualitative behavior of the nonautonomous term may be portrayed. Indeed, Eq. 2.7.3 shows (see Fig. 38c - 38d) that:

(2.7.4) 
$$\left\{ \begin{array}{l} 1. \quad g(\tau \geq 0^+, \bar{v}_s - v_s) \geq 0 \text{ at any instant following the beginning of the transition, since the denominator is found to be a positive quantity in the range of interest.} \\ 2. \quad g(\tau \rightarrow \infty, \bar{v}_s - v_s) = 0 \text{ asymptotically in time, i.e., times much longer than some external characteristic time scale depending on the given forcing function (e.g., } \tau_{\text{ext}} = 1/B_2). \end{array} \right.$$

Then, it follows that before and after (for  $\tau < \tau_{\text{ext}}$ ) the externally controlled transition, the rate of return of surface temperature toward the equilibrium value is governed by the autonomous term  $f(\bar{v}_s - v_s)$ , whose properties have been already illustrated in Secs. 2.4 - 2.5.

A qualitative picture of the behavior of the system governed by Eq. 2.7.2, under the conditions specified by Eq. 2.7.4 and for given initial conditions, can be portrayed in the plane  $dv_s/d\tau$  vs  $v_s$  (Fig. 39). Roots  $A_i$  and  $A_f$  (cf. Figs. 38a - 38b and 39) are respectively the statically stable initial and final equilibrium configurations. All trajectories (representing the history of the system) in Fig. 39 start from the root  $A_i$  and terminate either at the root  $A_f$  or at the origin of the axes (root C, dynamic extinction). In the qualitative portrait of Fig. 39 the nonlinear characteristics  $f(\bar{v}_s, i - v_s)$  at  $\tau = 0$  and  $f(\bar{v}_s, f - v_s)$  at  $\tau \rightarrow \infty$  have been represented. On the horizontal axis, the surface temperature corresponding to the branching point  $\bar{v}_s^{\text{ST}}$  at the operating pressure has been marked. This value (statically critical point) separates the statically stable roots ( $A_i, A_f$ ) from the statically unstable roots ( $B_i, B_f$ ). For a quasi-steady transition, the trajectories starting from root  $A_i$  progresses into the negative half-plane  $dv_s/d\tau < 0$ , since the term  $g(\tau, \bar{v}_s, i - v_s)$  initially dominates the term  $f(\bar{v}_s, i - v_s)$  in the ODE of Eq. 2.7.2.

But the sketch of Fig. 38d shows that  $g(\tau, \bar{\tau}_s - \tau_s)$  decreases monotonically toward zero. When  $g(\tau, \bar{\tau}_s - \tau_s)$  becomes negligible compared to  $f(\bar{\tau}_s - \tau_s)$ , the latter term might drive the trajectory toward the final root  $\lambda_f$ .

The rate of return of the surface temperature toward equilibrium for  $\tau \rightarrow \infty$  (in the sense  $\tau \gg \tau_{ext}$ ) is controlled only by the autonomous term. This means that, in the disturbance history, it is the intrinsic stability of the final state that tends to govern the behavior of the system. At a given value of pressure, the critical "no-return" point is defined by the statically unstable root  $\tau_s^{DY}$  (root  $\lambda_f$ ) associated with the final statically stable root  $\tau_s^{ST}$  (root  $\lambda_f$ ) through the function  $f(\bar{\tau}_s + \tau_s)$ . The whole segment between  $\tau_s^{ST}$  and  $\tau_s^{DY}$  is statically unstable but allows a dynamic burning regime. The statically unstable root  $\tau_s^{DY}$  in Fig. 39 represents a limiting condition which is a unique property of the system at the operating (final) pressure. This analysis can be repeated for different values of pressure, so that a dynamic stability boundary may be constructed as shown in Fig. 40 for standard ambient temperature (300 K) and no residual radiant flux. The dynamic stability boundary just determined will be called, for the remainder of this work, lower dynamic stability boundary (cf. § 2.7.2).

The statically unstable root  $\tau_s^{DY}$  in Fig. 39 represents a limiting condition which is a unique property of the propellant at the operating pressure (for a given set of parameters it depends only on the properties of the intended final state). The line connecting all the points  $\tau_s^{DY}$  is the lower dynamic stability boundary not only for aeradiation transients, monotonically decaying toward zero, but also for depressurization transients monotonically decaying. Since the unstable root  $\tau_s^{DY}$  is determined for  $\tau \rightarrow \infty$ , that is when the radiant flux is no longer acting, whether the propellant is or is not optically transparent is irrelevant. For aeradiation transients monotonically decaying toward zero, the transparency of the condensed phase has no influence on the dynamic stability. No problem arises if one wishes to consider the effect of other parameters, for example the ambient temperature, on the lower dynamic stability boundary: it is enough to determine the statically unstable root for each ambient temperature of interest.

The existence of a lower dynamic stability boundary different from the static (stability) boundary has been shown. Crossing of this boundary is enough to assure dynamic extinction. At least two large classes of situations can be envisaged. For the wide range of controlling parameters varying in time according to monotonically decreasing functions (e.g.: linear, parabolic, exponential, etc.) the lower dynamic stability boundary holds true instantaneously, in that crossing of the boundary at any instant, even during the action of the external disturbance, is sufficient to yield dynamic extinc-

tion. Indeed, for monotonically decreasing functions the effect of  $g(\tau, \bar{\tau}_s - \tau_s)$  is to favor extinction independently of  $f(\bar{\tau}_s - \tau_s)$ . For the wide range of controlling parameters varying in time according to levelling off (i.e. with zero final derivative in time) functions not necessarily monotonic (e.g., pulses of arbitrary shape), the lower dynamic boundary holds true "asymptotically", in that crossing of the boundary assures dynamic extinction only after the action of the external disturbance. Indeed, for levelling off functions the effect of  $g(\tau, \bar{\tau}_s - \tau_s)$  depends on the details of the specific function being used. A priori it can only be said that, following the action of the external disturbance (i.e., for  $\tau > \tau_{\text{ext}}$ ), the term  $g(\tau, \bar{\tau}_s - \tau_s) > 0$  and dynamic extinction is exclusively controlled by  $f(\bar{\tau}_s - \tau_s)$ .

A major problem in the theory of heterogeneous flame dynamics is the prediction of the maximum rate of change of a controlling parameter allowed without suffering dynamic extinction. No general answer can be given to this question, not even for the class of monotonically decreasing functions, since in general the full dynamic history of the system has to be considered. The best one can hope to do is to assign a criterion for a specific type of monotonically decreasing law, for example the exponential law of Eq. 2.7.1 for a de-radiation transient. In this case, the trajectories of Fig. 39 show that a critical value  $d\tau_s/d\tau^*$  for paths leaving root  $\bar{\tau}_j$  exists such that for  $|d\tau_s/d\tau| < |d\tau_s/d\tau^*|$  a recovery point subsequently occurs, whereas for  $|d\tau_s/d\tau| > |d\tau_s/d\tau^*|$  no recovery point is possible. However, no great importance is attached to this idea of obtaining an "early warning", being this strictly dependent on the specific external law being considered.

All criteria assigning critical conditions for predicting extinction are necessarily approximate, often to a unknown extent. Indeed, the lower dynamic stability boundary is uniquely defined as a property of the system and does not depend on the specific law externally assigned. Conversely, any prediction is necessarily associated to a specific law. Furthermore, it will be shown in 2.7.2 that dynamic extinction may occur in other, unexpected circumstances. Approximate criteria are not only of very limited use, but might also be badly mistaken.

In the general ODE formulation of Eq. 2.4.24 the influence of time varying external parameters is felt only through time derivatives. This implies that, if no change of pressure and/or radiant flux occurs, the system is only subjected to random intrinsic fluctuations and the results from the static stability analysis apply. It is also implied that, in the case that  $g(\tau, \bar{\tau}_s - \tau_s) = f(\bar{\tau}_s - \tau_s)$ , the dynamic stability boundary is a no-return boundary for any  $\tau$  and for any external law. Under these circumstances, the dynamic stability range coincides with the range of influence of the statically stable configuration  $\bar{\tau}_s$ .

### 6.2.7.2 - Lower and upper dynamic combustion instability

So far, only dynamic effects associated with a B-type root (see Figs. 12a and 12b) have been discussed. In fact, similar dynamic effects are also associated with a D-type root (see Fig. 12b). The former is called lower dynamic stability and the latter is called upper dynamic stability. Although the latter has been essentially neglected in the literature, both types of instabilities are very important in practice. Lower dynamic stability relates to extinction. Upper dynamic stability relates to vigorous accelerations of the combustion wave and pressure build-up due to large mass production; eventually mechanical failure of the enclosing vessel or dynamic extinction might follow.

With reference to Fig. 15a it is seen that a burning rate increase, occurring for  $\Omega_g = 156.2$  cal/g (no D-type root), is balanced by the strong stability character associated with the reacting equilibrium configuration of root A (see tab. 8a). Obviously, this is true only up to some finite size of the initial disturbance. With reference to Fig. 15, it is seen that for  $\Omega_g = 179$  cal/g the static restoring function features two dynamically unstable roots, B ( $\Omega_g = 0.65$ ) and D ( $\Omega_g = 1.15$ ), sitting at the sides of the stable steady state configuration A ( $\Omega_g = 0.95$ ). Under these circumstances, if the surface temperature during a transient goes past B or D, the combustion wave will accelerate respectively toward C ( $\Omega_g = 0$ ; lower dynamic instability) or E ( $\Omega_g = 1.29$ ; upper dynamic instability). In the case of lower dynamic instability, the fate of the combustion wave is dynamic extinction (cf. § 2.7.1). In the case of upper dynamic instability, the fate of the combustion wave is more involved. As soon as root D is passed, a vigorous acceleration occurs. The increase of burning rate may be of orders of magnitude. Root B, although strongly stable, is not allowed as stationary solution being a false equilibrium solution introduced by the approximate ODE formulation of the problem. Therefore, after reaching E, the combustion wave is violently recalled toward a stable steady state configuration. Depending on the dynamics of the whole process, this can be either the reacting mode A or the unreacting mode C (dynamic extinction due to overstability). Dynamic instability may be the unexpected result of a too fast pressurization (for example) transient.

Even more striking is the behavior of the system for  $\Omega_g = 200$  cal/g (Fig. 15b). In this case, the static restoring function features two stable roots, D ( $\Omega_g = 0.93$ ) and E ( $\Omega_g = 1.61$ ), neither of which is allowed as a stationary solution, sitting at the sides of the unstable stationary solution A ( $\Omega_g = 0.99$ ). Under these circumstances, even in a static environment, the burning propellant is not capable of finding an equilibrium reacting configuration and bounces back and forth around A under the competing influences of D and E. It is confirmed (see Fig. 69, e.g.) by numerical integration that, after a transient, the combustion wave undergoes sharp self-sustained oscillations around A with peaks near D and E. This suggests the existence of a limit cycle.

Being a limit cycle an overall property of the governing differential equation, once triggered this oscillatory behavior will not depend on the initial conditions of the system (see § 2.7.1). With this in mind, suppose, for a self-sustained combustion, substituting for the steady-state solution as steady-state solution, all previous conditions on transients are valid. If the normalized pressure is not arbitrarily gone enough ( $\bar{p} = 0.72$ ), the combustion wave will irreversibly undergo a phase C (dynamic extinction). This may happen if the combustion wave is pushed out (e.g., by decompression) and as a result, in trying to reestablish the combustion wave (e.g., by re-compression), the pressure goes too much past E during the initial transient, depending on the dynamics of the transient process, the wave may end up in a transient toward a state characterized by a unique restoring function of the type (C) in addition to a self-sustained oscillating combustion wave or dynamic extinction.

For  $\bar{p} = 0.72$  and  $\bar{p}_0 = 1$  (for clarity make not a requirement in Fig. 14b), the static restoring function is of the type (C) (unstable) and, as a consequence, the only possible solution, even in a steady-state transient, is the trivial unreacting state. Since the  $\bar{p}_0$  is no alternative solution, this should be considered as a limit extinction. The high surface heat release (adiabatic) and self-sustaining reacting solution exist as well as the low heat release heat feedback (or too large heat losses).

The values of the nondimensional surface temperature, associated with the various types of roots discussed, are listed in Tab. 4 in function of the nondimensional surface heat release at  $\bar{p} = 0.72$  atm. At this pressure, upper curve is slightly shifted up for  $\bar{p}_0 = 16$ ° cal/v. For decreasing pressures, the minimum value of  $\bar{p}_0$  at which upper dynamic instability occurs up to decreases (Tab. 5 and Figs. 41-46). This point is discussed in detail next.

### § 2.7.3 - Self-Sustained Oscillatory Burning of Solid Propellants

In this subsection results concerning specifically self-sustained oscillatory burning of solid propellants are given. First, a simple procedure for detecting the existence of a limit cycle is suggested. The simultaneous presence of two ingredients in the static restoring function is required: (1) A root unstable, and (2) D and E roots stable. The critical condition for satisfying the first requirement is the coalescence of A-E roots (cf. Fig. 16b); the second condition is satisfied as long as coalescence of B-E roots has not yet occurred. To detect the existence of a limit cycle at a given pressure, it is enough to plot the values of the relevant roots in function of the surface heat release at the given pressure. For example, in the case considered in Tab. 4 (adiabatic, opaque AP/PBAA No. 941 burning at

$P = 30$  atm and  $T_a = 300$  K), the existence of a limit cycle is expected between  $|\Omega_g| = 190$  cal/g (Z-D coalescence) and  $|\Omega_g| = 225$  cal/g (B-D coalescence). Similar plots can be made for any other set of operating conditions.

Results found in the range 10 - 60 atm are graphically illustrated in the bifurcation diagrams of Fig. 41 (10 atm), Fig. 42 (20 atm), Fig. 43 (30 atm), Fig. 44 (40 atm), Fig. 45 (50 atm) and Fig. 46 (60 atm) for an hypothetical family of solid propellant formulations; a summary is given in Tab. 5. In the bifurcation diagrams the values of the non-trivial roots A, B, D, E vs surface heat release (bifurcation parameter) are plotted for a given set of operating conditions. The plots of Figs. 41-46 were obtained implementing the ERS flame model with  $n=3$ . It can be seen that:

- (1) the fundamental A root monotonically increases with  $|\Omega_g|$ ;
- (2) B, D and E roots all lie on the same curve;
- (3) this S-shaped curve crosses the A- curve (bifurcation point);
- (4) the ratio  $C_g/C_c \neq 1$  moves the bifurcation point toward larger  $|\Omega_g|$  values (see Fig. 47).

For  $|\Omega_g|$  low enough, A and B are the only reacting roots; A defines the steady solution, while B defines the lower dynamic stability point. For increasing  $|\Omega_g|$ , D and E roots branch off; A still is the steady solution, while B and D respectively define the lower and upper dynamic stability points. For further increases of  $|\Omega_g|$ , A and D roots cross over and exchange their stability character; the steady solution, even in a static environment, is now self-sustained oscillatory burning, between D and E, around A. For  $|\Omega_g|$  even larger, B - D roots coalesce; under these circumstances there is no steady reacting solution.

Self-sustained oscillatory burning may only be found, at a given pressure, for  $|\Omega_g|$  values ranging between A - D roots coalescence and B - D roots coalescence. These particular intervals of  $|\Omega_g|$  values are plotted vs pressure in Tab. 5. Both A-B roots and B-D roots coalescence occur at increasing  $|\Omega_g|$  with increasing pressure. However, the extent of this critical  $|\Omega_g|$  interval shows only minor increases with increasing pressure. The physical upper limit for  $|\Omega_g|$  is also plotted in Tab. 5; this is defined by  $|\Omega_g| = C_c(\bar{T}_f - T_a)$  being  $C_c = C_g$  by assumption. The value  $|\Omega_g| = C_c(T_s - T_a)$ , finally plotted in Tab. 5, represents the maximum amount of surface heat release allowed by KTSS nonlinearized flame according to Eq. 2.3.10. No such a limitation exists for MTS flame.

Remark that  $|\Omega_g|$  ranging within the value of Tab. 5 is a necessary but not sufficient condition for the occurrence of self-sustained oscillatory burning. Dynamic extinction, due to decelerating deflagration waves or overstability, is always an alternative to the self-sustained oscillatory burning. Even without external disturbance, the actual range

of  $Q_s$  values for which self-sustained oscillatory burning may occur is narrower than indicated in Tab. 5. Indeed, in this oscillatory regime, the burning propellant bounces back and forth under the competing influence of D and E roots. For dynamic reasons the amplitude of these surface temperature oscillations has to be somewhat larger than  $0_s(E) - 0_s(D)$ . This implies that, especially near B - D roots coalescence, extinction will somewhat shrink the  $Q_s$  range of self-sustained oscillatory burning.

The frequency of these self-sustained burning oscillations is expected to be somewhat related to the condensed phase thermal wave relaxation time (at the final operating conditions of a burning transient):

$$(2.7.5) \quad \Omega = 1/\tau_{th,c} = \bar{R}^2(\Psi, F_o, 0_{\infty})$$

However, the exact meaning of this parameter is open to questions in the present context. This point will be dealt with further in next section.

A most significative way to summarize the findings of this investigation is shown in Fig. 48. This is a surface temperature vs pressure plot at constant  $Q_s$  (the standard burning rate vs pressure plot on logarithmic scale is inconvenient for graphical reasons). Root A corresponds to what is usually measured in a strand burner. However, for pressures less than A-D coalescence, A root becomes statically unstable and the solution is a self-sustained oscillatory burning peaking slightly above E and below D roots. For pressures less than B-D coalescence, in no way a reacting steady solution can be found. Therefore, for a given propellant, it can be concluded that pressure favors combustion stability. However, too large pressure might cause instability of the monodimensional heterogeneous deflagration wave (Ref. 89); but this is out of the range of validity of this study. On the other side, for decreasing pressures, the burning wave "jumps" abruptly from the usually steady configuration to a large amplitude self-sustained oscillations before getting fully extinguished. Exactly this same remark was made in Ref. 68 on a totally different basis. In view of this, experimental techniques (and the very concept of pressure deflagration limit) should be re-considered in this region of marginal burning. Pressure deflagration limit can be thought of as that critical value of pressure discriminating between self-sustained oscillations and no steady reacting solution. It follows that pressure deflagration limit is associated with loss of static burning stability.

A possible physical explanation of the above results is the following. Any self-sustained reactive system is capable of exothermic reactions. These partly occur in the gas phase ( $Q$ ) and partly in the condensed phase ( $H$ ). The total energy release  $Q(\Psi) + |H|$  is determined by the energy

balance on the overall steadily burning propellant for the given set of operating conditions. For a fixed set of operating conditions,  $\dot{q}_s$  increases while  $\dot{q}_{g,s}$  decreases for increasing burning rate. For low values of  $|H|$ , an increase of burning rate and thereby of  $\dot{q}_s + R|H|$  is counterbalanced through a simultaneous decrease of  $\dot{q}_{g,s} \sim 1/R$  and increase of the heat flux  $\dot{q}_{c,s} \sim R|H|$  absorbed into the condensed phase. However, for large values of  $|H|$ , an increase of burning rate might be destabilizing if  $\dot{q}_s$  increases more than  $(\dot{q}_{c,s} - \dot{q}_{g,s})$ . This implies an acceleration of the combustion wave, that is the appearance of a D-type root in the nonlinear static restoring function. On the other hand, for the same set of operating conditions, a large increase of burning rate (up to orders of magnitude, see Sec. 2.8) is strongly stabilizing. Indeed, under these circumstances, the increase of  $\dot{q}_{c,s}$  is much larger than the increase of  $(\dot{q}_c + \dot{q}_{g,s})$  due to the Arrhenius-type dependence of the surface on the burning rate. This corresponds to the appearance of an E-type root in the nonlinear static restoring function. Therefore, at each pressure (see Tab. 5) a critical (A-D coalescence) value of surface heat release exists above which the energy coupling between condensed and gas phases becomes locally unstable, i.e. a burning rate disturbance due to the change of heat flux absorbed into the condensed phase is counterbalanced only "in the large" (through a limit cycle process) by an appropriate change of heat feedback from the flame and the surface reacting layer. At each pressure a second larger critical (B-D coalescence) value of surface heat release exists above which the energy coupling between condensed and gas phases becomes totally unstable (except at the trivial root C), due to the excessively large thermal gradients occurring in the condensed phase near the burning surface.

As to the pressure effect, increasing pressure implies increasing  $Q$ , which subsequently required a larger value of  $|H|$  for destabilizing the combustion wave. Larger pressure require larger value of  $|H|$  for triggering both upper instability and the self-sustained oscillation mechanism.

#### § 2.7.4 - Ignition of solid propellants

Attempts are being made to extend the (nonlinear) dynamic combustion stability analysis to ignition transients. Just as dynamic extinction, ignition can be seen as a stability problem in which transition occurs between two statically stable configurations: from reacting to unreacting for dynamic extinction, viceversa for ignition. Obviously, for both problems the transition cannot rigorously be described by a transient model with quasi-steady gas phase. However, for both problems it is not easy to do better and probably not strictly necessary.

With this limitation in mind, numerical runs were performed under several operating conditions to check whether the pre-

viously defined lower dynamic stability boundary (cf. §2.7.1) singles out a critical condition for ignition transients too. In general, the answer is no. This is not surprising, since the lower dynamic stability boundary was evaluated by means of the static restoring function. In turn, this is based on finite disturbances of burning propellants from a stationary configuration. However, for some specific problems the dynamic stability analysis turned out useful. For example, for overdriven ignition transients the dynamic burning following the external energy source cut off may lead to extinction (Refs. 58-59). This is correctly predicted by the standard lower dynamic stability boundary. Under appropriate circumstances, whose extent is presently under study, this boundary assigns also a static requirement for ignition to occur.

#### § 2.7.5 - Final remarks on dynamic combustion stability

A graphical summary of the (nonlinear) combustion stability analysis is offered in Fig. 49. This is a standard  $R$  vs  $P$  plot. The curve  $R(P)$  is obtained experimentally; the same curve is reproduced by KTSS (both linearized and nonlinear versions) flame model. MTS flame model also reproduces the experimental  $R(P)$  curve, but with some tolerance due to the fitting procedure required to evaluate the proper gas phase parameters; however, this tolerance can be made negligible if enough care is exerted. The combustion stability analysis is then able to predict the lower dynamic stability boundary, the static stability boundary, the pressure deflagration limit and the self-sustained oscillatory burning regime. The region of dynamic stability is bounded also upward by an upper dynamic stability boundary (not drawn), which would lie somewhere above the  $R(P)$  curve, extending from the self-sustained oscillatory burning region up to some maximum pressure; in this pressure interval damped oscillatory burning is expected.

All stability features discussed in this study were determined within the framework of a thermal model of thin (quasi-steady) heterogeneous flames. Both static and dynamic combustion properties, including self-sustained oscillatory burning, are related to the thermokinetics of the deflagrating surface. Diffusive effects and wave propagation in the gas phase were neglected.

The general behavior of thin heterogeneous flames, for decreasing pressure, in the standard burning rate vs pressure plot (Fig. 49) includes stationary burning, damped oscillatory burning, self-sustained oscillatory burning, and no self-sustained reacting solution. The critical value of pressure under which self-sustained reacting solutions are no longer allowed is the pressure deflagration limit. The available quasi-steady flame models are questionable in this marginal burning domain; however, this new concept of pressure deflagration limit associated with heterogeneous (thermokinetic)

burning instability rather than nonadiabaticity of the combustions wave makes sense. Nonadiabacity increases the value of pressure deflagration limit; other stability boundaries are affected as well.

The overall picture of thin heterogeneous flames for the first time seems fully understood. Remark that the transient behavior of such flames is predicted for both pressure and radiation driven combustion waves. Thin heterogeneous flames are (Fig. 49) statically and dynamically unstable below the dynamic limit, statically and dynamically stable above the static limit (except for damped oscillations), statically unstable but dynamically stable in the region between the two limits. Recall that the dynamic limit is valid instantaneously for forcing functions monotonically decreasing in time, asymptotically ( $\tau \gg \tau_{ext}$ ) for forcing functions of arbitrary shape but levelling off in time (in particular, pressure or radiation pulses).

#### § 2.7.6 - Important remark on the static boundaries

Pressure deflagration limit has revealed its nature of boundary of steady burning stability associated with decreasing pressure. On the contrary, the "static burning stability boundary" introduced in § 2.6.2 has to be interpreted as a boundary between existing and nonexisting steady solutions associated with increasing heat loss and/or decreasing ambient temperature. It should be called more properly "static burning boundary"; in what follows, for the sake of clarity, it will be called "static burning (stability) boundary".

## Sec. 2.8 - NUMERICAL COMPUTATIONS

Computer checks were performed by solving numerically the complete PDE formulation of the general quasi-steady gas phase transient problem (see Sec. 2.2), whereas the combustion stability boundaries were determined by analytical means from considerations about the approximately equivalent ODE formulation (see Sec. 2.7).

### § 2.8.1 - Numerical Approach

In this subsection the numerical code employed for the solution of the PDE formulation of the problem is described. Quasi-steady gas phase transients can be simulated with any kind of law (exponential, parabolic, linear, pulsed, ...) for the history of the controlling parameters (pressure and/or radiation) and for several flame models (MTS, KTSS, KZ, and LC). Computations were mostly performed for the propellant AP/PBAA No. 941 whose properties are listed in Tab. 1.

The nonlinear parabolic PDE of Eq. 2.2.2 was integrated according to numerical schemes taken from Ref. 91. Consider the simple problem

$$(2.8.1) \quad \left\{ \begin{array}{l} \frac{\partial \theta}{\partial \tau} - \sigma \frac{\partial^2 \theta}{\partial x^2} = 0 \\ \theta(x, \tau = 0) = \text{given} \\ \text{boundary conditions} \end{array} \right.$$

where  $\theta = \theta(x, \tau)$  and  $\sigma$  is a constant assumed positive. The time derivative is numerically approximated (see Fig. 50) by a weighted average of the values in the neighborhood of the point we are solving for  $\theta_{j+1}^{n+1}$  (scheme No. 13, p. 191 of Ref. 91):

$$(2.8.2) \quad \begin{aligned} \frac{\partial \theta}{\partial \tau} &\approx \frac{1}{2} \frac{3/2 \theta_{j+1}^{n+1} - 2\theta_{j+1}^n + 1/2 \theta_{j+1}^{n-1}}{\Delta \tau} + \\ &\quad \frac{5}{6} \frac{3/2 \theta_j^{n+1} - 2\theta_j^n + 1/2 \theta_j^{n-1}}{\Delta \tau} + \\ &\quad \frac{1}{2} \frac{3/2 \theta_{j-1}^{n+1} - 2\theta_{j-1}^n + 1/2 \theta_{j-1}^{n-1}}{\Delta \tau} \end{aligned}$$

The second space derivative is numerically approximated by a standard central difference:

$$(2.8.3) \quad \frac{\partial^2 \theta}{\partial x^2} \approx \frac{\theta_{j+1}^{n+1} - 2\theta_j^{n+1} + \theta_{j-1}^{n+1}}{(\Delta x)^2}$$

This scheme is particularly convenient for rapidly varying functions and is known to be always stable. An estimate of the truncation error is given in Fig. 50.

An alternate numerical approach (see Fig. 50) also implemented in the code resorts to a simple Crank-Nicholson scheme (scheme No. 2, p. 189 of Ref. 91) for which the time derivative is simply

$$(2.8.4) \quad \frac{\partial \theta}{\partial t} \approx \frac{\theta_j^{n+1} - \theta_j^n}{\Delta t}$$

This classical Crank-Nicholson scheme, requiring two time levels, is always initiable since in our transients the first vector in time is just some steady state thermal profile (usually evaluated by analytical expressions). On the contrary, the scheme of Eq. 2.8.2 demands an initialization procedure since the knowledge of two previous time vectors  $\theta^{n-1}(x)$  and  $\theta^n(x)$  is required when solving for the current vector  $\theta^{n+1}(x)$ . The simpler scheme of Eq. 2.8.4 is therefore always implemented for the first few time integration steps. It is an user's option then to switch to the scheme of Eq. 2.8.2 (more suitable for rapidly varying phenomena) or to stick with the scheme of Eq. 2.8.4 (more suitable for continuous adjustments of the time step size).

However, our problem includes other lower order terms, such as the first space derivative in the convective term, which can jeopardize the utility of the above numerical schemes. It is shown in Ref. 91 (p. 195) that stability is unaffected by the presence of lower order terms with constant coefficients. In our case, the strong nonlinear dependence of the convective term not only affects the choice of the time step size but also might influence the stability of the overall approach. No general safe method exists for dealing with the complicated problem of Sec. 2.2 and the obvious method of using the above numerical schemes with sufficiently small discretization steps was adopted. The time step size is assigned within a range of values which are always a fraction more or less small (depending on the specific computation) of the corresponding condensed phase characteristic times. Moreover, with the scheme of Eq. 2.8.4 it is an easy matter to adjust the time step size  $\Delta t$  at each integration step by monitoring the tolerance of the predictor-corrector approach:

$$(2.8.5) \quad \frac{\theta_s^{n+1} - \theta^{n+1}(1)}{\theta^{n+1}(1)} \times 100 \equiv s_{tol}$$

where  $\theta_s$  is the predicted value of surface temperature (by parabolic extrapolation of the past 3 values) and  $\theta(1)$  is

the corrected value. The time step size  $\Delta t$  is adjusted automatically, within preassigned bounds, according to  $S_{tol}$  value. The practical consequence of this procedure is that the surface temperature gradient in time is usually very small. The space mesh size is discussed next.

Both the boundary conditions of Eq. 2.2.2 have a direct influence on the space net dimension, but their requirements are in opposing directions: BC2 requires an extended space net which goes deep inside the solid phase, while BC1 requires a fine space net. In order to avoid unnecessary expenditure of computer core and time, the temperature at the cold boundary is considered to be approximately zero when it is of several orders of magnitude less than the surface temperature. Computer runs performed for different sets of input data and operating conditions indicate that cold boundary temperatures  $0(X \rightarrow -\infty, t) = 0(10^{-6})$  or less have no appreciable influence on the structure of the thermal profile near the surface of the condensed phase. At each time step the total number JF of space steps is then chosen by requiring that  $0(X \rightarrow -\infty, t)$  is conveniently small but not too small (in such a case JF is decreased).

The numerical treatment of BC1 of Eq. 2.2.2 has proved to be most delicate. This is obvious if one considers that the coupling of the gas with the solid phase is expressed precisely through the energy balance of BC1. An error is introduced whenever the temperature gradient at the surface is evaluated using a too large space step. Physically, this is due to the fact that volumetric terms (radiation penetration, convective and unsteady effects) become important compared to the surface terms (collapsed reacting layer, condensed and gas phase side thermal gradients) and cannot be neglected in the energy balance across the finite thickness  $\Delta X$  required by the numerical approach. For each run the space mesh size  $\Delta X$  is then chosen by requiring that across the first  $\Delta X$

$$\text{BC1 error} \equiv \frac{\Delta \theta \text{ due to volumetric terms}}{\Delta \theta \text{ due to surface terms}} \ll 1$$

The above check is made at each time integration step. Computer runs performed for different sets of input data and operating conditions indicate that a BC1 error up to a few percent, at most, has no appreciable influence on the overall numerical solution.

The numerical molecule shown in Fig. 50 is associated with a single mesh of dimensions  $\Delta X \cdot \Delta t$  and implies the solutions of JF simultaneous algebraic equations on 3 (scheme of Eq. 2.8.2) or 2 (scheme of Eq. 2.2.4) time levels. The parameter JF is an integer assigning the total number of nodes in the space net. The algebraic system derived from

the discretization of the PDE of Eq. 2.2.2 is then cast in a very special form called a tridiagonal matrix. An efficient method of solution suitable for automatic computations is indicated in Ref. 91 (p. 199). Both the schemes shown in Fig. 50 are implicit and unconditionally stable (when applied to the simple diffusion problem discussed at the beginning of this section). However, scheme (a) is superior to scheme (b) in that, containing more "memory of the past", it better represents rapidly varying functions. Moreover, the truncation error for scheme (a) is of order  $(\Delta X)^4$  rather than  $(\Delta X)^2$  as it is for scheme (b). On the other hand, scheme (b) is more suitable for continuous adjustments of the time step size and does not require an initialization procedure.

A flow chart of the overall program is shown in Fig. 51a. The program allows the user to perform 4 different types of calculation by assigning the appropriate code value to the parameter IOP. Transients of ignition, depressurization, or deradiation and steady states can be computed for fixed values of external controlling parameters. The first step is the computation of the restoring function by PPSTPL subroutine. Giving an appropriate value to the parameter NOSTAB, values of the restoring function at different conditions are computed and printed. This computation can be avoided giving the value 0 to the parameter. As a second step, the steady state configuration corresponding to the arbitrary but fixed initial conditions is evaluated. This is done numerically by the subroutine RTMI (taken from an IBM scientific package) solving the nonlinear algebraic energy conservation equation by a bisection method (Ref. 90). The transient is, then, evaluated by implementing the numerical schemes already described.

The coupling of the condensed phase energy equation to the surface pyrolysis law through the convective term of the PDE of Eq. 2.2.2 requires an iterative procedure for the surface temperature  $\theta_s$ . Moreover, for the MTS flame model the coupling of the condensed phase energy equation to the gas phase heat feedback law, through BC2 of PDE, requires another iterative procedure for the flame temperature  $\theta_f$ . Notice in the flow chart of Fig. 51b that the  $\theta_f$  loop is internal to the  $\theta_s$  loop. Therefore, the overall approach consists in evaluating  $\theta_f$  for an assumed value of  $\theta_s$  and then in checking  $\theta_s$ . This is done with a simple trial and error procedure for the first new integration steps; successively, a predictor-corrector type of approach is implemented through a parabolic extrapolation. This is accomplished separately for both loops and for each of them a convergence test is applied at every integration step according to the following definition:

$$\text{loop error} = \frac{\text{corrected value} - \text{predicted value}}{\text{corrected value}}$$

Typically, an error of less than 0.3% is specified.

Typical values used for the time and space step sizes are:

$$\Delta t = 0.01 \text{ and } \Delta x = 0.01$$

Such values are by no means mandatory and have been adapted to specific situations with the overall goal of the best compromise of cost vs accuracy. A minimum number of about one hundred steps in time is usually performed. Since the surface temperature gradient usually changes in time, a variable time step size is used during the same computation according to the procedure mentioned above. A minimum number of about one thousand steps in space is usually adopted. However, particular situations (e.g., self-sustained oscillations of burning rate or oscillatory changes in time of external radiant flux intensity impinging on a sensibly transparent propellant or transients near pressure deflagration limit) may require much more tedious computations).

The program has been written in FORTRAN IV language and has been run mainly on UNIVAC 1100/80 computer. A typical run requires a core of about 50 K. Several subroutines are also available in BASIC and implemented on HP-85.

A series of checks were made, and some were incorporated permanently in the program, in order to make sure that the overall numerical approach was performing as intended. Actually, the difficulties inherent in the numerical solutions deserve a full study by themselves; therefore, only semi-empirical tests were performed. The first obvious check is to compare the results obtained in this study with those found in previous investigations. Likewise, very helpful is the comparison of the steady state solutions found numerically with the corresponding analytical solutions. These checks were used to localize all possible trivial errors upstream of the overall numerical approach. The appropriate choice of the time and space size was verified according to the standard procedure of varying the time and space mesh size in a programmed manner, while keeping the input data fixed, and making sure that no appreciable difference in the results could be detected by halving or doubling the mesh size. The stability of the overall numerical approach was checked by letting the computer run free on hypothetical transients with no change in time of the controlling parameters. Oscillations of negligibly small amplitude around the initial steady state configuration (known to be physically stable) were observed. All these checks, although successful, not only are not conclusive but also are, in principle, restricted to those specific situations in which they were performed. It was felt convenient to have some form of internal check in the program itself, so that each run could at least be considered self-consistent. Therefore, at each integration step, not only the cold boundary temperature and the BC1 error previously

mentioned, but also the integral balances of energy in the solid phase and across the whole deflagration wave are checked. Again, these also are not conclusive tests but must rather be viewed as effective warning signals whenever the integral balance is not satisfied at any stage of the transient.

#### § 2.8.2 - Dynamic extinction of solid propellants

Checks of the lower dynamic stability boundary were performed for several deradiation and depressurization transient laws (see Tab. 9). Since the lower dynamic stability boundary corresponds to statically unstable roots, it cannot be observed directly either experimentally or numerically. A go/no-go technique is required (see Figs. 52-53). Results obtained are graphically illustrated in Figs. 52-66 and summarized in Tab. 10. They confirm the analytical predictions as to the lower dynamic stability boundary; in particular:

- (1) its independence on the specific monotonic laws implemented (linear, bilinear, parabolic, exponential), Figs. 54-57.
- (2) its independence on the specific coefficient rate of a given monotonic law, Figs. 52-53.
- (3) its validity both for depressurization and/or deradiation transients, Figs. 61-62.
- (4) its validity for both optically opaque or transparent condensed phase, Fig. 63.
- (5) its validity for simultaneous or consequential monotonic forcing laws, Figs. 64-65.
- (6) its validity for pulsed forcing laws, Fig. 66.
- (7) its dependence on final operating conditions, Figs. 57-60.
- (8) its validity for MTS and KTSS nonlinear flames; no lower dynamic stability limit exists for KTSS linear, KZ, and LC flames.

It is further suggested that  $n = 3$  gives an excellent agreement for any transient with final pressure not larger than, say 30 atm. For larger final pressure either  $n < 3$  or more accurate numerical schemes (due to the strong dependence on initial conditions) are to be implemented; this is yet under study.

#### § 2.8.3 - Upper dynamic combustion stability

Results concerning the upper dynamic stability limit are illustrated in Figs. 67-68. Runs with exponential increase of pressure from  $P_i = 10$  atm to  $P_f = 30$  atm are plotted for several values of the surface heat release  $Q_s$  (cf. Tab. 4). As expected (cf. Fig. 43), for  $|Q_s|$  sufficiently low (Fig. 67), one observes a smooth transition from the initial to the final steady state equilibrium configuration (see, for example,  $Q_s = -150$  cal/g). For larger values of  $|Q_s|$ , a vigorous acceleration of the wave occurs (Fig. 68). Following this, the heterogeneous deflagration wave will relax toward a stationary solution (Fig. 69). This is the stable steady state reacting

configuration for  $|Q_S|$  less than the A-D roots coalescence value, self-sustained oscillations for  $|Q_S|$  larger than the A-D roots coalescence value, and the stable steady state unreacting configuration for  $|Q_S|$  larger than the B-D roots coalescence value or whenever the dynamics of the transient is too fast compared to the propellant response capability. This is discussed next.

#### § 2.8.4 - Self-sustained oscillatory burning of solid propellants

The pressurization runs from 10 to 30 atm shown in Fig. 69, for several values of  $Q_S$ , were computed implementing MTS flame. The results nicely confirm the existence of the three static burning regimes predicted by the bifurcation diagram of Fig. 43. Remark that  $|Q_S| = 180$  cal/g is less than the A-D roots coalescence values ( $|Q_S| = 190$  cal/g), while  $|Q_S| = 220$  cal/g is very close to the B-D roots coalescence value ( $|Q_S| = 222$  cal/g). Compare with Tab. 4. Notice that for increasing  $|Q_S|$ , the same external forcing function gives more pronounced dynamic burning effects. For example, see the succession of the initial surface temperature peaks in Fig. 69 for the three indicated value of  $Q_S$ . Large values of  $|Q_S|$  favor (dynamic) extinction, due to overstability, during the initial transient.

For  $|Q_S| = 200$  cal/g the numerical solution of the pressurization test confirms that, after a certain transient, the combustion wave undergoes characteristic, sharp self-sustained oscillations around A root ( $\Theta_S = 1.61$ ) and D ( $\Theta_S = 0.94$ ) roots. The results of further computer simulated tests are summarized in Tab. 11. No self-sustained oscillatory regime was found for several values of  $|Q_S| \leq 180$  cal/g and  $|Q_S| \geq 210$  cal/g. But for  $Q_S = -200$  cal/g, after a few transient cycles, exactly the same oscillatory pattern was found for exponential pressurization tests to 40 atm with  $B_p = 200$  from  $P_i = 10, 20$  and 30 atm. However, the amplitude and the period  $\tau$  of the surface temperature oscillations decreased, for increasing final pressure, according to the values listed in Tab. 11. Exponential pressurization tests to 50 atm, with  $B_p = 200$ , from  $P_i = 10$  or 40 atm confirmed this point. All this evidence neatly suggests that, for a propellant with the appropriate value of  $Q_S$ , the existence and the properties of the self-sustained oscillatory regime are uniquely defined by the final operating pressure (being all runs performed at fixed ambient temperature of 300 K and for adiabatic burning). In Tab. 11 for the reader's convenience, the values of  $\Theta_S(E)$ ,  $\Theta_S(D)$ , and  $\Theta_S(A)$  are plotted for  $n = 3$ . Likewise, the value of thermal wave relaxation time in the condensed phase,  $\tau_{th,c} = R^{-2}$ , are given. However, the exact meaning of this parameter in the present context is open to questions.

The previous computer simulated tests were obtained by implementing MTS flame. Pressurization tests with KTSS non-linear flame, from 10 to 30 atm with  $B_p = 1$ , were also performed. Unfortunately, the value of  $Q_S = -200$  cal/g falls

outside the range of applicability of the KTSS nonlineal flame at 10 atm; therefore no direct comparison with MTS flame was possible. The same pressurization test was then attempted for  $Q_s = 180$  cal/g. A self-sustained oscillatory regime was detected ( $\tau_p = 2.8$ ), with the same general features observed with MTS flame (see Fig. 70). A self-sustained oscillatory regime with KTSS nonlinear flame was also detected by Koecker and Nelson (Ref. 74), who found  $\tau_p = 1.36$  at 68 atm for  $|Q_s| = 105.8$  cal/g (their  $|H| = 0.88$ ).

The characteristic spikes, observed in all run, of the burning rate oscillations physically suggest a succession of thermal explosions of surface layers (strongly and in-depth heated by the intense heat source due to large  $|Q_s|$  values at the burning surface slowly regressing for most time) followed by similarly fast burning rate decrease (due to tight coupling condensed/gas phases at high burning rates) and slow thermal wave build-up (ignition lag). For any combination of pressure and surface heat release, a more or less narrow range of values exists for which self-sustained oscillatory burning is the only allowed combustion regime. In any event, within the framework of heterogeneous (thermokinetic) thin flame combustion stability theory, low pressure associated with large surface heat release favors self-sustained oscillatory burning.

A region of particular interest is near the pressure deflagration limit. It was predicted analytically (see § 2.7.3) and is confirmed numerically that low frequency self-sustained oscillations show up when the pressure is lowered down to the deflagration limit. Several experimental reports on this phenomenon can be found in the Soviet literature. A recent paper by Japanese authors (Ref. 92) further claims that low pressure self-sustained oscillations can also be associated with (steady) external radiation. Computer runs in agreement with this experimental observation are shown in Fig. 71: notice that frequency increases and amplitude decreases for increasing intensity of the impinging radiant flux.

#### § 2.8.5 - Effect of $C_g/C_c \neq 1$

The effect of specific heat ratio not (necessarily) unity is to make dynamic extinction more difficult due to both slight decrease of the lower dynamic stability boundary and larger resistance to changes of the instantaneous surface temperature. See Fig. 72. The overall effect is not large, though.

The consequence of  $C_g/C_c \neq 1$  on the self-sustained oscillatory burning is more sensible. At a given pressure, oscillations require larger  $|Q_s|_{ref}$  and, mainly, feature less important spikes than for  $C_g/C_c = 1$ . See Fig. 73. At a given  $Q_s, ref$ , oscillations show up for decreasing pressure until the deflagration limit is reached. See Fig. 74.

#### § 2.8.6 - Ignition of solid propellants

Several go/no-go ignition transients were performed. A significative example obtained with MTS flame is shown in Fig. 75. The two runs plotted in this figure are identical, except a negligibly faster cut-off of the external radiant source for the extinguished case. The minor dynamic effects associated with the cut-off of the external radiant source are not enough, for the ignited case, to lead the instantaneous surface temperature (or burning rate) below the corresponding critical value. Under the specific operating conditions of Fig. 75, the lower dynamic limit is seen to constitute a rather accurate boundary both for the static (minimum energy) and dynamic (smooth energy source cut-off) ignition requirements. This, however, cannot be generalized. Indeed the lower dynamic limit was evaluated for an initially steadily burning propellant. The exact connection, if any, between ignition and lower dynamic limit has yet to be investigated. On the other hand, in the case of dynamic extinction of steadily overdriven burning rates associated with ignition transients, the lower dynamic limit is expected to be fully valid.

Further computed simulated ignition transients are illustrated in Fig. 76 (exposure time  $\tau_e = 140$  and linear deradiation with  $B_r = 200$ ) and Fig. 77 ( $\tau_e = 112$  and  $B_r = 20$ ). Both examples show some dynamic burning effects associated with the external radiation source cut-off. Moreover, under the specific operating conditions of Fig. 77, the propellant is seen to ignite before reaching the lower dynamic limit. Very likely this is due to slow, volumetric heating of the propellant slab associated with low external radiant flux intensity. Slow, volumetric heating is also responsible for the large and fast surface temperature damped oscillations appearing in Figs. 76-77 but not in Fig. 75.

The radiative ignition map shown in Fig. 78 was obtained by numerical computations with a trapezoidal, monochromatic and perpendicularly impinging pulse of external radiation. MTS flame was implemented; a pressure range from 10 to 30 atm was explored for both optically opaque or transparent condensed phase. The results obtained show that the ignition boundary tends to be a straight line in the  $\lg/\lg$  plot (time of radiant heating vs radiant flux intensity). However, this straight line is no longer valid for low pressure and/or large radiant flux intensity. Dynamic extinction associated with cut-off of the radiant source made ignition impossible at 10 atm and large radiant flux; it was found necessary to decrease the rate of the radiant source cut-off. Optical transparency makes ignition more difficult (in that the minimum time of required radiant heating increases), since the heating effect is volumetrically diluted. All these effects are well known experimentally. An orientative comparison with experimental data collected in Refs. 3 or 59 is shown in Fig. 79: the solid lines fitting the experimental data are seen to correspond surpris-

ingly well with the computed points. Notice that the composition with no carbon should be less opaque to radiation than the composition with 1% carbon.

The general behavior of computed ignition transients is shown in Fig. 80 where surface temperature, flame temperature, and heat feedback are plotted vs time for a given radiation pulse. Remark that numerical modeling of ignition can be attempted only with MTS or KTSS nonlinear flames. However, in the very low burning rate region it was found necessary to tailor these flame models to obtain a well behaved limit for  $\theta_s \rightarrow 0$ . The following steps were taken for  $\theta_s < \theta_k$ :

$$\theta_f = \theta_s (\theta_{f,k}/\theta_k)$$

$$\dot{q}_{g,s} = R \left[ Q - \frac{C_g}{C_c} (\theta_f - \theta_s) \right]$$

where  $\theta_{f,k}$  is obtained from Eq. 2.2.7 letting  $\theta_s = \theta_k$ . This minor modification should work with any suitable flame model and makes sure that

$$\lim_{\theta_s \rightarrow 0} \dot{q}_{g,s} (\Psi, R) / R = 0$$

#### § 2.8.7 - Further computer runs on dynamic combustion stability

Computer simulated burning transients triggered by a variety of pressure and/or radiation pulses are being performed. The purpose is to check the validity of the analytical predictions in the case of forcing functions of arbitrary shape but levelling off in time. The results so far obtained are extremely encouraging. An example of radiative pulse was shown in Fig. 66; another example, dealing with pressure pulse, is discussed in Ch. 3 with reference to shock tube experiments.

### Sec. 2.9 - STATE OF THE ART OF THE NONLINEAR APPROACH

The problem of the quasi-steady gas phase burning of a solid propellant is being dealt with in a rather general form. In order to retain the nonlinearity of the problem, an approximate formulation in terms of an ODE was written. This was done by means of an integral approach limited to situations in which no inflection point in the history of the condensed phase thermal profiles would occur. It is shown that important facts (see below) of heterogeneous combustion may be ascertained. The two fundamental regimes of static (intrinsic random perturbations) and dynamic (externally assigned changes of the controlling parameters) stability of heterogeneous flames, allowing for finite size disturbances, are examined.

The following facts emerge from the nonlinear static stability analysis. For a given set of parameters:

1. a stable stationary nonreacting equilibrium configuration (trivial solution) is always found.
2. a stable, stationary (low  $|Q_s, \text{ref}|$  and/or large pressure) or self-sustained oscillating (large  $|Q_s, \text{ref}|$  and/or low pressure), reacting equilibrium configuration may be found.
3. a stable stationary reacting equilibrium configuration is found before A-D roots coalescence occurs.
4. self-sustained oscillations are found between A-D roots coalescence and B-D roots coalescence.
5. after B-D roots coalescence, no stable reacting equilibrium solution is found.
6. the static burning (stability) boundary, for small but finite size random intrinsic disturbances, is the locus of A-B roots coalescence at fixed pressure.
7. the pressure deflagration limit, for small but finite size random intrinsic disturbances, is the locus of B-D roots coalescence obtained by lowering the pressure for fixed chemical composition (i.e., fixed  $Q_s, \text{ref}$ ) and fixed set of operating conditions.
8. the static stability of the steady state equilibrium configurations can be measured by the slope of the static restoring function vs surface temperature at the point  $\bar{\theta}_s$  of interest.
9. The effect of the relevant parameters can be easily evaluated by considering the corresponding bifurcation diagrams.

The following facts emerge from the nonlinear dynamic stability analysis. For a given monotonic or pulsed law of timewise decrease of the controlling parameters:

1. extinction may occur even though the final point of the transition is statically stable.
2. the lower dynamic stability boundary, for finite size disturbances consequent to timewise changes of the controlling parameters, is the locus of the statically unstable roots (B-type) associated with the final operating conditions. It holds true instantaneously for monotonic forcing functions, asymptotically for pulsed forcing functions.

3. the lower dynamic stability boundary holds true both for deradiation and/or depressurization runs, and is not affected by the details of the specific forcing law implemented.
4. upper dynamic instability is related to D root and may cause vigorous acceleration of the combustion wave or dynamic extinction.

The following facts emerge by comparing several flame models:

1. the KTSS linear, KZ, and LC flame models are physically meaningless for burning rate less than about 90% of the steady value.
2. the KTSS nonlinear flame model is physically questionable for burning rate near zero.
3. the MTS flame model is in principle acceptable over the whole range of burning rate.

The following facts emerge by changing the order  $n$  of the polynomial approximating the disturbance thermal profile:

1. C and A roots are not affected.
2. B, D, and E roots are affected.
3. the static burning(stability) boundary can be predicted independently of  $n$ .
4. the pressure deflagration limit is predicted in function of  $n$ .
5. the dynamic stability boundaries (both lower and upper) are predicted in function of  $n$ .
6. the polynomial of order  $n=3$  gives accurate results up to 30 atm of final pressure,  $n < 3$  may be more suitable for larger values of pressure. This point is not yet definitive.

The physical meaning of the stability boundaries is the following. The static burning (stability) boundary defines that ultimate burning rate or surface temperature, for a given pressure, below which steady self-sustained burning is no longer allowed. The dynamic stability boundary defines that ultimate burning rate or surface temperature, for a given set of operating conditions, below which extinction necessarily follows. The fundamental importance of this distinction is stressed by the fact that, under dynamic conditions, the propellant may momentarily burn also in a region of statically forbidden configurations. It is shown that the dynamic stability boundary collapses to the range of influence of the statically stable equilibrium configuration when the rate of change of the externally controlled parameters is negligible. The pressure deflagration limit defines that ultimate pressure, for a given chemical composition and set of operating conditions, below which steady self-sustained burning is no longer allowed.

Notice that numerical values have been given only for a particular composite propellant (AP/PBAA No. 941). This was done simply because for this particular propellant properties and good flame models were readily available. It is felt, however, that all analyses were conducted from a broad point of

view, and in no way were they dependent on the particular type of propellant chosen as datum case. Therefore, the conceptual results are expected to hold, although in different ranges of the relevant parameters, for a wide variety of solid propellants.

In particular, the nonlinear stability theory of heterogeneous thin flames developed in this report shows that:

1. pressure deflagration limit can be predicted even for adiabatic combustion waves.
2. self-sustained oscillatory burning is found for both increasing  $|Q_{s,ref}|$  (at a fixed pressure) and decreasing pressure (with a fixed chemical composition).
3. damped oscillatory burning is found for both increasing  $|Q_{s,ref}|$  (at a fixed pressure) and decreasing pressure (with a fixed chemical composition) before the self-sustained oscillatory burning.
4. the effect of  $C_g/C_c \neq 1$  is appreciable in reducing the amplitude of self-sustained oscillatory burning.
5. the effect of radiative heat loss from the burning surface is negligible.
6. ignition transients in general cannot be fully predicted.
7. all findings have a clear interpretation in the standard pressure vs burning rate plot.

## CHAPTER 3 - EXPERIMENTAL UNSTEADY BURNING RESULTS

### Sec. 3.1 - SHOCK TUBE EXPERIMENTS

The pressure deflagration limits of the three propellant formulations under consideration (an AP-based composite, a catalyzed DB and a noncatalyzed DB) were determined in the actual operating conditions of the shock tube (Fig. 81a). These experiments were conducted statically, i.e. a propellant sample was placed in the test section of the shock tube (end wall) and ignition was attempted by means of an electrically heated wire (Fig. 81b). The ignition was considered successful only if a self-sustained flame would develop. The test was repeated for several pressurizing gases (nitrogen, air, oxygen) and for ambient pressure parametrically changed. Results for the composite propellant are shown in Fig. 82 (not self-sustained flame means that a visible flame would develop but disappear immediately after an electrical heating of several seconds duration). The samples were cylindrical pellets of 8 mm diameter and about 10 mm thickness. Tests with noncatalyzed DB samples of 16 mm diameter did not show any appreciable difference.

Samples were then placed at the same location, ignited by an electrically heated wire and, once steadily burning, subjected to shock waves of different strength. The overall experimental apparatus is sketched in Fig. 83. The light emitted by the burning propellant was detected by means of a photodiode directionally selective and sensitive in the visible and near infrared (spectral response peak at  $0.8 \mu\text{m}$ ). Several tests with different propellants, ignition pressures, pressurizing gases, and shock speeds failed to show conclusive trends as to the dynamic burning rate behavior (as revealed by the light emission). The basic difficulty is the fast succession of shock waves and expansion fans impinging on the surface of the burning propellant during the same test. For example, see Figs. 50-51 of Ref. 8a (in which the period of the pressure pulse is about 10 ms). In this series of tests, complete extinguishment of the propellant was never achieved.

In order to overcome the problem just mentioned, the shock tube was slightly modified to work as a piston tube. At present, a teflon piston weighting 150 g is used (Fig. 84). In this operating configuration, a longer period (about 50 ms) of the pressure pulses can be obtained and, in general, a better control of the whole experimental apparatus is possible. A series of experiments was performed with the piston tube in order to study the effects of compression waves on a burning solid propellant. Tests were conducted with two different propellants: an AP-based composite and a noncatalyzed double base. Samples of propellant were located on the end wall of the piston tube and, while steadily burning, were subjected to the effects of compression waves. The tests were carried on with different initial conditions, changing the initial pressure between 0.5 and 1 atmosphere and with three different test gases (ni-

trogen, air, oxygen) in order to change the initial concentration of oxygen.

Preliminary results obtained with a noncatalyzed DB were shown in Figs. 52-55 of Ref. 8a. In those runs it was observed that extinction of the burning sample could occur under the action of compression waves. Further, systematic experimental analysis was then performed with a noncatalyzed DB and a composite propellant (AP/PVC); a detailed description of experiments and results was reported in Ref. 16. It was confirmed that burning stability of solid propellants can be very much influenced by rapid pressure variations, especially in the presence of oxygen in the surrounding atmosphere. A permanent extinction of the burning propellant was observed in several cases.

A further series of experiments at the piston tube rig (Refs. 8b, 16) was performed with the aid of high speed cinematography. A composite propellant (AP/PBHT) was tested. A sketch of the experimental apparatus is shown in Fig. 85. Samples of propellant (16 mm diameter) were located on the end wall of the piston tube and, while steadily burning, were subjected to compression waves. The initial pressure in the test section was 1 atm and the initial concentration of oxygen was changed, using three different test gases (nitrogen, air, oxygen). The maximum pressure reached in the test was of the order of 130 atm and the duration of the pressure pulse was of about 15 ms. During each run, pressure and luminosity were measured respectively with a piezoelectric pressure transducer (PCB-113 A) and a photodiode (Hewlett-Packard HP 5082-4205); moreover, in order to better visualize the combustion phenomena, high speed color movies were taken, using a Hitachi 16 HD camera at speeds ranging from 3000 to 7000 pps.

A typical series of photographs, obtained testing in air, is reported in Fig. 86; the corresponding pressure and luminosity traces are shown in Fig. 87. The photographs show a rapid increase of burning during the pressurization, followed by flame detachment and extinction. The maximum luminosity is reached while the pressure is still increasing. A similar behavior was observed in all the runs, also with different test gases. Usually, after the extinction, the propellant starts burning again under the effect of the following pressure pulses; however, in some instances (about 5% of the tests) the samples of extinguished propellant were recovered after the run.

Another typical feature of the combustion, observed in the tests, is a very sharp decrease of flame luminosity occurring during the pressurization; this is reported in Fig. 88 showing two photographs taken at an interval of 0.25 ms. This effect was observed in all the tests.

Both the photodiode and the high speed camera cannot show clearly what is going on near the surface of the burning propellant, because they see the luminosity emitted by the burning gases in the whole volume of the test chamber. In order to detect the combustion near the propellant surface, a different technique, based upon the measurement of gas ionization, was tried. A schematic layout of the experimental setup, for the measurement of the ionization near the propellant surface, is shown in Fig. 89 (the propellant was placed on the side wall for assembling convenience). Two small copper wires of 0.2 mm diameter were placed through the propellant sample, divided by a gap of 3 mm and protruding about 0.5 mm from the surface. The variation of resistance through the gap, due to ionization, was measured as a voltage and recorded during the tests. A typical oscilloscope trace corresponding to steady burning, is shown in Fig. 90. Results obtained in unsteady conditions with the piston tube are reported in Fig. 91 and Fig. 92. Fig. 91 shows a sharp increase of ionization corresponding to the first pressure step, followed by a rapid fall to zero, with pressure still increasing; this seems to confirm the occurrence of an extinction of the flame at the propellant surface; by comparison with the luminosity trace shown in Fig. 87, it can be seen that the falling to zero of the ionization, corresponds to the minimum of luminosity detected by the photodiode. Fig. 92 shows a series of pressure pulses with successive extinctions and reignitions.

Computer simulated runs were also performed, within the limitations of a quasi-steady flame kinetically non modified by the pressure pulses. An example is shown in Fig. 93.

### Sec. 3.2 - DEPRESSURIZATION EXPERIMENTS

Depressurization runs were realized in a pressurizable combustion chamber, about 350 cm<sup>3</sup> volume, connected to the ambient atmosphere by means of exhaust valves. A first series of data was performed with a relatively large (12.7 mm orifice diameter) valve manually operated. A second series of data was performed combining several solenoid valves (orifice diameter ranging from 1.2 to 4.0 mm) simultaneously operated. The third and last series of data was performed with the same combination of solenoid valves, but in addition a closed loop circuit was implemented to keep the combustion pressure constant prior to the abrupt opening of the solenoid valves. All runs were realized at ambient temperature by exhausting to atmospheric pressure. Next serie of depressurization data will be collected with the final pressure parametrically changed.

The combustion chamber contains the ignition system (a nichrome wire of 0.8 mm diameter), a strand fuse wire system to measure the steady state burning rate of the propellant prior to depressurization, two plexiglass windows for direct observation of the relevant phenomena. The propellant samples are cylinders, about 6 x 50 mm, cut from a relatively large grain. The lateral surface is inhibited to combustion by successive coatings of teflon spray, dope, and teflon spray. Extinguished samples showed a very flat burning surface. All runs were performed with an AP/PVC composition burning in a nitrogen atmosphere. Details about the experimental apparatus and procedure are given in Ref.5 (burning rate measurement and data processing), Ref. 14 (closed loop circuit for constant combustion pressure) and Ref.15 (depressurization combustion chamber).

After pressurizing the combustion chamber (up to about 40 atm in the results to be presented here) and igniting the propellant sample, enough time is allowed to create a steady heterogeneous deflagration wave. The steady state burning rate is, then, measured by means of (typically) three fuse wires. When the last fuse wire is burnt, the combustion chamber is suddenly exhausted to atmospheric pressure. The pressure drop is of exponential nature for solenoid valves, more rounded for manual valves (see Fig. 94). The overall, qualitative but important, result of extinction or continued burning is observed.

Usually, the following parameters are measured and/or recorded by means of a multichannel (UV sensitive paper) galvanometric recorder: the ignition current and time; the flame appearance by means of photodiode; the combustion pressure by a water cooled, piezoelectric transducer; the initial steady state burning rate by means of a standard fuse wire technique and using the recorder time marker.

Experimental results obtained from depressurization tests of AP/PVC samples, from some initial pressure to atmospheric pressure, are summarized in Fig. 95. This is a  $[dp(t)/dt]_{\max}$  vs  $P_i$  plot, as already done by several investigators in the past. However, according to our nonlinear burning stability theory, no special meaning whatsoever is attached to the maximum depressurization rate. The fate of a depressurization test, extinction vs continued burning, rather is the integrated result of the

whole history of the burning propellant (initial conditions, de-pressurization law, etc.). The critical boundary, as defined in Sec. 2.7, is a local property of the burning propellant; but whether it will be reached or not depends on the previous history of the burning propellant. Obviously, high  $[dP(t)/dt]_{\max}$  for exponential depressurization implies that the whole transient is faster and this favors dynamic extinction. Experimentally, different depressurization transients were obtained by changing the total exhaust orifice area (e.g., by simultaneous operation of more or less solenoid valves). On a linear  $[dP(t)/dt]_{\max}$  vs  $P_i$  plot, a straight boundary is found to separate quite neatly the extinction from the continued burning region.

A summary of experimental results obtained in this paper, by Merkle (Ref. 29), and Von Elbe (Ref. 24) is shown in Fig. 96. Remark that the maximum depressurization rate occurs at mid de-pressurization for manual valves but at the very beginning of the depressurization history for solenoid valves. Depressurization rates were measured by considering the time required for pressure to drop from  $(P_i - 1)$  atm to  $(P_f + 1)$  atm for manual valves. For a fair comparison one should consider depressurization rates about 3 times lower. Even so, the two plots found in this work do not correspond. With the same maximum depressurization rate, the depressurization history of Fig. 94b is more effective than the exponential depressurization of Fig. 94a in extinguishing the sample. This spectrum of results is not surprising from the point of view of our theory, rather is welcome. Indeed this offers another, and perhaps more reliable, way to compare closely experimental and theoretical results. For lack of time, no detailed results of this comparison will be given here.

However, remember that the agreement between analytical and numerical results was already successful. The numerical approach is able to reproduce depressurization transients for several aspects more detailed than any experimental information. The qualitative aspects of the numerical solutions agree with experimental information. Figures such as Fig. 95 can be constructed numerically as well; this is in our opinion the first and perhaps more meaningful task of any close comparison in this area. Remark that extinction was assumed to occur in the numerical solutions when unbounded decrease of burning rate toward zero was observed; this in turn occurs when the analytically predicted lower dynamic stability boundary is crossed. Comparing experimental and computed boundaries (between extinction and continued burning) in Fig. 95 shows that resistance to dynamic extinction is larger than predicted. Better flame models and/or more realistic description of the properties shall be implemented in order to attempt to bridge the gap.

Obviously, the most wanted piece of information is the burning rate history during depressurization transients. Unfortunately, no reliable experimental technique is available yet. An up-to-date review of experimental methods measuring transient combustion response was recently offered (Ref. 93); in particular, a microwave phase shift technique seems to be promising (Ref. 94).

REFERENCES

- (1) De Luca L., "Nonlinear Stability Analysis of Solid Propellant Combustion", II International Symposium on Dynamics of Chemical Reactions, University of Padova, Italy, 15-17 December 1975. Proceedings, pp. 245-256, 1975.
- (2) De Luca L., "Instability of Heterogeneous Deflagration Waves", VI International Symposium on Detonation, San Diego, California, USA, 24-27 August 1976. Proceedings, pp. 281-289, 1976.
- (3) De Luca L., "Solid Propellant Ignition and Other Unsteady Combustion Phenomena Induced by Radiation", Ph.D. Thesis, Department of Aerospace and Mechanical Sciences, Princeton University, AMS Report No. 1192-T, November 1976.
- (4) De Luca L., Galfetti L., and Zanotti C., "Dynamic Extinction of Composite Solid Propellant", XIX Israel Conference on Aviation and Astronautics, Technion, Haifa, Israel, 2-3 March 1977. Israel Journal of Technology, Vol. 16, No. 16, pp. 159-168, 1978.
- (5) De Luca L. and Zanotti C., "Measurement of Steady Solid Propellant Burning Rate and Data Processing", XXXII Congresso Nazionale Associazione Termotecnica Italiana (ATI), Roma, 20-23 September 1977. Proceedings, pp. 256-275, 1977.
- (6) De Luca L., Galfetti L., and Zanotti C., "Evaluating the Kinetic and Diffusion Time Constants in the MTS Flame Model", XXXII Congresso Nazionale Associazione Termotecnica Italiana (ATI), Roma, 20-23 September 1977. Proceedings, pp. 278-301, 1977.
- (7a) De Luca L., "Theoretical Studies on Heterogeneous Deflagration Waves: I. A Partial Differential Equation Formulation of the Problem", Meccanica, Vol. 13, No. 1, pp. 16-27, 1978.
- (7b) De Luca L., "Theoretical Studies on Heterogeneous Deflagration Waves: II. An Approximate Ordinary Differential Equation Formulation of the Problem", Meccanica, Vol. 13, No. 2, pp. 71-77, 1978.
- (8a) De Luca L., Coghe A., and Reggiori A., "The Dynamics of Solid Propellant Combustion", European Research Office of USA, Istituto di Macchine, Politecnico di Milano (Grant No. DA-ERO 78-G-029), 1st Annual Technical Report, November 1978.
- (8b) De Luca L., Coghe A., and Reggiori A., "The Dynamics of Solid Propellant Combustion", European Research Office of USA, Istituto di Macchine, Politecnico di Milano (Grant No. DA-ERO 78-G-029), 2nd Annual Technical Report, November 1979.
- (9) De Luca L., Galfetti L., and Zanotti C., "Comparison of Two Flame Models Used in Solid Rocket Propellant Unsteady Combustion", XXVI Convegno Nazionale delle Comunicazioni, Genova, Italy, 5-7 October 1978. Proceedings, pp. 442-453, 1978.
- (10) De Luca L., "Self-Sustained Oscillatory Combustion of Solid Rocket Propellants", The Propulsion and Energetics Panel of AGARD, 53rd Meeting on Solid Rocket Motor Technology, Oslo, Norway, 2-5 April 1979. AGARD Conference Proceedings No. 259, pp. 24/1-24/14, July 1979.

- (11) De Luca L., Galfetti L., and Zanotti C., "Ignition and Extinguishment of Solid Rocket Propellants", The Propulsion and Energetics Panel of AGARD, 53rd Meeting on Solid Rocket Motor Technology, Oslo, Norway, 2-5 April 1979. AGARD Conference Proceedings No. 259, pp. 4/1-4/14, July 1979.
- (12) Coghe A., De Luca L., Sensulari G.L., and Volpi A., "Gas Phase Velocity Measurements in Solid Rocket Propellants by Laser-Doppler Anemometry", The Propulsion and Energetics Panel of AGARD, 53rd Meeting on Solid Rocket Motor Technology, Oslo, Norway, 2-5 April 1979. AGARD Conference Proceedings No. 259, pp. 31/1-31/14, July 1979.
- (13) De Luca L., Coghe A., Ferrari G.C., Galfetti L., Martinelli L., Volpi A., Zanotti C., Casci C., and Basso A., "Recent Research on Unsteady Combustion at CNPM", VI International Symposium on Combustion Processes, Karpacz, Poland, 26-30 August 1979. Archives of Thermodynamics and Combustion, on print.
- (14) De Luca L., Casarini A., Pastore G., Portaro A., Tanturli L., and Zanotti C., "Experimental Results on the Steady Burning of Solid Rocket Propellants", XXXIV Congresso Nazionale Associazione Termotecnica Italiana (ATI), Palermo, 8-12 October 1979. Proceedings, Vol. 2, pp. 79-106, 1979.
- (15) De Luca L., Dondè R., and Zanotti C., "Experimental Dynamic Extinction by Depressurization of a Composite Solid Rocket Propellant", XXXIV Congresso Nazionale Associazione Termotecnica Italiana (ATI), Palermo, 8-12 October 1979. Proceedings, Vol. 2, pp. 51-78, 1979.
- (16) Reggiori A., De Luca L., and Germi R., "Experimental Investigation on Solid Rocket Propellant Burning Instability by Shock Tube", V Congresso Nazionale dell'Associazione Italiana di Aeronautica e Astronautica (ALDA), Milano, Italy, 22-26 October 1979. Aerotecnica Missili e Spazio, Vol. 58, No. 2/3 pp. 158-166, 1979.
- (17) De Luca L., Riva G., Galfetti L., and Tabacco U., "Unstable Burning of Thin Solid Propellant Flames", XVI AIAA/SAE/ASME Joint Propulsion Conference, Hartford, Connecticut, USA, 30 June - 2 July 1980. AIAA Paper 80-1126.
- (18) De Luca L., "Nonlinear Burning Stability Theory of Heterogeneous Thin Flames", XVIII International Symposium on Combustion, University of Waterloo, Canada, 17-22 August 1980. Proceedings, on print.
- (19) De Luca L., Riva G., Galfetti L., and Zanotti C., "Theoretical and Experimental Nonlinear Dynamics of Heterogeneous Deflagration Waves", VI Heat and Mass Transfer Conference, Byelorussian Academy of Sciences, Minsk, USSR, 10-12 September 1980. Proceedings, Vol. III, pp. 83-91, 1980.
- (20) Ciepluch C.C., "Effect of Rapid Pressure Decay on Solid Propellant Combustion", ARS J., Vol. 31, November 1961, pp. 1584-1586, 1961.

- (21) Ciepluch C.C., "Effect of Composition on Combustion of Solid Propellants During a Rapid Pressure Decrease", NASA TN D-1559, 1962.
- (22) Ciepluch C.C., "Spontaneous Reignition of Previously Extinguished Solid Propellants", NASA TN D-2167, 1964.
- (23) Von Elbe G., "Solid Propellant Ignition and Response of Combustion to Pressure Transients", AIAA Paper No. 66-668, 1966.
- (24) Von Elbe G. and McHale E.T., "Extinguishment of Solid Propellants by Rapid Depressurization", AIAA J., Vol. 6, No. 7, pp. 1417-1419, 1968.
- (25) Horton M.D., Bruno P.S. and Graesser E.C., "Depressurization Induced Extinction of Burning Solid Propellant", AIAA J., Vol. 6, No. 2, pp. 292-297, 1968. See also ICRPG/AIAA 2nd Solid Propulsion Conference, pp. 232-239, June 1967.
- (26) Wooldridge C.E. and Marxman G.A., "Nonlinear Solid Propellant Burning Rate Behavior During Abrupt Pressure Excursion", AIAA Paper No. 69-172, 1969.
- (27) Wooldridge C.E. and Marxman G.A., "A Comparison between Theoretical and Experimental Extinction Behavior of Solid Propellants", AIAA Paper No. 70-666, 1970.
- (28) Jensen G.E. and Brown R.S., "An Experimental Investigation of Rapid Depressurization Extinguishment", 6th ICRPG Combustion Conference, CPIA Publication No. 192, pp. 411-423, 1969.
- (29a) Merkle C.L. and Summerfield M., "Extinguishment of Solid Propellant Flames: a Theory Based on a New Feedback Law", Princeton University, AMS Report No. 838, Presentation Version, 1968.
- (29b) Merkle C.L., Turk S.L. and Summerfield M., "Extinguishment of Solid Propellant by Rapid Depressurization", Princeton University, AMS Report No. 880, 1969.
- (29c) Merkle C.L., Turk S.L., and Summerfield M., "Extinguishment of Solid Propellant by Depressurization: Effects of Propellant Parameters", AIAA Paper No. 69-176, 1969.
- (30a) Coates R.L. and Horton M.D., "Prediction of Conditions Leading to Extinguishment", 6th ICRPG Combustion Conference, CPIA Publication No. 192, pp. 399-409, 1969.
- (30b) Coates R.L., and Horton M.D., "Further Evaluation of a Simplified Theoretical Model for Solid Propellant Extinguishment", 7th Jannaf Meeting, CPIA Publication No. 204, pp. 369-377, 1971.
- (31) Coates R.L. and Horton M.D., "Predicted Effects of Motor Parameters on Solid Propellant Extinguishment", JSR, Vol. 7, No. 12, pp. 1468-1470, 1970.

- (32) Steinz J.A. and Selzer H., "Depressurization Extinguishment of Composite Solid Propellants: Flame Structure, Surface Characteristics, and Restart Capability", CST, Vol.3, pp. 25-36, 1971.
- (33) Steinz J.A. and Selzer H., "Depressurization Extinguishment for Various Starting Pressures and Solid Propellant Types", AIAA Paper No. 71-631, 1971.
- (34) Baer A.D., Ryan N.W., and Schulz E.B., "Spectra and Temperature of Propellant Flames during Depressurization", AIAA J., Vol. 9, No. 5, pp. 869-875, 1971. See also: AIAA Paper No. 70-663, 1970.
- (35) Park C.P., Ryan N.W., and Baer A.D., "Extinguishment of Composite Propellants at Low Pressures", AIAA Paper No. 73-175, 1973.
- (36) Selzer H., "Depressurization Extinguishment of Composite Solid Propellants: Influence of Composition and Catalysts", AIAA J., Vol. 11, No. 9, pp. 1221-1222, 1973.
- (37) Mongia H.C. and Ambs L.L., "A Model for the Combustion and Extinction of Composite Solid Propellants During Depressurization", CF, Vol. 22, pp. 59-69, 1974. See also Comments, CF, Vol. 23, pp. 401-402, 1974.
- (38) T'ien J.S., "A Theoretical Criterion for Dynamic Extinction of Solid Propellants by Fast Depressurization", CST, Vol. 9, pp. 37-39, 1974.
- (39) T'ien J.S., "The Effects of Perturbations on the Flammability Limits", CST, Vol. 7, No. 4, pp. 185-188, 1973.
- (40a) Baliga B.R. and T'ien J.S., "Flammability Limits and the Oscillatory Burning of Solid Propellants at Low Pressure", Department of Fluid Thermal and Aerospace Sciences, Case Western Reserve University, Report FTAS/TR-74-100, April 1974.
- (40b) Baliga B.R. and T'ien J.S., "Unsteady Effects on Low-Pressure Extinction Limit of Solid Propellants", AIAA J., Vol. 13, No. 12, pp. 1653-1656, 1975.
- (41) Subhas H.K. and Bose T.K., "A Mathematical Model to Predict Transient Burning Rate and Pressure Decay Rates for Extinction of Composite Propellants", CF, Vol. 28, pp. 145-153, 1977. See also Comments, CF, Vol. 31, pp. 329-332, 1978.
- (42) Krier H., "Solid Propellant Burning Rate During a Pressure Transient", CST, Vol. 5, pp. 69-73, 1972. See also Comments, CST, Vol. 9, p. 195, 1974.
- (43) Zeldovich Ya. B., "On the Theory of Combustion of Powder and Explosives", JEPT, Vol. 12, No. 11-12, pp. 498-524, 1942.
- (44) Zeldovich Ya. B., "The Burning Velocity of Powder under Variable Pressure", JPMTF, Vol. 5, No. 3, pp. 126-130, 1964.

- (45) Istratov A.G., Librovich V.B., and Novozhilov B.V., "An Approximate Method in the Theory of Unsteady Burning Velocity of Powder", JPMTF, Vol. 5, No. 3, p. 139, 1964.
- (46) Novozhilov B.V., "Nonstationary Burning of Powders Having a Variable Surface Temperature", JPMTF, Vol. 8, No. 1, pp. 54-63, 1967.
- (47) Summerfield M., Caveny L.H., Battista R.A., Kubota N., Gostintsev Yu.A., and Isoda H., "Theory of Dynamic Extinguishment of Solid Propellants with Special Reference to Non-Steady Heat Feedback", Vol. 8, No. 3, pp. 251-258, 1971. See also AIAA Paper No. 70-667, 1970.
- (48) Battista R.A., Caveny L.H., and Summerfield M., "Nonsteady Combustion of Solid Propellants", Princeton University, AMS Report No. 1049, October 1972.
- (49) Novozhilov B.V., "Nonstationary Combustion of Solid Rocket Fuels", Nauka, Moscow, 1973. Translation AFSC No.FTD-MT-24-317-74.
- (50) Frost V.A., "Extinction of a Powder with a Change in Pressure", JPMTF, Vol. 13, No. 5, pp. 113-118, 1972.
- (51) Frost V.A. and Yumashev V.L., "Study of the Extinction of Gunpowder in the Combustion Model with a Variable Surface Temperature", JPMTF, Vol. 14, No. 3, pp. 92-100, 1973.
- (52) Frost V.A. and Yumashev V.L., "Extinction of a Solid Propellant Accompanying a Fall in Pressure as a Loss of Combustion Stability", FGV, Vol. 2, No. 4, pp.548-555, 1976.
- (53) Assovskii I.G., Istratov A.G., and Leypunskiy O.I., "Extinction of a Propellant with a Pressure Drop", FGV, Vol. 13, No. 2, pp. 200-205, 1977.
- (54) Zemskikh V.I., Istratov A.G., Leypunskiy O.I., and Marshakov V.N., "Three Characteristic Ballistic Powder Combustion Modes with a Pressure Drop", FGV, Vol. 13, No. 1, pp. 14-19, 1977.
- (55) Librovich V., "Non-steady Burning Processes for Powder and Solid Propellants", XII International Symposium on Space Technology and Science, Tokyo, Japan, pp. 585-590, 1977.
- (56) Ivashchenko Y.S. and Komarov A.S., "Extinction of a Ballasted Powder due to Pressure Drop", FGV, Vol. 14, No. 1, pp. 151-153, 1978.
- (57) Strand L.D., Schultz A.L., and Reedy G.K., "Microwave Doppler Shift Technique for Determining Solid Propellant Transient Regression Rates", JSR, Vol. 11, No. 2, pp. 75-83, 1974.
- (58) Ohlemiller T.J., Caveny L.H., De Luca L., and Summerfield M., "Dynamic Effects of Ignitability Limits of Solid Propellants Subjected to Radiative Heating", Presented at XIV Symposium (International) on Combustion, 20-25 August, 1972. Proceedings, pp. 1297-1307, 1973.

- (59) De Luca L., Ohlemiller T.J., Caveny L.H., and Summerfield M., "Radiative Ignition of Double Base Propellants: II. Pre-Ignition Events and Source Effects", AIAA J., Vol. 14, No. 8, pp. 1111-1117, 1976.
- (60) Khlevnoi S.S., "Quenching of Explosives Following Interruption of the Ignition Light Flux", FGV, Vol. 7, No. 2, pp. 178-188, 1971.
- (61) Mikheev V.F. and Levashov Yu. V., "Experimental Study of Critical Conditions during the Ignition and Combustion of Powders", FGV, Vol. 9, No. 4, pp. 506-510, 1973.
- (62) Assovskii I.G., "Transient Combustion of Powder Subjected to Intense Light", FGV, Vol. 9, No. 6, pp. 874-883, 1973.
- (63) Costintsev Yu. A., "Extinction of a Steady State Burning Powder by a Pulse of Thermal Radiation", FGV, Vol. 10, No. 5, pp. 764-767, 1974.
- (64) Boggs T.L. and Zinn B.T. editors, "Experimental Diagnostics in Combustion of Solids", AIAA Progress in Astronautics and Aeronautics, Vol. 63, pp. 173-187, 1978.
- (65a) Huffington J.D., "The Burning and Structure of Cordite", Trans. Faraday Soc., Vol. 47, pp. 864-876, 1951.
- (65b) Huffington J.D., "The Unsteady Burning of Cordite", Trans. Faraday Soc., Vol. 50, pp. 942-952, 1954.
- (66) Clemmow D.M. and Huffington J.D., "An Extension of the Theory of Thermal Explosion and its Application to the Oscillatory Burning of Explosives", Trans. Faraday Soc., Vol. 52, pp. 385-396, 1956.
- (67) Frank-Kamenetskii D.A., "Diffusion and Heat Exchange in Chemical Kinetics", Princeton University Press, 1955, Chapters 6-9.
- (68) Shkadinskii K.G., Khaikin B.I., and Merzhanov A.G., "Propagation of a Pulsating Exothermic Reaction Front in the Condensed Phase", FGV, Vol. 7, No. 1, 1971, pp. 19-28.
- (69) Librovich V.B. and Makhviladze G.M., "One Limiting Scheme for the Propagation of a Pulsating Exothermic Reaction Front in a Condensed Medium", JPMTF, Vol. 15, No. 6, pp. 107-116, 1974.
- (70) Svetlichnyi I.B., Margolin A.D., and Pokhil P.F., "Low Frequency Self-Oscillatory Processes in Propellant Combustion", FGV, Vol. 7, No. 2, pp. 188-194, 1971.
- (71) Ilyukhin V.S., Mysov V.G., and Novikov S.S., "Low Frequency Nonacoustic Fluctuations During Combustion of Nitroglycerine Powder", FGV, Vol. 10, No. 3, pp. 334-337, 1974.
- (72) Ilyukhin V.S., Margolin A.D., Mysov V.G., and Novikov S.S., "Role of Heterogeneity of Composite Solid Fuels in the Mechanism of Pulsating Burning", FGV, Vol. 11, No. 3, pp. 498-501, 1975.
- (73) Brulard J., Kuentzmann P., and Kling R., "Réponse d'un Propergol Solid à un Echelon de Pression", La Recherche Aérospatiale, No. 5, pp. 279-287, 1975. See also ONERA T.P. No. 1975-138, 1975.

- (74) Kooker D.E. and Nelson C.W., "Numerical Solution of Solid Propellant Transient Combustion", *J. Heat Transfer*, Vol. 101, pp. 359-364, 1979.
- (75) T'ien J.S., "Oscillatory Burning of Solid Propellants Including Gas Phase Time Lag", *CST*, Vol. 5, No. 2, pp. 47-54, 1972.
- (76) Peters N., "Theory of Heterogeneous Combustion Instabilities of Spherical Particles", XV Symposium (International) on Combustion, pp. 363-375, 1975.
- (77) Matkowsky B.J. and Sivashinsky G.I., "Propagation of a Pulsating Reaction Front in Solid Fuel Combustion", *SIAM J. Appl. Math.*, Vol. 35, No. 3, pp. 465-478, 1978.
- (78) Goodman T.R., "Application of Integral Methods to Transient Nonlinear Heat Transfer", *Advances in Heat Transfer*, Vol. 1, Academic Press, pp. 51-122, 1964.
- (79) Kuo K.K., "Theory of Flame Front Propagation in Porous Propellant Charges Under Confinement", Ph.D. Thesis, Princeton University, AMS Dept., 1971.
- (80) Peretz A., Coveny L.H., Kuo K.K., and Summerfield M., "The Starting Transient of Solid Propellant Rocket Motors with High Internal Gas Velocities", Princeton University, AMS Dept. Report No. 1100, April 1973.
- (81) Gostintsev Yu. A., "Method of Reduction to Ordinary Differential Equations in Problems of the Nonstationary Burning Solid Propellants", *FGV*, Vol. 3, No. 3, pp. 218-220, 1967.
- (82a) Steinz J.A., Stang P.L., and Summerfield M., "The Burning Mechanism of Ammonium Perchlorate Based Composite Propellants", Princeton University, AMS Report No. 830, February 1969.
- (82b) Steinz J.A., Stang P.L., and Summerfield M., "Effects of Oxidizer Particle Size on Composite Solid Propellant Burning: Normal Burning, Plateau Burning and Intermediate Pressure Extinction", AMS Report No. 810, Princeton University, Presentation Version, October 1967.
- (82c) Steinz J.A. and Summerfield M., "Low Pressure Burning of Composite Solid Propellants", Reprinted from *Advances in Chemistry Series* No. 88, 1969.
- (82d) Steinz J.A. "State of Knowledge of Mechanism of Steady State Burning of Composite Ammonium Perchlorate Solid Propellants", manuscript, Princeton University, March 1965.
- (82e) Steinz J.A. and Stang P.L., "The Burning Mechanism of Ammonium Perchlorate Based Composite Solid Propellant", AIAA Paper No. 68-658, June 1968.
- (83a) Krier H., T'ien J.S., Sirignano W.A., and Summerfield M., "Nonsteady Burning Phenomena of Solid Propellants": Theory and Experiments", *AIAA J.*, Vol. 6, No. 2, pp. 278-285, 1968.

- (83b) Summerfield M., Krier H., Tien J.S., and Sirignano W.A., "Non-steady Burning Phenomena of Solid Propellants": Theory and Experiment (I)", AMS Report No. 793, Princeton University, July 1967.
- (83c) Krier H., "Solid Propellant Burning in Nonsteady Pressure Fields", Ph.D. Thesis, Princeton University, September 1968.
- ((84) Summerfield M., Sutherland G.S., Webb M.J., Taback H.J., and Dell R.P., "Burning Mechanism of Ammonium Perchlorate Propellants", ARC Progress in Astronautics and Rocketry: Solid Propellant Research, Vol. 1, edited by M. Summerfield, Academic Press, New York, 1960, pp. 141-182.
- (85) Blair D.W., Bassett B.K., Normance C.E., Hall R.E., and Summerfield M., "Some Research Problem in the Steady State Burning of Composite Solid Propellant", AIAA Journal, 28-29 January 1969.
- (86) Kooker D.E. and Zinn B.T., "Numerical Investigation of Non-Linear Axial Instabilities in Solid Rocket Motors", BRL Contract Report No. 141, March 1974.
- (87) Levine J.N. and Colick P.H.C., "Nonlinear Analysis of Solid Rocket Combustion Instability", AFRL TR-74-75, October 1974.
- (88) Andronov A.A., Vitt A.A., and Khaikin S.E., "Theory of Oscillators", English Edition by Pergamon Press Ltd., London; U.S.A. Edition distributed by Addison-Wesley, Mass., 1966.
- (89) Strahle W.C., "One-Dimensional Stability of AP Deflagrations", AIAA J., Vol. 9, No. 4, pp. 565-569, 1971.
- (90) Salvadori M.C. and Barton R.L., "Numerical Methods in Engineering", Prentice Hall Inc., 1964.
- (91) Richter R.D. and Morton K.W., "Difference Methods for Initial-Value Problems", Interscience Publishers, New York, 1967.
- (92) Saito T. and Iwasa A., "Laser Ignition Behavior of Carboxyl-Terminated Polybutadiene/Ammonium Perchlorate Propellants at Subatmospheric Pressures", ISAS Research Note, Tokyo University, 1979.
- (93) Levine J.N. and Andreponi W.C., "Measurement Methods of Transient Combustion Response Characteristics of Solid Propellant - An Assessment", AIAA Paper No. 79-1209, 1979.
- (94) Boggs T.L. and Zinn B.T. editors, "Experimental Diagnostics in Combustion of Solids", AIAA Progress in Astronautics and Aeronautics, Vol. 63, pp. 155-172, 1978.

NOTATION

$a_\lambda$	= volume optical absorption coefficient, $\text{cm}^{-1}$
$A_M$	= constant used in MTS flame model (see Eq. 2.3.2)
$B_M$	= constant used in MTS flame model (see Eq. 2.3.3)
$B_P$	= nondimensional rate coefficient for pressure changes (see Table 9).
$B_r$	= nondimensional rate coefficient for radiation changes (see Table 9).
$c$	= specific heat, $\text{cal/g K}$
$d$	= layer thickness, $\text{cm}$
$E/R$	= activation temperature, $\text{K}$
$f(\bar{\phi}_s - \phi_s)$	= static restoring function (see Eq. 2.4.21)
$\Gamma$	= nondimensional radiant flux intensity
$F_o$	= nondimensional radiant flux intensity impinging on the burning surface
$g(\tau, \bar{\phi}_s - \phi_s)$	= nonautonomous function (see Eq. 2.4.22)
$h$	= nondimensional surface heat release
$I$	= radiant flux intensity, $\text{cal/cm}^2 \text{ s}$
$I_o$	= radiant flux intensity impinging on the burning surface, $\text{cal/cm}^2 \text{ s}$
$M$	= average molecular weight, $\text{g/gmole}$
$n$	= exponent in ballistic burning rate law; also: order of the approximating polynomial (see Eq. 2.4.9)
$N_t$	= transparency factor (see Eq. 2.2.2)
$p$	= ammonium perchlorate percent, %
$P$	= pressure, atm
$q_{c,s}$	= nondimensional heat conducted away in condensed phase
$q_{g,s}$	= nondimensional heat feedback from gas phase
$q_1$	= nondimensional heat loss from burning surface
$q_r$	= nondimensional radiant flux from external source
$q_s$	= nondimensional net heat release at burning surface
$Q$	= nondimensional flame heat release
$Q_f$	= flame heat release, $\text{cal/g}$
$Q_s$	= surface heat release, $\text{cal/g}$
$r_\lambda$	= surface optical reflectivity, %
$R$	= universal gas constant, $\text{cal/gmole K}$

$\dot{R}$	= burning rate, cm/s
$R$	= nondimensional burning rate
$s_A$	= volume optical scattering coefficient, $\text{cm}^{-1}$
$t$	= time, s
$T$	= temperature, K
$T$	= nondimensional temperature (see Eq. 2.2.1b)
$v$	= nondimensional finite size disturbance of temperature (see Eq. 2.1.1)
$v_x$	= nondimensional finite size disturbance of thermal gradient (see Eq. 2.4.8)
$u$	= nondimensional gas velocity
$x$	= space variable, cm
$X$	= nondimensional space variable
$w$	= exponent in KTGSS surface pyrolysis law (see Eq. 2.2.3b)
$z$	= constant used in K2 flame model (see Eq. 2.3.14)

#### Greek Symbols:

$\alpha$	= thermal diffusivity, $\text{cm}^2/\text{s}$
$\beta$	= reaction order used in K2 flame model
$\delta$	= nondimensional layer thickness
$\Delta$	= finite difference of a quantity evaluated between $X = 0$ and $X = -\delta$ (see Eq. 2.4.14)
$\epsilon$	= small quantity
$\theta$	= nondimensional temperature (see Eq. 2.2.1a)
$\lambda$	= wavelength, $\mu\text{m}$ ; also: thermal conductivity, $\text{cal}/\text{cm s K}$
$\xi$	= nondimensional thickness of disturbance thermal layer (see Eq. 2.4.11)
$\rho$	= density, $\text{g}/\text{cm}^3$
$\tau$	= nondimensional time
$\tau'$	= nondimensional time parameter $\tau' = \tau (\lambda_c \lambda_g) (C_g / C_c) (C_c / C_g)$
$\dot{\phi}_{c,s}$	= heat conducted away in condensed phase, $\text{cal}/\text{cm}^2\text{s}$
$\dot{\phi}_{g,s}$	= heat feedback from gas phase, $\text{cal}/\text{cm}^2\text{s}$
$\dot{\phi}_j$	= heat loss from burning surface, $\text{cal}/\text{cm}^2\text{s}$
$\dot{\phi}_r$	= radiant flux from external source, $\text{cal}/\text{cm}^2\text{s}$
$\dot{\phi}_s$	= net heat release at burning surface, $\text{cal}/\text{cm}^2\text{s}$
$\psi$	= nondimensional pressure
$\omega$	= mass reaction rate per unit volume, $\text{g}/\text{cm}^3\text{s}$

AD-A100 043

POLITECNICO DI MILANO (ITALY) IST DI MACCHINE  
THE DYNAMICS OF SOLID PROPELLANT COMBUSTION.(U)  
DEC 80 L DE LUCA, A COGHE, A REGGIORI

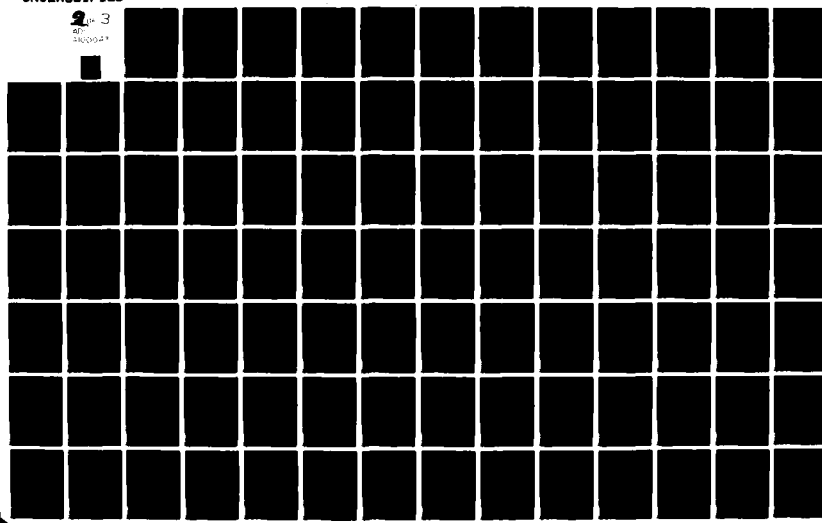
F/G 21/9.2

DA-ERO-78-6-029

NL

UNCLASSIFIED

2 in 3  
400048



Subscripts and Superscripts:

a	= ambient; also: absorption layer
c	= condensed phase
$\xi$	= penetration depth
f	= final; also: flame
g	= gas phase
i	= initial
p	= pressure
r	= radiant
s	= surface
v	= vaporization
$c, s$	= surface from condensed phase side
cr	= crystal
di	= diffusion
$g, s$	= surface from gas phase side
ki	= kinetic
re	= reaction
st	= static
th	= thermal
ext	= external
ref	= reference
$\overline{\quad}$	= steady state average value
$-\infty$	= far upstream
$+\infty$	= far downstream

Abbreviations:

A	= Ammonia ( $\text{NH}_3$ )
AFSC	= Air Force System Command
AIAA	= American Institute of Aeronautics and Astronautics
AIMETA	= Associazione Italiana di Meccanica Teorica ed Applicata
AMS	= Aerospace and Mechanical Sciences Department
AP	= Ammonium Perchlorate ( $\text{NH}_4\text{ClO}_4$ )
ATI	= Associazione Termotecnica Italiana
BC	= Boundary Condition
BC1	= Boundary Condition at $x = 0$
BC2	= Boundary Condition at $x = -\infty$
BRL	= Ballistic Research Laboratory

CF	= Combustion and Flame
CPIA	= Chemical Propulsion Information Agency
CST	= Combustion Science and Technology
DB	= Double Base
PCV	= Combustion, Explosion and Shock Waves
GDF	= Granular Diffusion Flame (model of steady state burning)
IC	= Initial Condition
JETP	= Journal of Experimental and Theoretical Physics
JPMTP	= Journal of Applied Mechanics and Technical Physics
JSR	= Journal of Spacecraft and Rockets
KTSS	= Krieger-Tsirognoc-Sumerfield
RZ	= Rooker-Zinn
LC	= Levine-Culick
MTS	= Merkle-Turk-Sumerfield
NC	= Nitrocellulose
NG	= Nitroglycerine
NOFS	= Naval Ordnance Test Station
NWC	= Naval Warfare Center
ODE	= Ordinary Differential Equation
ONERA	= Office National d'Etudes et de Recherches Aéronautiques
PA	= Perchloric Acid ( $\text{HClO}_4$ )
PBA	= PolyButadiene Acrylic Acid
PBCT	= PolyButadiene Carboxyl Terminated
PBH	= PolyButadiene Hydroxyl Terminated
PDE	= Partial Differential Equation
PICF	= PolyIsoButylene Carboxyl Terminated
PU	= PolyUrethane
PVC	= PolyVinylChloride
SRI	= Stanford Research Institute
UTC	= United Technology Center

## LIST OF TABLES

Tab. 1 - Properties of solid composite propellant AP/PBAA No. 941 used as datum case in this study. Surface heat release positive if endothermic. Optical properties evaluated at 10.6  $\mu\text{m}$ . Values taken from Refs. 29, 82, 86-87.

Tab. 2 - Steady surface temperature dependence on surface heat release in the pressure range 10 to 60 atm. MTS flame with  $A_M = 0.338$  and  $B_M = 2.350$ ,  $C_g/C_c = 1$ ,  $\epsilon = 0$ . KTSS nonlinear, KTSS linearized and LC recover the experimental curve.

Tab. 3 - Surface temperature and burning rate associated with roots A and B in the pressure range 10 to 60 atm. Root A (steady reacting solution) is independent of the order of the approximating polynomial, while root B (unsteady reacting solution) does depend. Nonlinear static restoring function evaluated for standard conditions ( $T_a = 300$  K,  $Q_{s,\text{ref}} = -158.2$  cal/g, adiabatic burning) and  $C_g/C_c = 1$ ,  $\epsilon = 0$ .

Tab. 4 - Roots associated with the nonlinear static restoring function, for MTS flame with  $n=3$ , at standard conditions ( $P=30$  atm,  $T_a = 300$  K, adiabatic burning) showing the existence of three static regimes. For all cases root C, corresponding to the trivial unreacting solutions  $\theta_s = 0$ , is also found and is always stable.  $C_g/C_c = 1$ ,  $\epsilon = 0$ .

Tab. 5 - Maximum range of values of surface heat release, for which self-sustained oscillating combustion may occur, in function of pressure. Static restoring function evaluated for MTS flame with  $n=3$  at standard conditions ( $T_a = 300$  K, adiabatic burning) and  $C_g/C_c = 1$ ,  $\epsilon = 0$ .

Tab. 6 - Static stability limits, in the pressure range 10 to 60 atm for MTS flame at standard conditions ( $T_a = 300$  K,  $Q_{s,\text{ref}} = -158.2$  cal/g), evaluated directly from heat feedback law.  $C_g/C_c = 1$ ,  $\epsilon = 0$ .

Tab. 7 - Static stability limits, in the pressure range 10 to 60 atm for MTS flame at standard conditions ( $T_a = 300$  K,  $Q_{s,\text{ref}} = -158.2$  cal/g), evaluated through static restoring function with  $n=3$ .  $C_g/C_c = 1$ ,  $\epsilon = 0$ .

Tab. 8a - Stabilizing effect of large radiant flux and destabilizing effect of large surface heat release or ambient temperature on stability strength of steady reacting solutions. Nonlinear static restoring function evaluated from MTS flame with  $n=3$  at standard conditions ( $P=30$  atm,  $T_a = 300$  K),  $C_g/C_c = 1$ ,  $\epsilon = 0$ .

Tab. 8b - Compared stabilizing effect of large pressure on stability strength of steady reacting solution according to Lyapunov. Nonlinear static restoring function evaluated for MTS, KTSS nonlinear, and KTSS linearized flames with  $n=3$  at standard conditions ( $Q_{s,ref} = -158.2$  cal/g,  $T_a=300$  K, adiabatic burning),  $C_g/C_c = 1$ ,  $\epsilon = 0$ .

Tab. 8c - Effect of the approximating polynomial order on stability strength of steady reacting solution according to Lyapunov. Nonlinear static restoring function evaluated for MTS flame at standard conditions ( $Q_{s,ref} = -158.2$  cal/g,  $T_a=300$  K, adiabatic burning),  $C_g/C_c = 1$ ,  $\epsilon = 0$ .

Tab. 8d - Compared effect of specific heat ratio on stability strength of steady reacting solution according to Lyapunov. Nonlinear static restoring function evaluated for MTS and KTSS nonlinear flames at standard conditions ( $Q_{s,ref} = -158.2$  cal/g,  $T_a=300$  K, adiabatic burning) and  $\epsilon = 0.75$ .

Tab. 9 - Forcing laws used for computer simulated deradiation and depressurization transients.

Tab. 10 - Computer simulated go/no-go tests showing agreement with the predicted lower dynamic stability boundary. All runs performed with  $T_a=300$  K and  $Q_{s,ref} = -158.2$  cal/g. KTSS linear, KZ, and LC flame models do not include extinction.

Tab. 11 - Computer simulated transient tests showing agreement with bifurcation diagram predictions. All runs performed for adiabatic burning and  $T_a=300$  K.

TABLE 1

Properties of solid composite propellant AP/PBAA  
 No. 941 used as datum case in this study.  
 Surface heat release positive if endothermic.  
 Optical properties evaluated at 10.6  $\mu\text{m}$ .  
 Values taken from Refs. 29, 82, 86-87.

<u>ASSUMED OR MEASURED PROPERTIES</u>	
AP crystal transition heat, $Q_{\text{cr,AP}}$	2.000 E+01 cal/g
AP vaporization heat, $Q_{\text{v,AP}}$	5.260 E+02 cal/g
AP decomposition heat, $Q_{\text{A/PA}}$	-8.000 E+02 cal/g
Binder vaporization heat, $Q_{\text{v,Binder}}$	2.250 E+02 cal/g
AP weight fraction, $p$	8.000 E+01 %
Ballistic burn rate exponent, $n$	4.600 E-01
Pyrolysis law pressure power, $n_s$	0
KTSS pyrolysis law power, $w$	6.000
Surface activation temperature, $E_s/\theta$	8.081 E+03 K
Flame activation temperature, $E_f/\theta$	1.010 E+04 K
KZ flame reaction order, $\beta$	1.7
Condensed density, $\rho_c$	1.540 g/cm <sup>3</sup>
Condensed specific heat, $C_c$	3.300 E-01 cal/g K
Condensed thermal diffusivity, $\alpha_c$	1.400 E-03 cm <sup>2</sup> /s
Gas thermal conductivity, $k_g$	1.000 E-04 cal/cm K s
Average product molecular weight, $\bar{M}$	2.600 E+01 g/mole
Optical surface reflectivity, $r_\lambda$	3.800 %
Optical volumetric scattering, $s_\lambda$	0 cm <sup>-1</sup>
Minimum temperature for reactions, $T_m$	3.000 E+02 K
Matching temperature for pyrolysis, $T_k$	4.050 E+02 K
<u>COMPUTED PROPERTIES</u>	
Net surface heat release, $Q_s, \text{ref}$	-1.582 E+02 cal/g
Condensed thermal conductivity, $k_c$	7.115 E-04 cal/cm K s
MTS chemical time constant, $\Delta M$	3.380 E-01
MTS diffusion time constant, $B_M$	2.350
Adiabatic flame temperature, $\bar{T}_f(P)$	$T_{f,\text{ref}} - (50/68) \cdot (P_{\text{ref}} - \bar{P})$
<u>REFERENCE PROPERTIES</u>	
Pressure, $P_{\text{ref}}$	6.800 E+01 atm
Temperature, $T_{\text{ref}}$	3.000 E+02 K
Burning Rate, $\mathcal{R}_{\text{ref}} = \mathcal{R}(P_{\text{ref}})$	8.370 E-01 cm/s
Surface temperature, $T_s, \text{ref} = T_s(P_{\text{ref}})$	1.000 E+03 K
Flame temperature, $T_f, \text{ref} = T_f(P_{\text{ref}})$	2.430 E+03 K
Distance, $x_{\text{ref}} = \alpha_c / \mathcal{R}_{\text{ref}}$	1.673 E-03 cm
Time, $t_{\text{ref}} = \alpha_c / \mathcal{R}_{\text{ref}}^2$	1.998 E-03 s
Heat, $Q_{\text{ref}} = C_c (T_s, \text{ref} - T_{\text{ref}})$	2.310 E+02 cal/g
Energy flux, $I_{\text{ref}} = \rho_c C_c \mathcal{R}_{\text{ref}} (T_s, \text{ref} - T_{\text{ref}})$	2.978 E+02 cal/cm <sup>2</sup> s

TABLE 2

Steady surface temperature dependence on surface heat release in the pressure range 10 to 60 atm. MTS flame with  $A_M = 0.338$  and  $B_M = 2.350$ ;  $C_g/C_C = 1$ ,  $\varepsilon = 0$ . KRSS nonlinear, KRSS linearized, and LC recover the experimental curve.

Net Surface Heat Release $Q_{s,ref}$ , cal/g	P R E S S U R E				
	P=10 atm	P=20 atm	P=30 atm	P=40 atm	P=50 atm
-120	0.823	0.875	0.906	0.927	0.943
-140	0.839	0.890	0.921	0.941	0.957
-158.2	0.860	0.909	0.937	0.957	0.972
-170	0.876	0.922	0.949	0.969	0.984
-180	0.891	0.935	0.962	0.980	0.995
-200	0.932	0.969	0.992	1.009	1.022
-220	0.986	1.014	1.032	1.047	1.061
Experimental $\frac{E_p}{E_p - P_{ref}}$	0.863	0.910	0.939	0.960	0.977
					0.990

TABLE 3

Surface temperature and burning rate associated with roots A and B in the pressure range 10 to 60 atm. Root A (steady reacting solution) is independent on the order of the approximating polynomial, while root B (unsteady reacting solution) does depend. Nonlinear static restoring function evaluated for standard conditions ( $T_a^0 = 300$  K,  $Q_s^0$  ref = 158.2 cal/g, adiabatic burning and  $C_g/C_c = 1$ ,  $\epsilon = 0$ ).

Pressure P, atm	MTS flame						K <sup>n</sup> SS nonlinear flame					
	$\theta_s$ (A)	R (A)	$\theta_s$ (B)	R (B)	$\theta_s$ (B)	R (B)	$\theta_s$ (A)	R (A)	$\theta_s$ (B)	R (B)	$\theta_s$ (B)	R (B)
	n = 2						n = 3					
10	0.860	0.415	0.667	0.084	0.618	0.052	0.863	0.414	0.571	0.035		
20	0.909	0.575	0.691	0.107	0.646	0.070	0.910	0.570	0.610	0.051		
30	0.937	0.687	0.709	0.126	0.663	0.083	0.939	0.686	0.633	0.065		
40	0.957	0.775	0.719	0.138	0.674	0.093	0.960	0.783	0.651	0.076		
50	0.972	0.849	0.729	0.151	0.684	0.101	0.977	0.868	0.664	0.086		
60	0.984	0.913	0.737	0.161	0.692	0.108	0.990	0.944	0.675	0.095		

TABLE 4

Roots associated with the nonlinear static restoring function, for MTS flame with  $n=3$ , at standard conditions ( $P=30$  atm,  $T_a=300$  K, adiabatic burning) showing the existence of three static regimes. For all cases root C, corresponding to the trivial unreacting solution  $\phi_s = 0$ , is also found and is always stable.  $C_Q/C_C = 1$ ,  $\epsilon = 0$ .

Predicted Solution	surface heat release, $Q_s, \text{ref}$ cal/g	Nondimensional surface temperature, $\phi_s$			root E
		root B (lower dynamic stability)	root A (steady burning)	root D (upper dynamic stability)	
steady burning	-150	0.66	0.929	=	=
	-155	0.66	0.934	=	=
	-158.2	0.66	0.937	=	=
	-165	0.67	0.944	=	=
	-170	0.63	0.949	1.14	1.29
	-175	0.68	0.955	1.08	1.38
	-180	0.69	0.962	1.04	1.43
damped oscillations	-185	0.69	0.968	1.00	1.48
	-190	0.70	0.976	0.976	1.53
	-195	0.71	0.934	0.96	1.57
	-200	0.72	0.992	0.94	1.61
	-205	0.73	1.001	0.92	1.64
	-210	0.75	1.011	0.90	1.69
	-215	0.76	1.021	0.88	1.71
self-sustained oscillations	-220	0.78	1.032	0.86	1.75
	-225	=	1.044	=	1.78
	-230	=	1.057	=	1.81
	max range				
	extinction				

TABLE 5

Maximum range of values of surface heat release, for which self-sustained oscillating combustion may occur, in function of pressure. Static restoring function evaluated for NTS flame with  $n=3$  at standard conditions ( $T_a = 300$  K, adiabatic burning) and  $C_g/C_c = 1, \epsilon = 0$ .

Pressure $P$ , atm	Net Surface Heat Release, $Q_s, \text{ref}, \text{cal/g}$			$Q_s, \text{ref} = C_c (\bar{T}_f - T_a)$ at standard conditions	$Q_s, \text{ref} = C_c (\bar{T}_s - T_a)$ at standard conditions
	D-E roots coalescence	A-D roots coalescence	B-D roots coalescence		
10	-146	-167	-196	-688.4	-199.4
20	-160	-182	-212	-691.2	-210.2
30	-168	-190	-222	-693.7	-216.9
40	-174	-196	-231	-696.0	-221.8
50	-179	-201	-236	-698.5	-225.7
60	-182	-205	-241	-700.9	-228.7

TABLE 6

Static stability limits, in the pressure range 10 to 60 atm for MS flame at standard conditions ( $T_a = 300\text{ K}$ ,  $Q_{s,\text{ref}} = -158.2 \text{ cal/g}$ ), evaluated directly from heat feedback law.  
 $C_g/C_c = 1$ ,  $\varepsilon = 0$ .

Pressure P, atm	Overall Heat Loss $\dot{Q}_1, \text{cal/cm}^2\text{s}$	Nond. Heat Feedback			Nond. Burning Rate R
		$\dot{Q}_{g,s}$	$\theta_s$	Nond. Surface Temperature	
10	-40.5	1.40x10 <sup>-1</sup>	7.12x10 <sup>-1</sup>		1.30x10 <sup>-1</sup>
20	-65.0	2.36x10 <sup>-1</sup>	7.69x10 <sup>-1</sup>		2.10x10 <sup>-1</sup>
30	-85.0	3.14x10 <sup>-1</sup>	7.91x10 <sup>-1</sup>		2.60x10 <sup>-1</sup>
40	-101.5	3.80x10 <sup>-1</sup>	8.15x10 <sup>-1</sup>		3.00x10 <sup>-1</sup>
50	-116.0	4.36x10 <sup>-1</sup>	8.23x10 <sup>-1</sup>		3.20x10 <sup>-1</sup>
60	-129.5	4.91x10 <sup>-1</sup>	8.40x10 <sup>-1</sup>		3.60x10 <sup>-1</sup>

TABLE 7

Static stability limits, in the pressure range 10 to 60 atm for MTS flame at standard conditions ( $T_a = 300$  K,  $Q_{s,ref} = 158.2$  cal/g), evaluated through static restoring function with  $n=3$ .  $C_g/C_c = 1$ ,  $\epsilon = 0$ .

Pressure P, atm	Overall Heat Loss $\dot{q}_1$ , cal/cm <sup>2</sup> s	Nond. Surface Temperature		Nond. Burning Rate R
		$\theta_s$	$\theta$	
10	-38	0.747		0.175
20	-62	0.793		0.255
30	-82	0.817		0.305
40	-98	0.837		0.354
50	-112	0.853		0.396
60	-126	0.863		0.423

TABLE 8a

Stabilizing effect of large radiant flux and destabilizing effect of large surface heat release or ambient temperature on stability strength of steady reacting solutions. Nonlinear static restoring function evaluated from MTS flame with  $n=3$  at standard conditions

( $P=30$  atm,  $T_a=300$  K),  $C_g/C_c = 1$ ,  $\epsilon = 0$ .

$I_o, \text{cal/cm}^2 \text{ s}$	$Q_s, \text{ref}, \text{cal/g}$	$T_a, \text{K}$	$(df/d\theta_s)_{\bar{\theta}_s}$
0	-158.2	300	-3.53
10	-158.2	300	-3.89
20	-158.2	300	-4.03
30	-158.2	300	-4.27
40	-158.2	300	-4.50
60	-158.2	300	-5.18
80	-158.2	300	-6.01
100	-158.2	300	-7.05
120	-158.2	300	-8.29
-10	-158.2	300	-3.33
-20	-158.2	300	-3.14
-30	-158.2	300	-2.78
-40	-158.2	300	-2.33
-50	-158.2	300	-1.85
-60	-158.2	300	-1.50
-70	-158.2	300	-1.35
-80	-158.2	300	-0.52
0	-110	300	-0.71
0	-120	300	-2.10
0	-130	300	-3.02
0	-135	300	-3.30
0	-140	300	-3.55
0	-145	300	-3.73
0	-150	300	-3.74
0	-155	300	-3.62
0	-160	300	-3.51
0	-165	300	-3.24
0	-170	300	-2.86
0	-180	300	-1.75
0	-190	300	-0.05
0	-200	300	+2.41
0	-210	300	+5.85
0	-220	300	+10.60
0	-230	300	+17.17
0	-240	300	26.23
0	-158.2	250	-3.84
0	-158.2	200	-3.57
0	-158.2	350	-3.38
0	-158.2	400	-2.73
0	-158.2	500	-1.05

TABLE 8b

Compared stabilizing effect of large pressure on stability strength of steady reacting solution according to Lyapunov. Nonlinear static restoring function evaluated for MTS, KTSS nonlinearized and KTSS linearized flames with  $n=3$  at standard conditions ( $Q_s, \text{ref} = -158.2 \text{ cal/g}; T_a = 300 \text{ K}$ , adiabatic burning),  $C_g/C_c = 1, \varepsilon = 0$ .

$P, \text{atm}$	MTS	$(df/d\theta_s) \bar{\theta}_s$	KTSS NONLIN.	KTSS LIN.
2	+0.33 (0+)		-0.24	-0.29
4	+0.23		-0.06	-0.11
6	+0.02		-0.18	-0.15
8	-0.25		-0.46	-0.43
10	-0.54		-0.75	-0.73
20	-2.10		-2.29	-2.27
30	-3.53		-3.86	-3.79
40	-4.92		-5.40	-5.24
50	-6.02		-6.91	-6.63
60	-7.26		-8.37	-7.96
68	-8.06		NA	NA

TABLE 8c

Compared effect of the approximating polynomial order on stability strength of steady reacting solution according to Lyapunov. Nonlinear static restoring function evaluated for MTS flame at standard conditions ( $Q_{s,ref} = 158.2 \text{ cal/g}$ ,  $T_a = 300 \text{ K}$ , adiabatic burning),  $C_g/C_c = 1$ ,  $\epsilon = 0$ .

P, atm	$(df/d\theta_s) \bar{\theta}_s$		
	n = 2	n = 3	n = 4
10	+0.18	-0.54	-1.01
20	-1.06	-2.10	-2.76
30	-2.29 (0)	-3.53	-4.27
40	-3.61	-4.92	-5.69

TABLE 8d

Compared effect of specific heat ratio on stability strength of steady reacting solution according to Lyapunov. Nonlinear static restoring function evaluated for MTS and KTSS nonlinear flames at standard conditions ( $Q_{s,ref} = 158.2 \text{ cal/g}$ ,  $T_a = 300 \text{ K}$ , adiabatic burning) and  $\epsilon = 0.75$ .

Pressure P, atm	Flame Model	$(df/d\theta_s)_{\theta_s=0}$		
		$C_g/C_c = 1$	$C_g/C_c = 1.12$	$C_g/C_c = 1.24$
10	MTS	-0.54	-0.66	-0.81
	KTSS NL *	-0.75	-0.62	-0.49
20	MTS	-2.10	-2.48	-2.88
	KTSS NL	-2.29	-2.26	-2.22
30	MTS	-3.53	-4.14	-4.72
	KTSS NL	-3.86	-3.91	-3.95
40	MTS	-4.92	-5.49	-6.28
	KTSS NL	-5.40	-5.51	-5.61
50	MTS	-6.02	-6.71	-7.62
	KTSS NL	-6.91	-7.05	-7.17
60	MTS	-7.27	-7.99	-8.44
	KTSS NL	-8.37	-8.54	-8.65

(\*) KTSS NL stays for KTSS nonlinear flame model.

TABLE 9

Forcing laws used for computer simulated deradiation  
and depressurization transients.

Linear deradiation	$F_O(\tau) = (1-r_\lambda) \cdot (F_{O,i} - B_r \cdot \tau)$	
Bilinear deradiation	$F_O(\tau) = (1-r_\lambda) \cdot (F_{O,i} - B_{r,1} \cdot \tau)$	$F_{O,i} \geq F_O(\tau) \geq F_m$
	$F_O(\tau) = (1-r_\lambda) \cdot (F_m - B_{r,2} \cdot \tau)$	$F_m \geq F_O(\tau) \geq F_{O,f}$
Parabolic deradiation	$F_O(\tau) = (1-r_\lambda) \cdot (F_{O,i} - B_r \cdot \tau^2)$	
Exponential deradiation	$F_O(\tau) = (1-r_\lambda) \cdot (F_{O,i} - (F_{O,i} - F_{O,f}) \cdot (1 - \exp(B_r \cdot \tau)))$	
Exponential depressurization	$\Psi(\tau) = \Psi_1 - (\Psi_1 - \Psi_f) \cdot (1 - \exp(B_p \cdot \tau))$	

TABLE 10

Computer simulated go/no-go tests showing agreement with the predicted lower dynamic stability boundary. All runs performed with  $T_a=300K$  and  $Q_{s,ref} = -158.2$  cal/g. KTSS linear, KZ, and LC flame models do not include extinction.

final pressure P, atm	forcing law	optical absorption $a_\lambda \text{cm}^{-1}$	rate coeff.	flame model	$\frac{C_g}{C_c}$	minimum surface temperature numerically observed	predicted (n=3)
10	linear deradiation	$\infty$	100	MTS	1.00	0.627	0.618
10	bilinear deradiation	$\infty$	100/20	MTS	1.00	0.626	0.618
10	parabolic deradiation	$\infty$	640	MTS	1.00	0.625	0.618
10	exponential deradiation	$\infty$	5	MTS	1.00	0.627	0.618
10	exponential deradiation	$\infty$	10	MTS	1.00	0.619	0.618
10	exponential deradiation	2000	10	MTS	1.00	0.610	0.618
10	exponential deradiation	1000	10	MTS	1.00	0.618	0.618
10	exponential deradiation	500	10	MTS	1.00	0.620	0.618
10	exponential depressuriz.	NAp*	10	MTS	1.00	0.615	0.618
10	exponential depressuriz.	NAp	variable	MTS	1.00	0.621	0.618
10	simultaneous exponential depress. and deradiation	$\infty$	10/10	MTS	1.00	0.622	0.618
10	sequential exponential depress. and deradiation	$\infty$	10/10	MTS	1.00	0.624	0.618
20	linear deradiation	$\infty$	200	MTS	1.00	0.655	0.647
20	exponential deradiation	$\infty$	10	MTS	1.00	0.649	0.647
20	exponential deradiation	$\infty$	10	KTSS nonl.	1.00	0.632	0.610
20	linear deradiation	2000	500	MTS	1.00	0.660	0.647
20	linear deradiation	1000	500	MTS	1.00	0.690	0.647
30	exponential deradiation	$\infty$	10	MTS	1.00	0.685	0.663
40	exponential deradiation	$\infty$	10	MTS	1.00	0.706	0.674
10	parabolic deradiation	$\infty$	200	MTS	1.12	0.601	0.611
20	parabolic deradiation	$\infty$	200	MTS	1.12	0.680	0.638
40	linear deradiation	$\infty$	1000	MTS	1.12	0.679	0.665
10	trapezoidal radiation	$\infty$	200	MTS	1.00	0.619	0.618
10	trapezoidal radiation	$\infty$	variable	MTS	1.00	0.612	0.618
20	trapezoidal radiation	$\infty$	200	MTS	1.00	0.638	0.647

(\*) NAp stands for not applicable

TABLE 11

Computer simulated transient tests showing agreement with bifurcation diagram predictions. All runs performed for adiabatic burning and  $T_a = 300$  K.

$Q_s$ , ref cal/g	flame model	$C_g/C_c$	$P_i/P_f/B_p$	forcing function	solution	$\theta_s$ , max			$\theta_s$ , min numerically observed	$\theta_s$ (E)	$\theta_s$ (D)	$\theta_s$ (A)	$\tau_{th,c}$
-180	MIS	1.00	10/30/1	expon.	stat.	NAP	NAP	1.43	1.04	0.962	1.56		
-190	MIS	1.00	10/30/1	expon.	(*) small damping	1.45	0.82	1.53	0.976	0.976	1.32		
-200	MIS	1.00	10/30/1	expon.	osc.	1.65	0.82	1.5	0.94	0.992	1.10		
-210	MIS	1.00	10/30/1	expon.	ext.	NAP	NAP	1.68	0.90	1.011	0.88		
-200	MIS	1.00	10/30/200	expon.	osc.	1.65	0.82	1.5	0.94	0.992	1.10		
-200	MIS	1.00	10/30/40	linear	osc.	1.65	0.83	1.5	0.94	0.992	1.10		
-200	MIS	1.00	28/30/1	expon.	osc.	1.64	0.83	1.5	0.94	0.992	1.10		
-200	MIS	1.00	10/40/200	expon.	osc.	1.58	0.84	1.3	1.60	0.99	1.009	0.90	
-200	MIS	1.00	20/40/200	expon.	csc.	1.58	0.84	1.3	1.50	0.99	1.009	0.90	
-200	MIS	1.00	30/40/200	expon.	osc.	1.58	0.84	1.3	1.60	0.99	1.009	0.90	
-200	MIS	1.00	10/50/200	expon.	osc.	1.45	0.86	1.2	1.59	1.022	1.022	0.78	
-200	MIS	1.00	40/50/200	expon.	osc.	1.45	0.86	1.2	1.59	1.022	1.022	0.78	
-180	KTSS NL <sup>4</sup>	1.00	10/30/1	expon.	osc.	1.83	0.82	2.8	NAV <sup>5</sup>	0.939	2.12		
-190	MIS	1.12	10/30/10	linear	damping	NAP	NAP	1.374	1.03	0.983	1.22		
-200	MIS	1.12	10/30/10	linear	osc.	1.39	0.85	1.54	1.16	0.97	0.998	1.02	
-209	MIS	1.12	10/30/10	linear	osc.	1.53	0.85	1.26	1.53	0.94	1.012	0.87	
-210	MIS	1.12	10/30/10	linear	ext.	NAP	NAP	1.54	0.934	1.014	0.85		
-215	MIS	1.24	10/30/10	linear	osc.	1.42	0.86	1.14	1.44	0.944	1.028	0.74	
-216	MIS	1.24	10/30/10	linear	ext.	NAP	NAP	1.44	0.939	1.03	0.72		

(4) KTSS NL stays for KTSS nonlinear flame model

(\*) values taken at the 7th cycle

(5) NAP stands for not applicable

(6) NAV stands for not available

LIST OF FIGURES

Fig. 1a - Schematic diagram of the physical problem.  
1b - Schematic diagram of energy balance at burning surface.

Fig. 2a - Evaluating the gas phase constants required in MTS flame (composite propellant AP/HTPB).

Fig. 2b - Evaluating the gas phase constants required in MTS flame (composite propellant AP/PBAA No. 941).

Fig. 3 - Effect of fitting pressure range on the MTS gas phase constants.

Fig. 4 - Steady state dependence on pressure of MTS flame parameters.

Fig. 5 - Steady state dependence on pressure of KTSS nonlinear flame parameters.

Fig. 6 - Diffusive, kinetic, and total heat feedback law according to MTS flame.

Fig. 7 - Compared heat feedback laws according to linearized and nonlinear KTSS flames.

Fig. 8 - Compared heat feedback laws according to MTS and linearized KTSS (or KZ or LC) flames.

Fig. 9 - Working map (burning rate vs heat feedback) according to MTS flame.

Fig. 10 - Effect of ambient temperature on heat feedback according to MTS flame.

Fig. 11 - MTS steady burning rate affected by surface heat release (for given values of gas phase constants).

Fig. 12a- Qualitative sketch of the nonlinear static restoring function, for different pressure values, illustrating the existence of three equilibrium configurations:  $A_i$  and  $B_i$  (for the reacting mode),  $C$  (for the unreacting mode). Roots  $B_i$  are statically unstable. The branching value  $\theta_s^{ST}$ , at fixed pressure, can be approached only by increasing heat loss from the burning propellant or decreasing ambient temperature.

Fig. 12b- Qualitative sketch of the nonlinear static restoring function, for increasing surface heat release, illustrating the appearance of a second pair of roots,  $D$  and  $E$ , for the reacting mode (upper dynamic instability). Similar effect is obtained by decreasing pressure.

Fig. 13 - Stabilizing effect of pressure on both reacting modes. MTS flame,  $n = 3$ ,  $C_g/C_c = 1$ .

Fig. 14 - Stabilizing effect of residual radiant flux intensity on lower dynamic stability boundary. MTS flame,  $n=3$ ,  $C_g/C_c = 1$ .

Fig. 15a- Destabilizing effect of large surface energy release on upper dynamic stability boundary. MTS flame,  $n=3$ ,  $C_g/C_c = 1$ .

Fig. 15b - Coalescence of A-D roots for  $Q_s = -190$  cal/g at 30 atm; the steady reacting mode is stationary for  $|Q_s| < 190$  cal/g and self-sustained oscillating for  $|Q_s| > 190$  cal/g. MTS flame,  $n = 3$ ,  $C_g/C_c = 1$ .

Fig. 16 - Coalescence of A-D roots for  $Q_s = -170$  cal/g at 10 atm. MTS flame,  $n = 3$ ,  $C_g/C_c = 1$ .

Fig. 17 - Coalescence of A-D roots for  $P = 6$  atm at  $Q_s = -158.2$  cal/g. MTS flame,  $n = 3$ ,  $C_g/C_c = 1$ .

Fig. 18 - Negligible influence of ambient temperature on non-linear static restoring function (for the indicated range of values). MTS flame,  $n = 3$ ,  $C_g/C_c = 1$ .

Fig. 19 - Stabilizing effect of pressure on both reacting modes. KTSS nonlinear flame,  $n = 3$ .  $C_g/C_c = 1$ .

Fig. 20 - Destabilizing effect of large surface heat release on static restoring function. KTSS nonlinear flame,  $n = 3$ ,  $C_g/C_c = 1$ .

Fig. 21 - KTSS linearized flame (or KZ or LC) applying for surface temperatures near or above the steady reacting value.  $C_g/C_c = 1$ ,  $n = 3$ .

Fig. 22 - Compared static restoring functions for MTS, KTSS nonlinear, KTSS linearized (or KZ or LC) flames.  $C_g/C_c = 1$ ,  $n = 3$ .

Fig. 23 - Effect of the approximating polynomial order on static restoring function at 10 atm of pressure. MTS flame,  $C_g/C_c = 1$ .

Fig. 24 - Effect of the approximating polynomial order on static restoring function at 20 atm of pressure. MTS flame,  $C_g/C_c = 1$ .

Fig. 25 - Effect of the approximating polynomial order on static restoring function at 30 atm of pressure. MTS flame,  $C_g/C_c = 1$ .

Fig. 26 - Effect of the approximating polynomial order on static restoring function at 40 atm of pressure. MTS flame,  $C_g/C_c = 1$ .

Fig. 27 - Negligible effect of  $C_g/C_c \neq 1$  on gas phase working map. KTSS nonlinear flame,  $C_g/C_c = 1.12$  or 1.

Fig. 28 - Important effect of  $C_g/C_c \neq 1$  on static restoring function in the region of upper burning instability. MTS flame,  $n = 3$ ,  $C_g/C_c = 1.12$  or 1.

Fig. 29 - Static instability of burning propellants for large surface heat release. MTS flame,  $C_g/C_c = 1$ .

Fig. 30 - Approximate construction of the static burning (stability) boundary and its meaning. MTS flame,  $C_g/C_c = 1$ .

Fig. 31 - Rigorous construction of the static burning (stability) boundary for  $Q_s = -120$  cal/g. MTS flame,  $C_g/C_c = 1$ .

Fig. 32 - Rigorous construction of the static burning (stability) boundary for  $Q_s = -158.2$  cal/g. MTS flame,  $C_g/C_c = 1$ .

Fig. 33 - Rigorous construction of the static burning (stability) boundary for  $Q_s = -200$  cal/g. MTS flame,  $C_g/C_c = 1$ .

Fig. 34 - Evaluating the static burning limit through the static restoring function at 20 atm of pressure. MTS flame,  $n = 3$ ,  $C_g/C_c = 1$ .

Fig. 35 - Evaluating the static burning limit through the static restoring function at 30 atm of pressure. MTS flame,  $n = 3$ ,  $C_g/C_c = 1$ .

Fig. 36 - Evaluating the static burning limit through the static restoring function at 40 atm of pressure. MTS flame,  $n = 3$ ,  $C_g/C_c = 1$ .

Fig. 37 - Evaluating the static burning limit through the static restoring function at 50 atm of pressure. MTS flame,  $n = 3$ ,  $C_g/C_c = 1$ .

Fig. 38a - Representative time histories of burning rate during deradiation showing possible occurrence of a recovery point.

Fig. 38b - Corresponding trajectories in burning rate vs heat feedback plane.

Fig. 38c - Nomenclature used for deradiation transients.

Fig. 38d - Nature of nonautonomous function for monotonic decay of externally controlled parameters.

Fig. 39 - The range of possible unstable equilibrium points in dynamic burning regime is limited by the no-return point  $B_f$  (the unstable root associated to the static restoring function for  $t \rightarrow \infty$ ).

Fig. 40 - Static burning and dynamic stability boundaries on a burning rate vs heat feedback plot. MTS flame,  $n = 3$ ,  $C_g/C_c = 1$ .

Fig. 41 - Bifurcation diagram at 10 atm of pressure. MTS flame,  $n = 3$ ,  $C_g/C_c = 1$ .

Fig. 42 - Bifurcation diagram at 20 atm of pressure. MTS flame,  $n = 3$ ,  $C_g/C_c = 1$ .

Fig. 43 - Bifurcation diagram at 30 atm of pressure. MTS flame,  $n = 3$ ,  $C_g/C_c = 1$ .

Fig. 44 - Bifurcation diagram at 40 atm of pressure. MTS flame,  $n = 3$ ,  $C_g/C_c = 1$ .

Fig. 45 - Bifurcation diagram at 50 atm of pressure. MTS flame,  $n = 3$ ,  $C_g/C_c = 1$ .

Fig. 46 - Bifurcation diagram at 60 atm of pressure. MTS flame,  $n = 3$ ,  $C_g/C_c = 1$ .

Fig. 47 - Bifurcation diagram at 30 atm of pressure. MTS flame,  $n = 3$ ,  $C_g/C_c = 1.12$ .

Fig. 48 - Surface temperature vs pressure plot for  $Q_s = -180$  cal/g predicting existence of stationary reacting solution, damped oscillatory burning, self-sustained oscillatory burning, and no stationary reacting solution. MTS flame,  $n = 3$ ,  $C_g/C_c = 1$ .

Fig. 49 - Burning rate vs pressure plot for  $Q = -158.2$  cal/g predicting static burning (MTS flame) and dynamic stability limits (MTS and KTSS nonlinear flames,  $n = 3$ ). Stationary reacting solution (experimental and MTS fitting with  $A_M = 0.338$ ,  $B_M = 2.350$ ), damped oscillations self-sustained oscillations, and pressure deflagration limit are shown too.  $C_g/C_c = 1$ .

Fig. 50 - Numerical molecules implemented for numerical solutions.

Fig. 51a - Flow chart of overall computer code.

Fig. 51b - Flow chart of subroutine FLAME.

Fig. 52 - Go/no-go computed exponential deradiation tests showing occurrence of dynamic extinction ( $B_r = 5$ ) at 10 atm of pressure. MTS flame,  $C_g/C_c = 1$ .

Fig. 53 - Go/no-go computed exponential deradiation tests showing occurrence of dynamic extinction ( $B_r = 10$ ) at 10 atm of pressure. MTS flame,  $C_g/C_c = 1$ .

Fig. 54 - Computed dynamic extinction following linear deradiation at 10 atm of pressure (opaque condensed phase). MTS flame,  $C_g/C_c = 1$ .

Fig. 55 - Computed dynamic extinction following bilinear deradiation at 10 atm of pressure (opaque condensed phase). MTS flame,  $C_g/C_c = 1$ .

Fig. 56 - Computed dynamic extinction following parabolic deradiation at 10 atm of pressure (opaque condensed phase). MTS flame,  $C_g/C_c = 1$ .

Fig. 57 - Computed dynamic extinction following exponential deradiation at 10 atm of pressure (opaque condensed phase). MTS flame,  $C_g/C_c = 1$ .

Fig. 58 - Computed dynamic extinction following exponential deradiation at 20 atm of pressure (opaque condensed phase). MTS flame,  $C_g/C_c = 1$ .

Fig. 59 - Computed dynamic extinction following exponential deradiation at 30 atm of pressure (opaque condensed phase). MTS flame,  $C_g/C_c = 1$ .

Fig. 60 - Computed dynamic extinction following exponential deradiation at 40 atm of pressure (opaque condensed phase). MTS flame,  $C_g/C_c = 1$ .

Fig. 61 - Computed dynamic extinction following exponential depressurization from a parametrically changed initial pressure. MTS flame,  $C_g/C_c = 1$ .

Fig. 62 - Computed dynamic extinction following exponential depressurization with a parametrically changed depressurization rate. MTS flame,  $C_g/C_c = 1$ .

Fig. 63 - Computed dynamic extinction following exponential deradiation at 10 atm of pressure (t-transparent condensed phase,  $\alpha=500 \text{ cm}^{-1}$ ). MTS flame,  $C_g/C_c = 1$ .

Fig. 64 - Computed dynamic extinction following simultaneous deradiation (opaque condensed phase) and depressurization. MTS flame,  $C_g/C_c = 1$ .

Fig. 65 - Computed dynamic extinction following consecutive deradiation (opaque condensed phase) and depressurization. MTS flame,  $C_g/C_c = 1$ .

Fig. 66 - Computed dynamic extinction following a radiation pulse (opaque condensed phase). MTS flame,  $C_g/C_c = 1$ .

Fig. 67 - Computed pressurization tests showing no oscillatory burning for low values of surface heat release. MTS flame,  $C_g/C_c = 1$ .

Fig. 68 - Computed pressurization tests showing oscillatory burning or extinction for large values of surface heat release. MTS flame,  $C_g/C_c = 1$ .

Fig. 69 - Computed pressurization tests showing three possible static regimes (stationary after damped oscillations for  $Q_s = -180 \text{ cal/g}$ , self-sustained oscillating for  $Q_s = -200 \text{ cal/g}$ , extinguished for  $Q_s = -220 \text{ cal/g}$ ). MTS flame,  $C_g/C_c = 1$ .

Fig. 70 - Computed pressurization tests showing self-sustained oscillatory burning for KTSS nonlinear flame ( $Q_s = -180 \text{ cal/g}$ ).  $C_g/C_c = 1$ .

Fig. 71 - Computed frequency and amplitude of radiation assisted self-sustained oscillations. MTS flame,  $C_g/C_c = 1$ .

Fig. 72 - Computed dynamic extinction following parabolic deradiation at 10 atm of pressure (opaque condensed phase). MTS flame,  $C_g/C_c = 1.12$ .

Fig. 73 - Computed pressurization tests showing three possible static regimes (stationary after damped oscillations for  $Q_{s,\text{ref}} = -190 \text{ cal/g}$ , self-sustained oscillating for  $Q_{s,\text{ref}} = -209 \text{ cal/g}$ , extinguished for  $Q_{s,\text{ref}} = -210 \text{ cal/g}$ ). MTS flame,  $C_g/C_c = 1.12$ .

Fig. 74 - Computed pressurization test showing three possible static regimes (stationary after damped oscillations for  $P_f = 8 \text{ atm}$ , self-sustained oscillating for  $P_f = 3 \text{ atm}$ , extinguished for  $P_f = 1.9 \text{ atm}$ ). MTS flame,  $C_g/C_c = 1.12$ .

Fig. 75 - Computed radiative ignition tests showing dynamic extinction following radiation source cut-off. MTS flame,  $C_g/C_c = 1$ .

Fig. 76 - Computed radiative ignition tests showing sharp burning peak associated with prolonged heating at low radiant flux intensity. MTS flame,  $C_g/C_c = 1$ .

Fig. 77 - Computed radiative ignition tests showing successful ignition for surface temperature forced close to, but less than, lower dynamic combustion stability limit. MTS flame,  $C_g/C_c = 1$ .

Fig. 78 - Computed radiative ignition map showing importance of dynamic burning at low pressure and/or large radiant flux. MTS flame,  $C_g/C_c = 1$ .

Fig. 79 - Experimental vs computed (MTS flame,  $C_g/C_c = 1$ ) radiative ignition map showing agreement in the tested range of operating conditions.

Fig. 80 - Computed radiative ignition test with detailed history of relevant variables. MTS flame,  $C_g/C_c = 1$ .

Fig. 81a - Sketch of shock tube apparatus.  
81b - Sketch of shock tube test section.

Fig. 82 - Static pressure deflagration limits of the tested composite propellant as measured in the shock tube test section. AP/PVC.

Fig. 83a - Schematic layout of overall experimental apparatus.  
Fig. 83b - Nomenclature used in the schematic layout.

Fig. 84 - Piston used in the shock tube apparatus.

Fig. 85 - Sketch of the experimental apparatus with high speed camera.

Fig. 86 - Typical series of photograms of AP propellant burning in air. AP/PBHT.

Fig. 87 - Pressure and luminosity traces of the test of Fig. 86.

Fig. 88 - Sharp decrease of luminosity during depressurization of AP propellant burning in air. AP/PBHT.

Fig. 89 - Experimental set-up for ionization measurement at the propellant burning surface.

Fig. 90 - Oscilloscope trace of ionization, steady burning of AP propellant. AP/PBHT.

Fig. 91 - Pressure and ionization traces during unsteady burning of AP propellant; single pressure pulse. AP/PBHT.

Fig. 92 - Pressure and ionization traces during unsteady burning of AP propellant; multiple pressure pulses. AP/PBHT.

Fig. 93 - Computed response of burning composite propellant to piston tube pressurization (unreacting atmosphere). MTS flame,  $C_g/C_c = 1$ . AP/PVC.

Fig. 94 - Sketch illustrating experimental pressure decay of depressurization strand burner when solenoid valves (top) or manual valves (bottom) are used.

Fig. 95 - Computed and experimental boundaries, between extinction and continued burning, vs initial pressure.

Fig. 96 - Compared experimental boundaries, between extinction and continued burning, vs initial pressure obtained from several investigators.

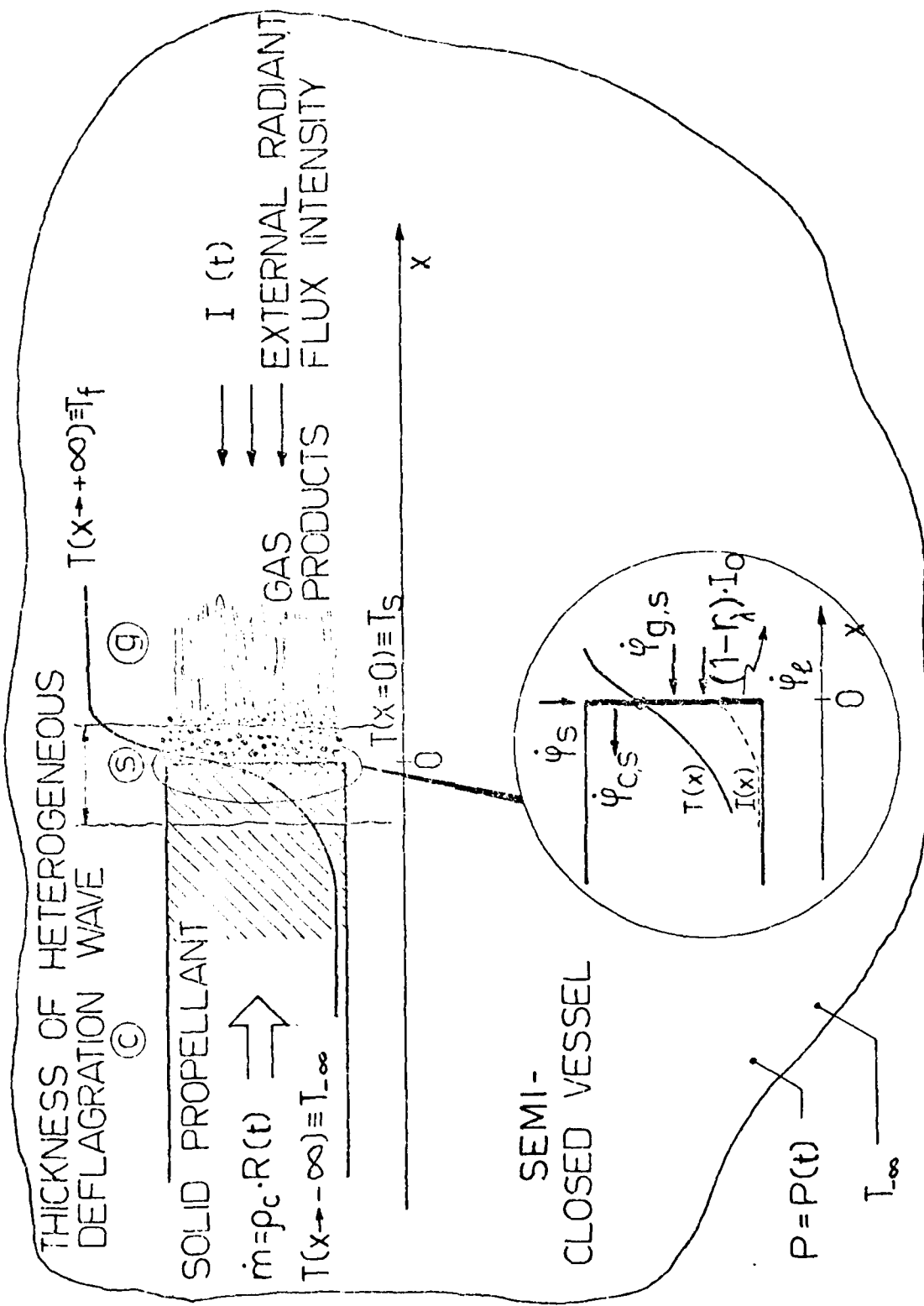


Fig. 1

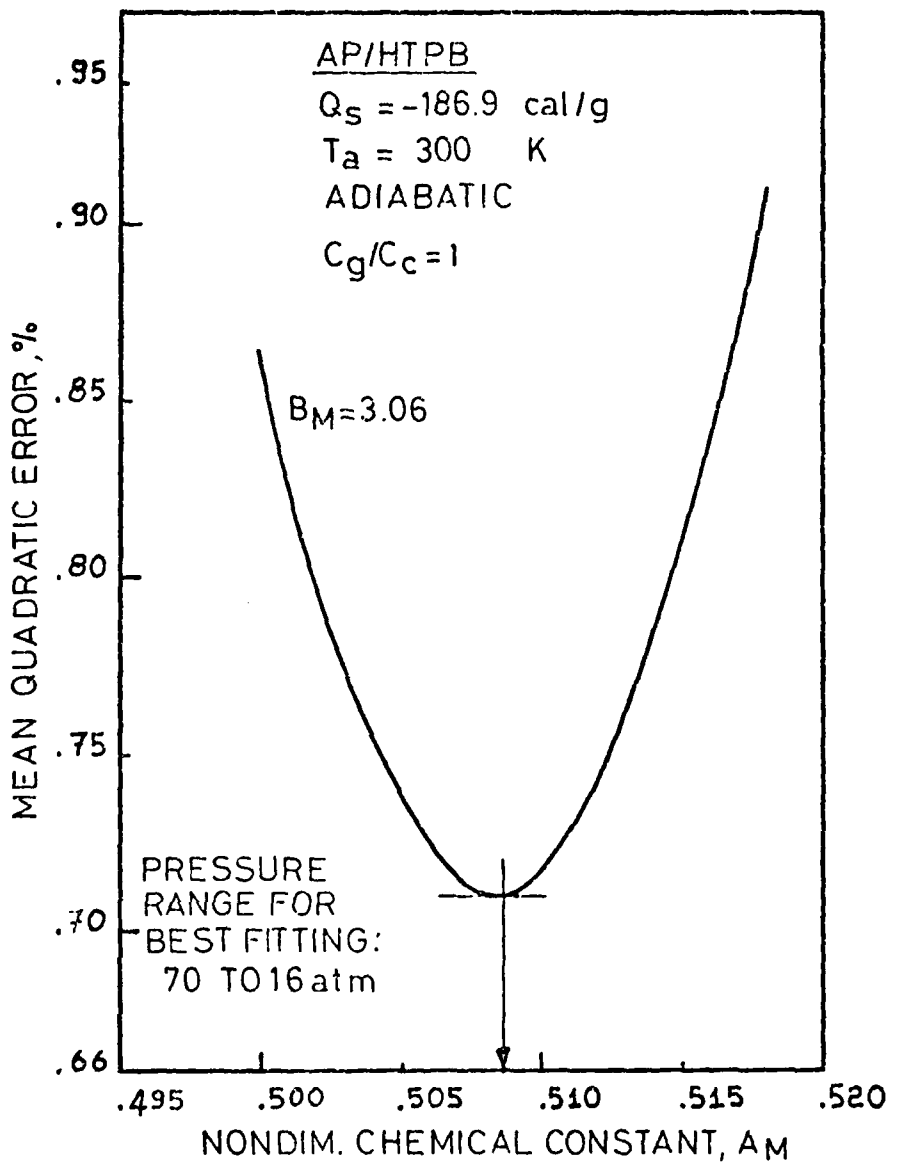


FIG. 2a

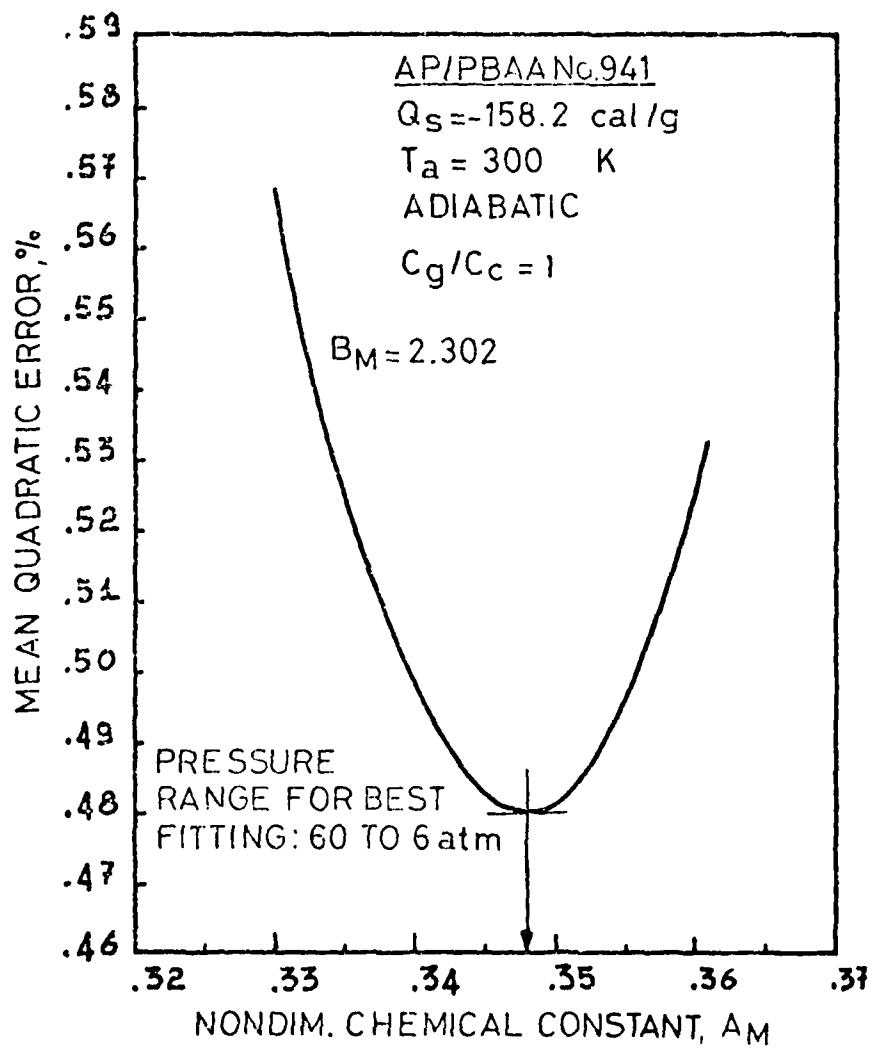


FIG. 2b

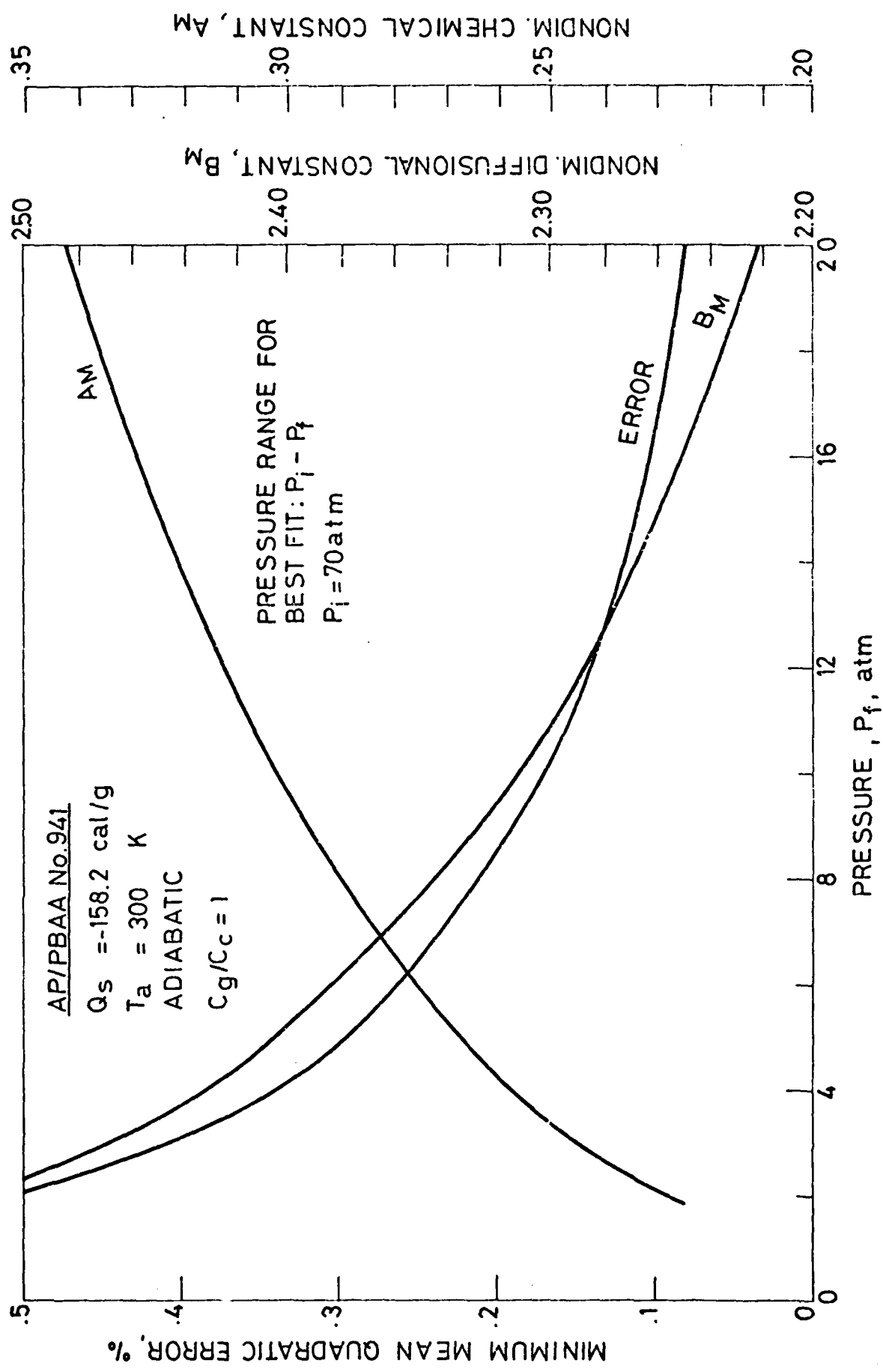


FIG. 3

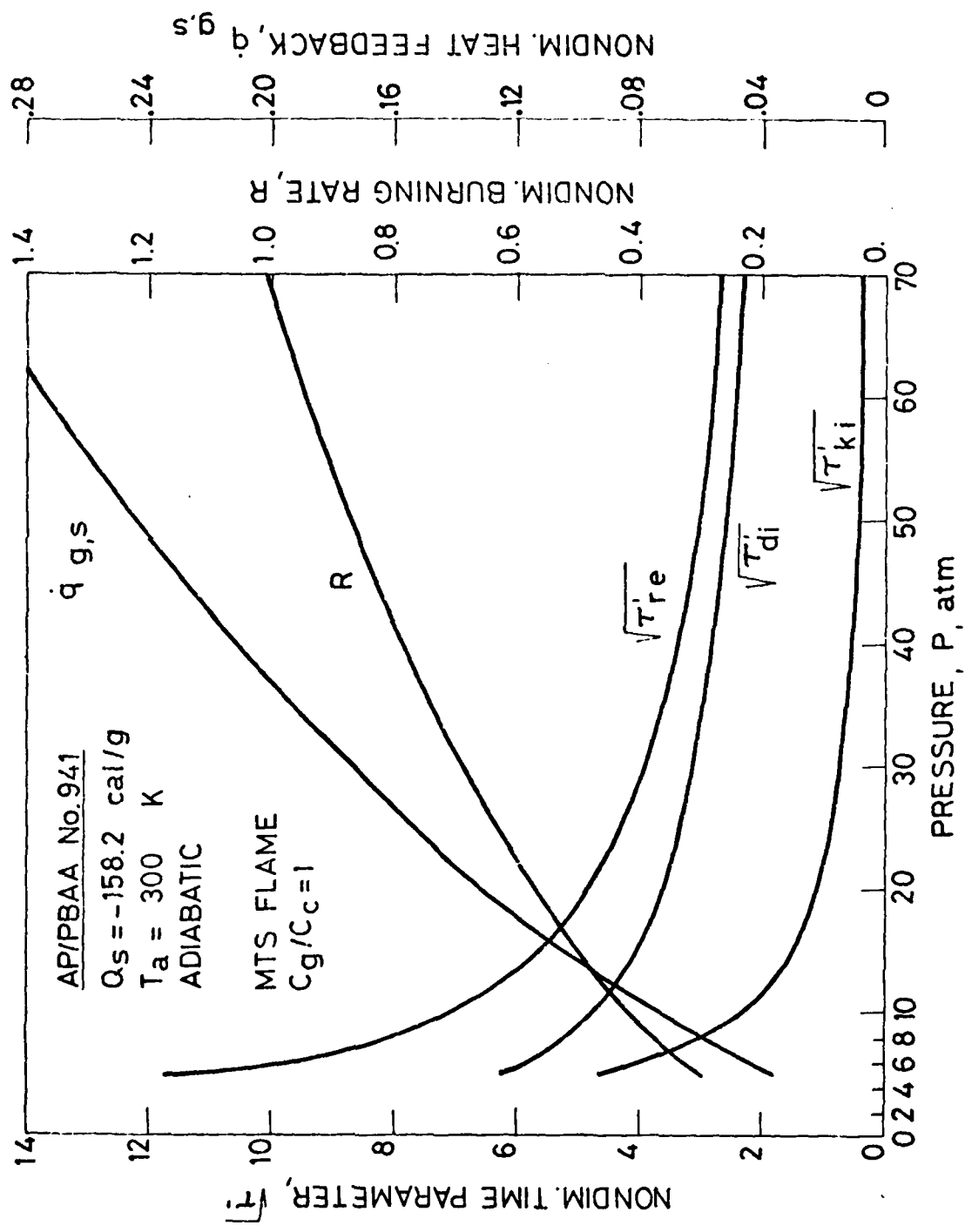


FIG. 4

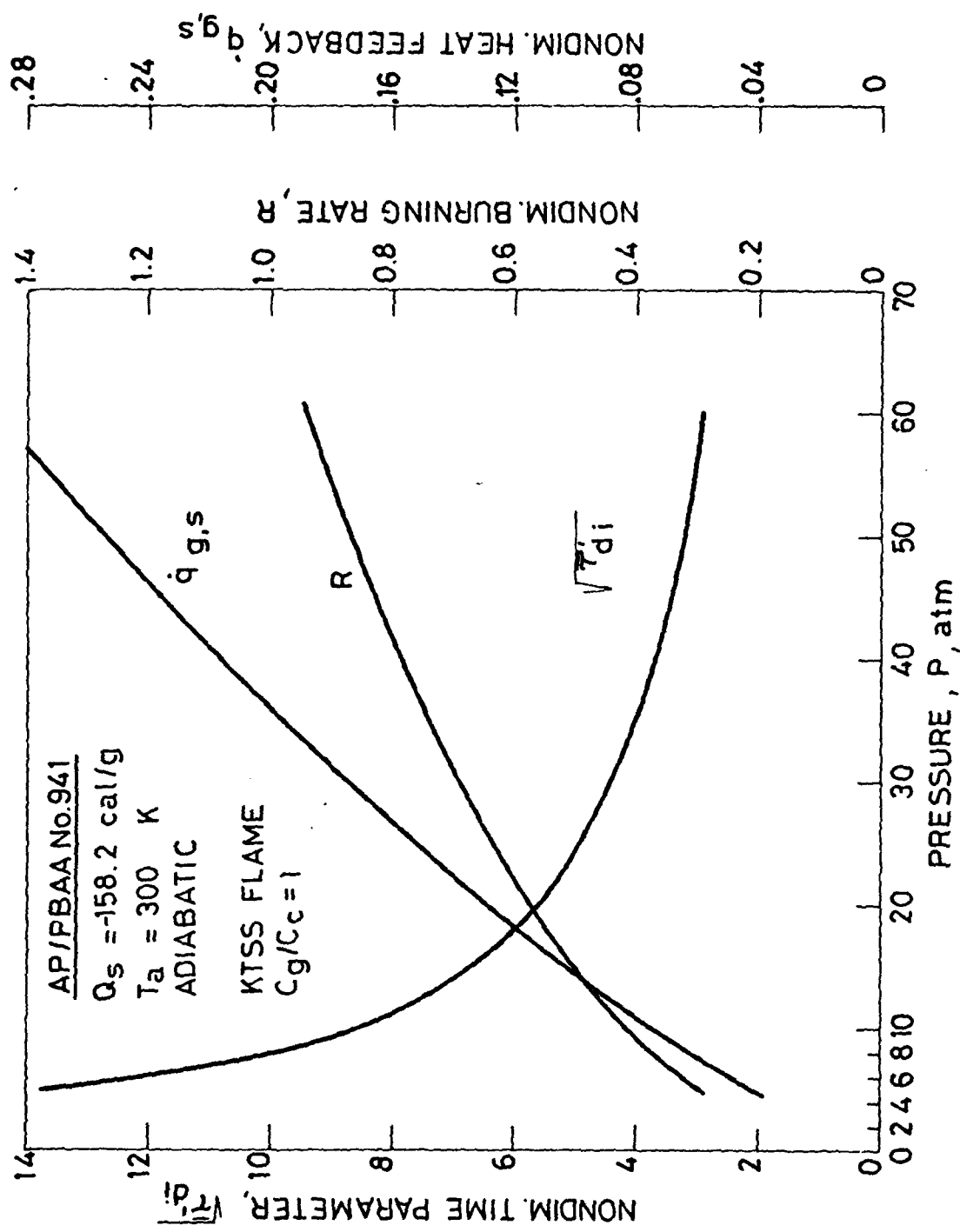


FIG. 5

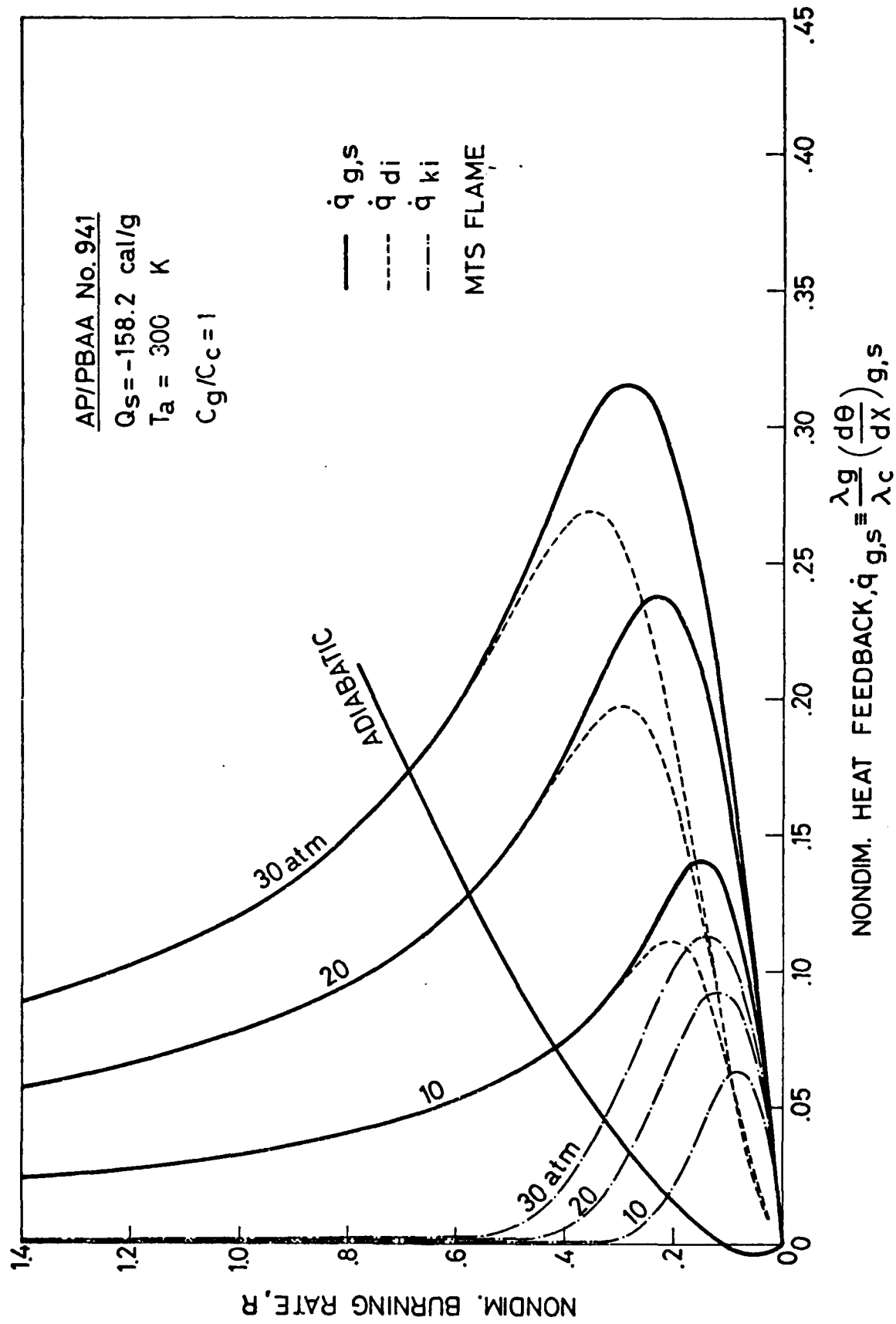


FIG. 6

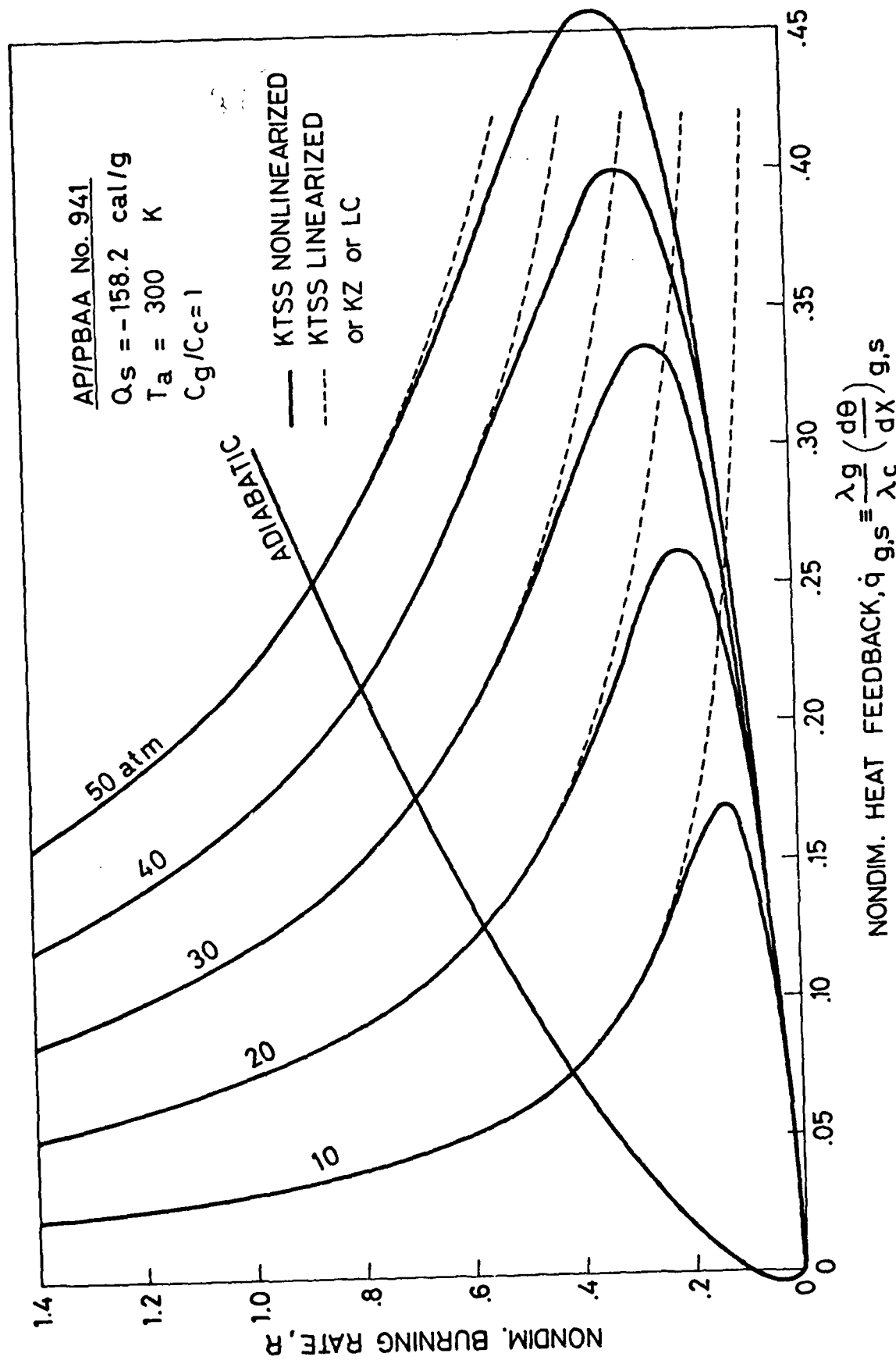


FIG. 7

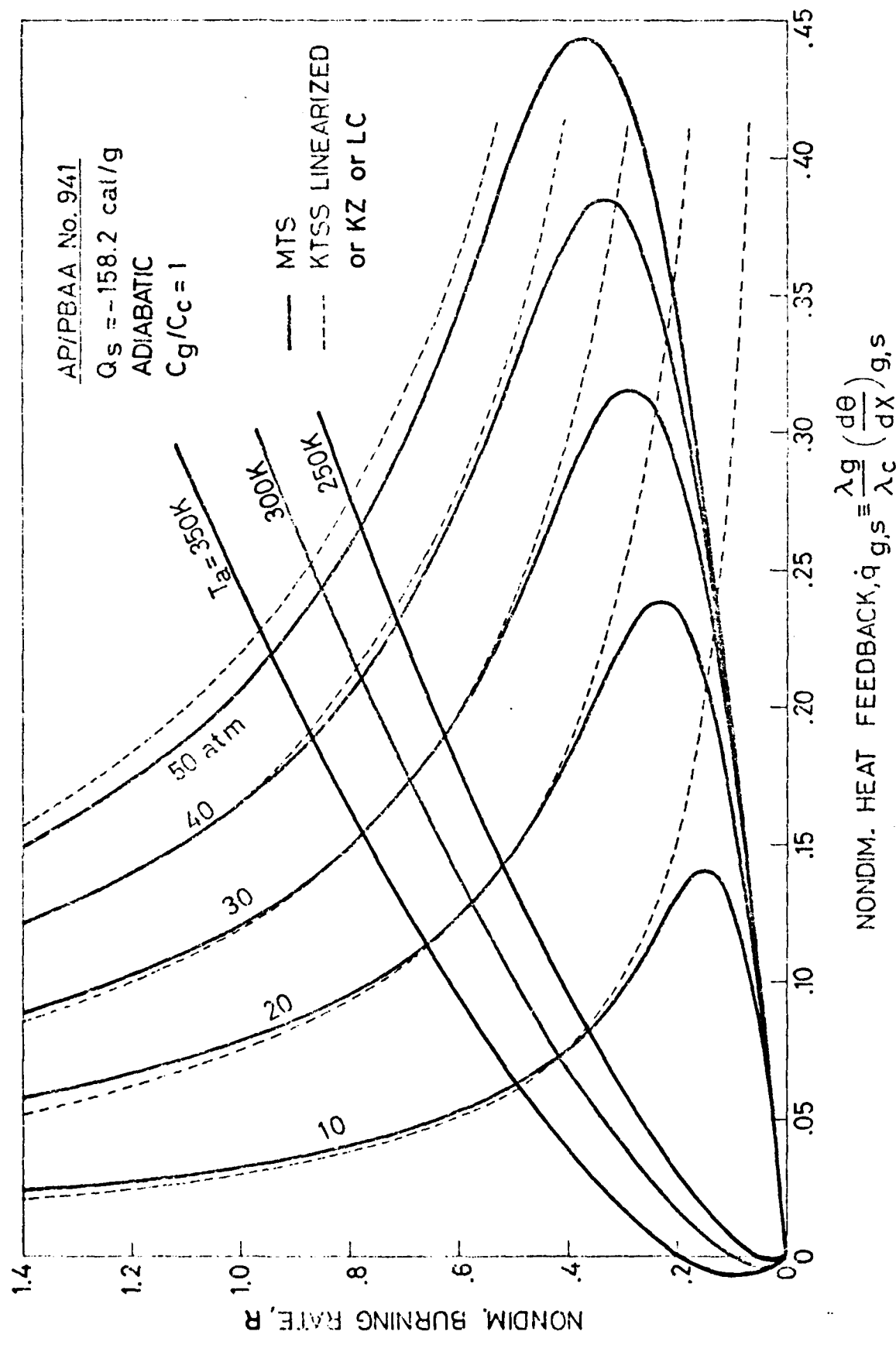


FIG. 5

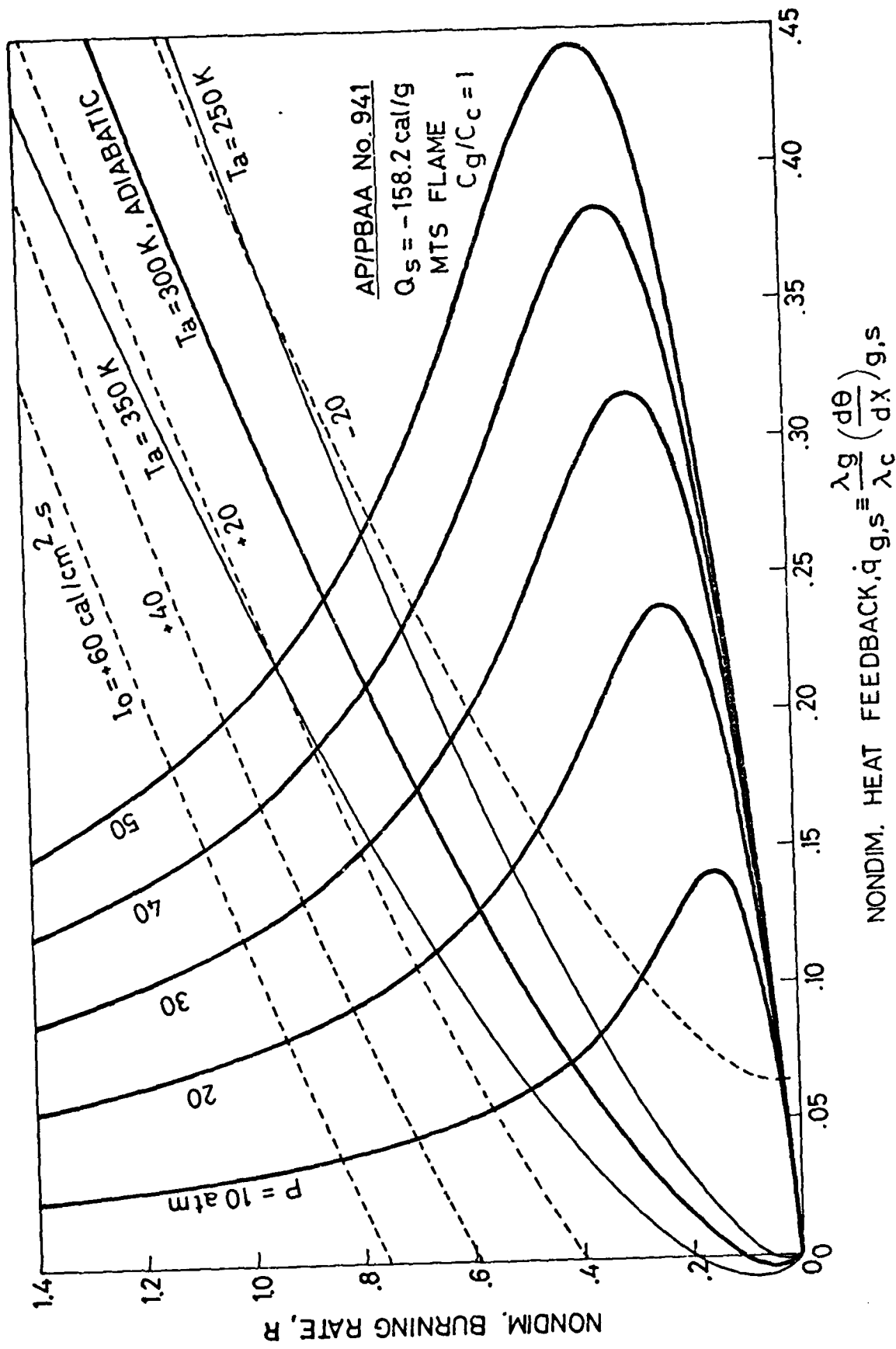


FIG. 9

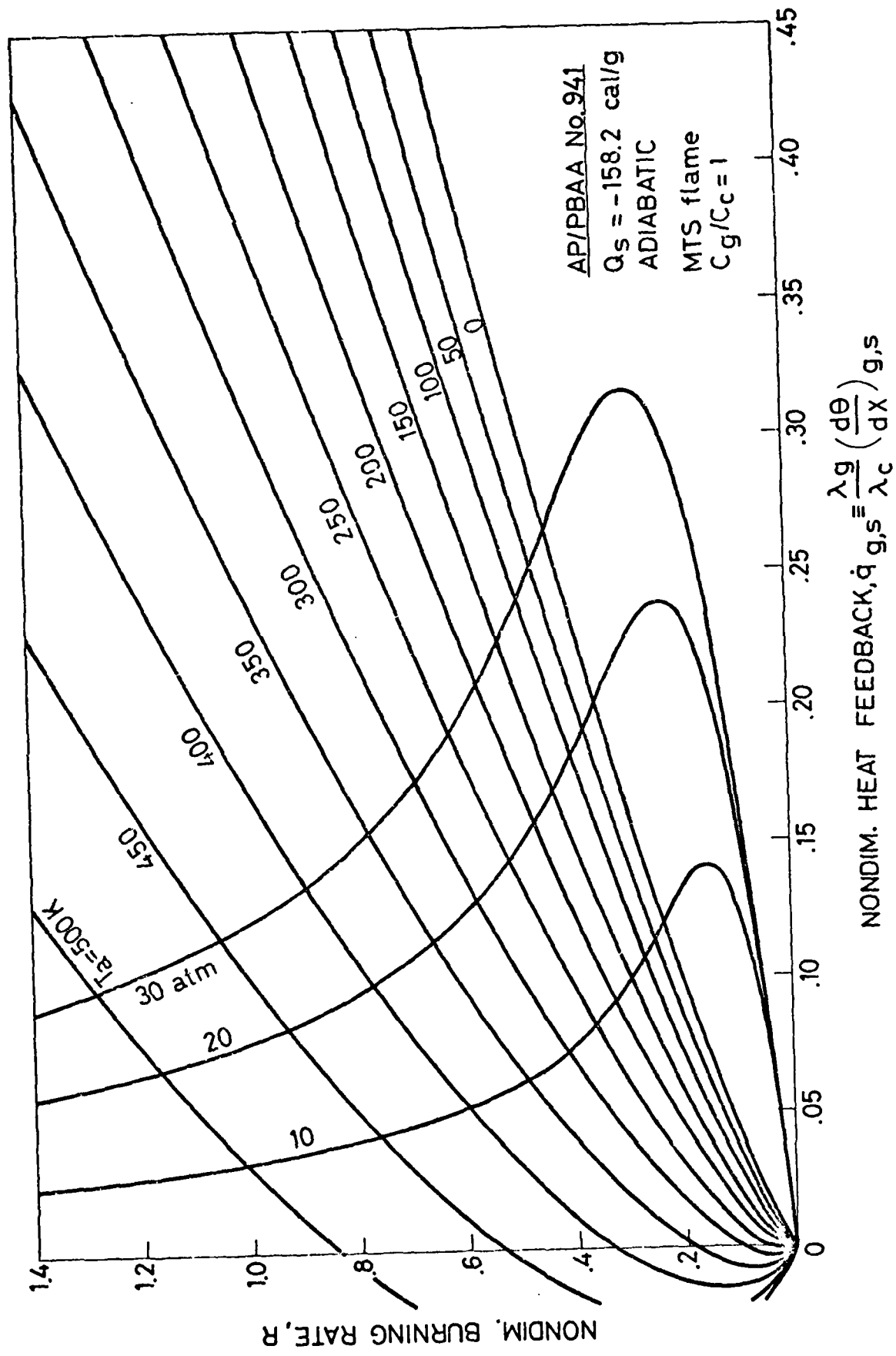


FIG. 10

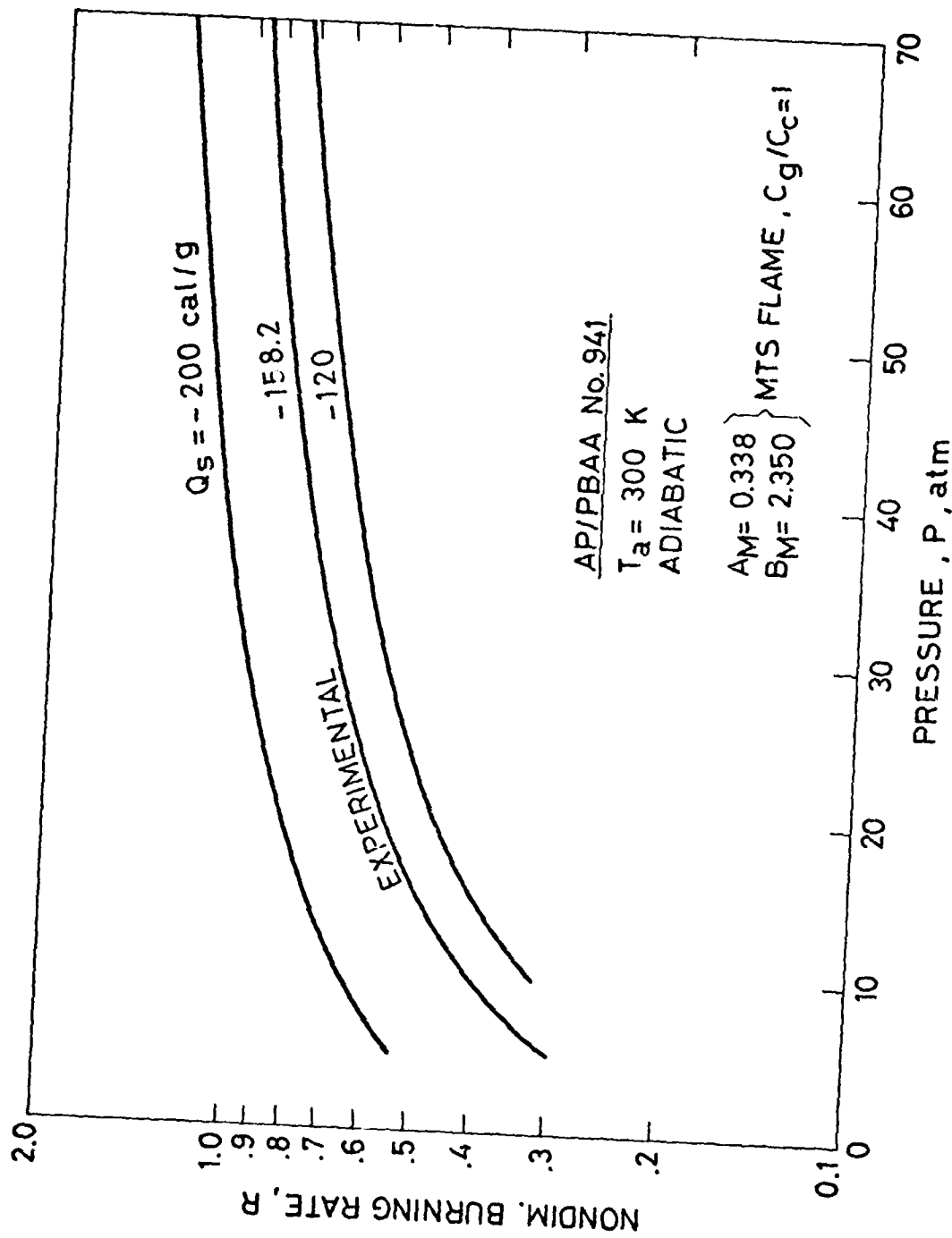


FIG. 11

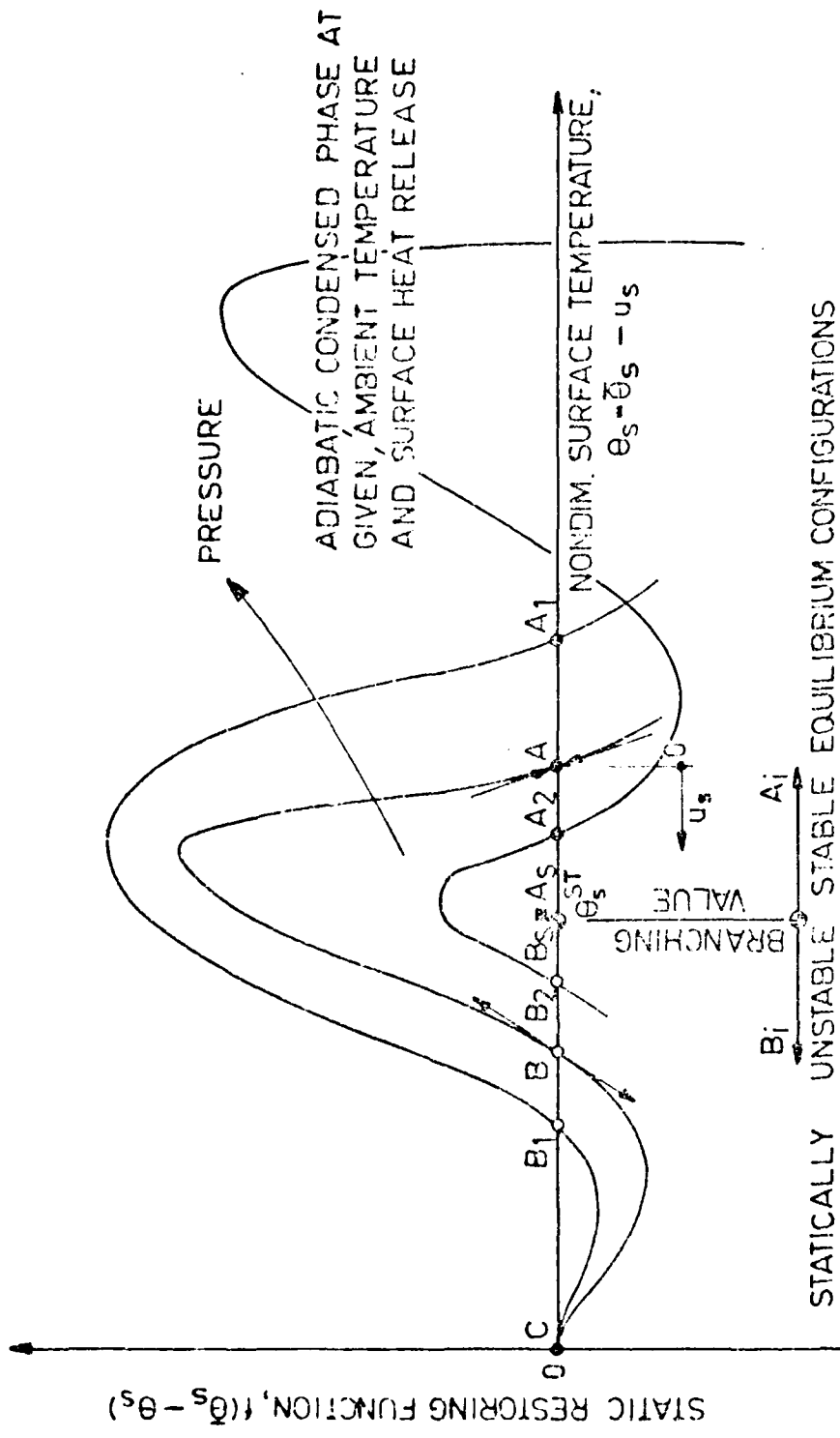


FIG. 12a

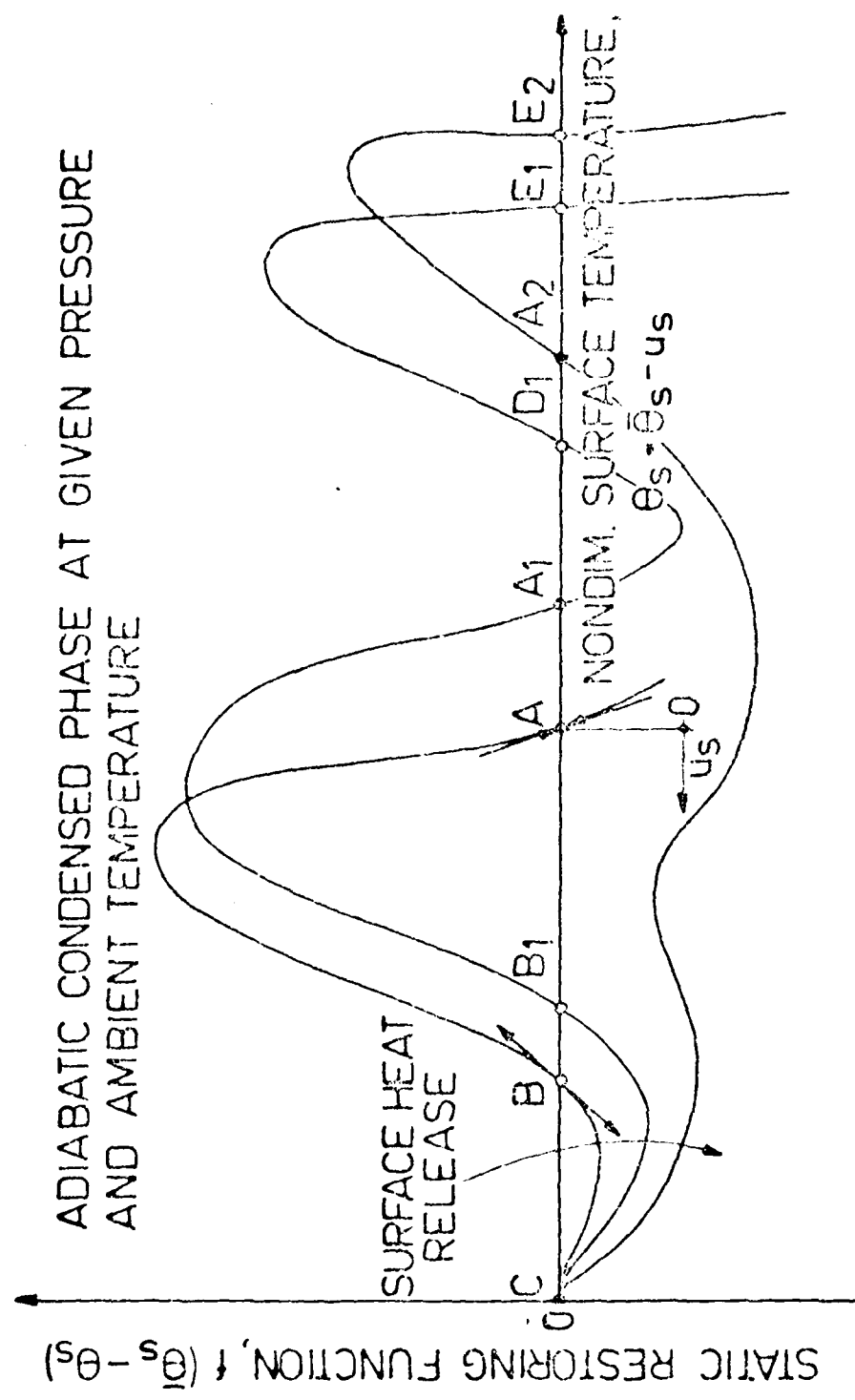


FIG. 12 b

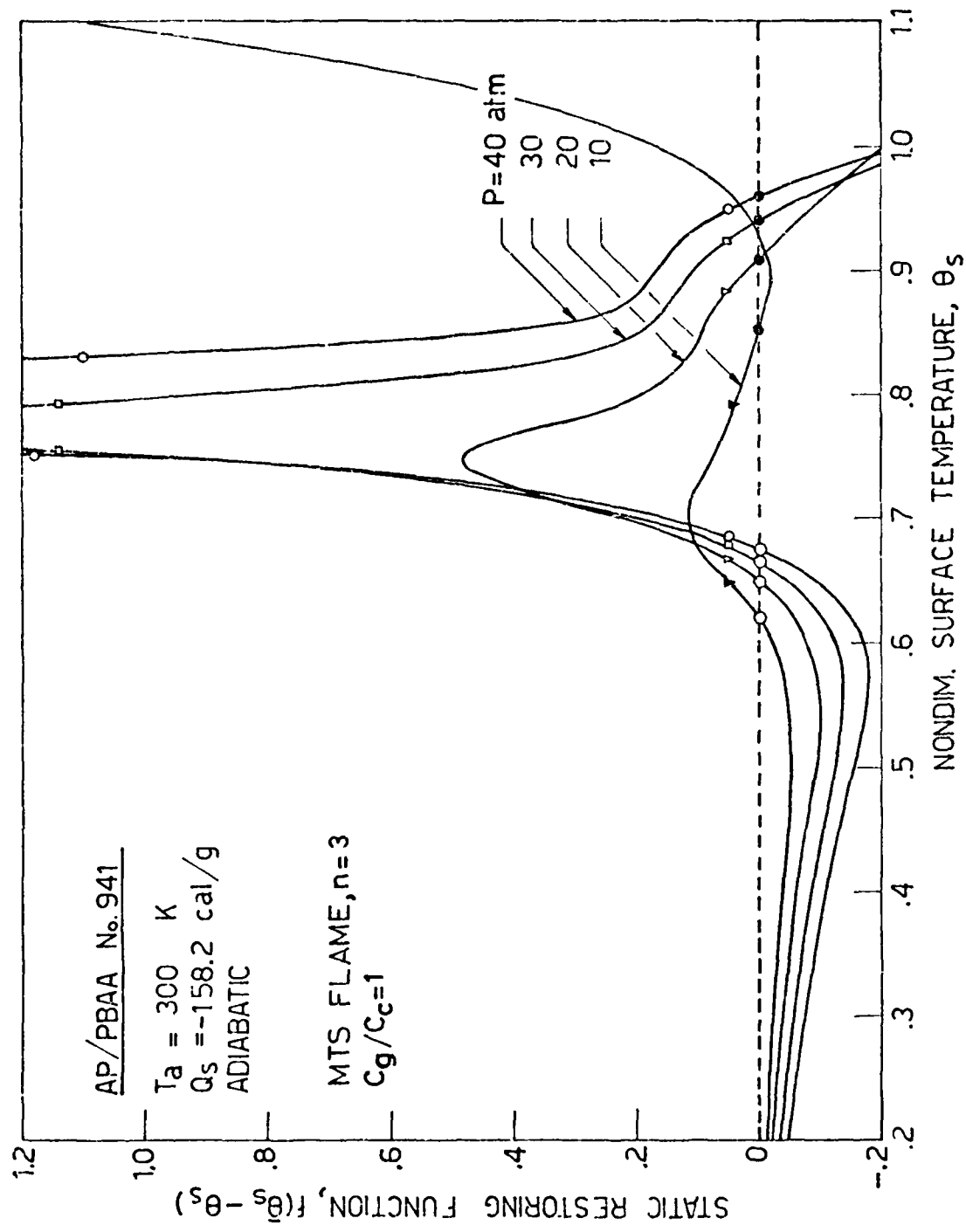


FIG. 13

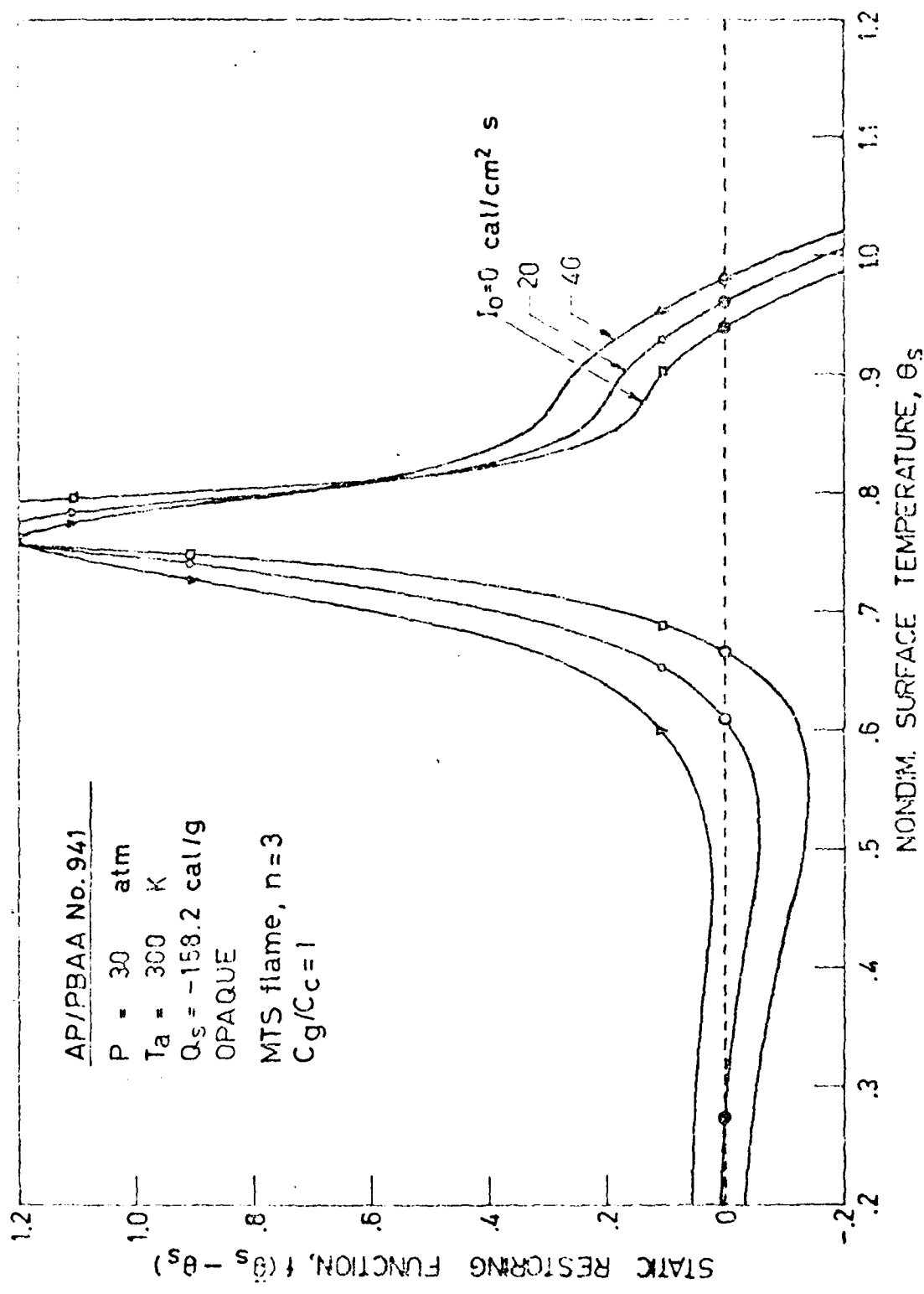


FIG. 14

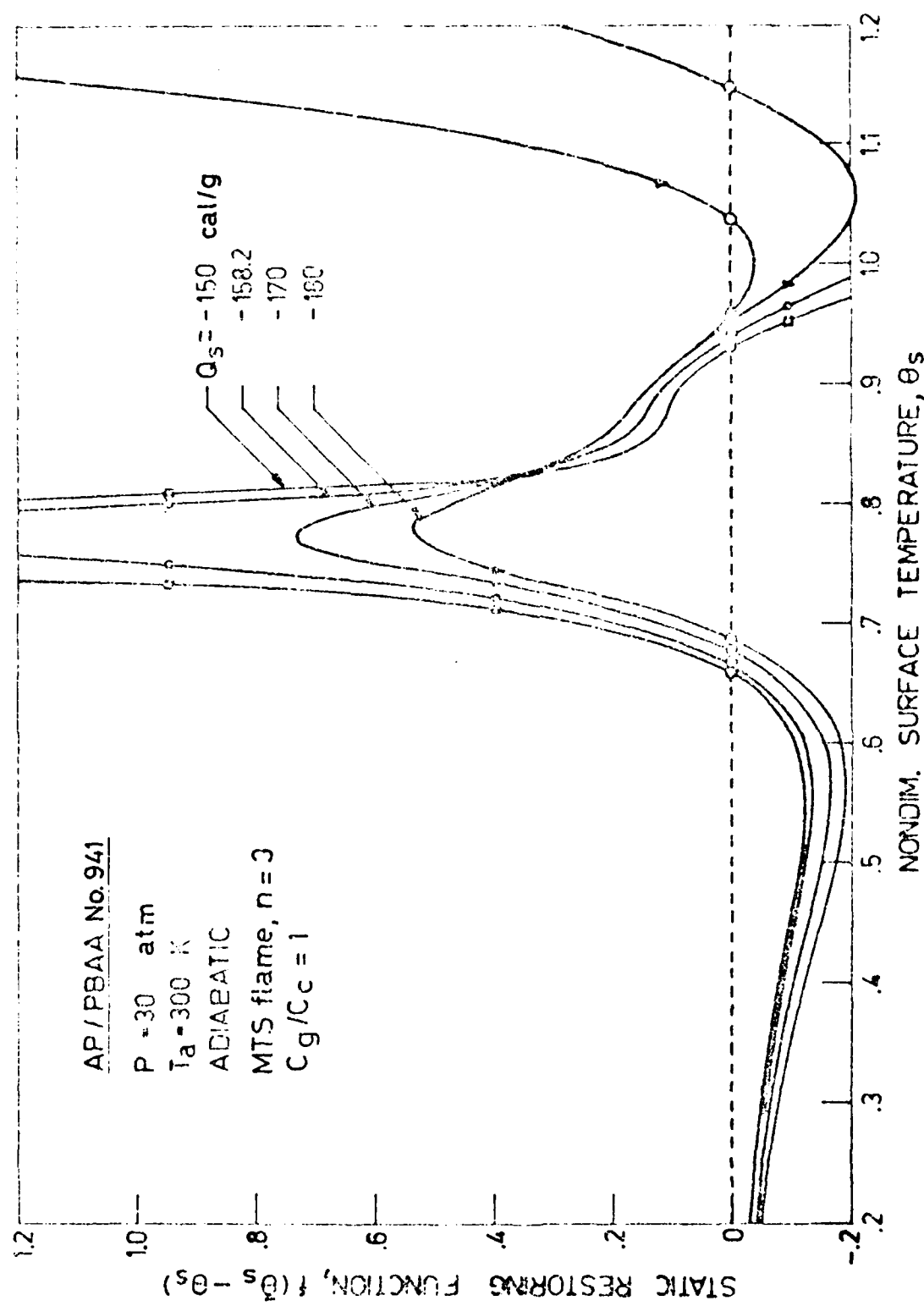


FIG. 15a

1.2  
AP/ PBAA No. 941

P - 30 atm

T<sub>a</sub> - 300 K

ADIABATIC

MTS flame, n = 3

C<sub>g</sub>/C<sub>c</sub> = 1

Q<sub>s</sub> - 200 cal/g

-190

-180

-170

STATIC RESTORING FUNCTION, f(θ<sub>s</sub> - θ<sub>0</sub>)

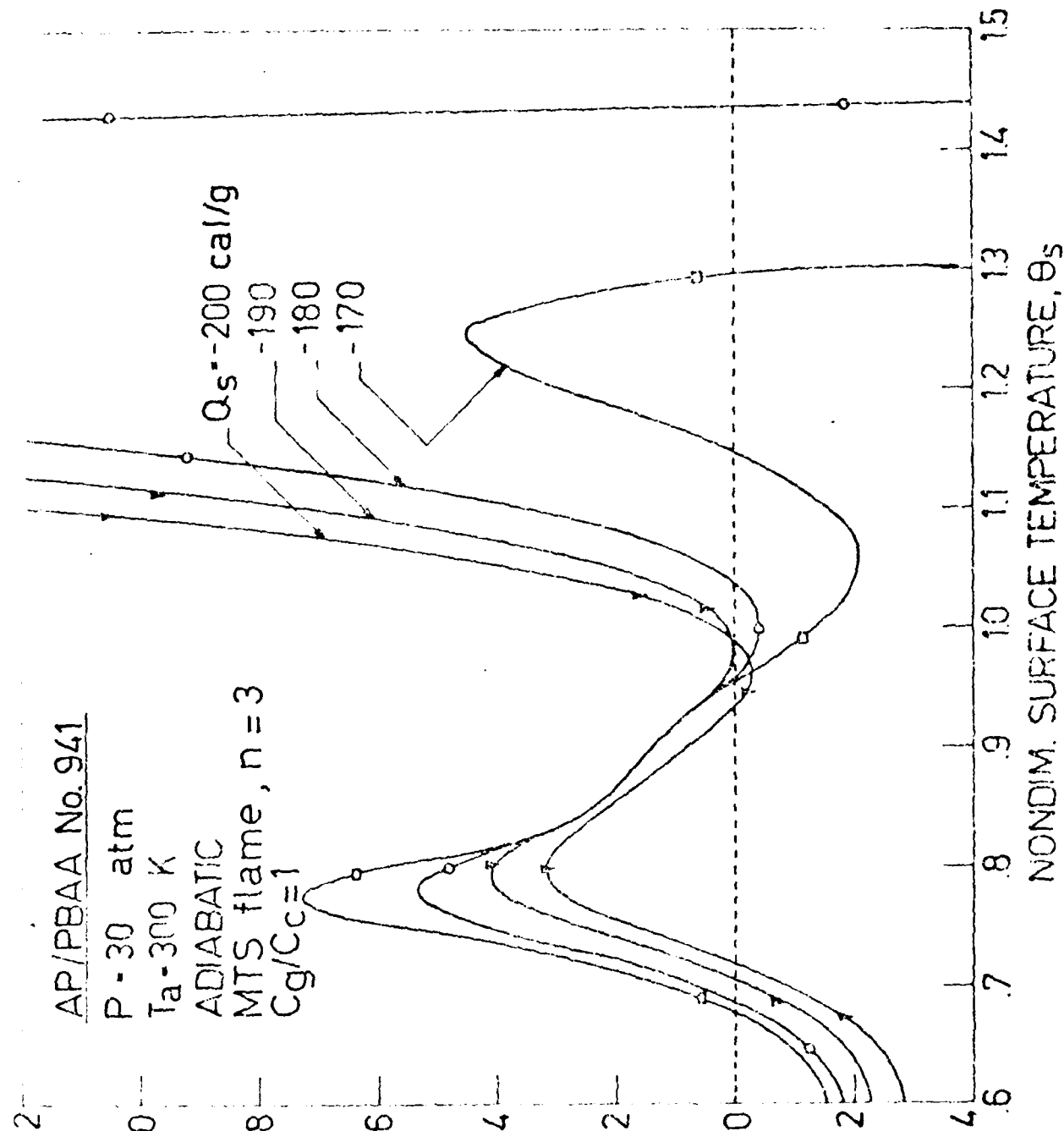


FIG. 15 b

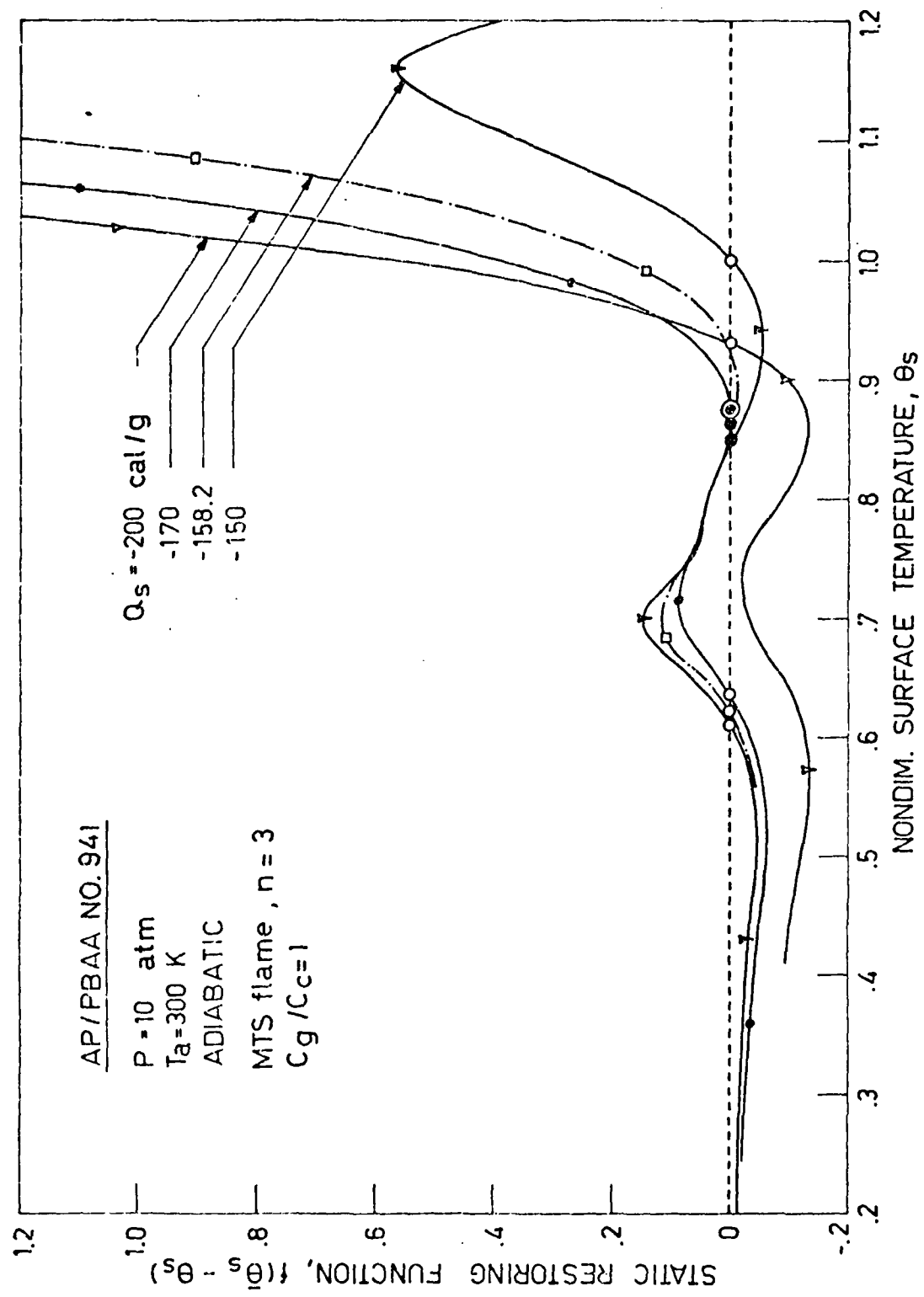


FIG. 16

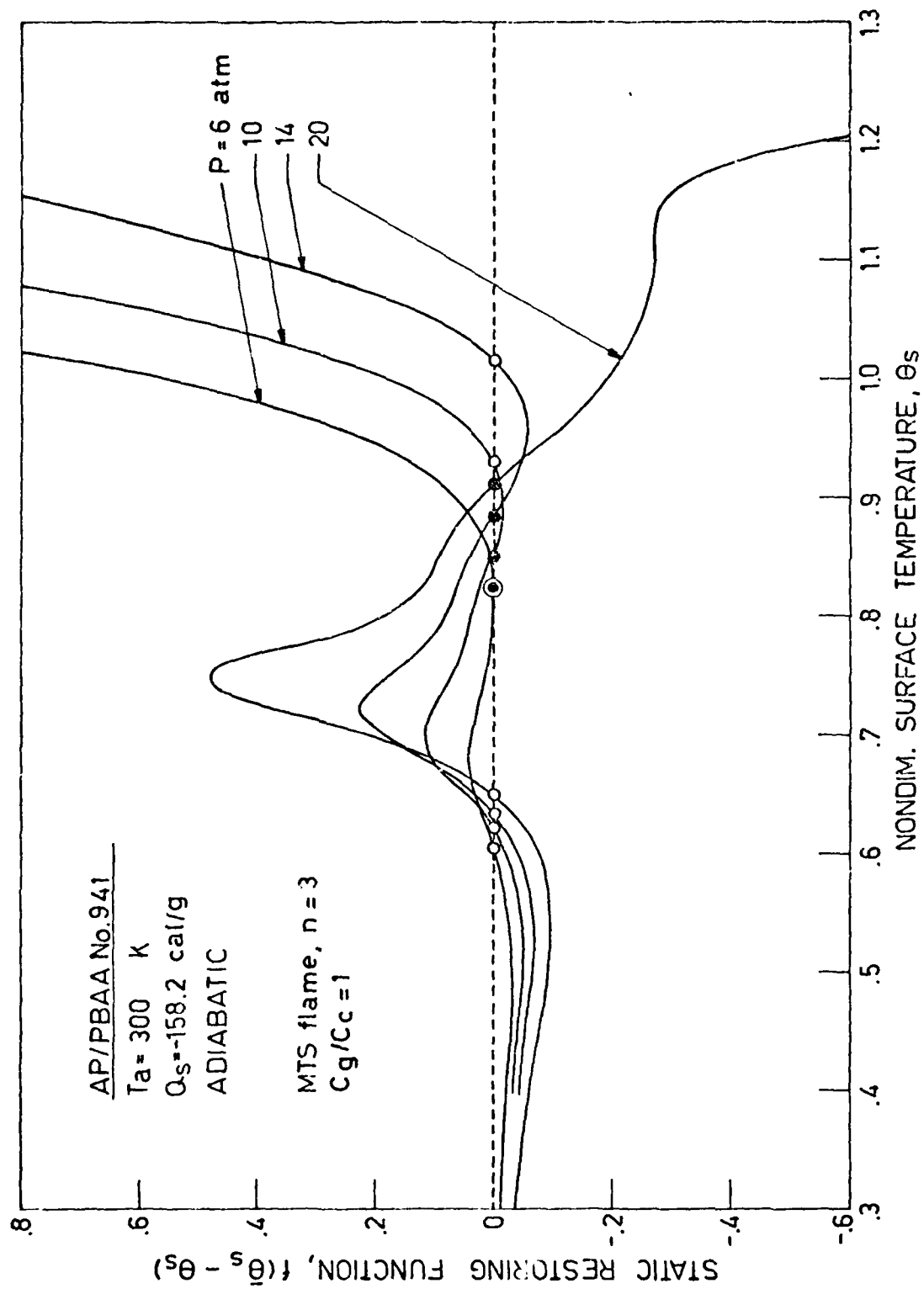


FIG. 17

AP/PBAA No. 941

$P = 3^n$  atm  
ADI, ATIC  
 $Q_s = i_s = .2$  cal/g  
MTS flame,  $n = 3$   
 $C_g/C_c = 1$

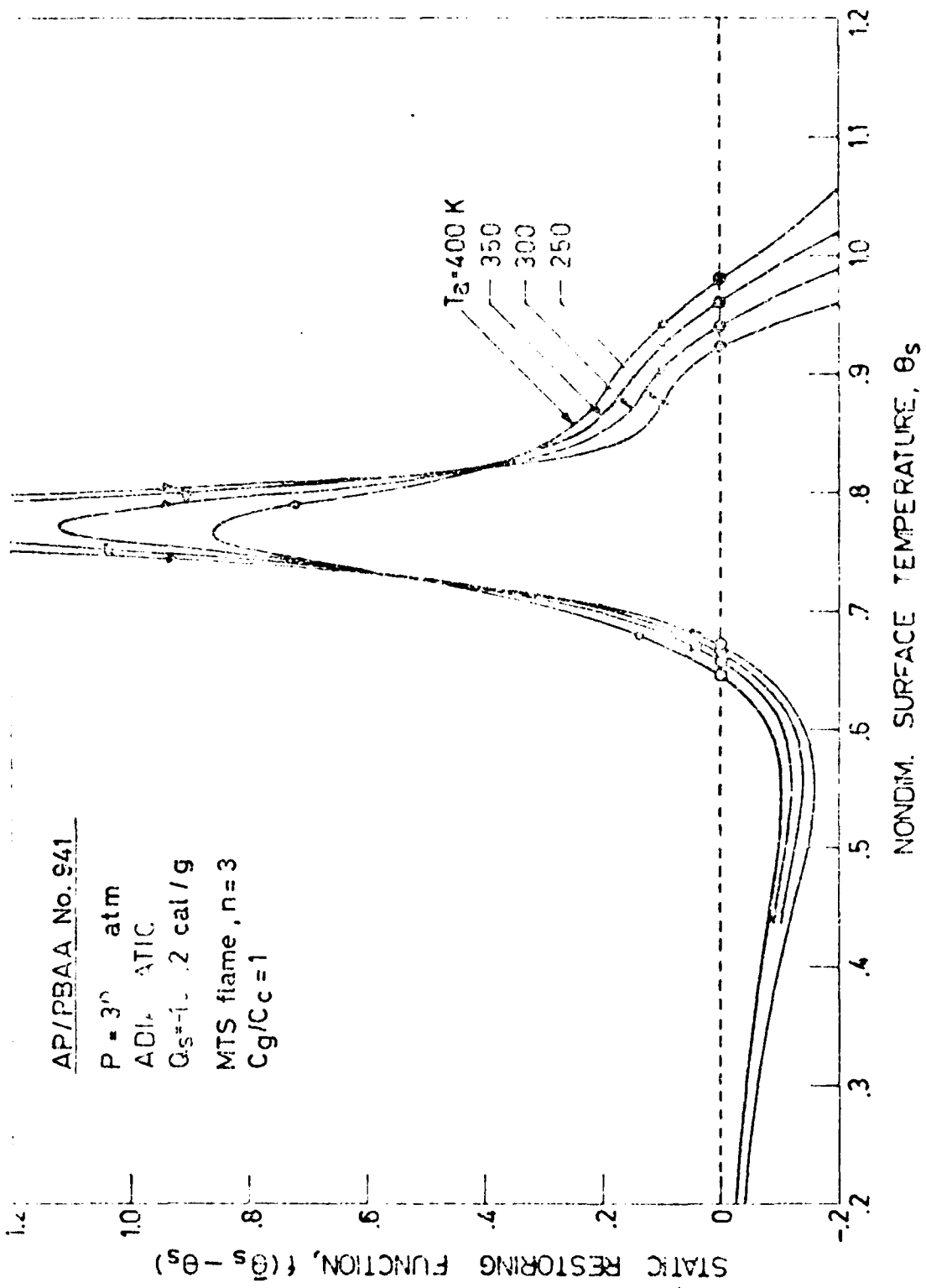


FIG. 12

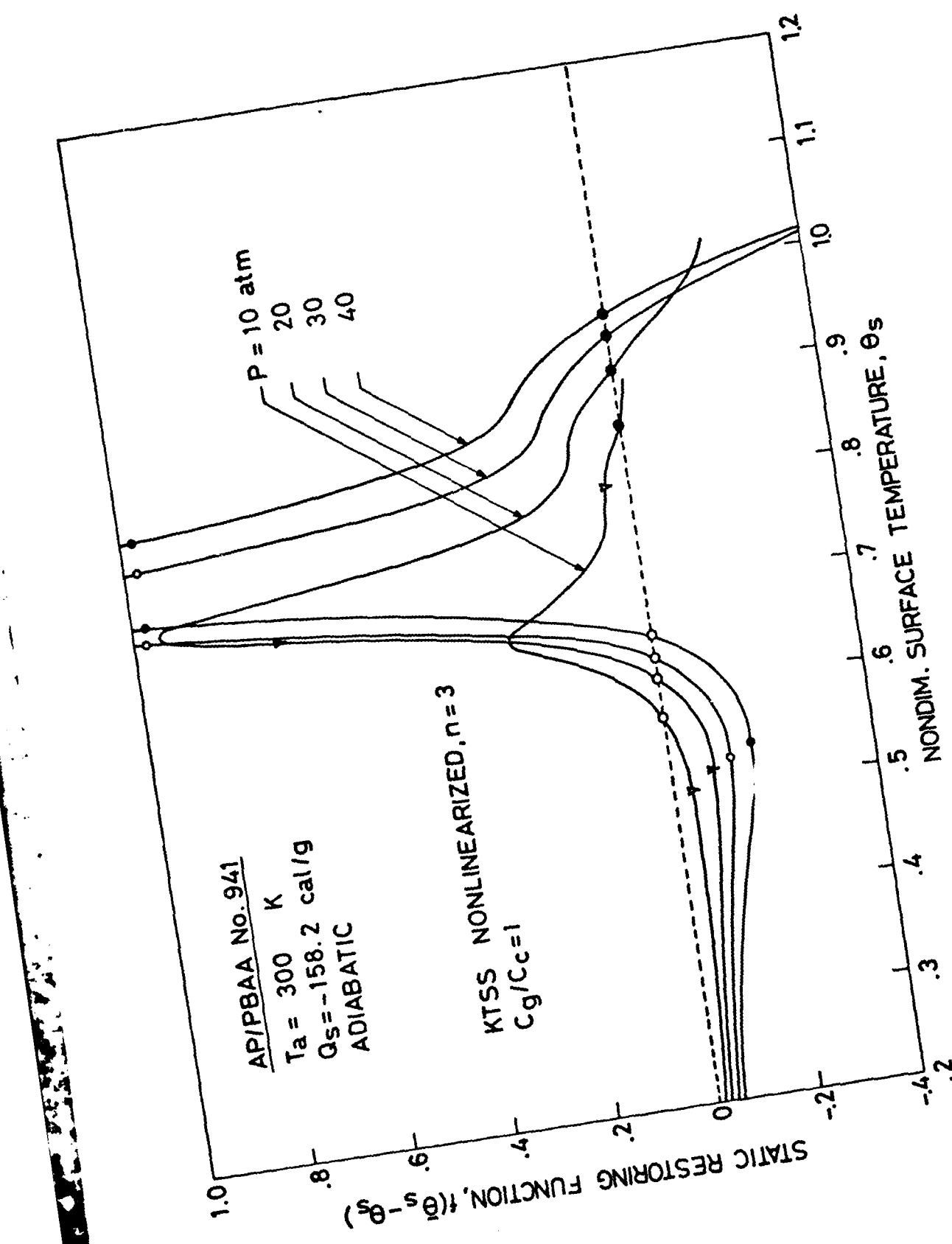


FIG. 19

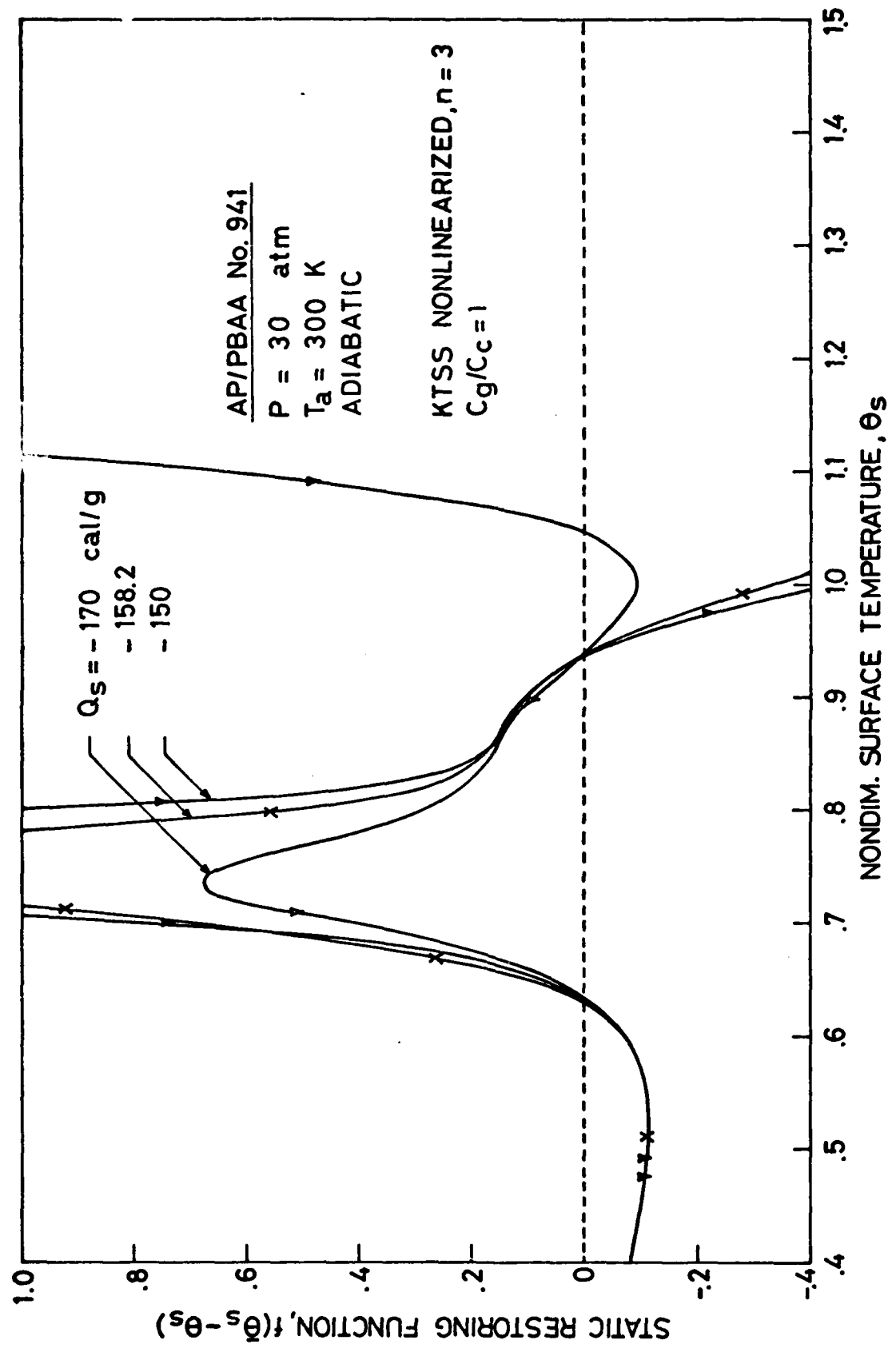


FIG. 20

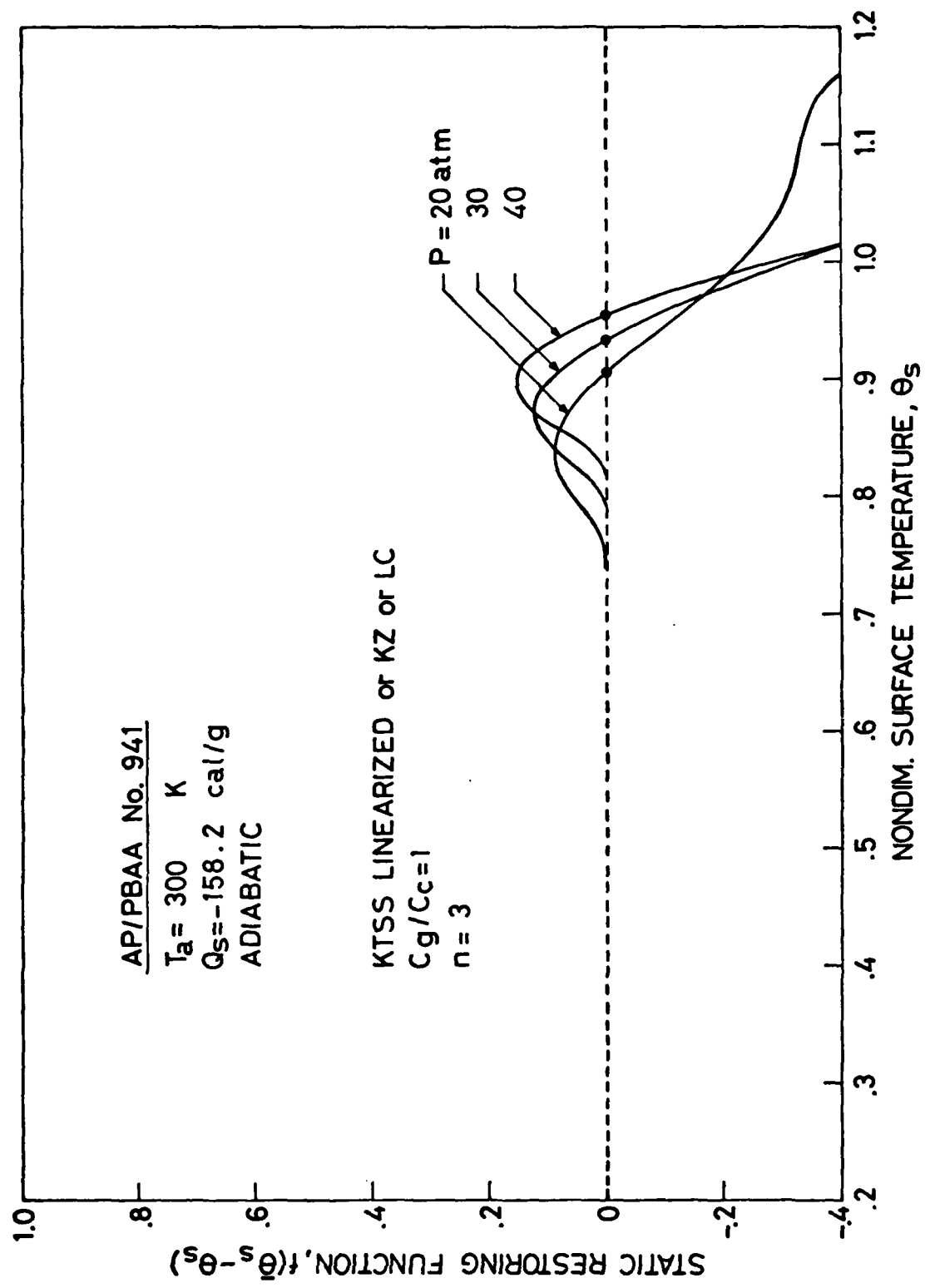


FIG. 21

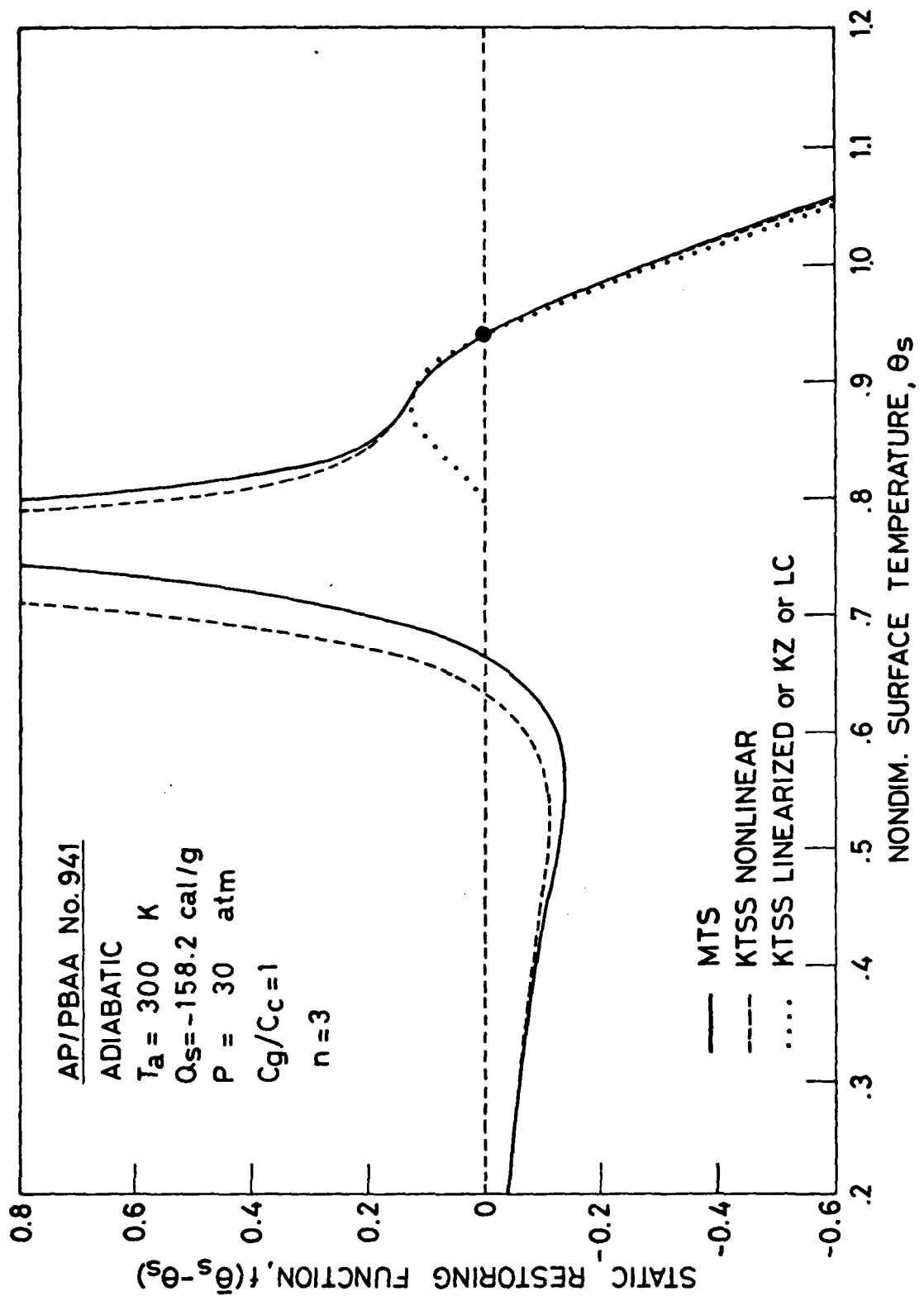


FIG. 22

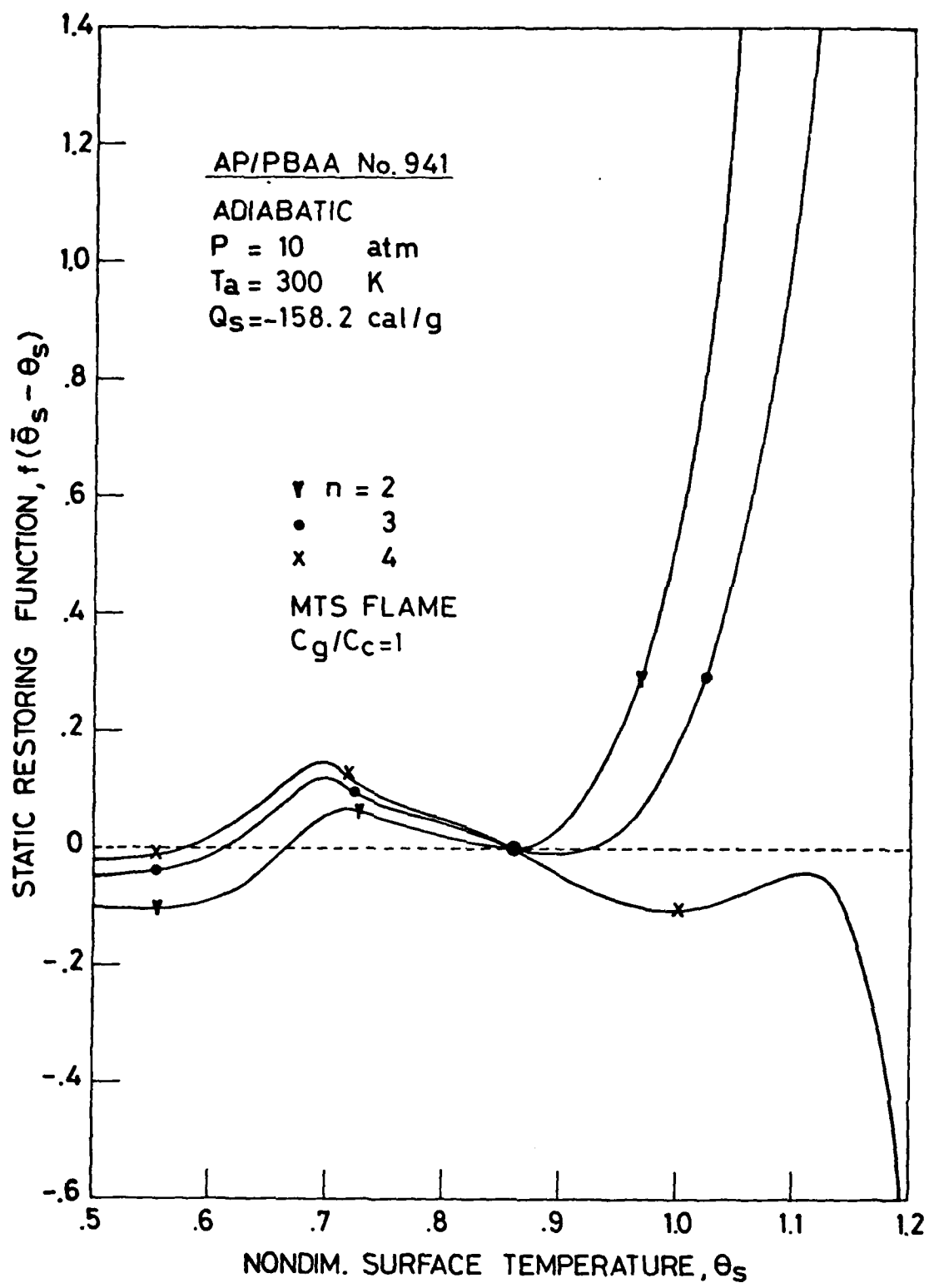


FIG. 23

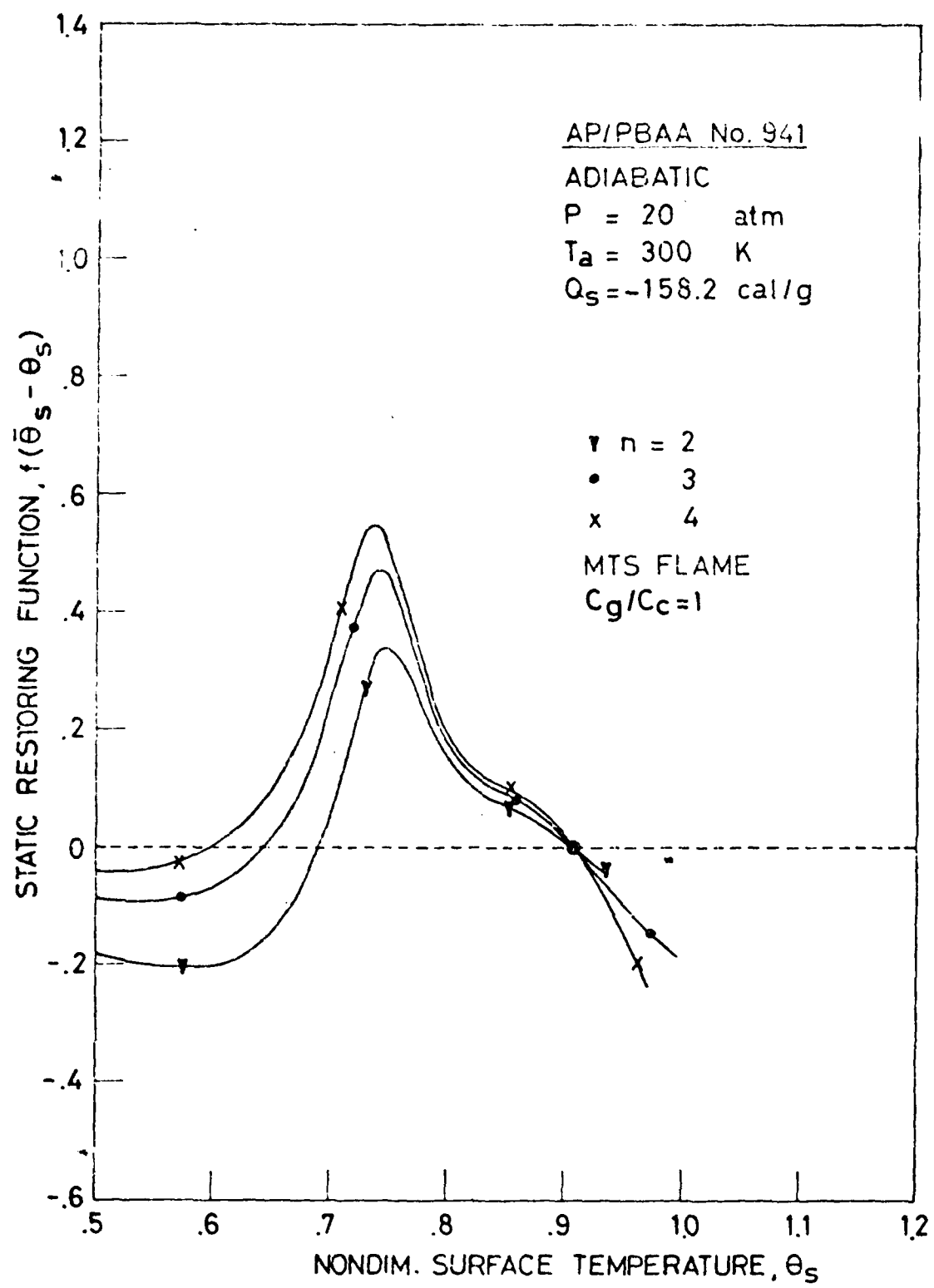


FIG. 24

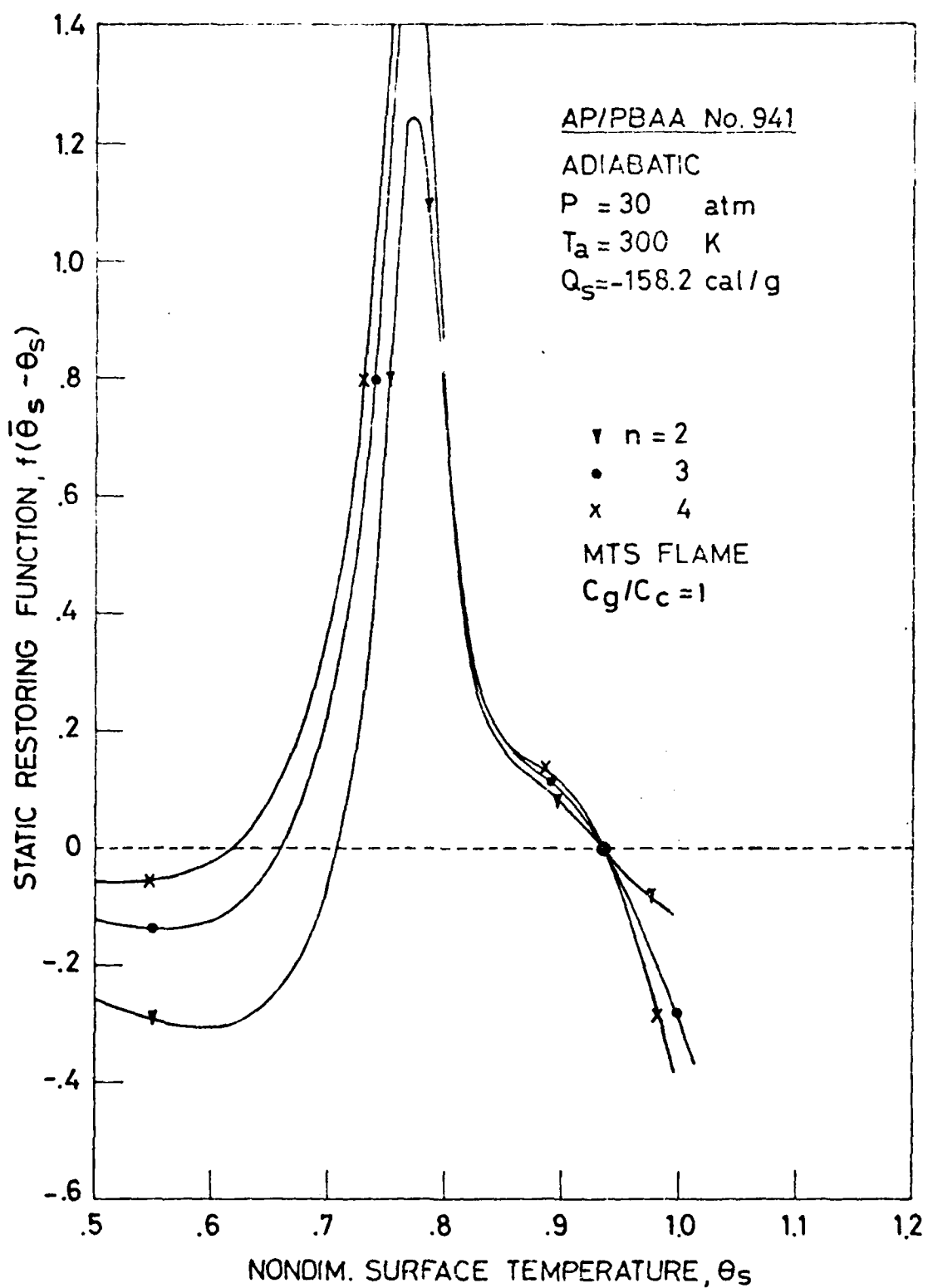


FIG. 25

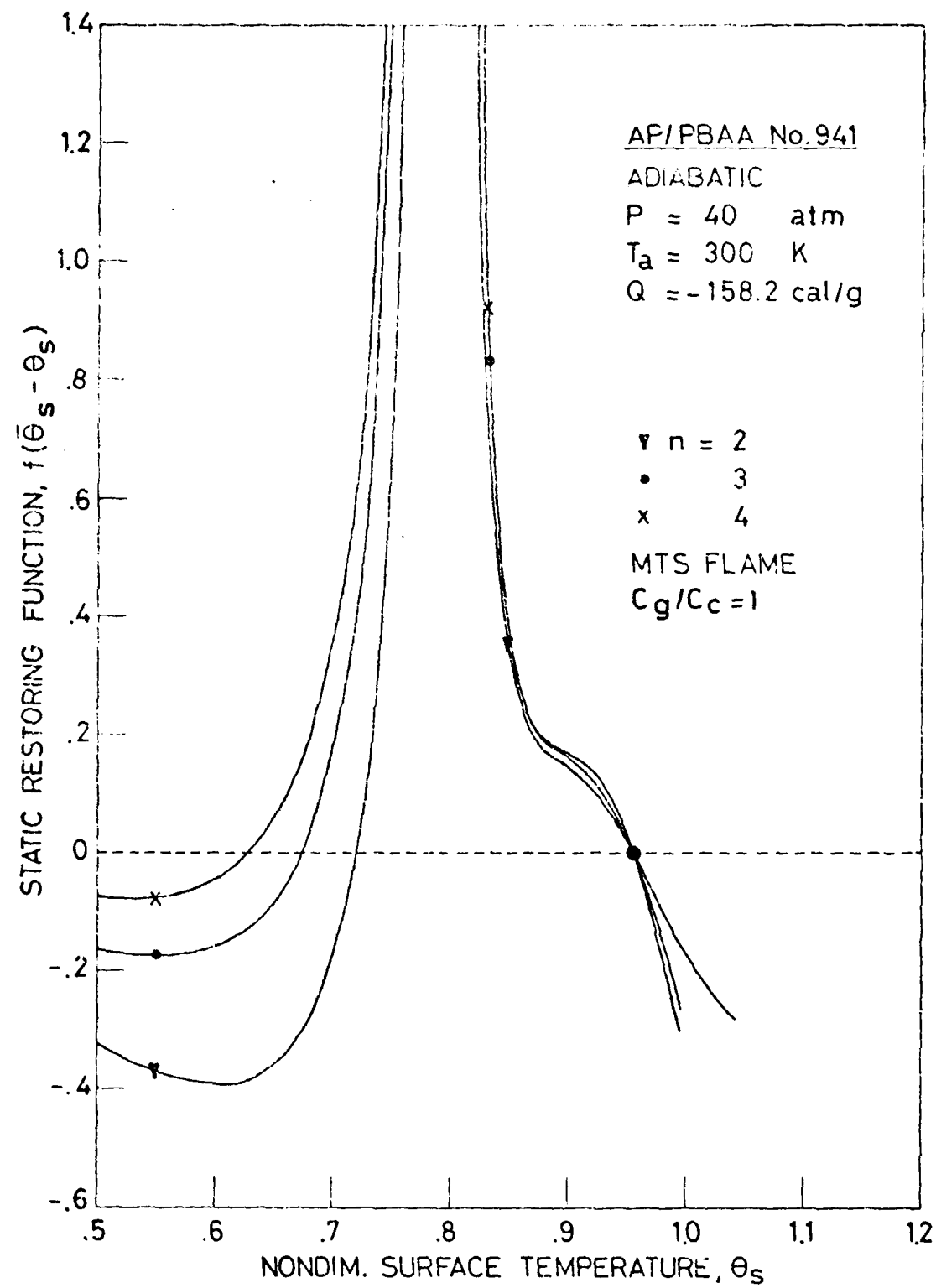


FIG 26

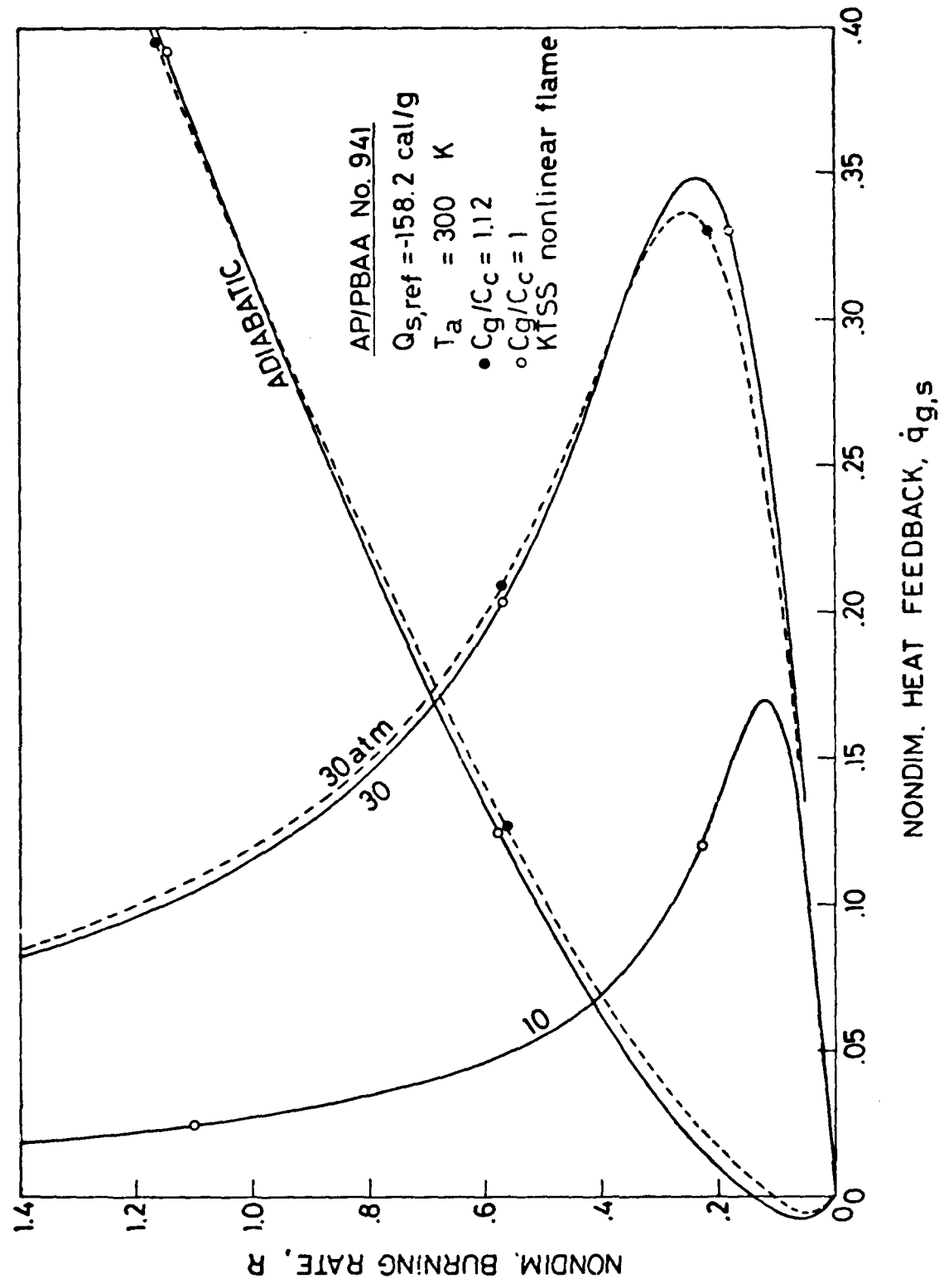


FIG. 17

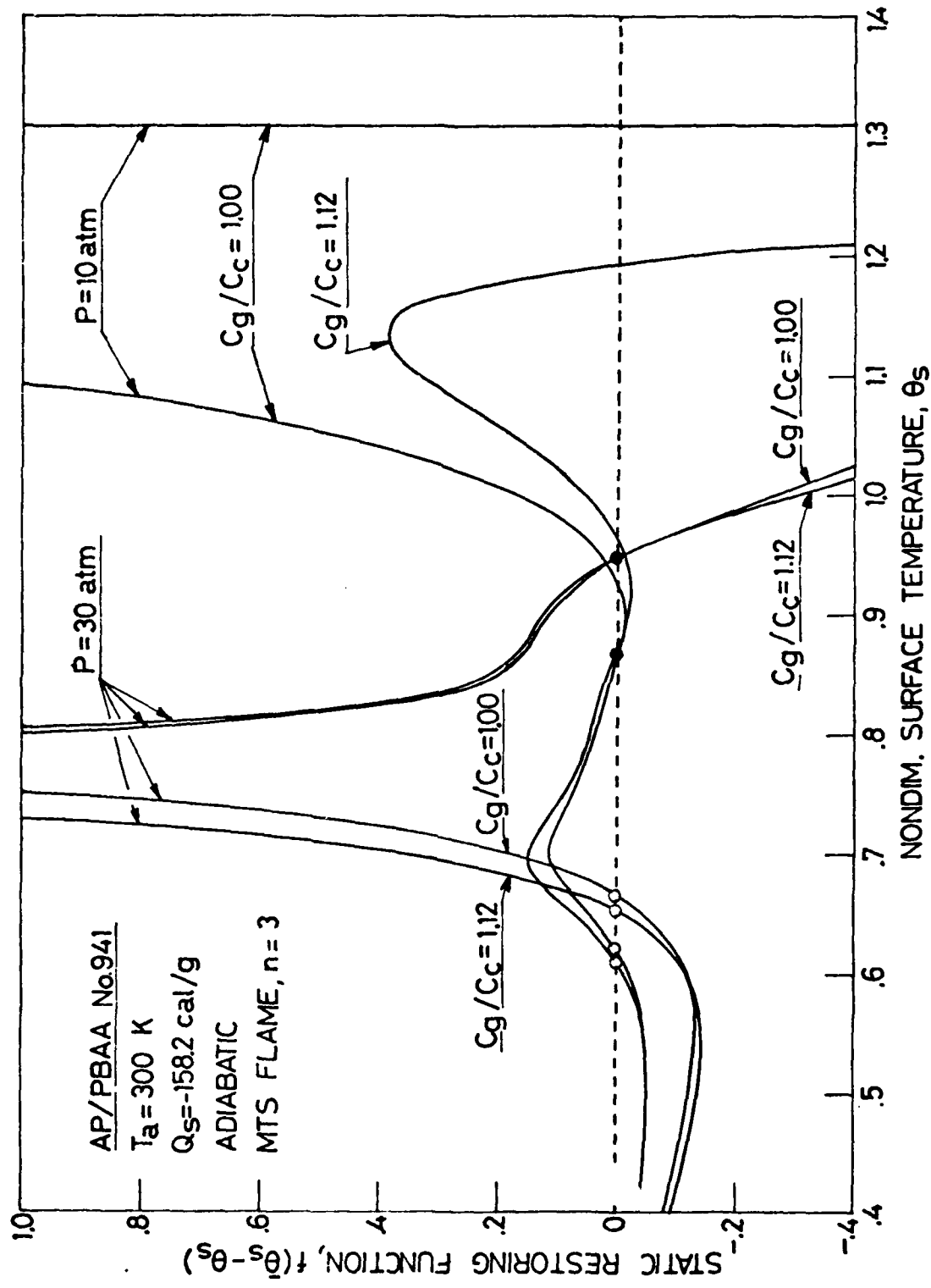


FIG. 28

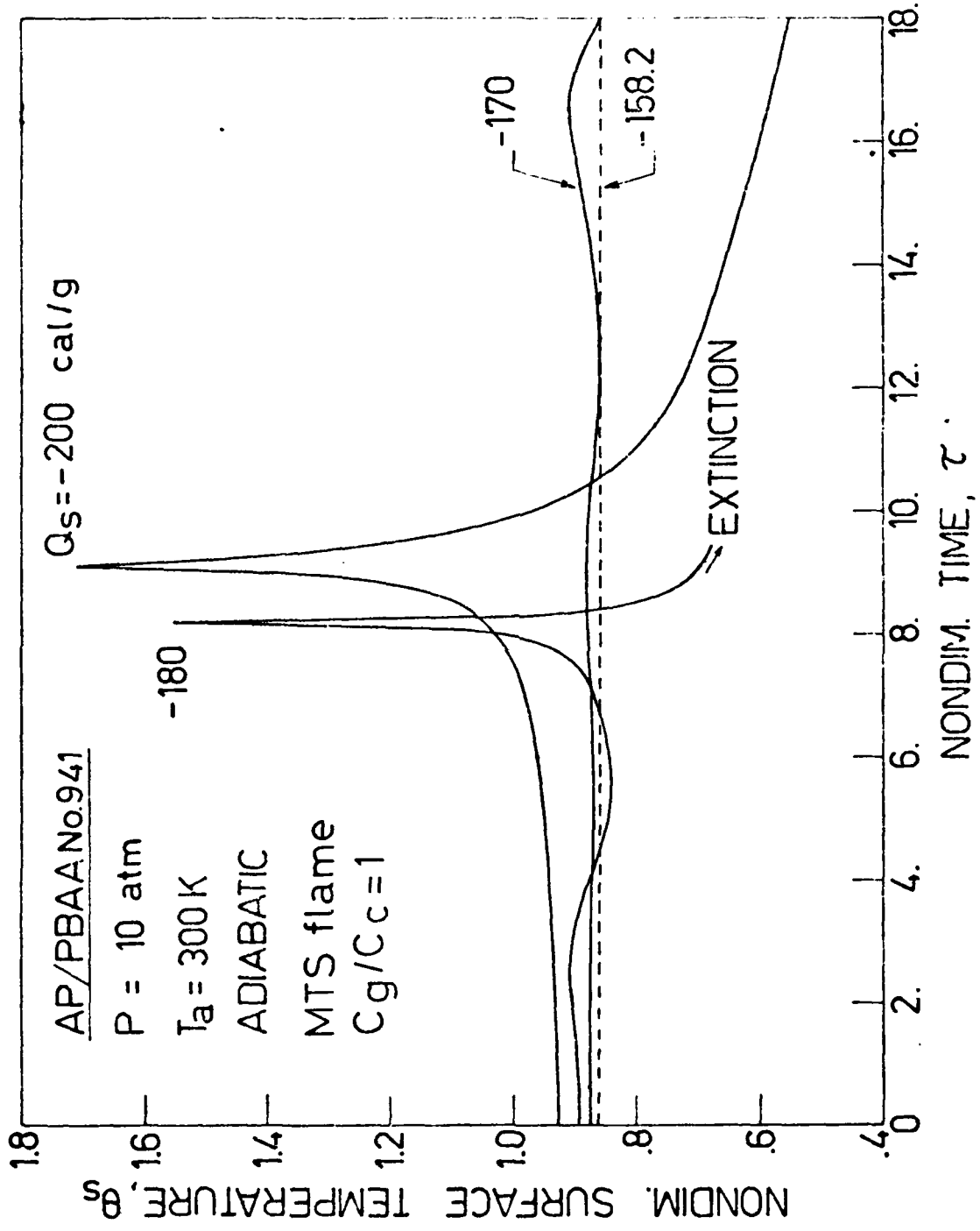


FIG. 29

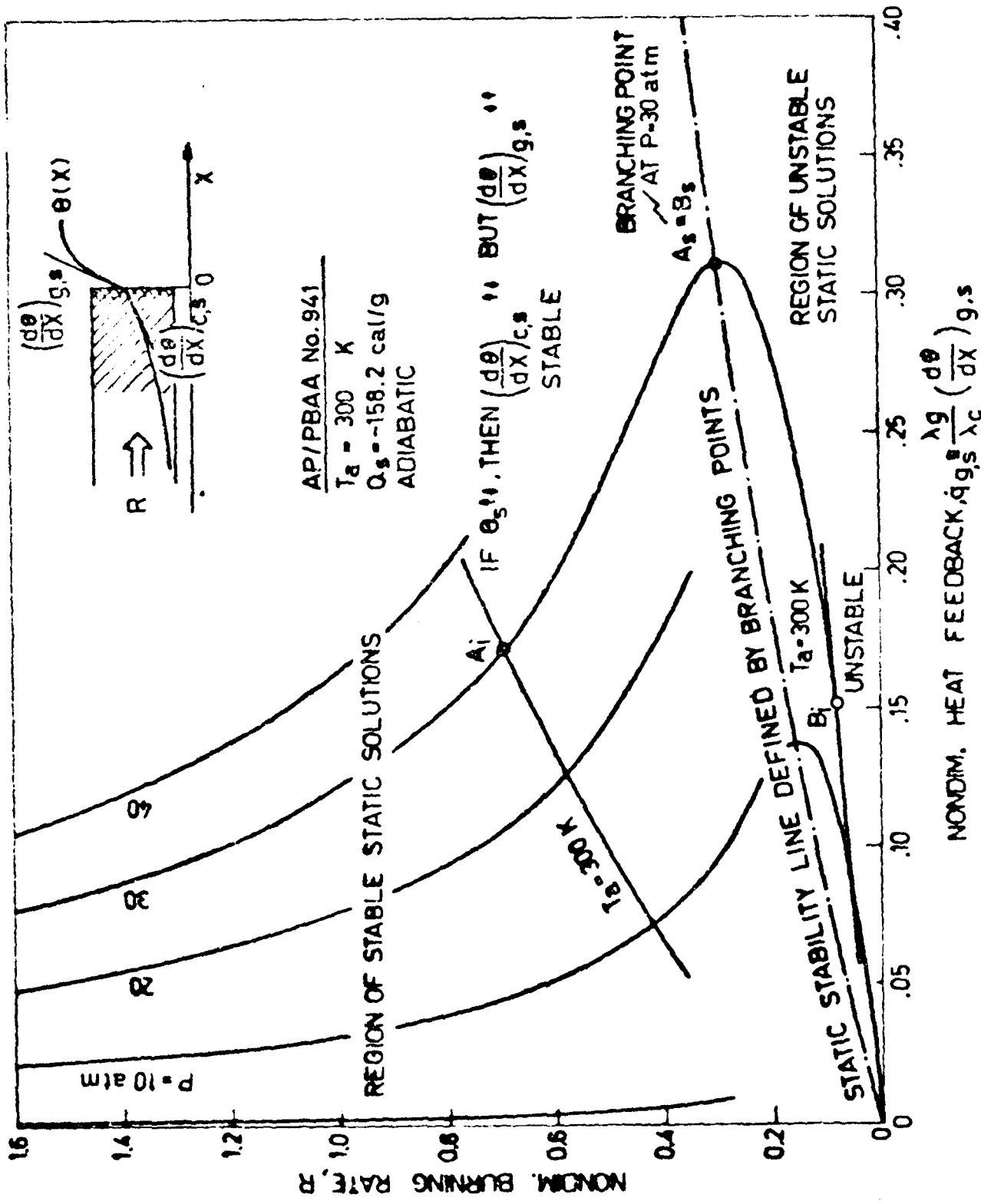


FIG. 30

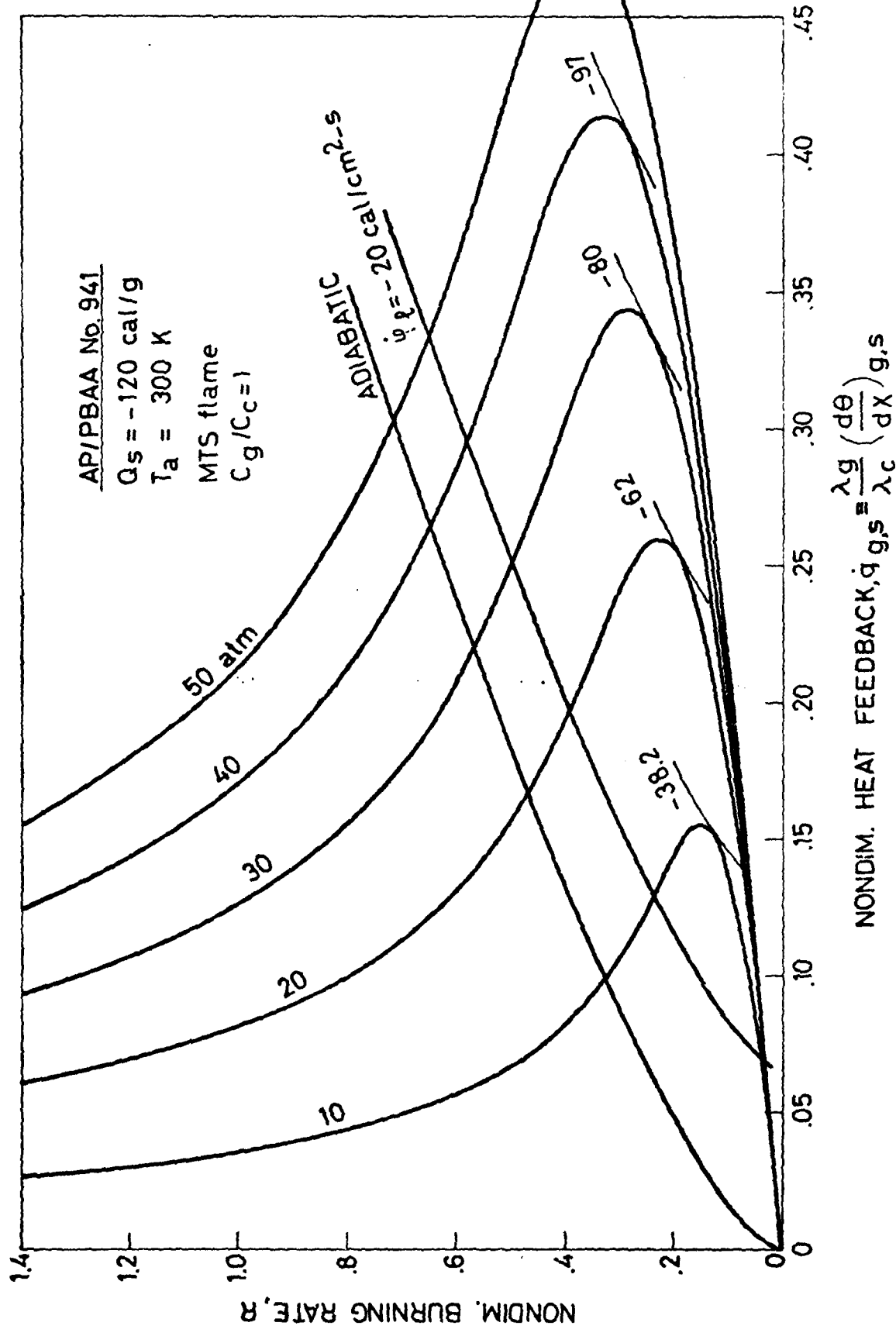


Fig. 31

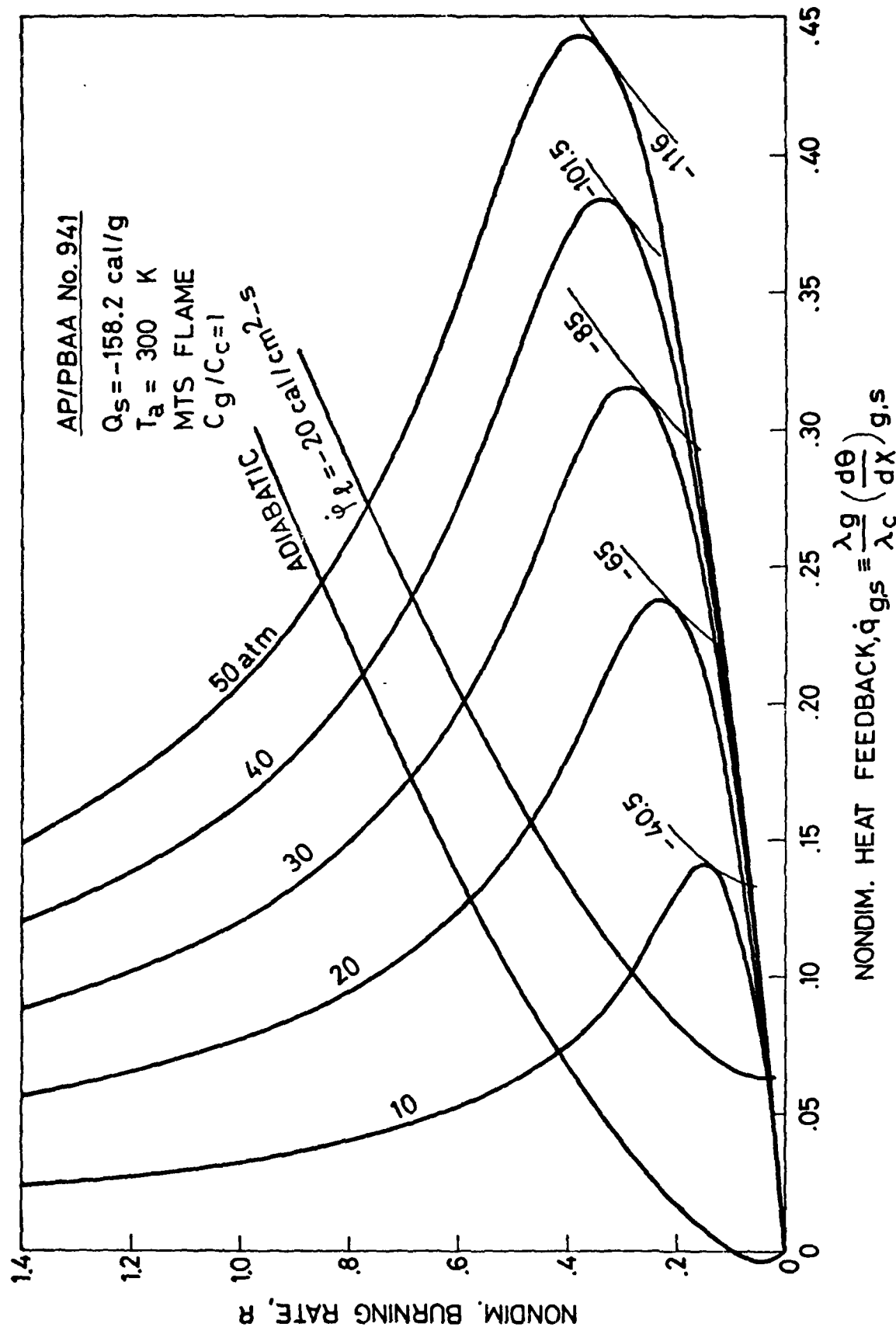


FIG. 2

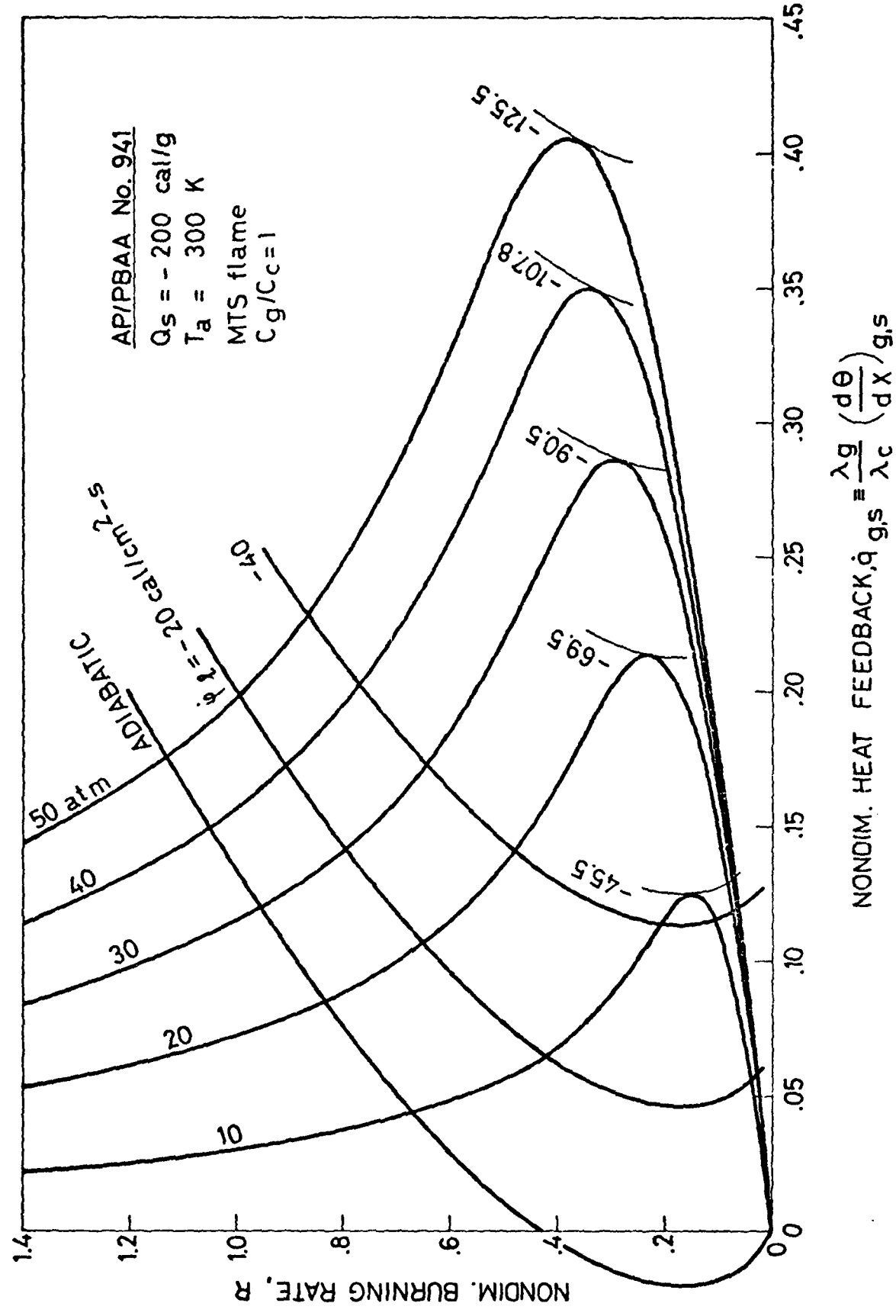


FIG. 33

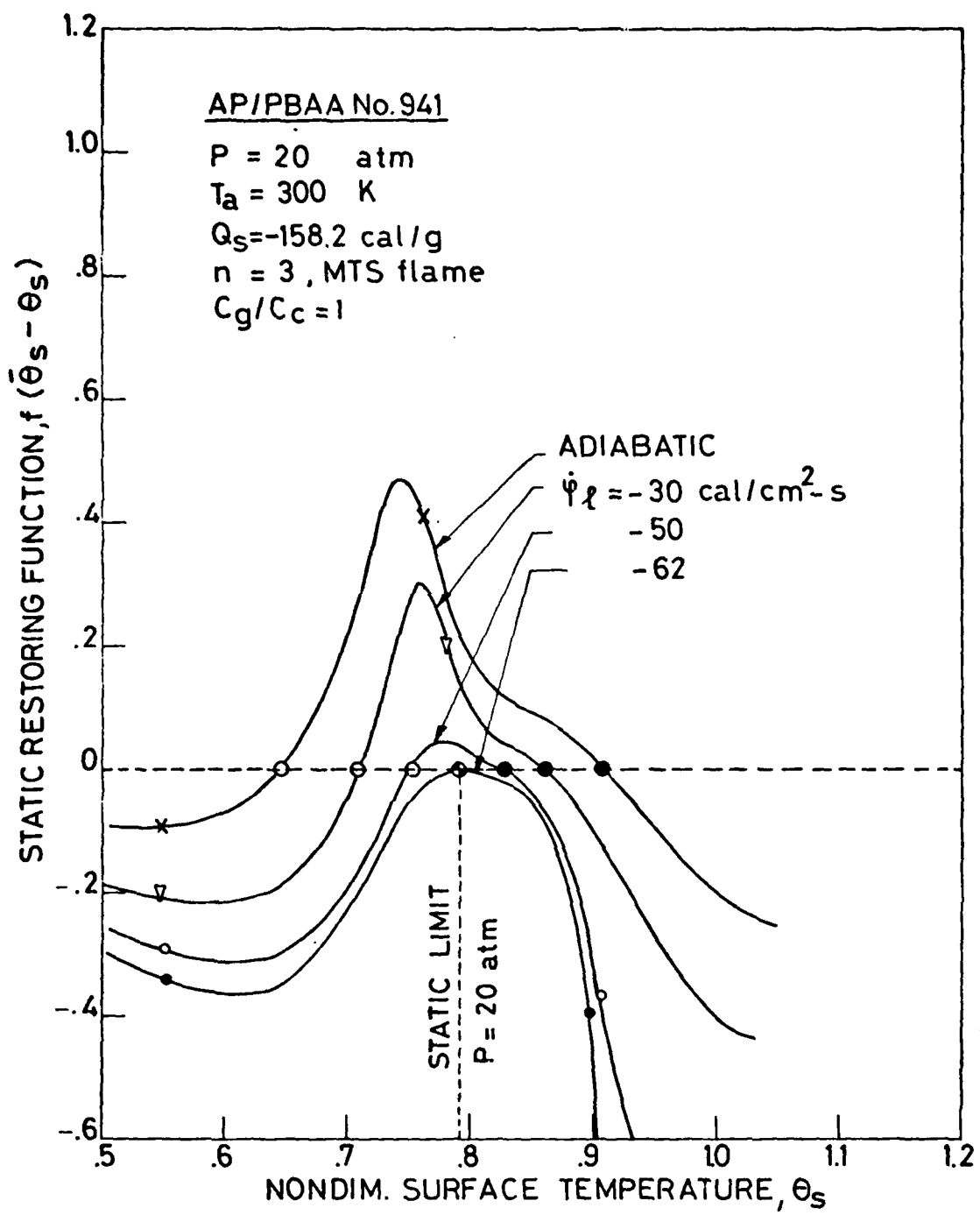


FIG. 34

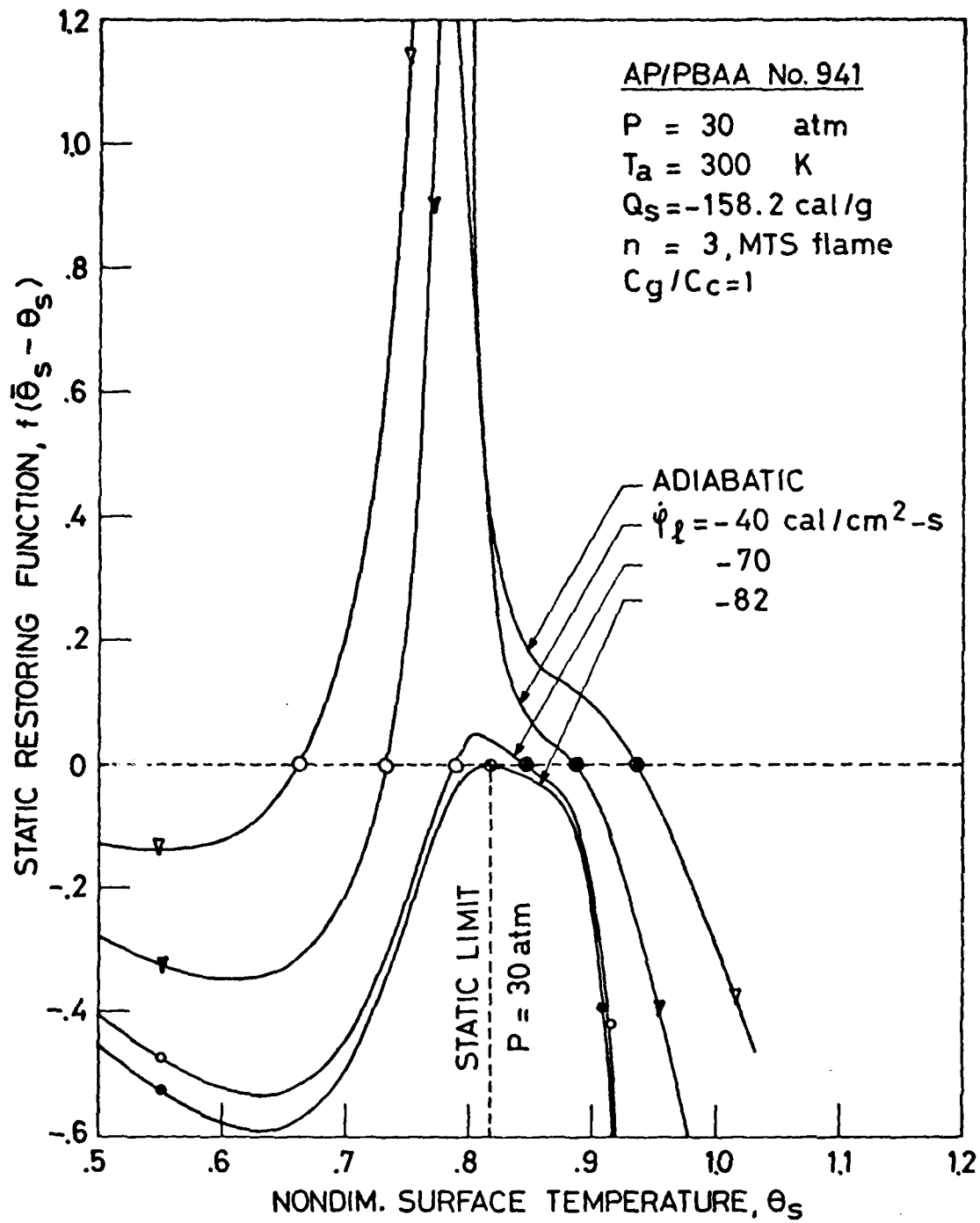


FIG. 35

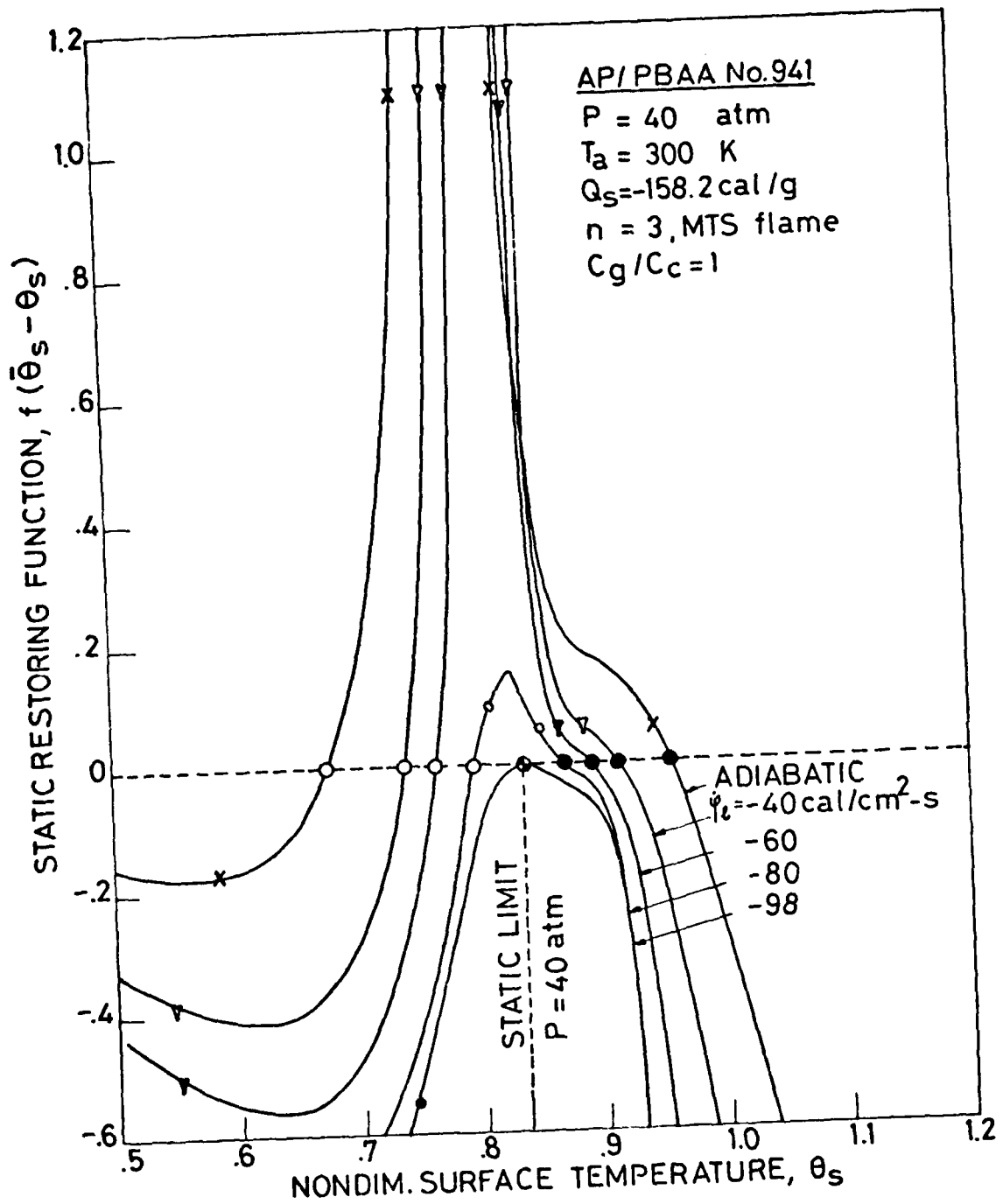


FIG. 36

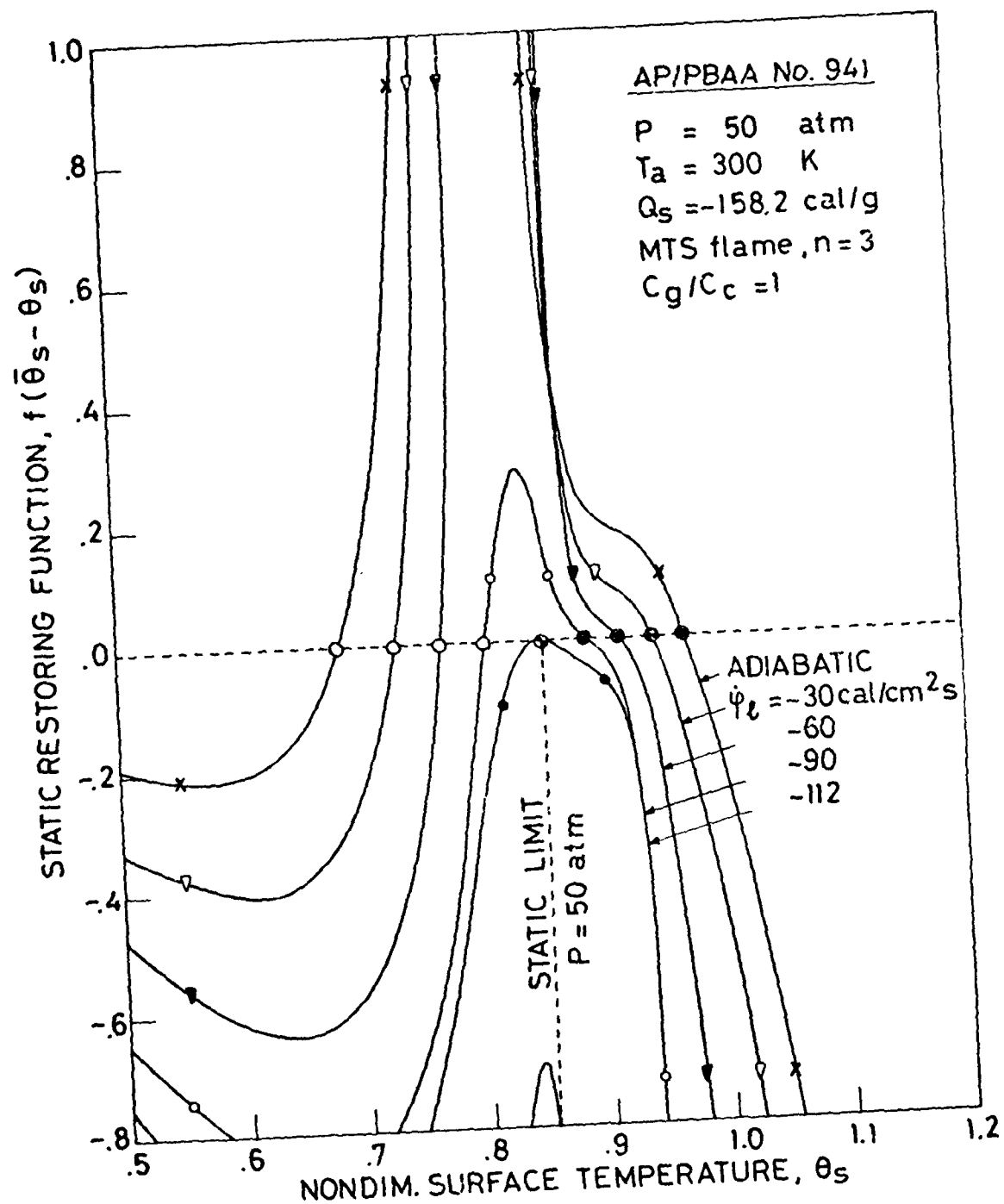
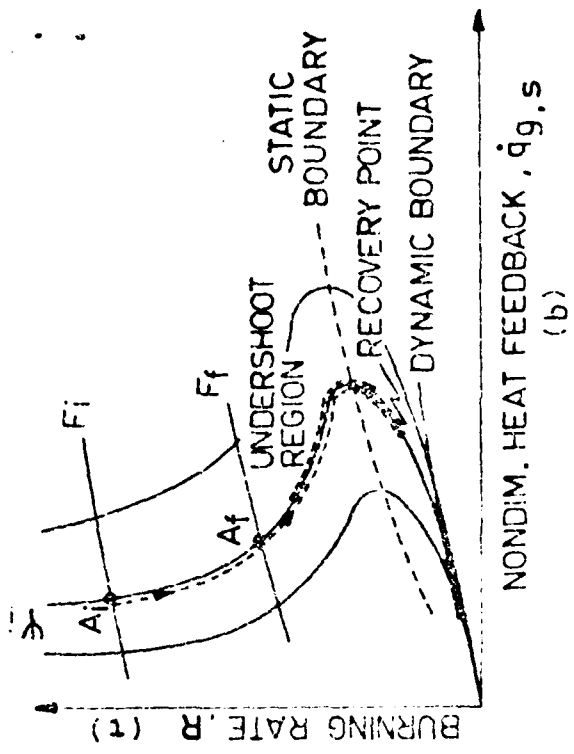


FIG. 37



NONDIM. HEAT FEEDBACK,  $q_g.s$

(b)

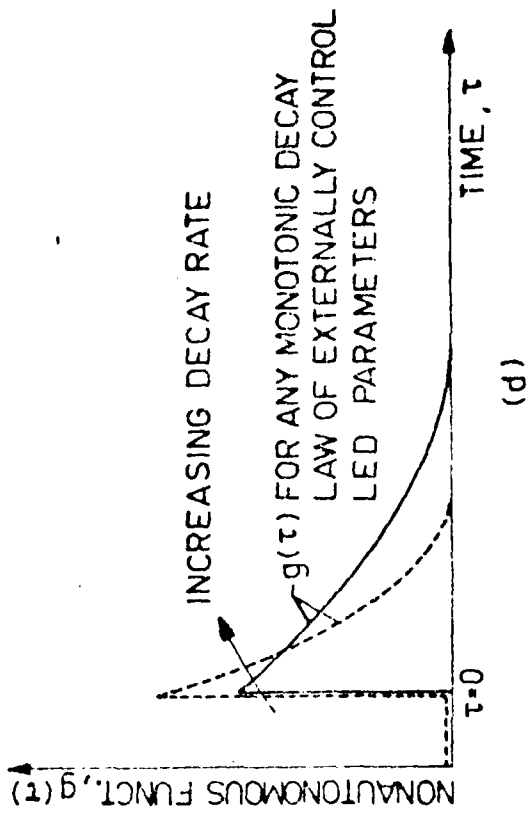
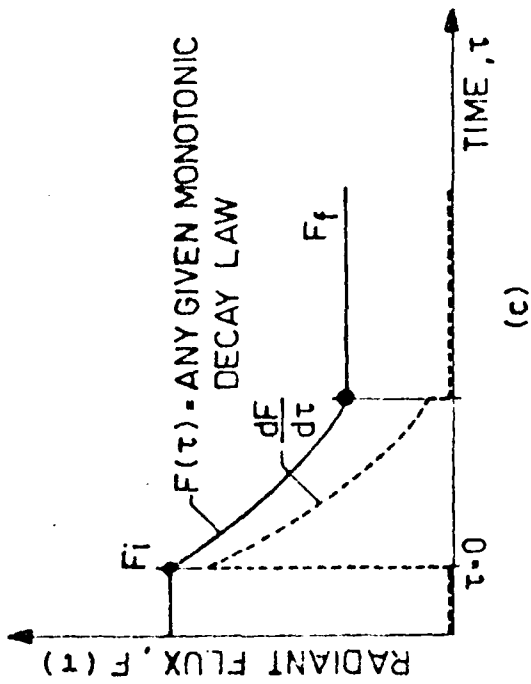


FIG. 3.5

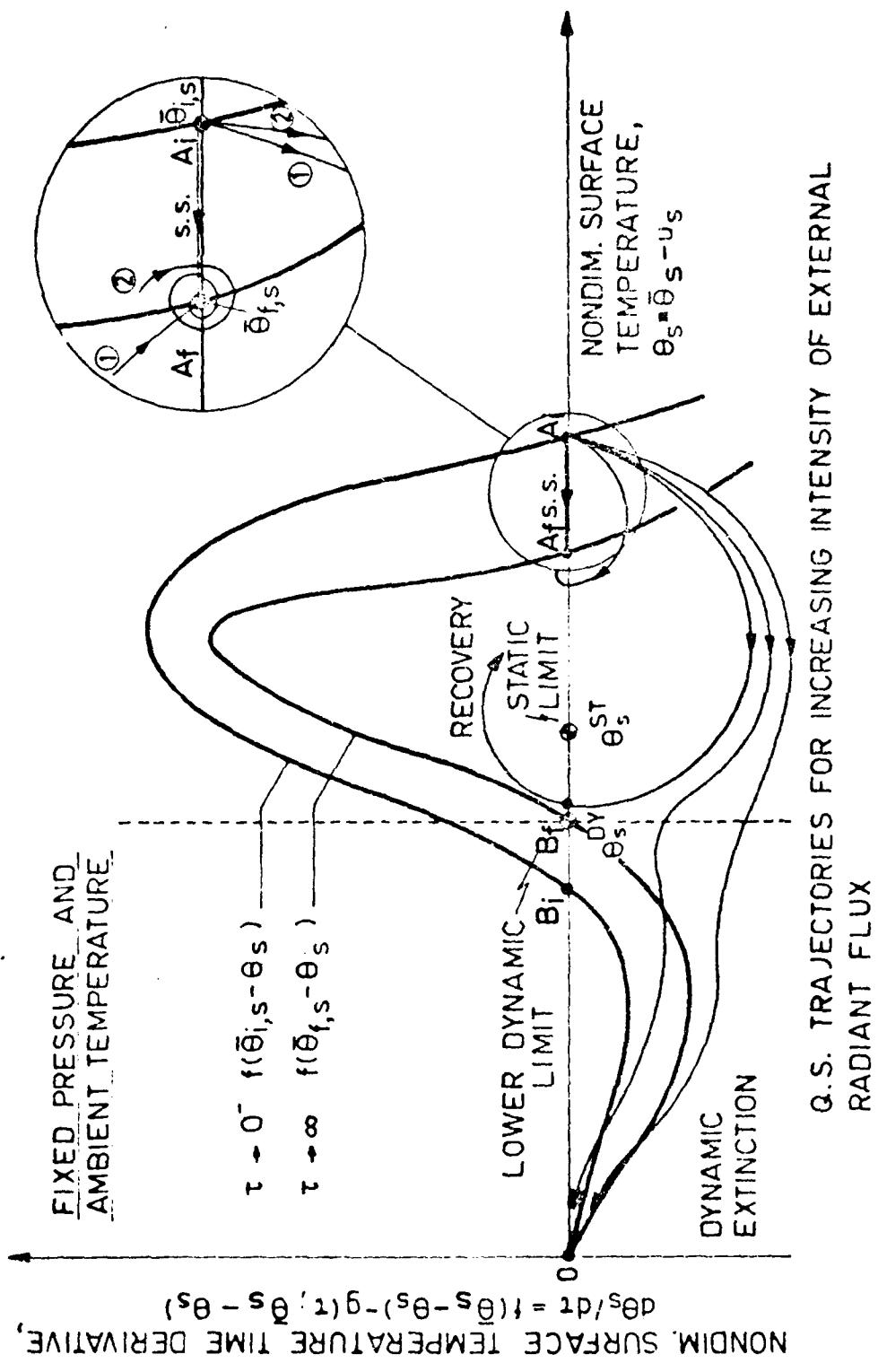


FIG. 32

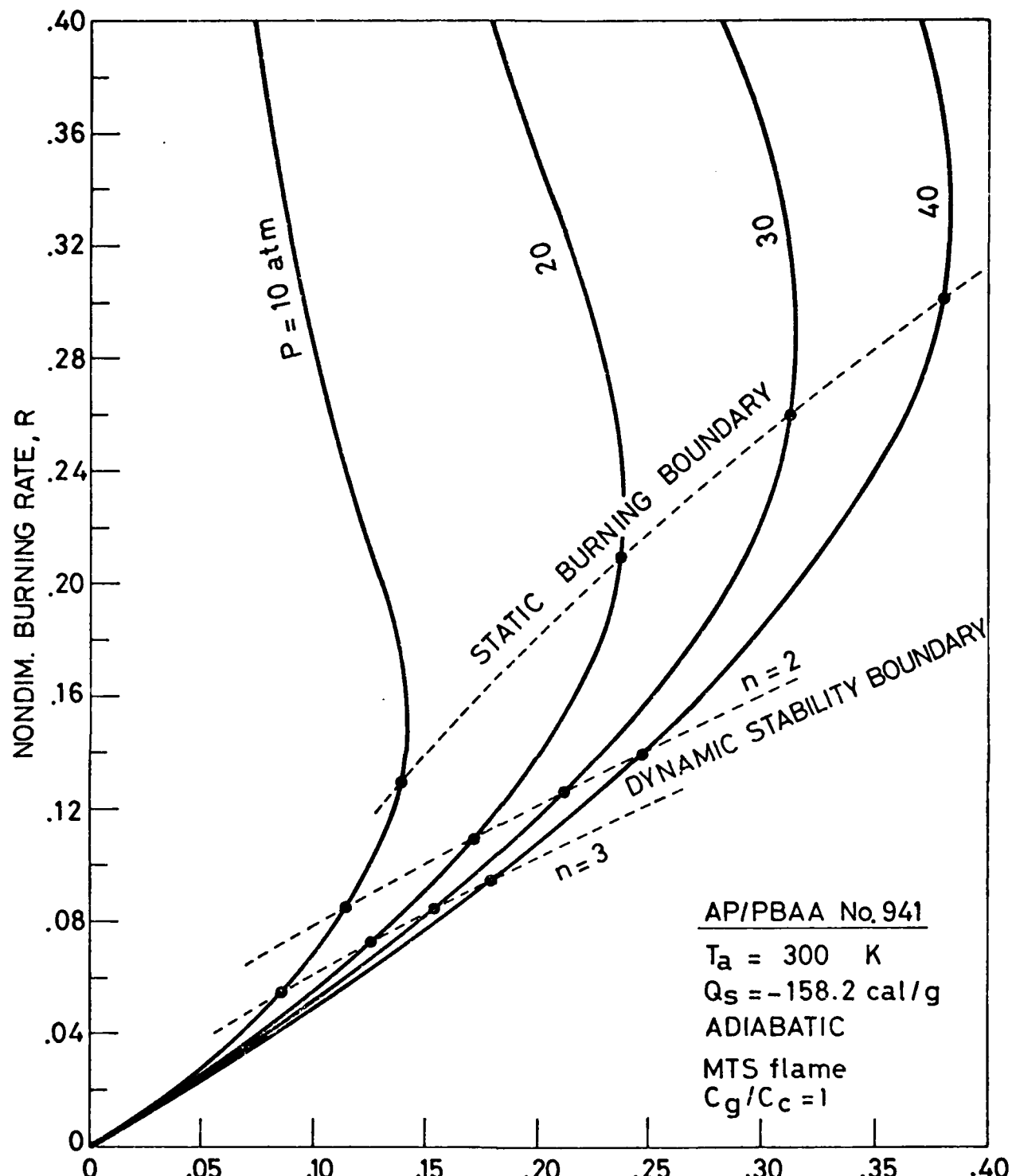


FIG. 40

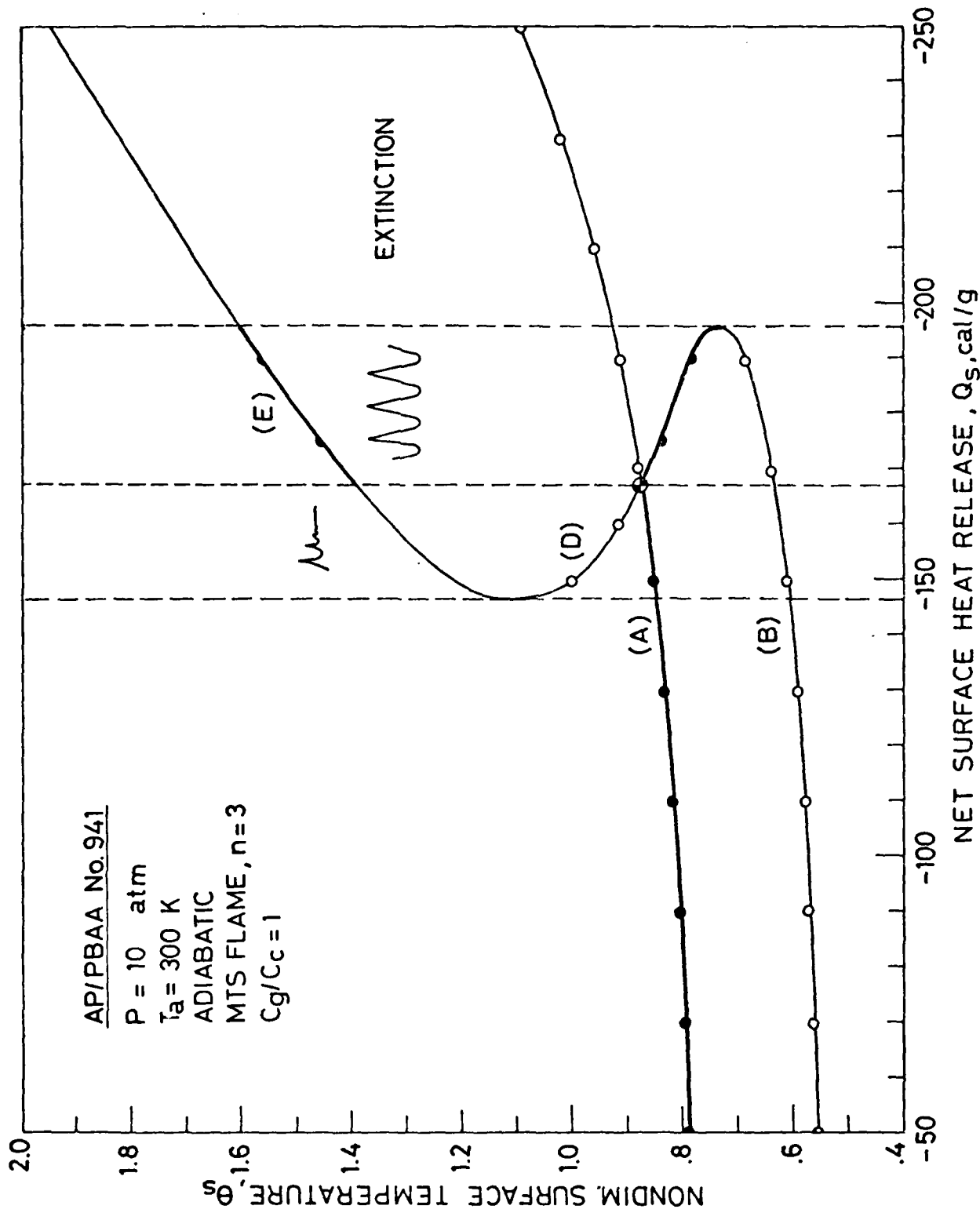


FIG. 41

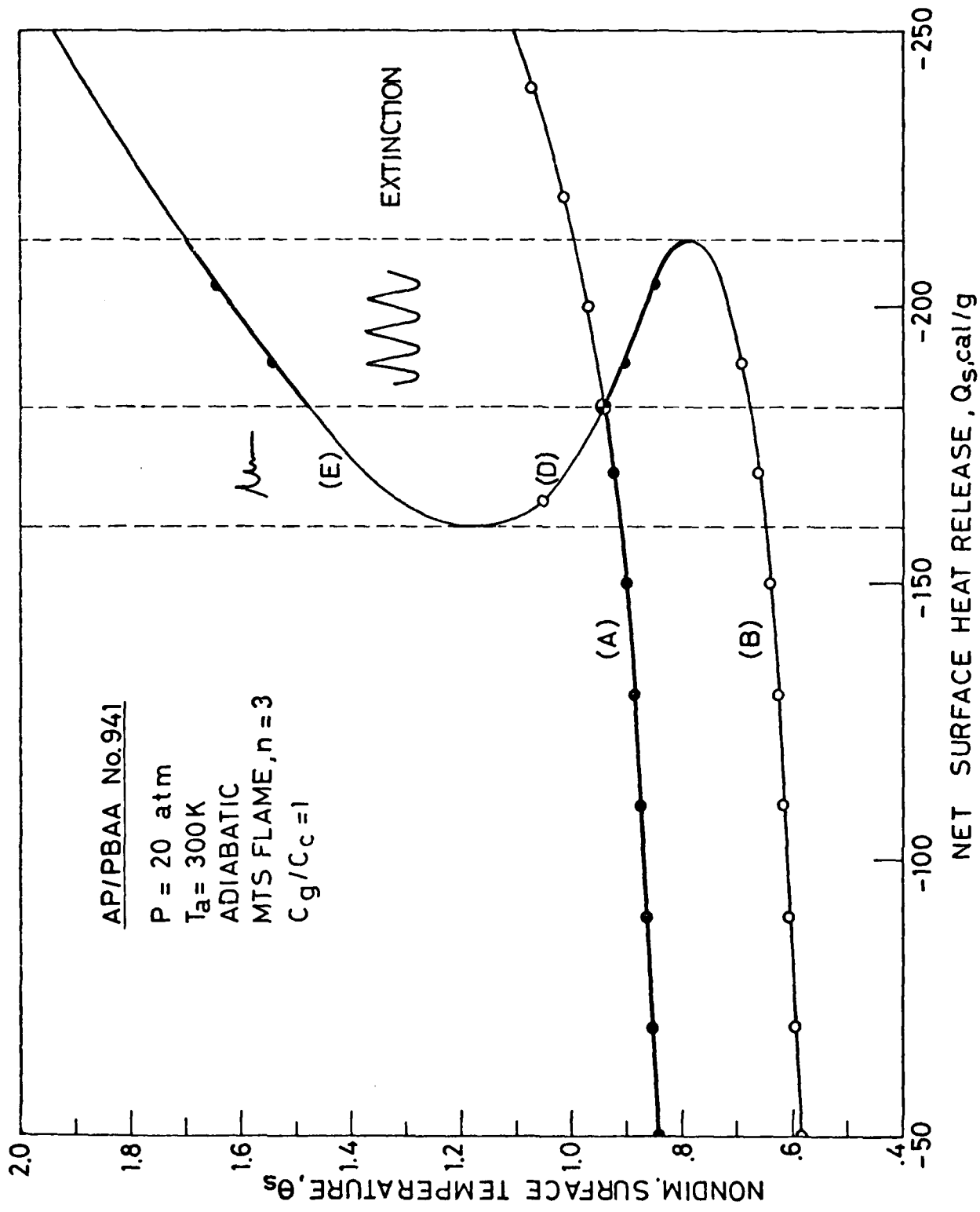


FIG. 42

AP/PBAA No. 941

$P = 30$  atm

$T_a = 300$  K

ADIABATIC

MTS FLAME,  $n=3$

$C_g/C_c = 1$

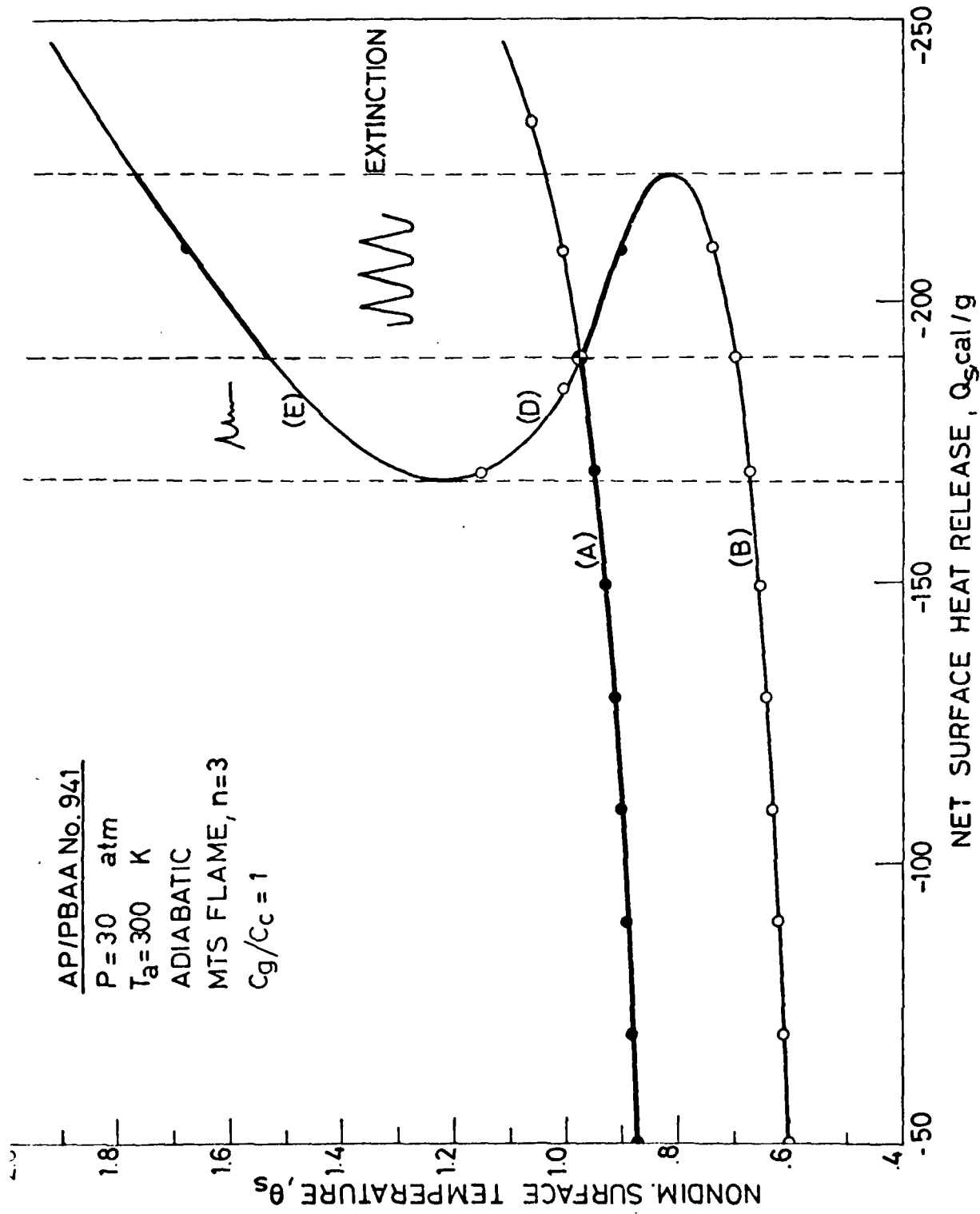


FIG. 43

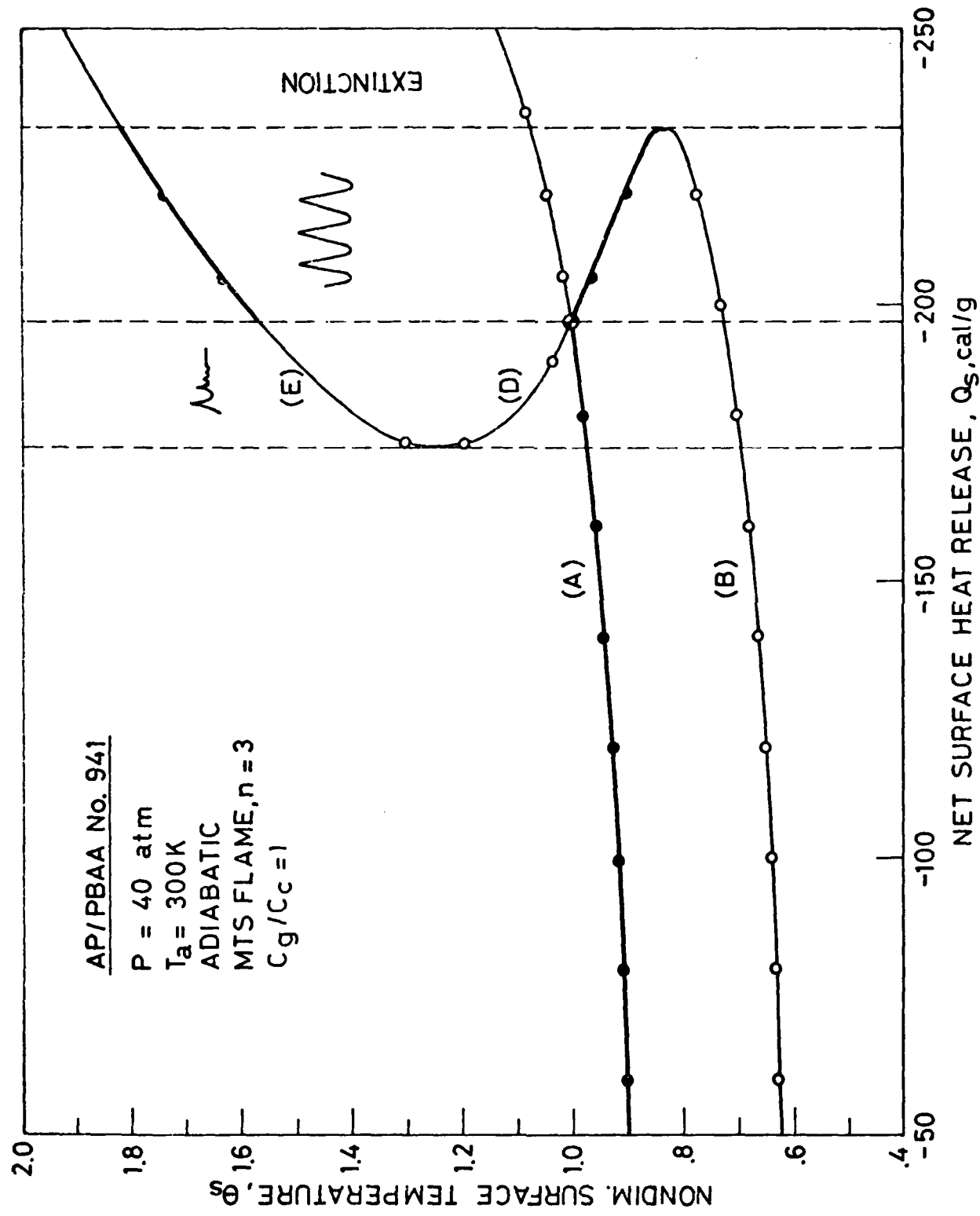


FIG. 4.4

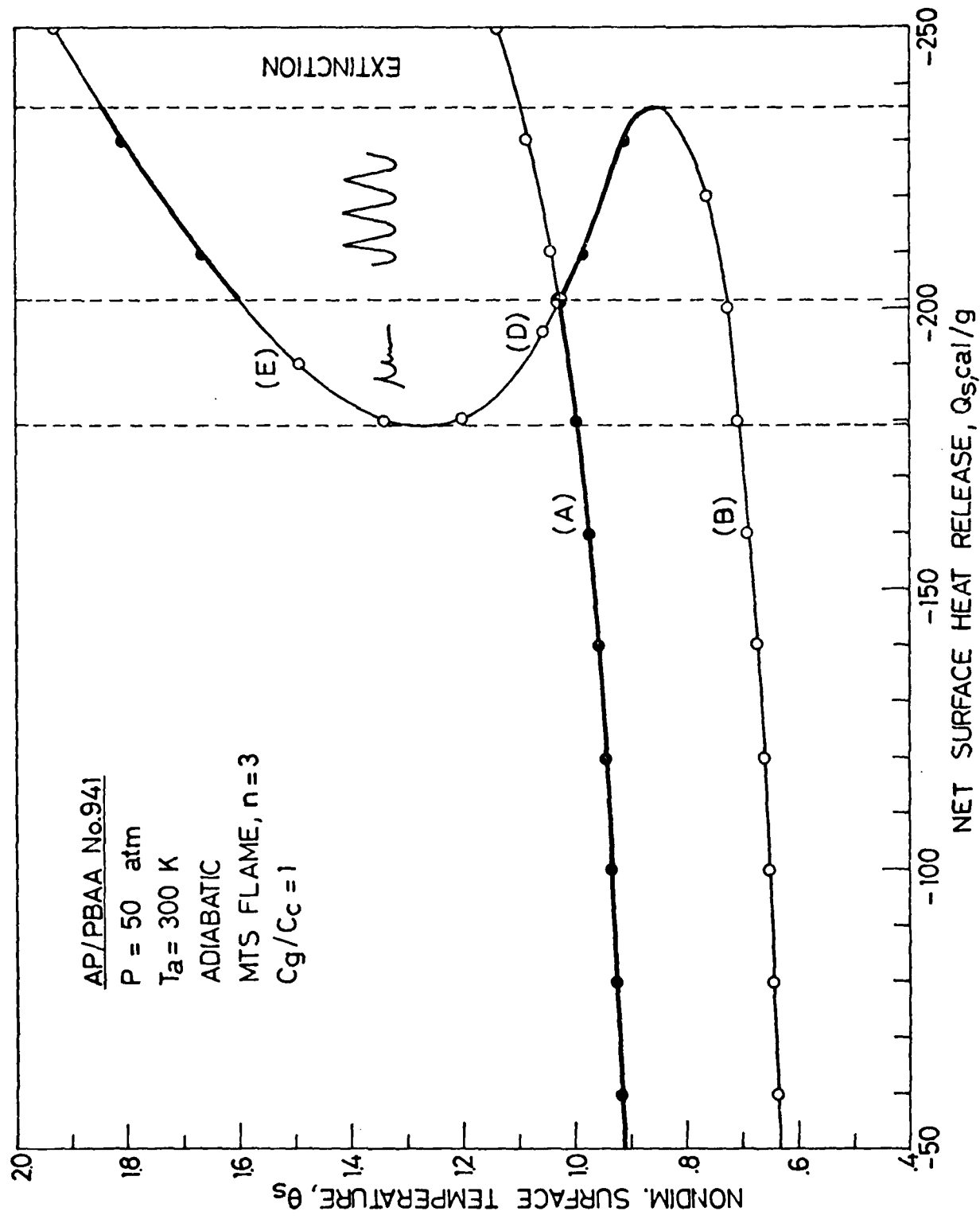


FIG. 45

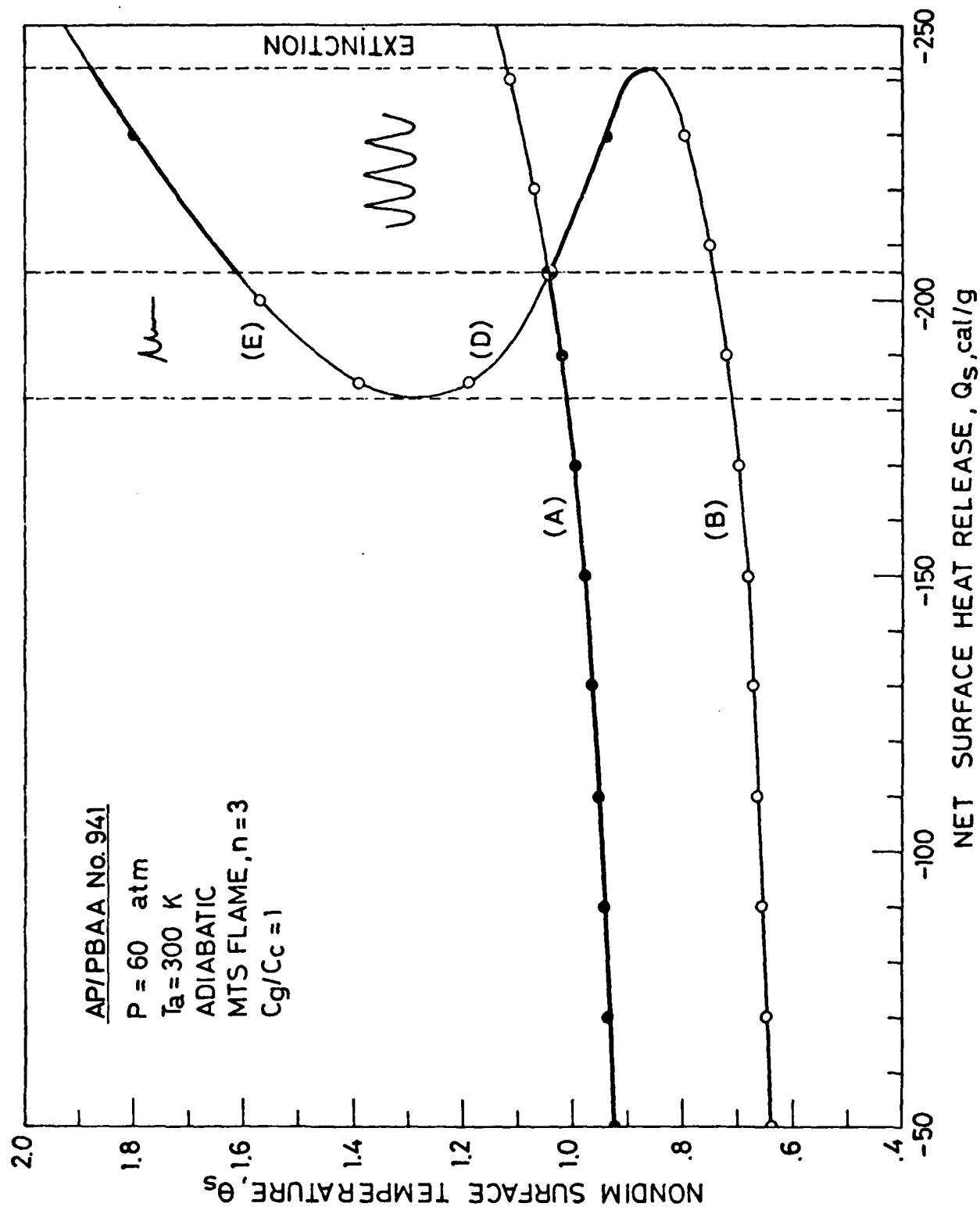


FIG. 46

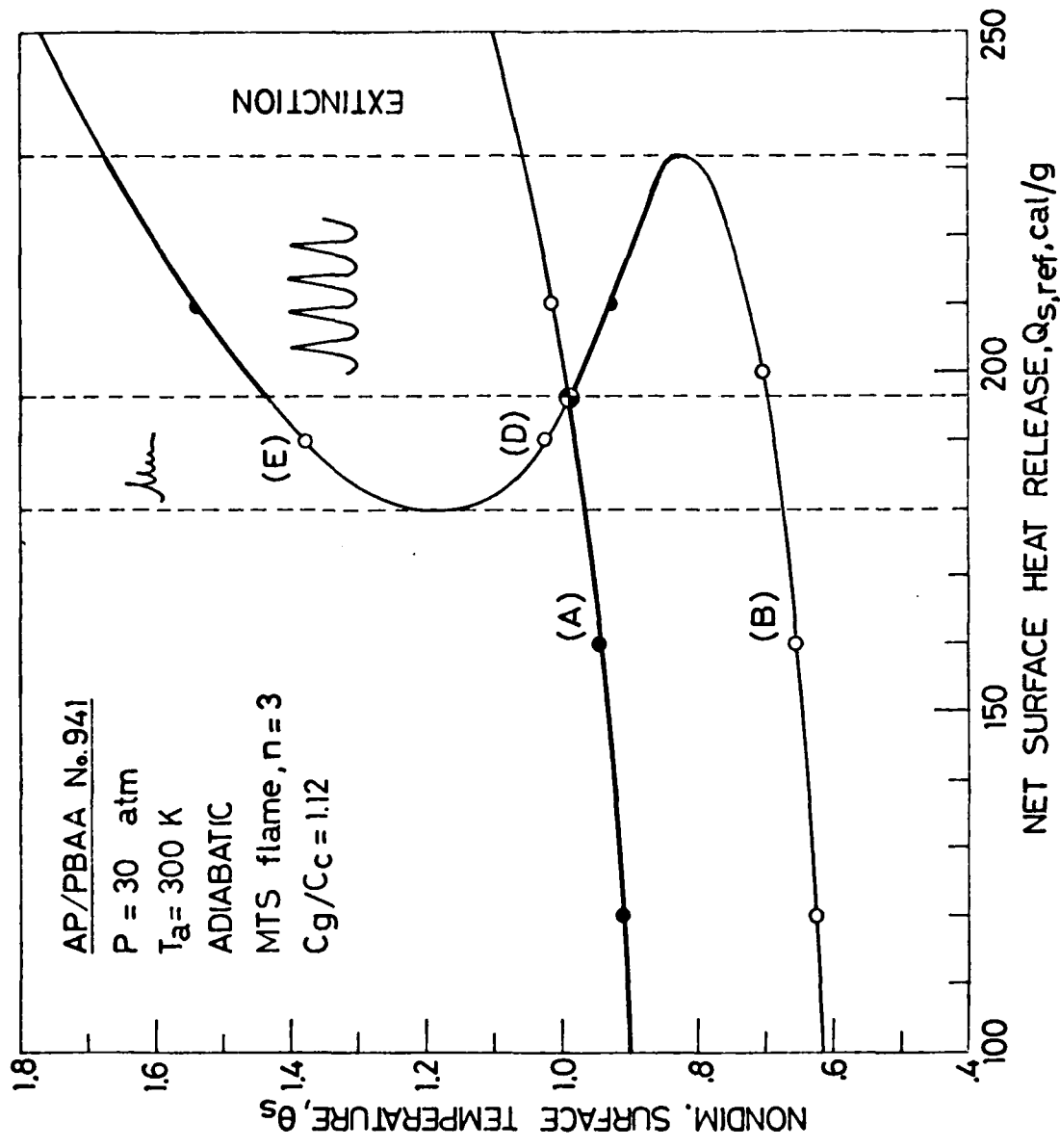


FIG. 47

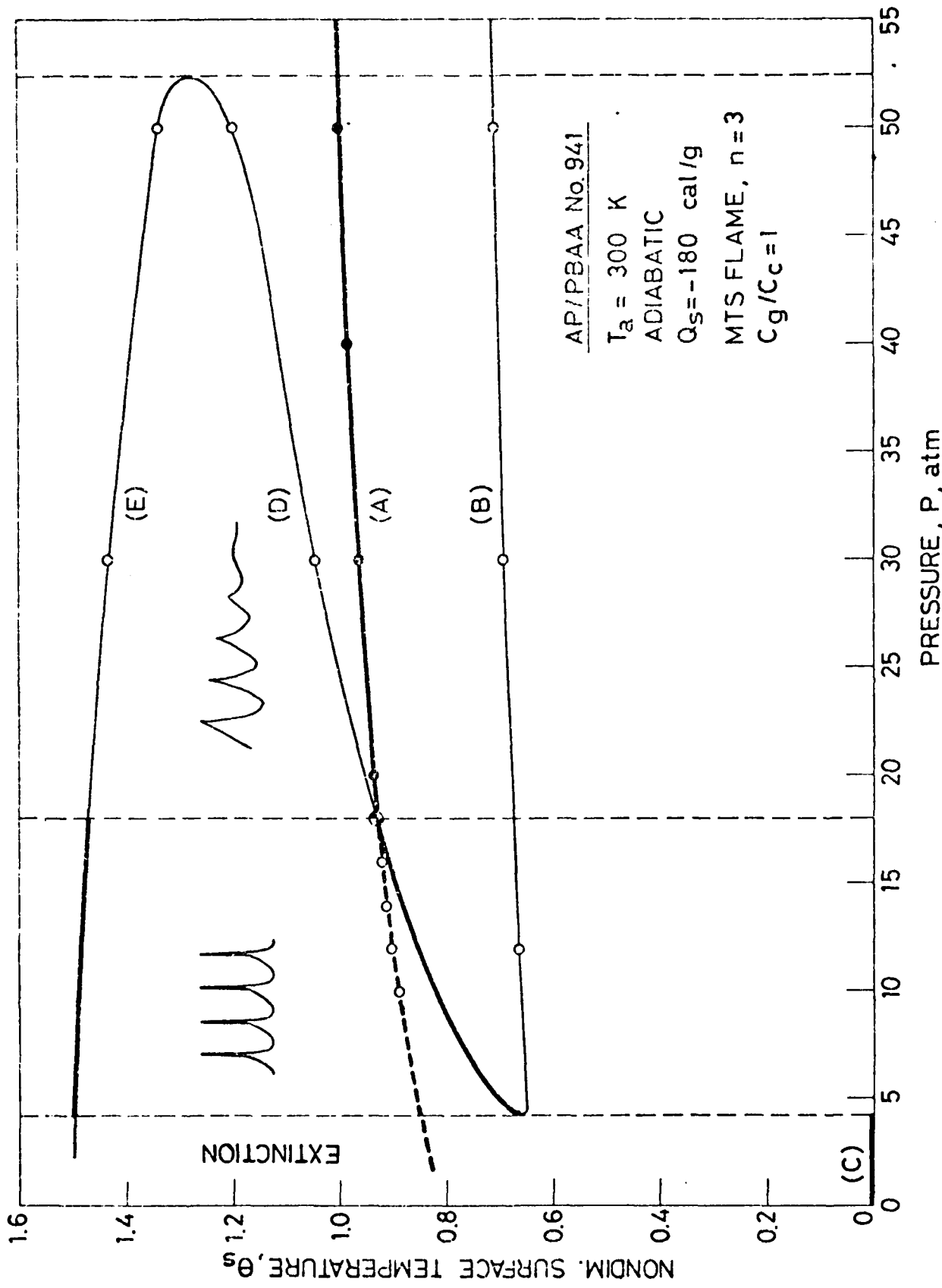


FIG. 4.3

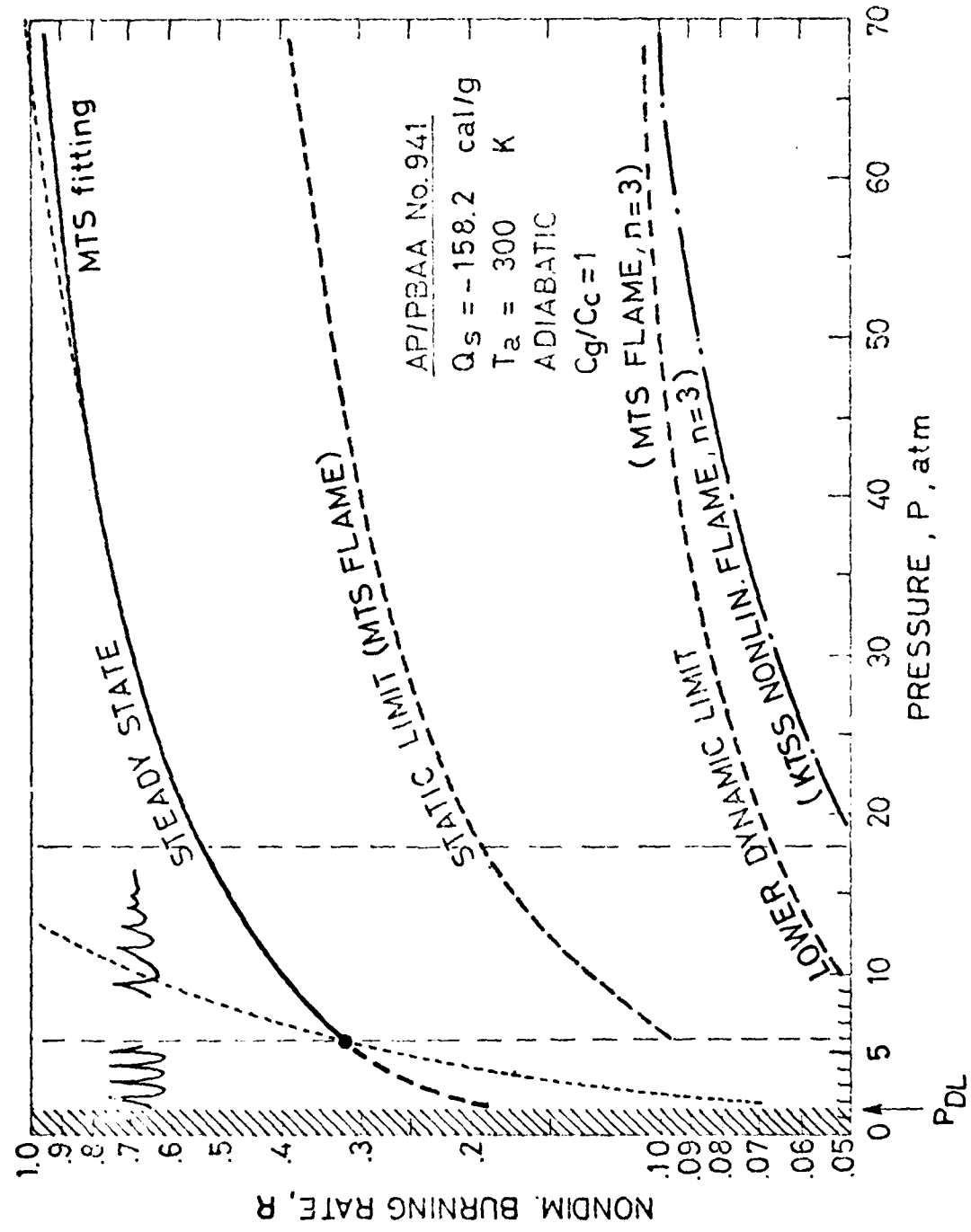
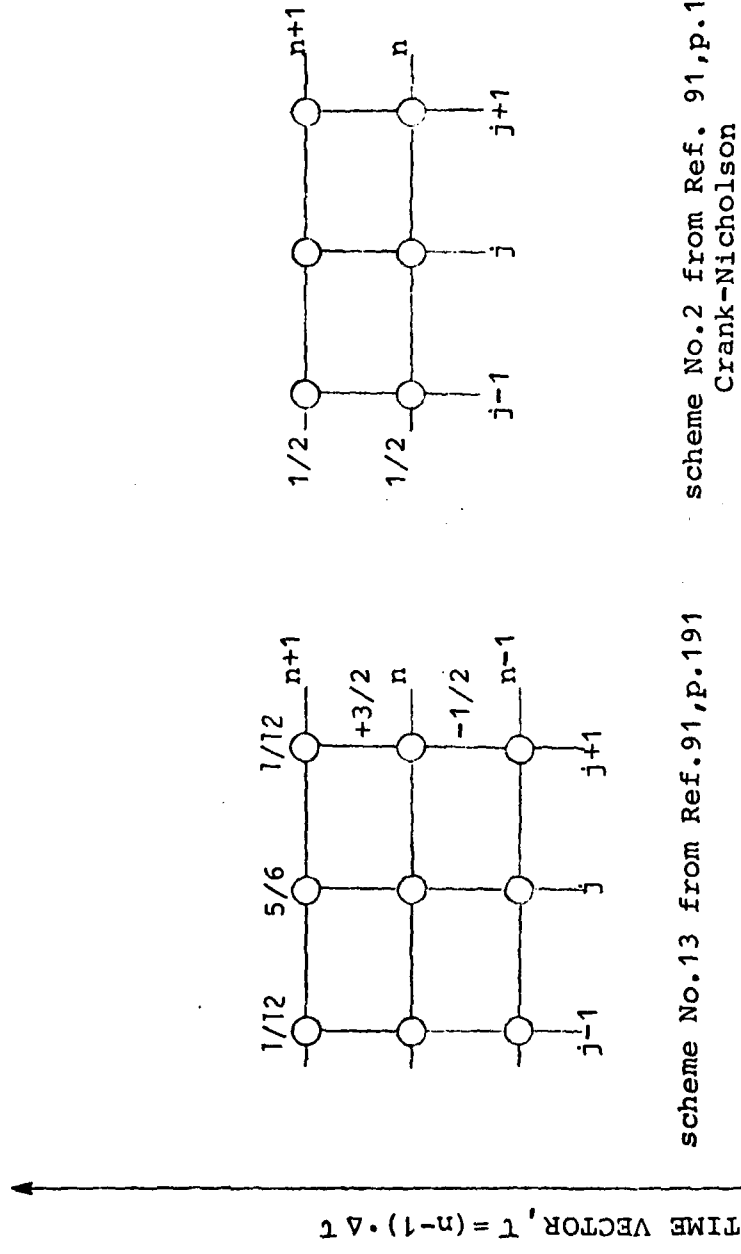


FIG. 10



scheme No. 2 from Ref. 91, p. 189  
Crank-Nicholson

scheme No. 13 from Ref. 91, p. 191

Implicit, always stable  
error =  $[(\Delta t)^2] + o[(\Delta x)^4]$

Fig. 50

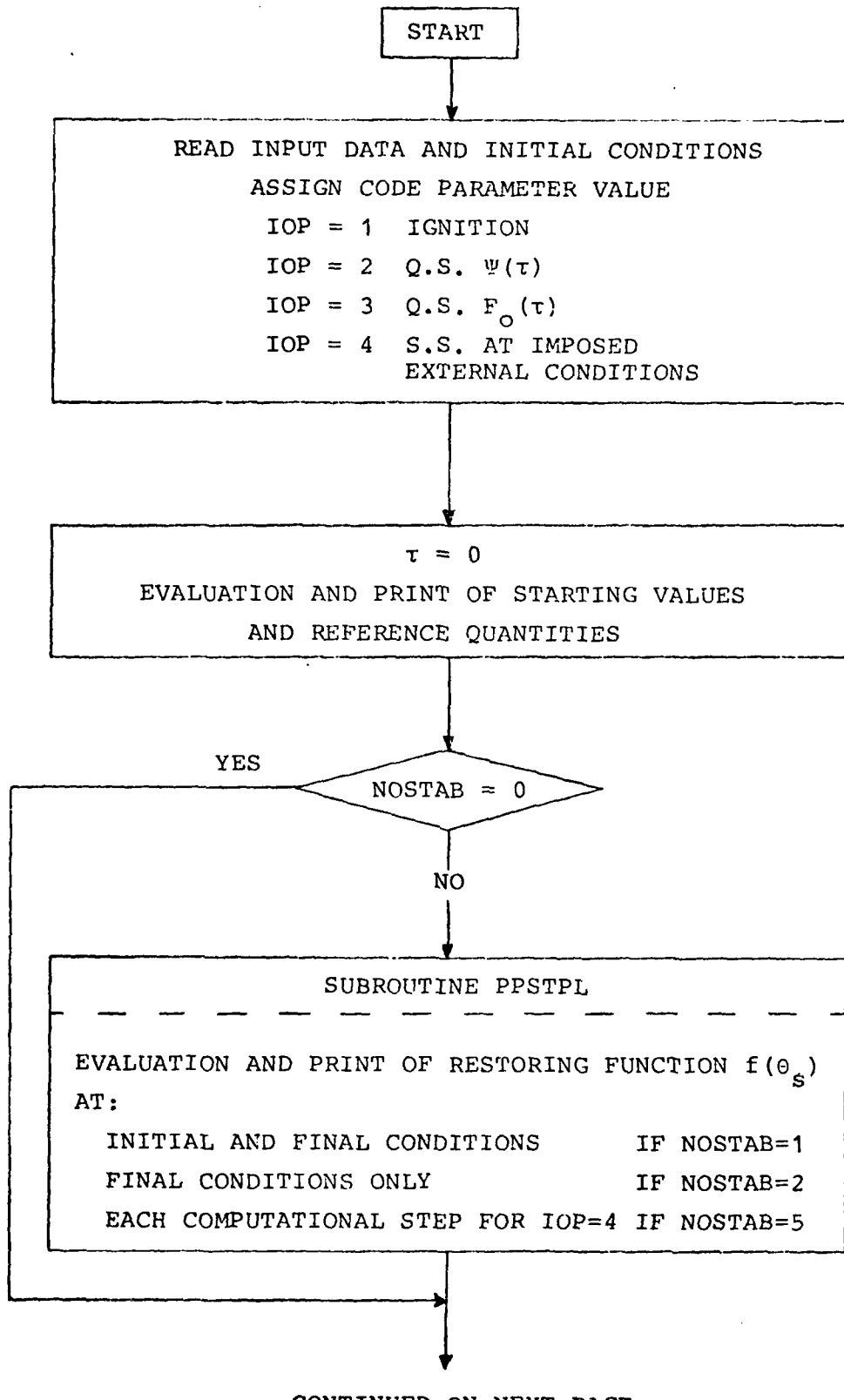
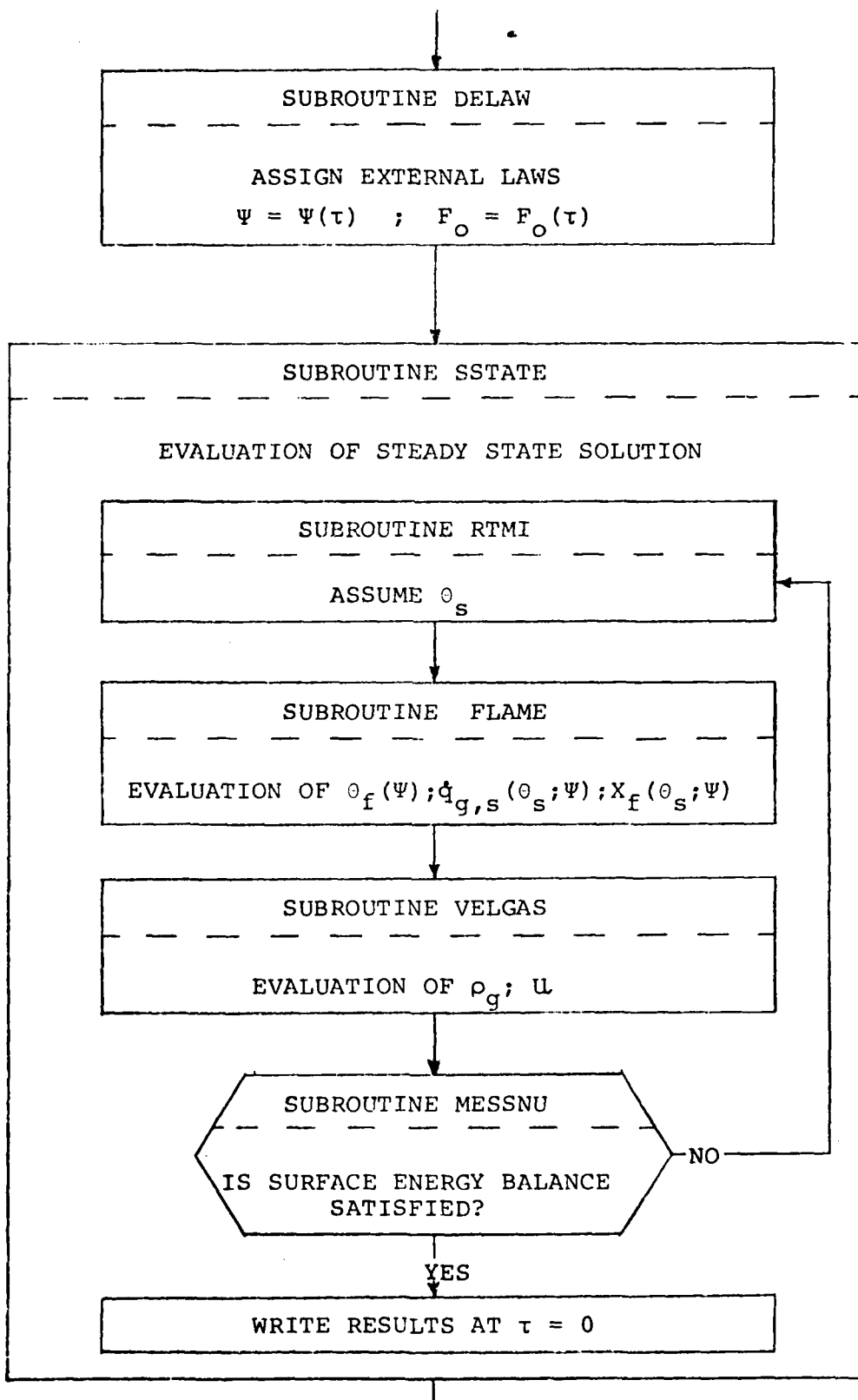


FIG. 51a

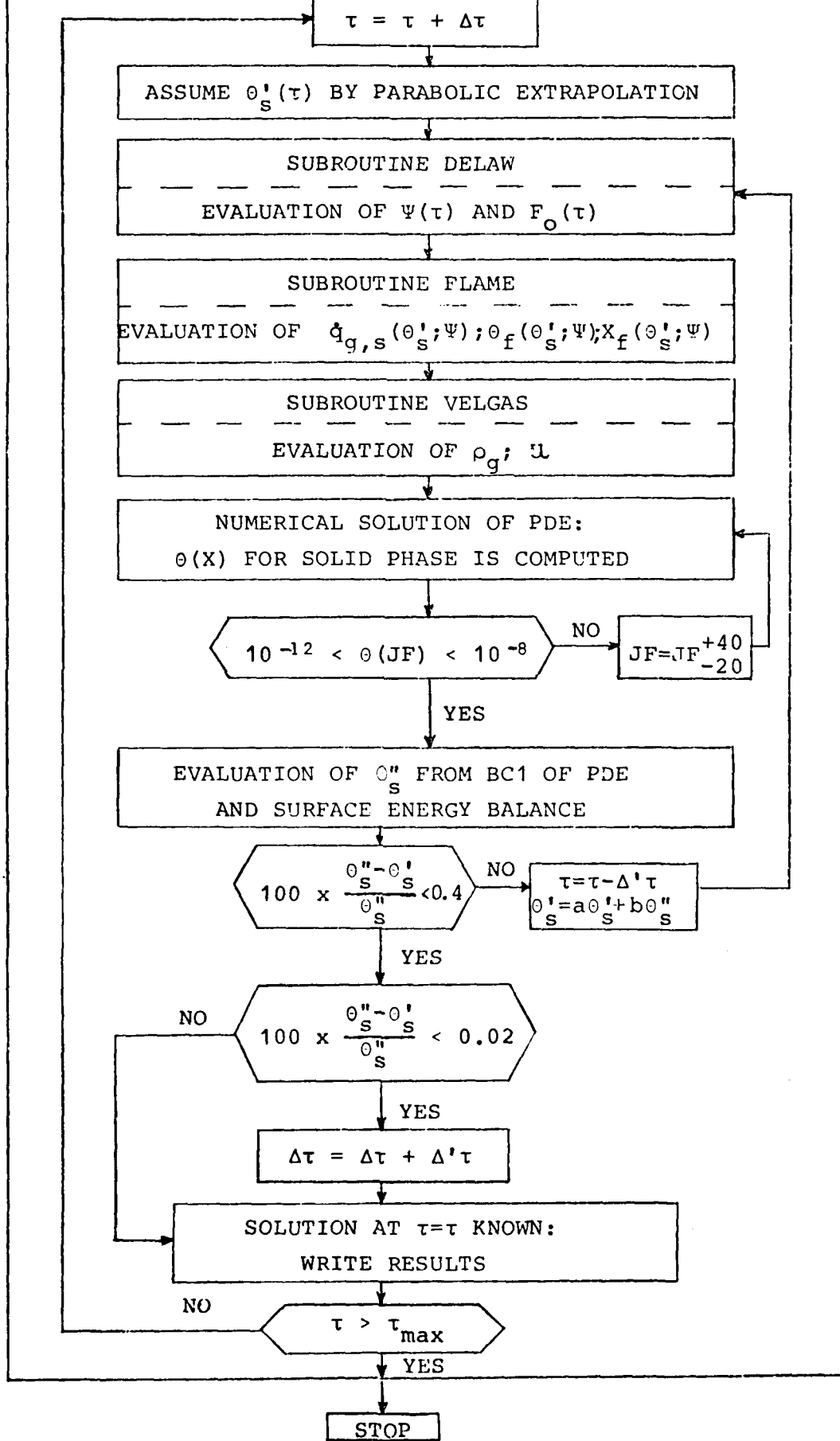
CONTINUED FROM PREVIOUS PAGE



CONTINUED ON NEXT PAGE

CONTINUED FROM PREVIOUS PAGE

UNSTEADY SOLUTION WITH QUASI-STEADY GAS PHASE



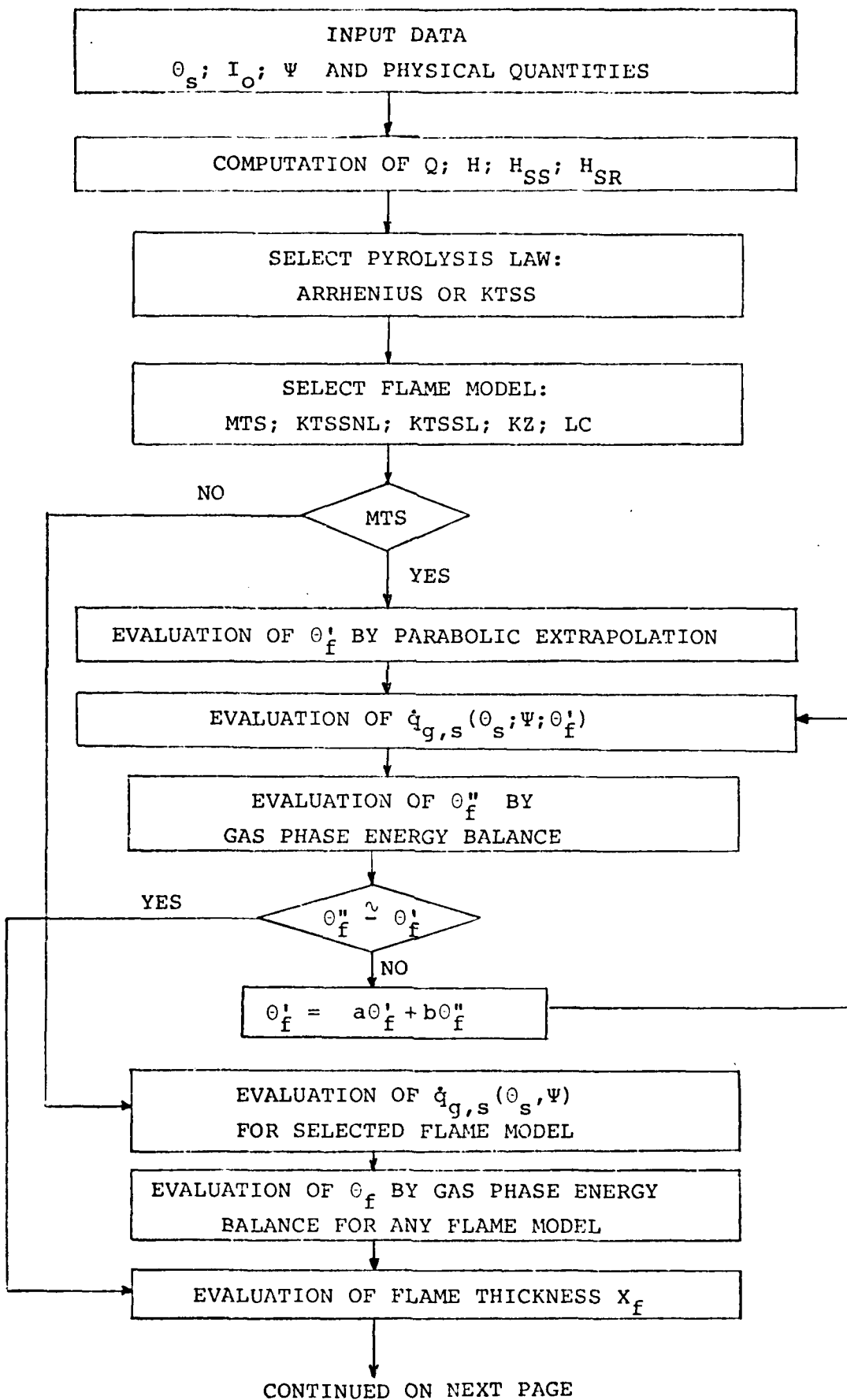
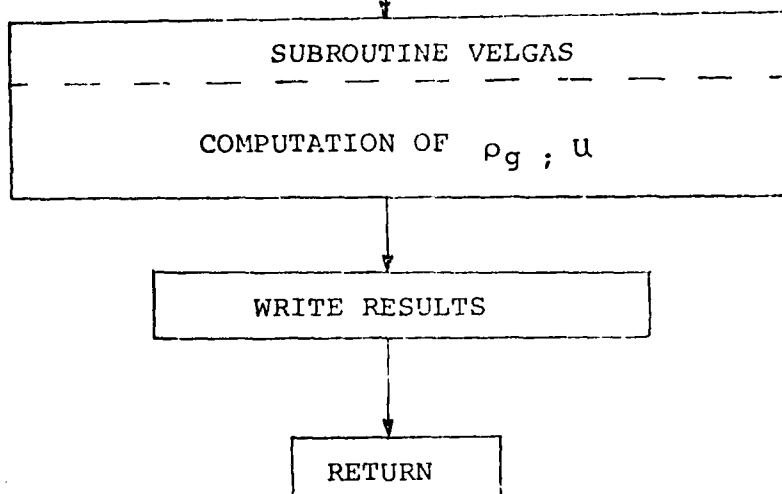


FIG. 541

CONTINUED FROM PREVIOUS PAGE



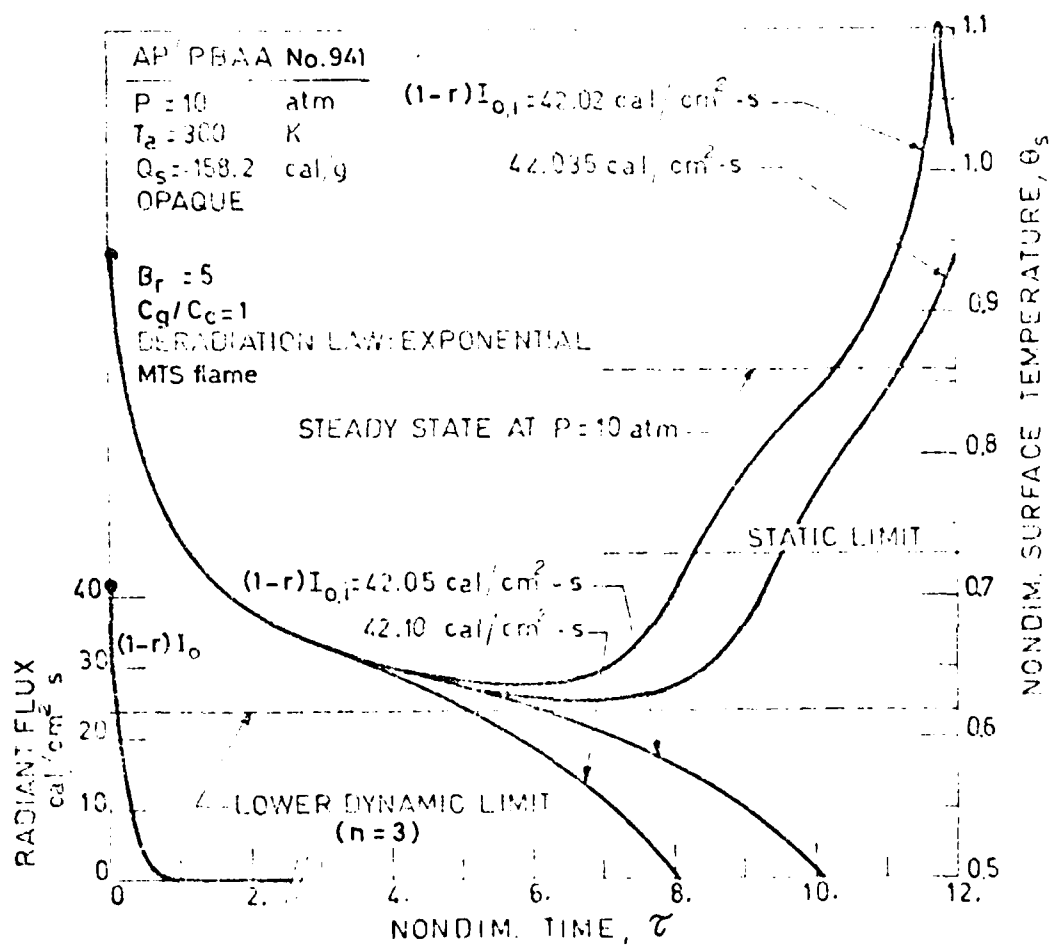


FIG. 52

AP/PBAA No. 941

$P = 10$  atm  
 $T_a = 300$  K  
 $Q_s = -158.2$  cal/g  
OPAQUE

$B_r = 10$   
MTS FLAME  
DERADIATION LAW: EXPONENTIAL  
 $C_g/C_c = 1$

$\theta_s(\tau)$

$(1-r)I_{0,i} = 40.29 \text{ cal/cm}^2 \cdot \text{s}$

$\text{RADIAN FLUX}$   
 $\text{cal/cm}^2 \text{s}$   
 $(1-r)I_0$

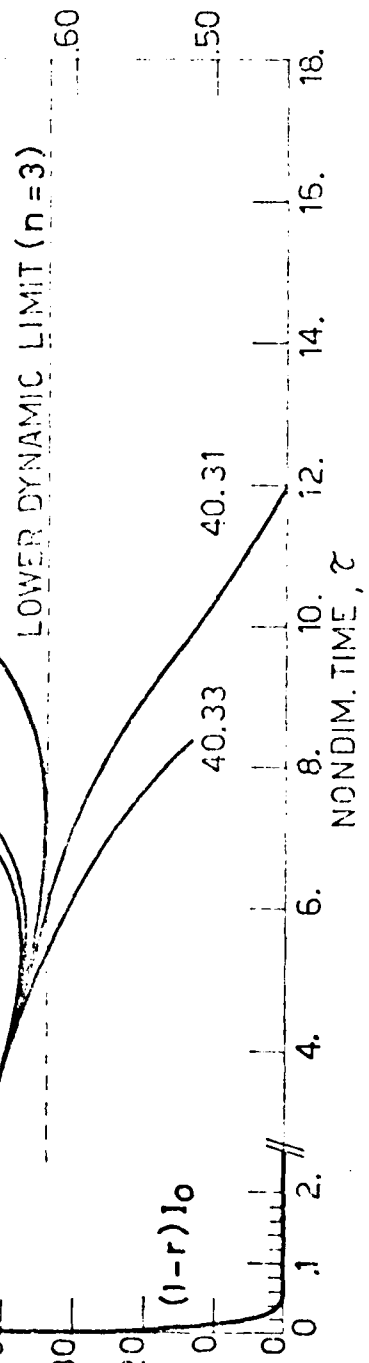
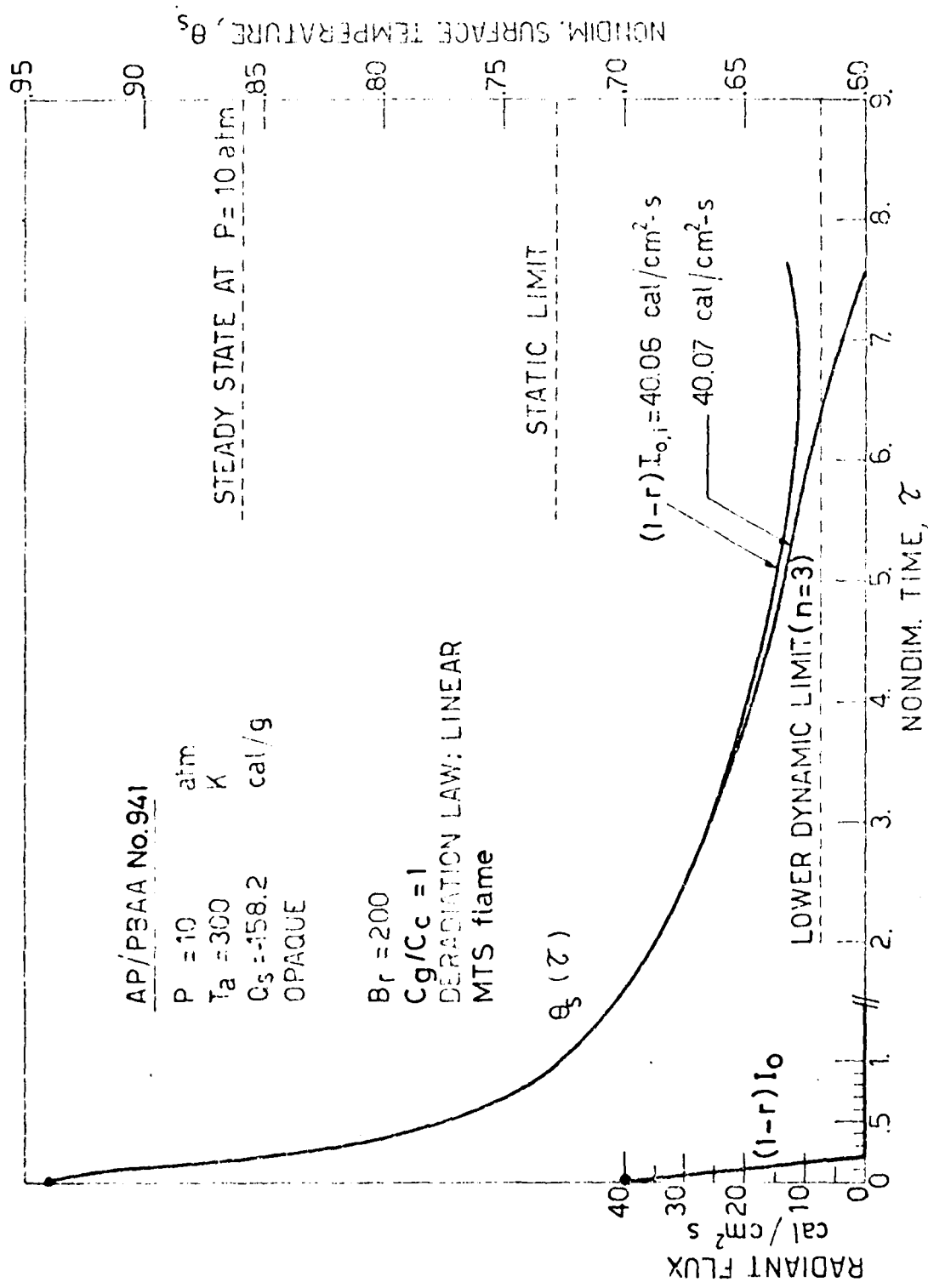


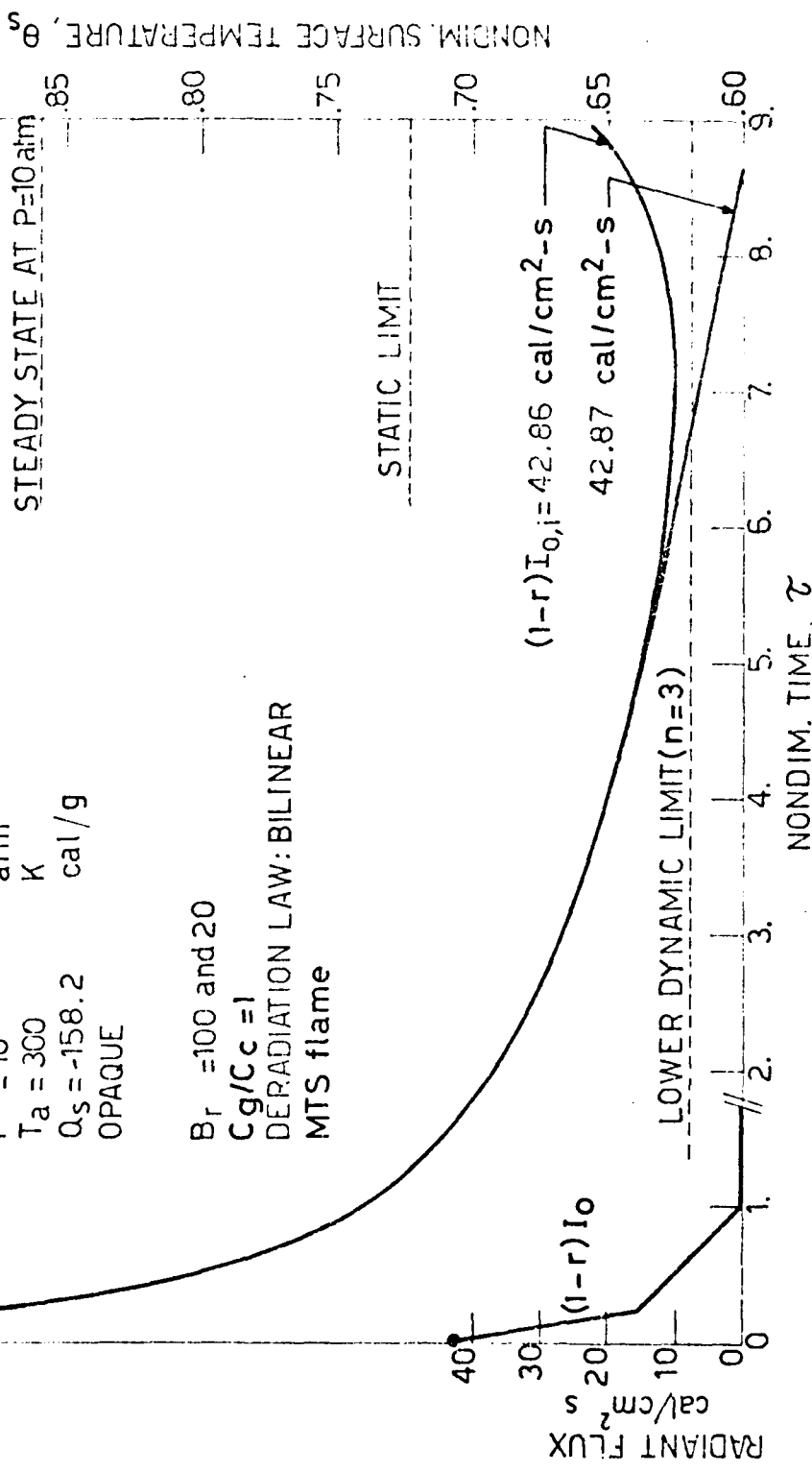
FIG. 5.3



RADIATION SUSTAINED STEADY STATE AT  $P=10$  atm

AP/PBAA No. 941

$P = 10$  atm  
 $T_a = 300$  K  
 $Q_s = -158.2$  cal/g  
 OPAQUE



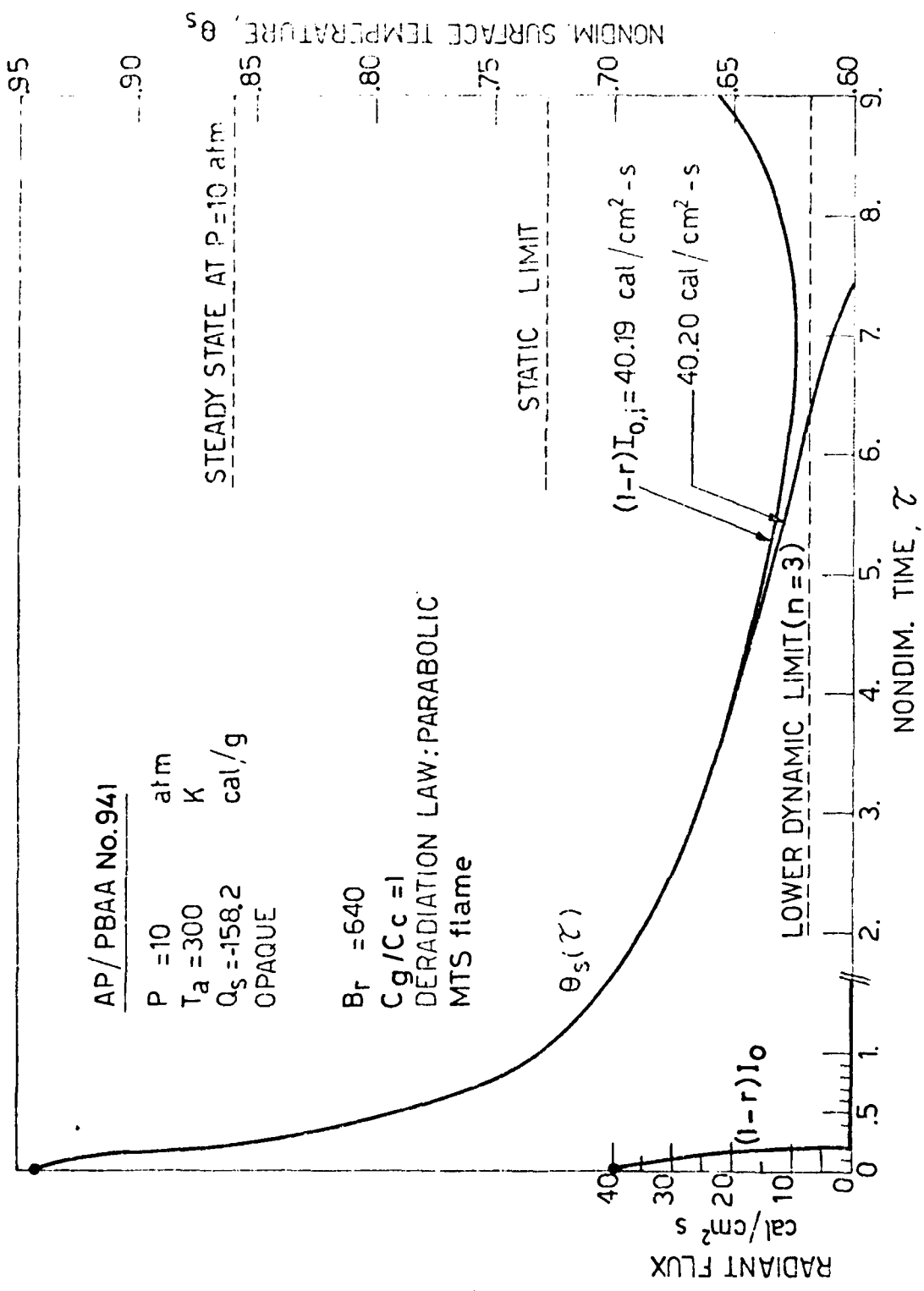


FIG. 58

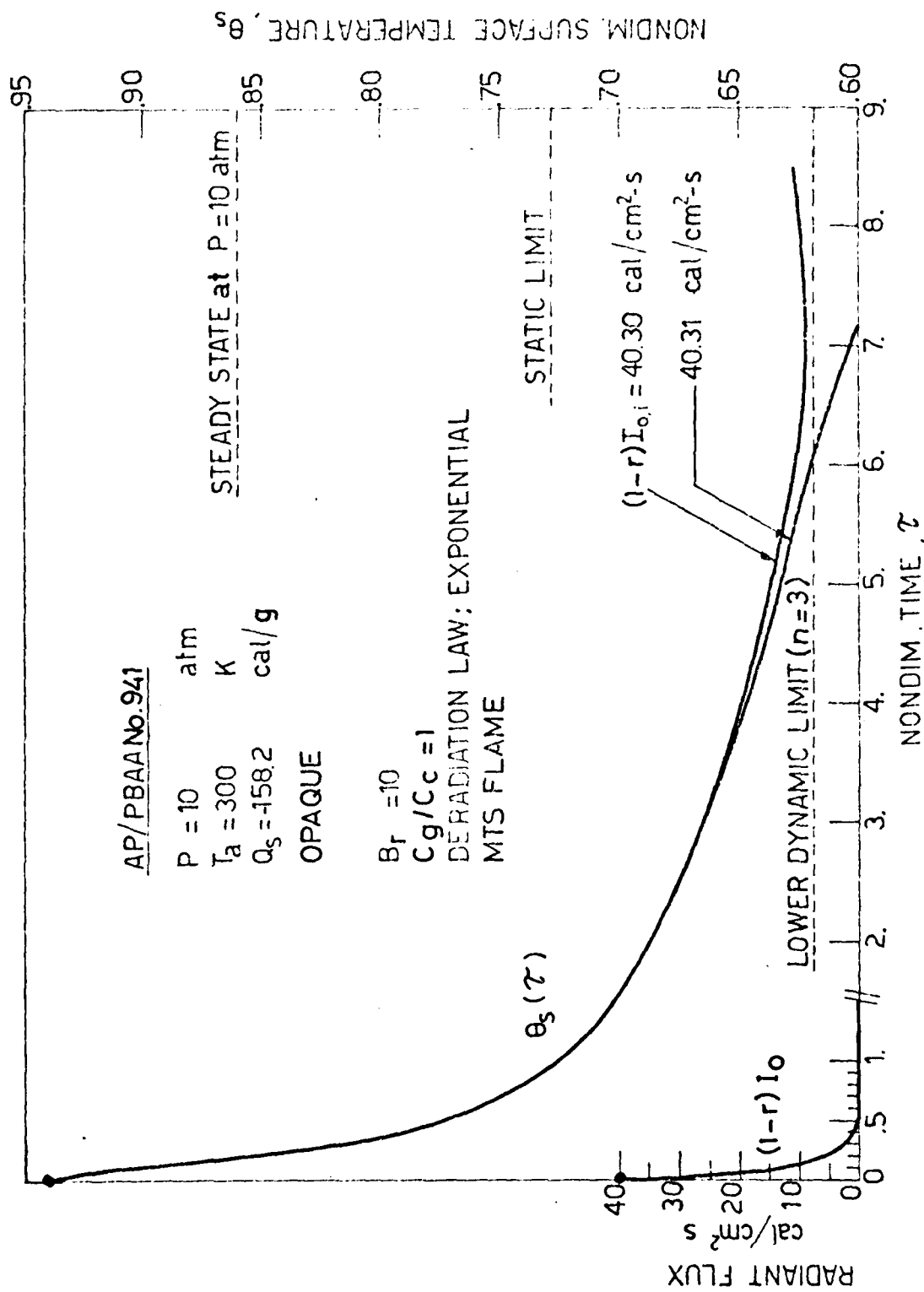


FIG. 57

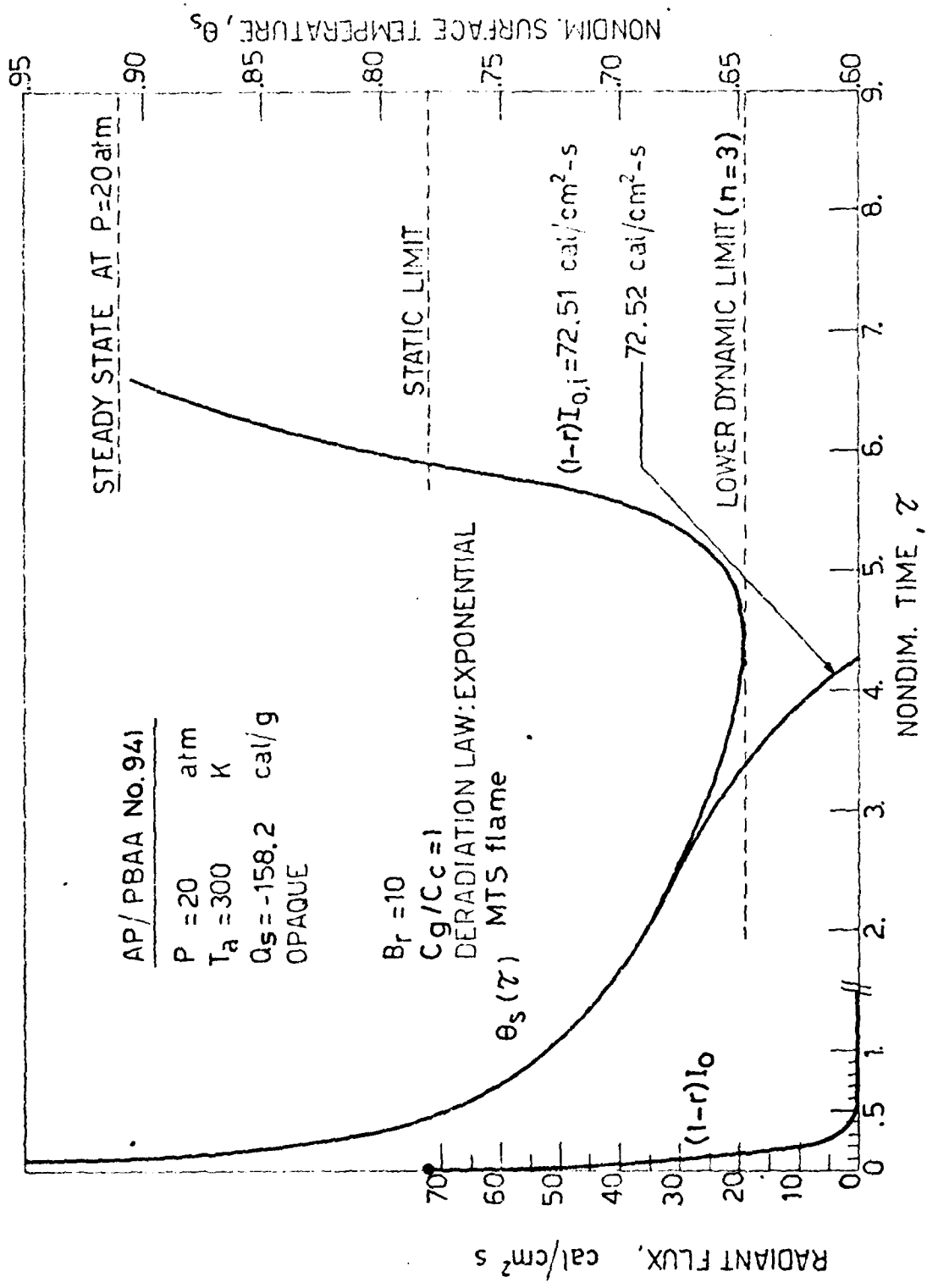


FIG. 58

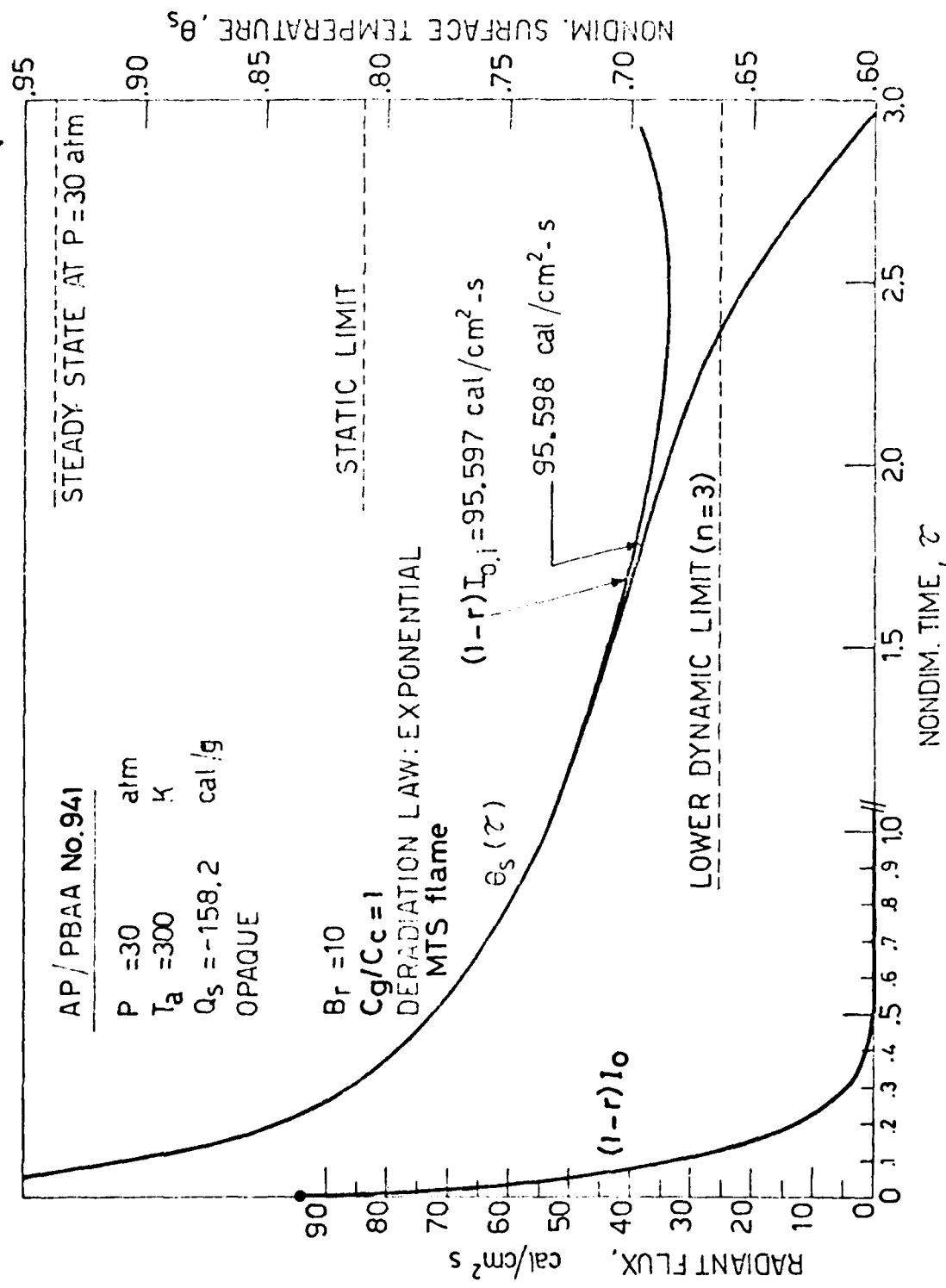


FIG. 59

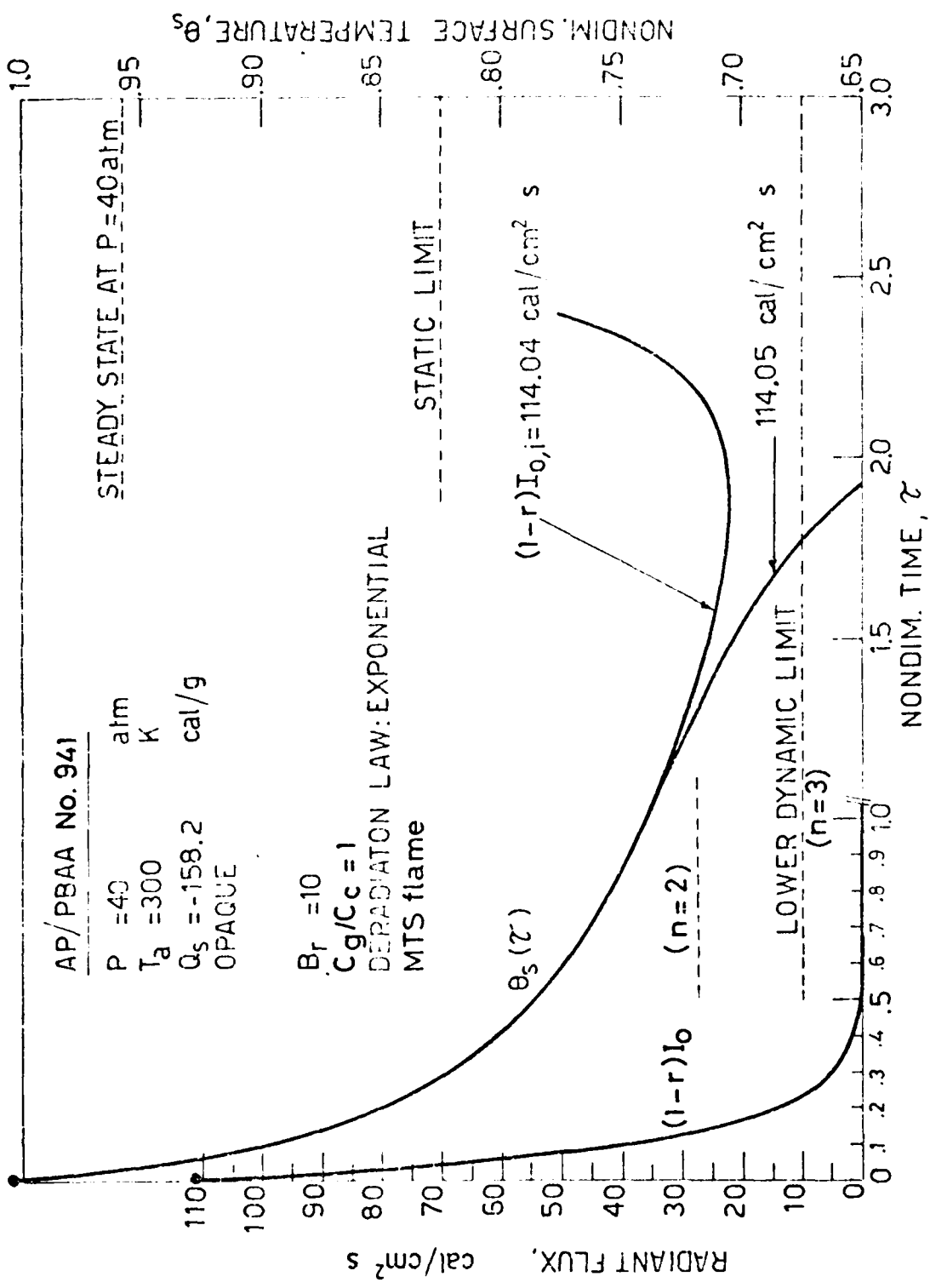


FIG. 60

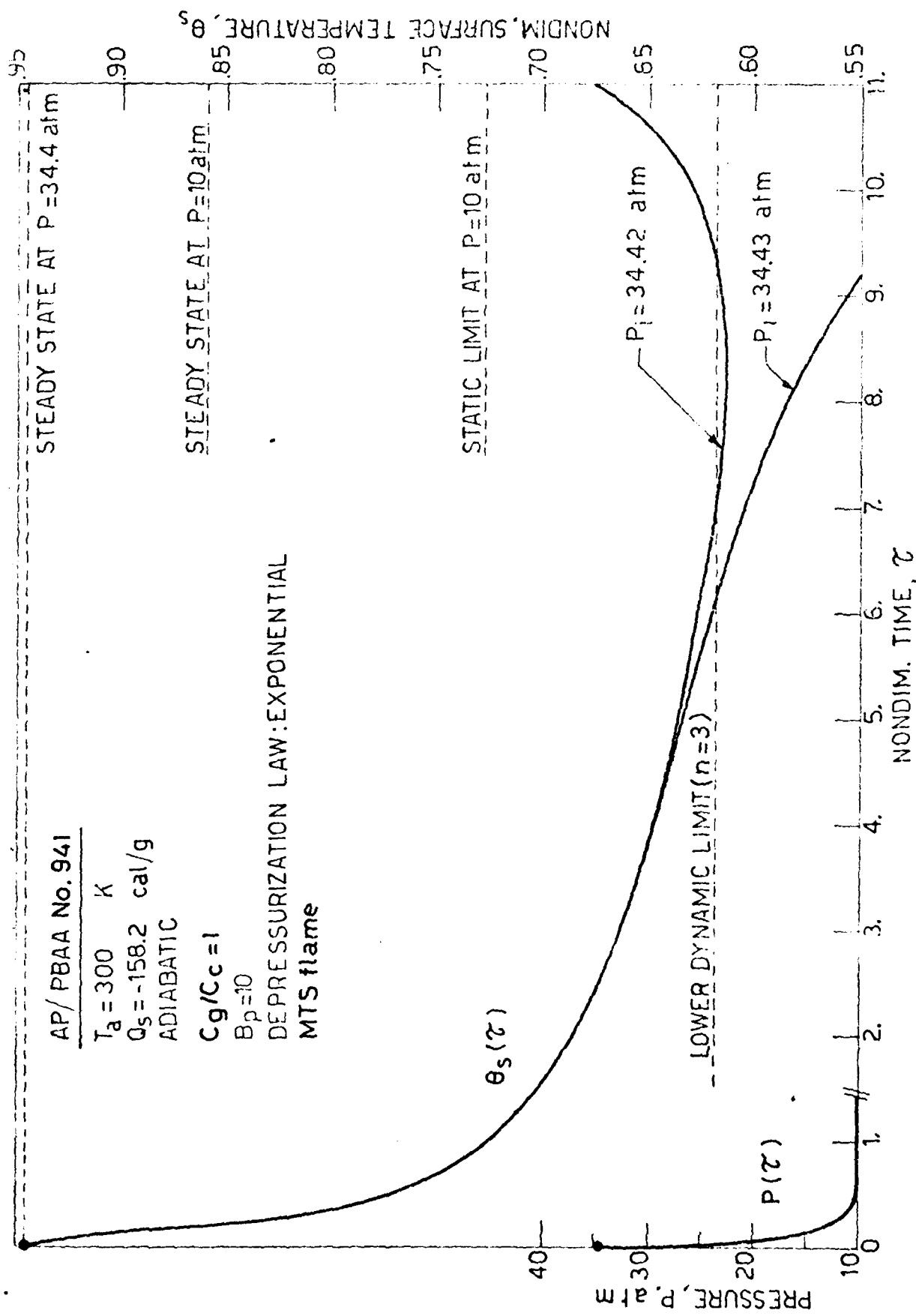


FIG. 61

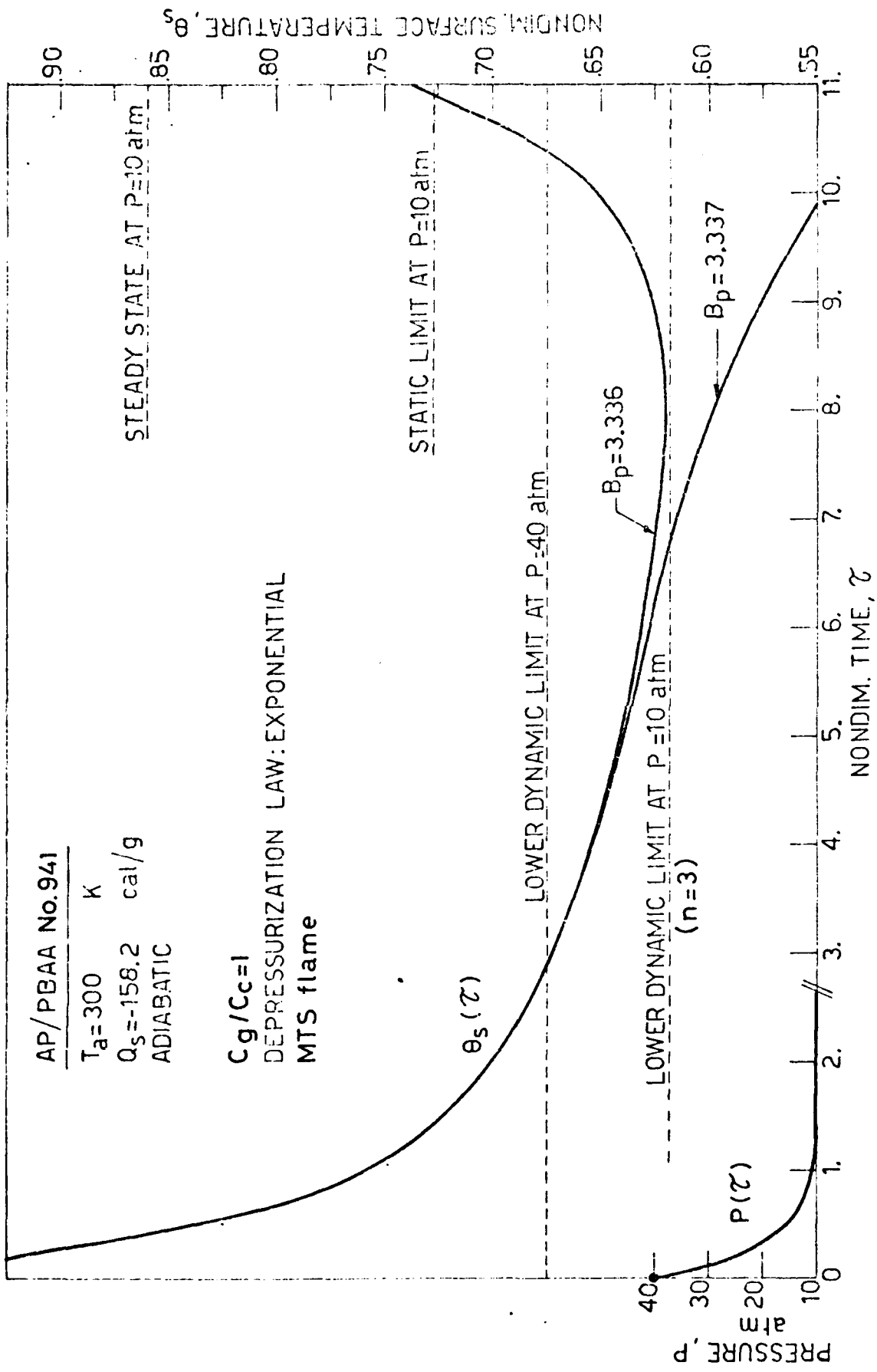


FIG. 52

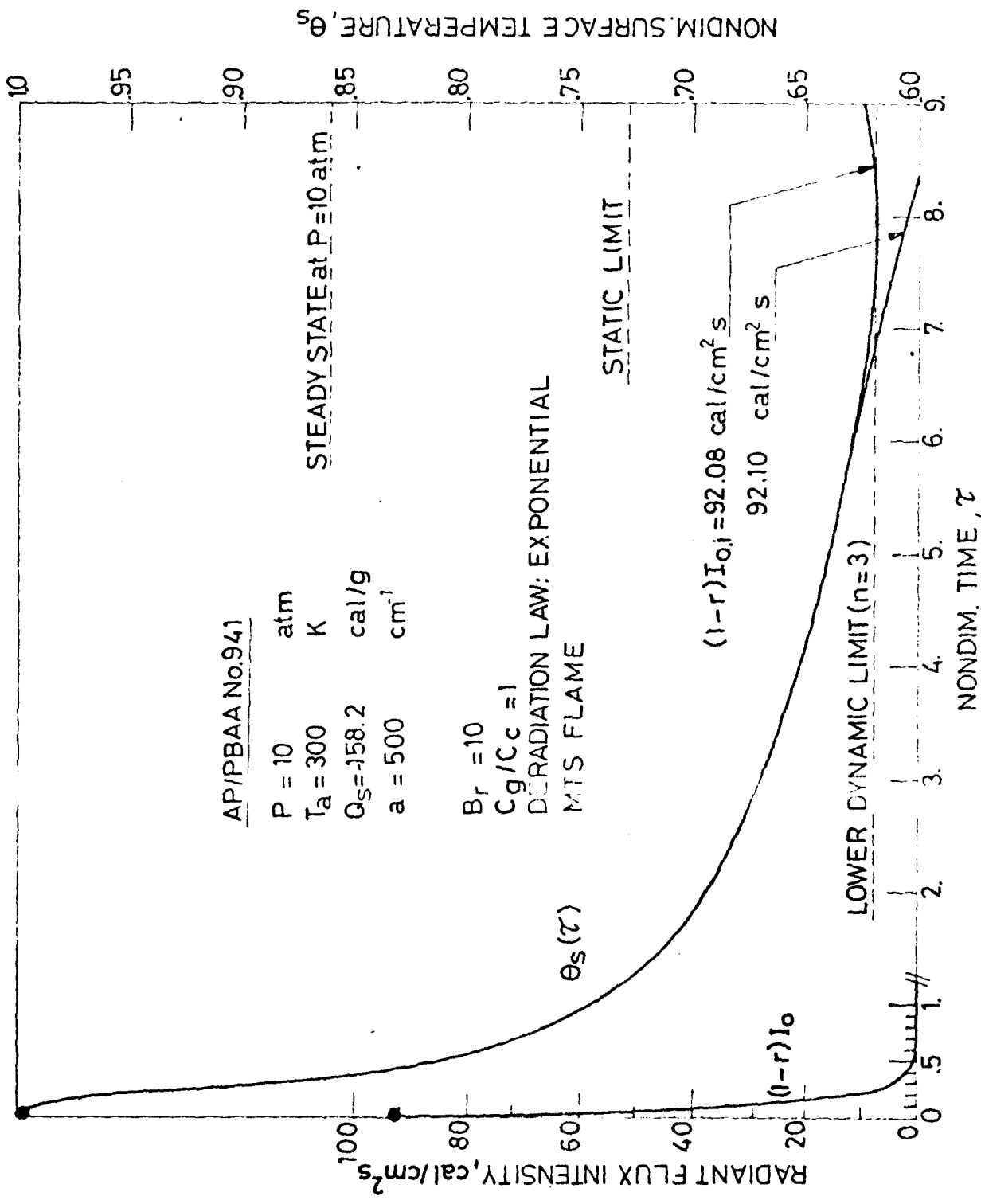


FIG. 6.2

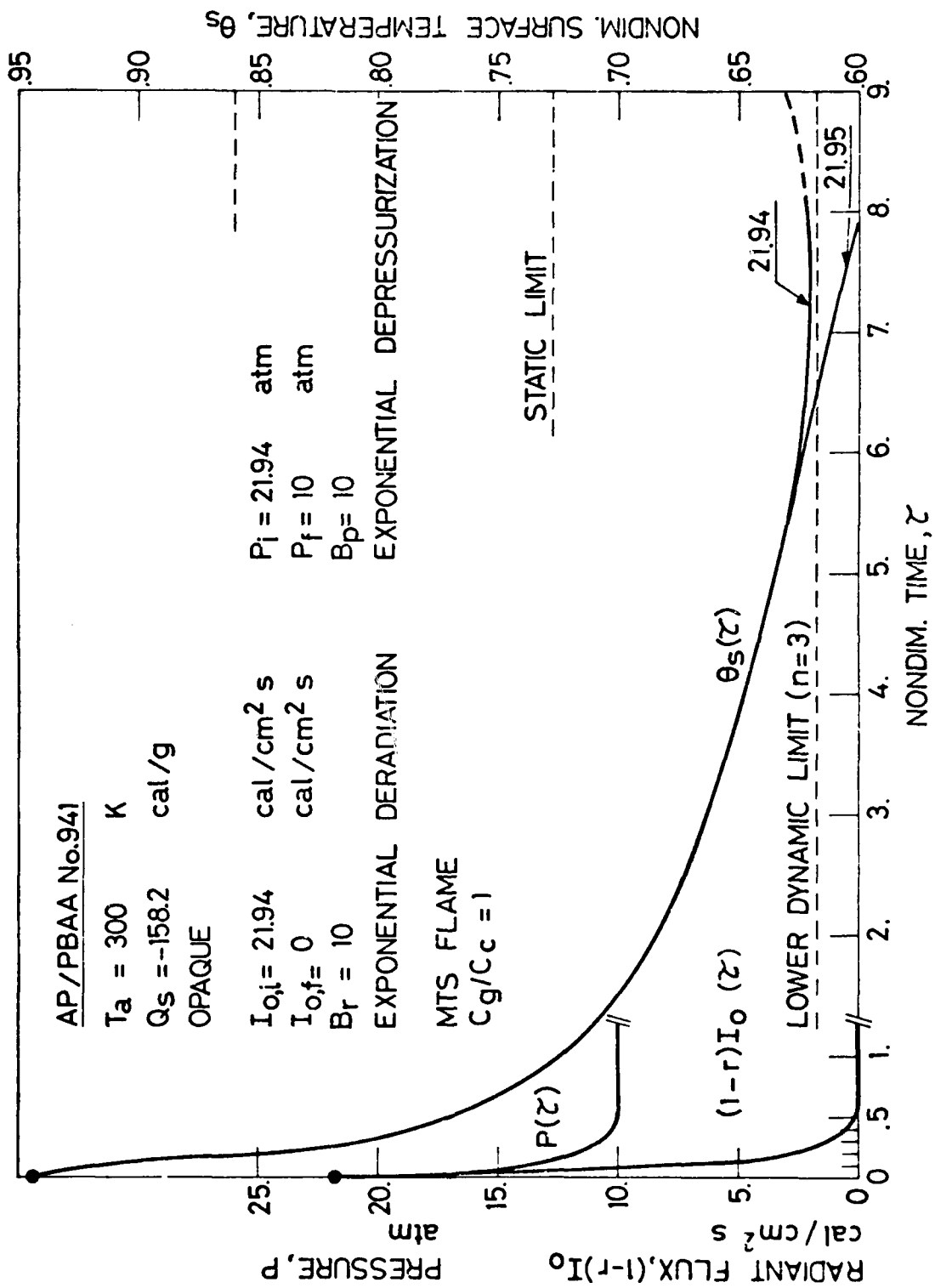


FIG. 64

AD-A100 043

POLITECNICO DI MILANO (ITALY) IST DI MACCHINE  
THE DYNAMICS OF SOLID PROPELLANT COMBUSTION. (U)  
DEC 80 L DE LUCA, A COGHE, A REGGIORI

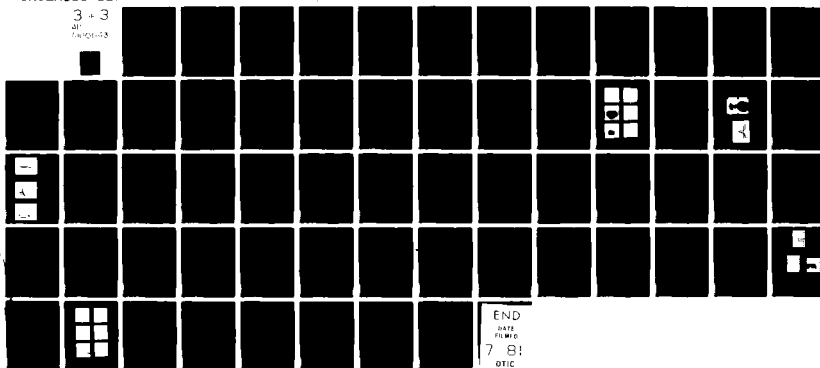
F/G 21/9.2

DA-ERO-78-6-029

NL

UNCLASSIFIED

3 + 3  
4H  
14/01/83



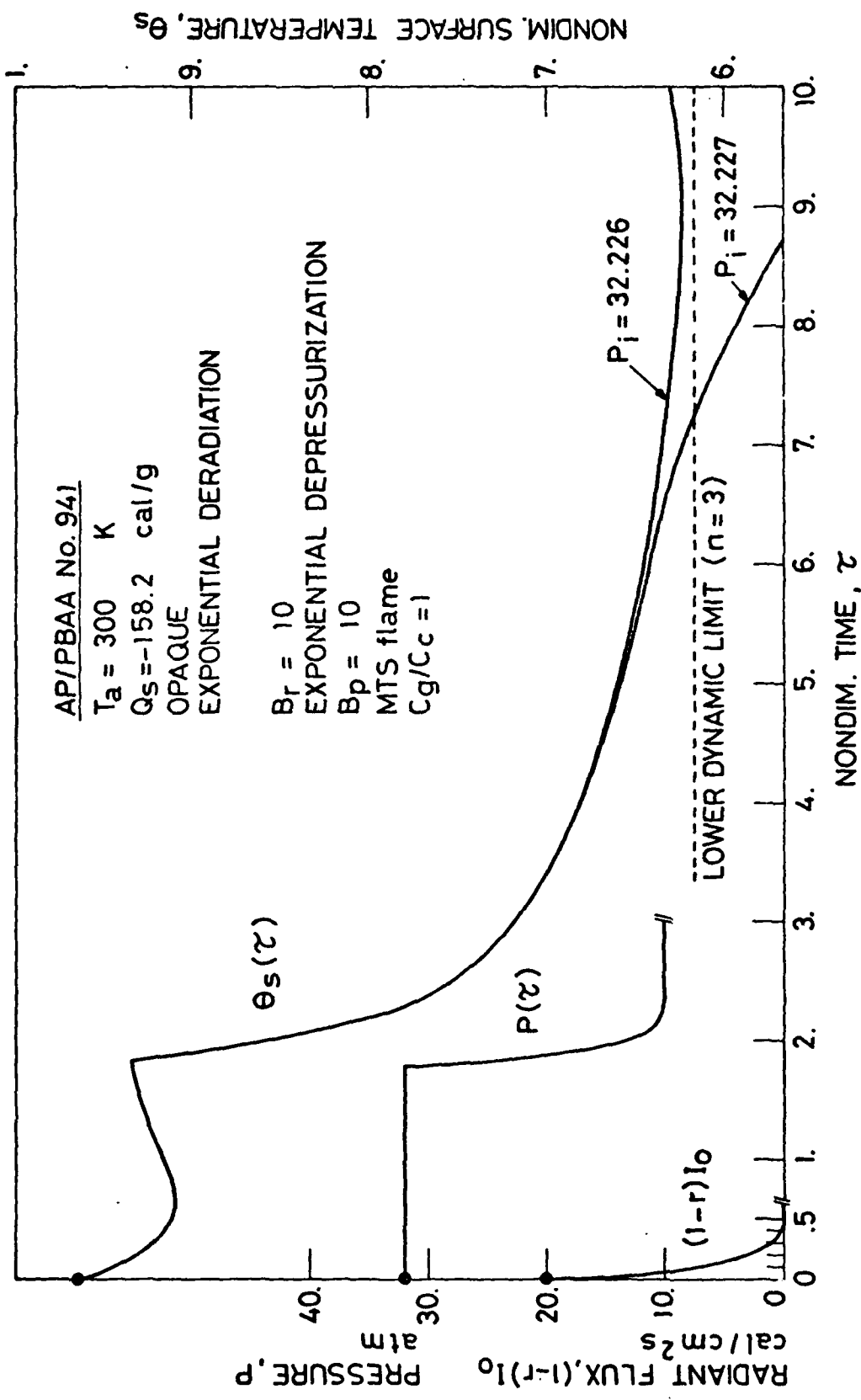


FIG. 65

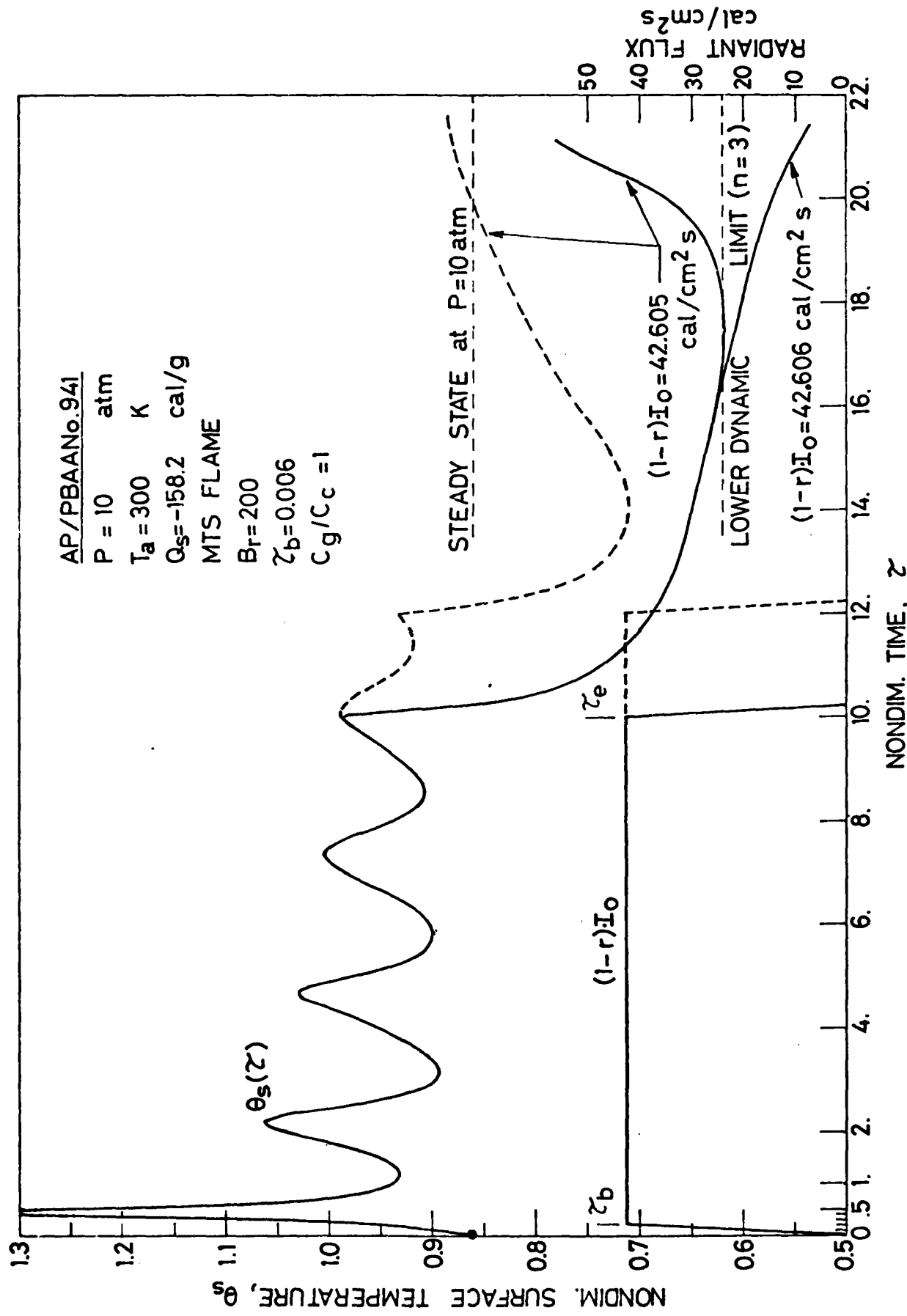


FIG. 66

API/PBAA No. 941

$T_a = 300$  K

ADIABATIC

$P_i = 10$  atm

$P_f = 30$  atm

$B_p = 1.0$

MRS FLAME

$C_g/C_c = 1$

$Q_s = 158.2$  cal/g

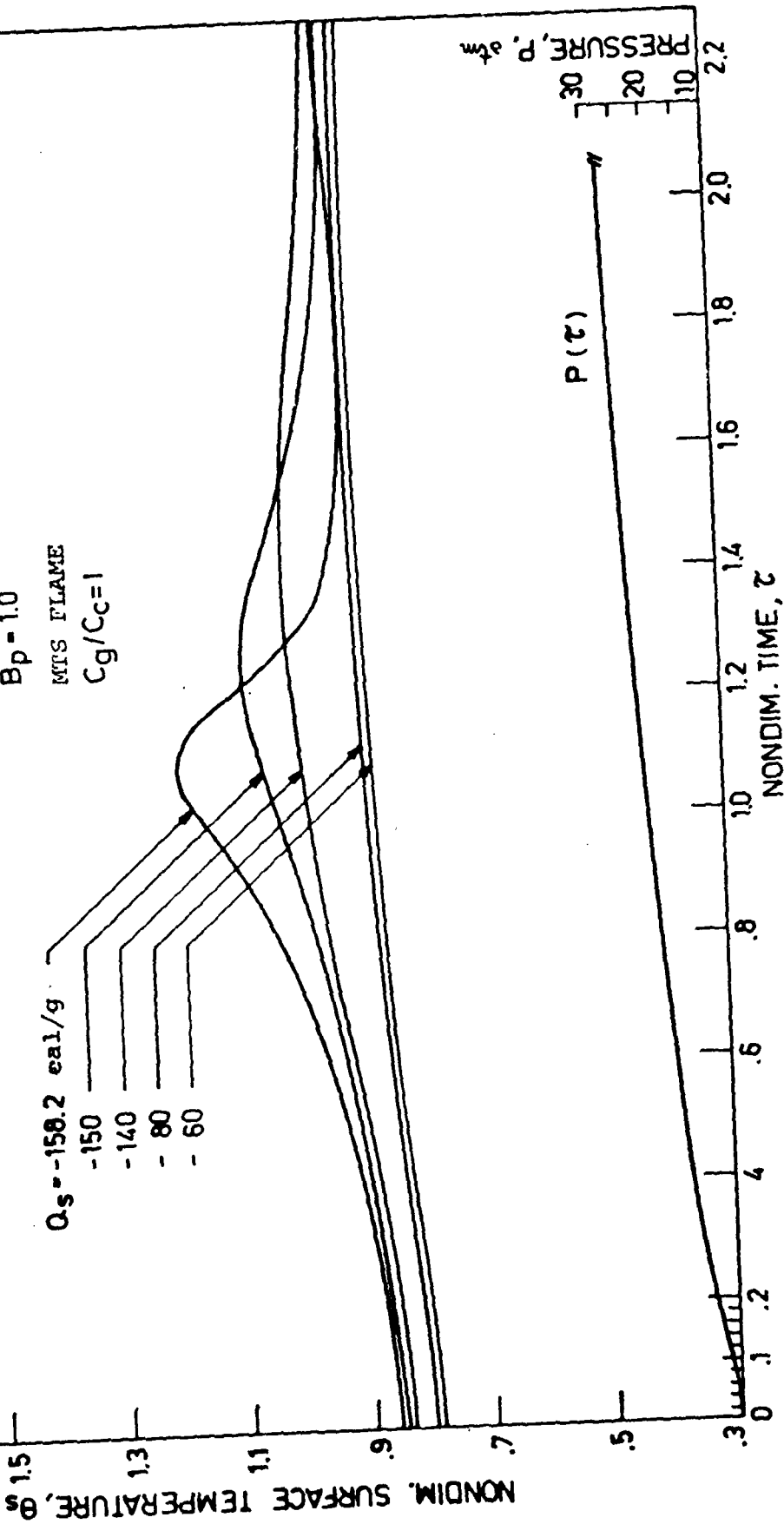


FIG. 67

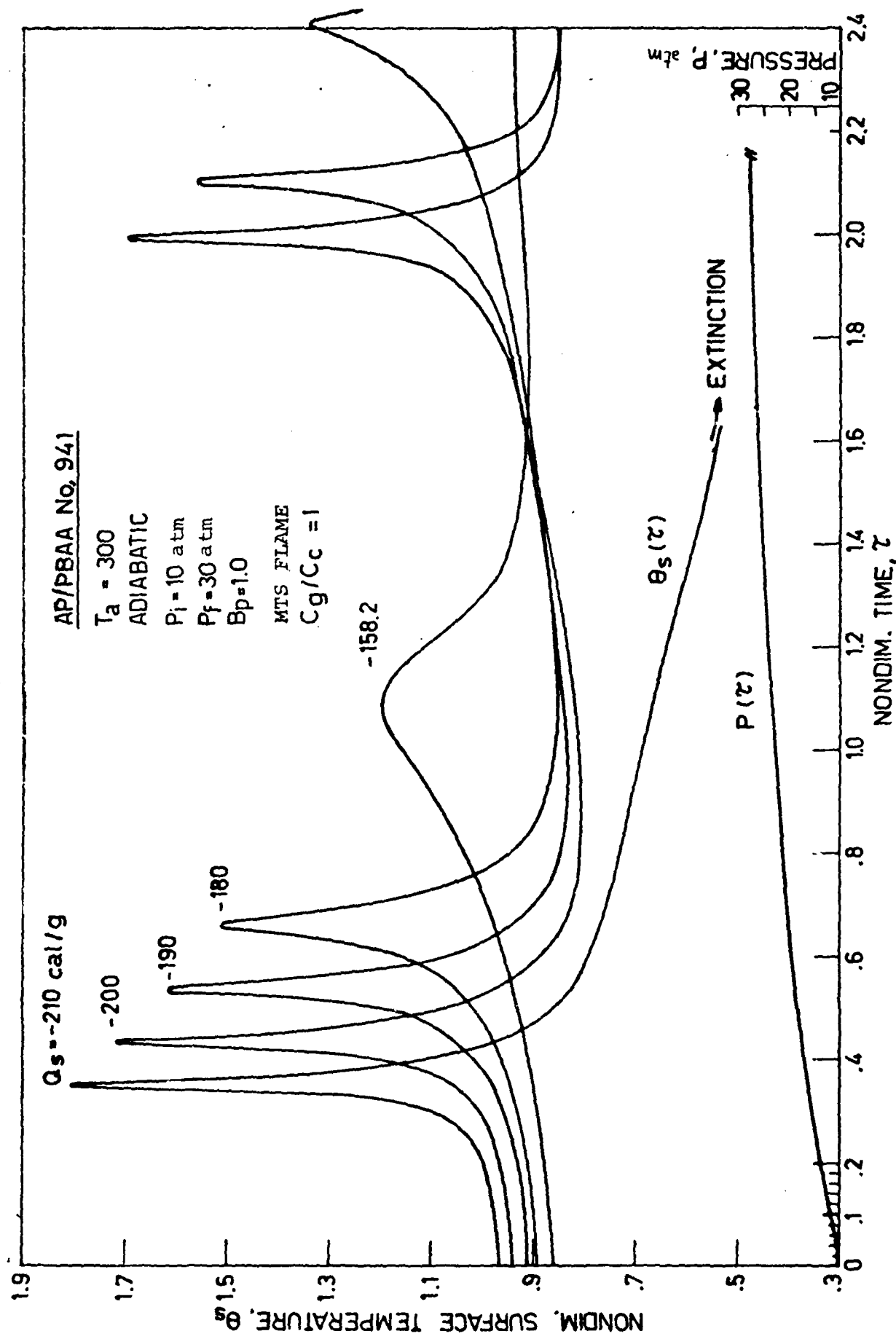


FIG. 68

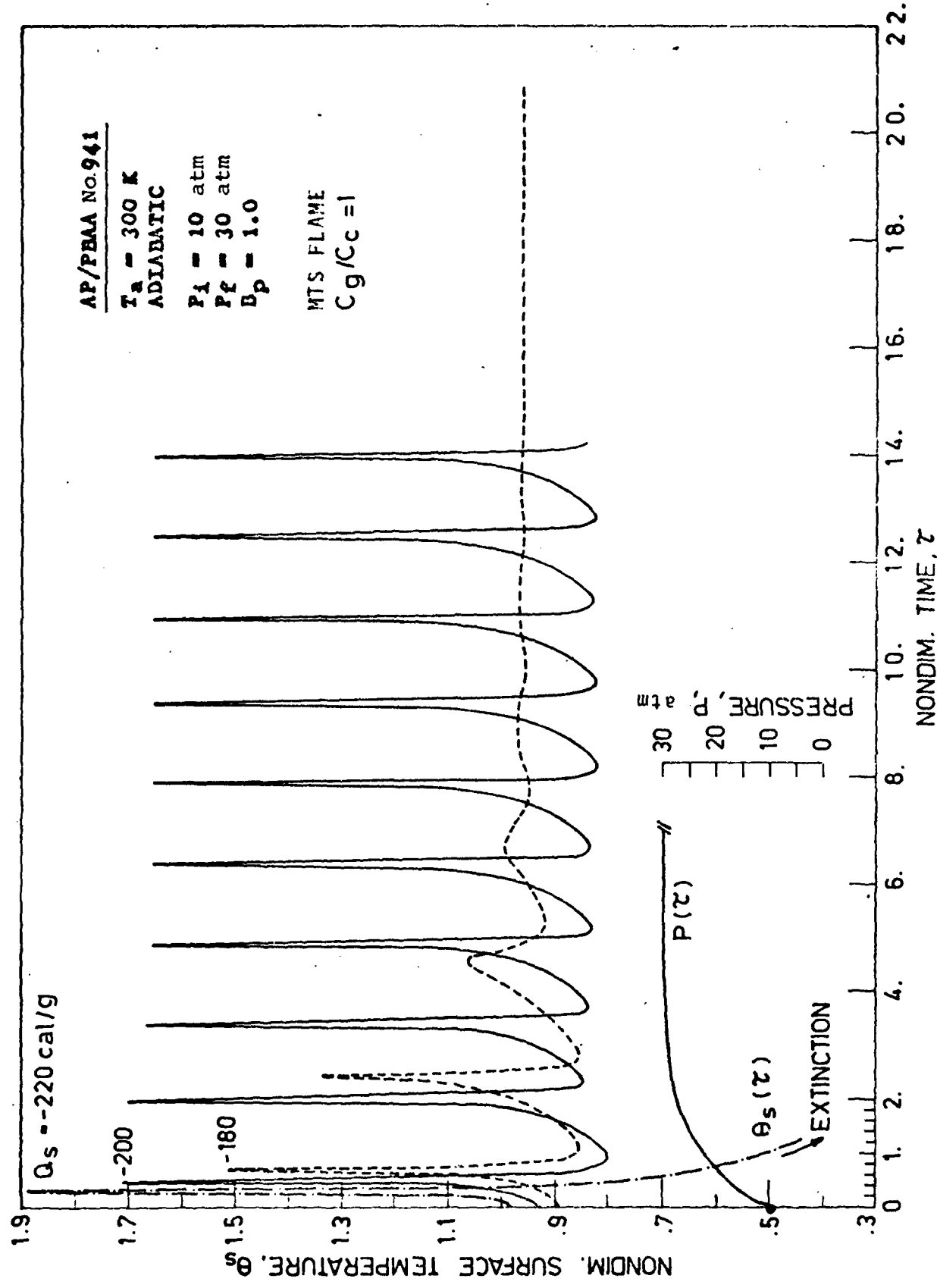


FIG. 6.9

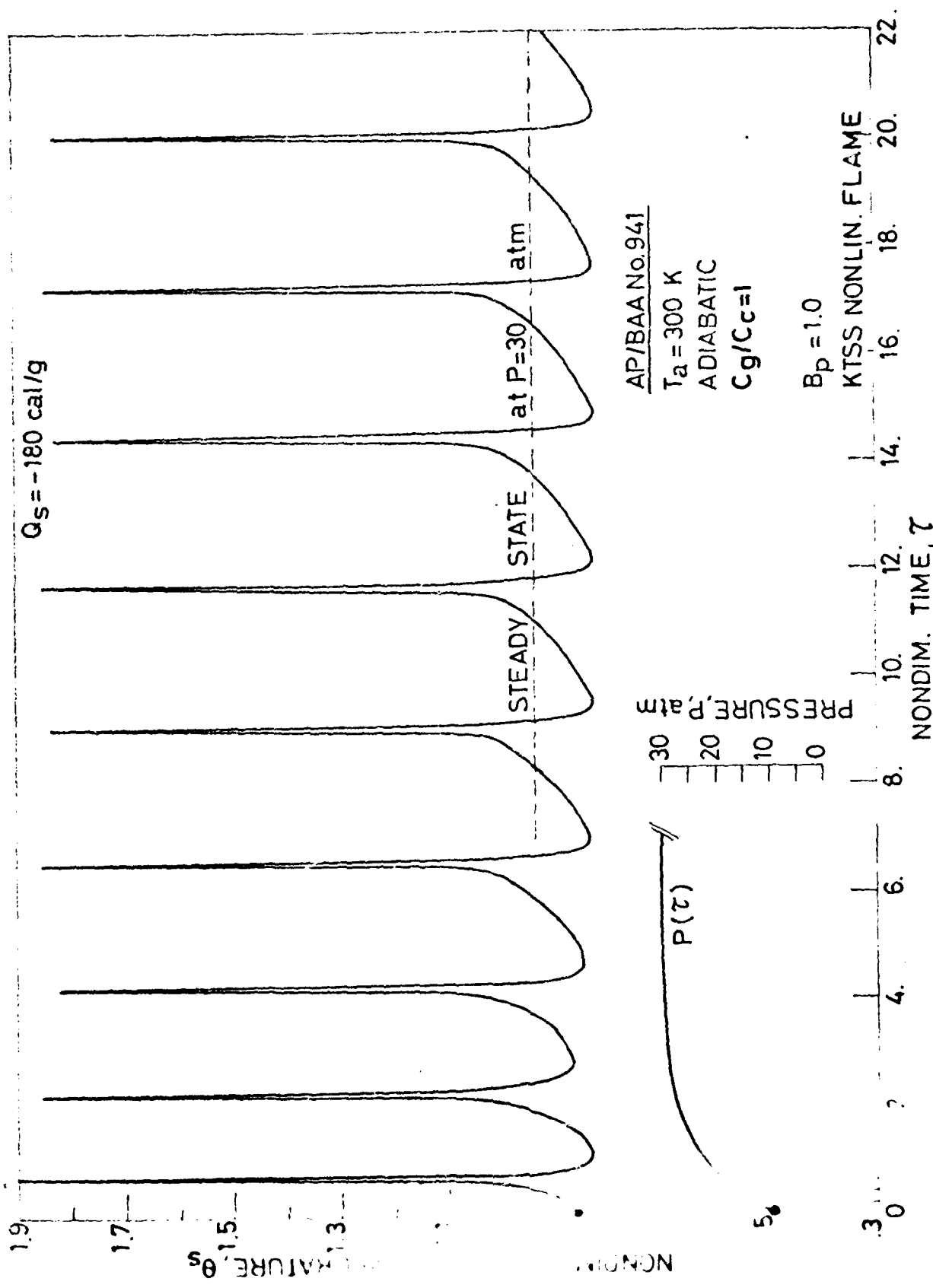
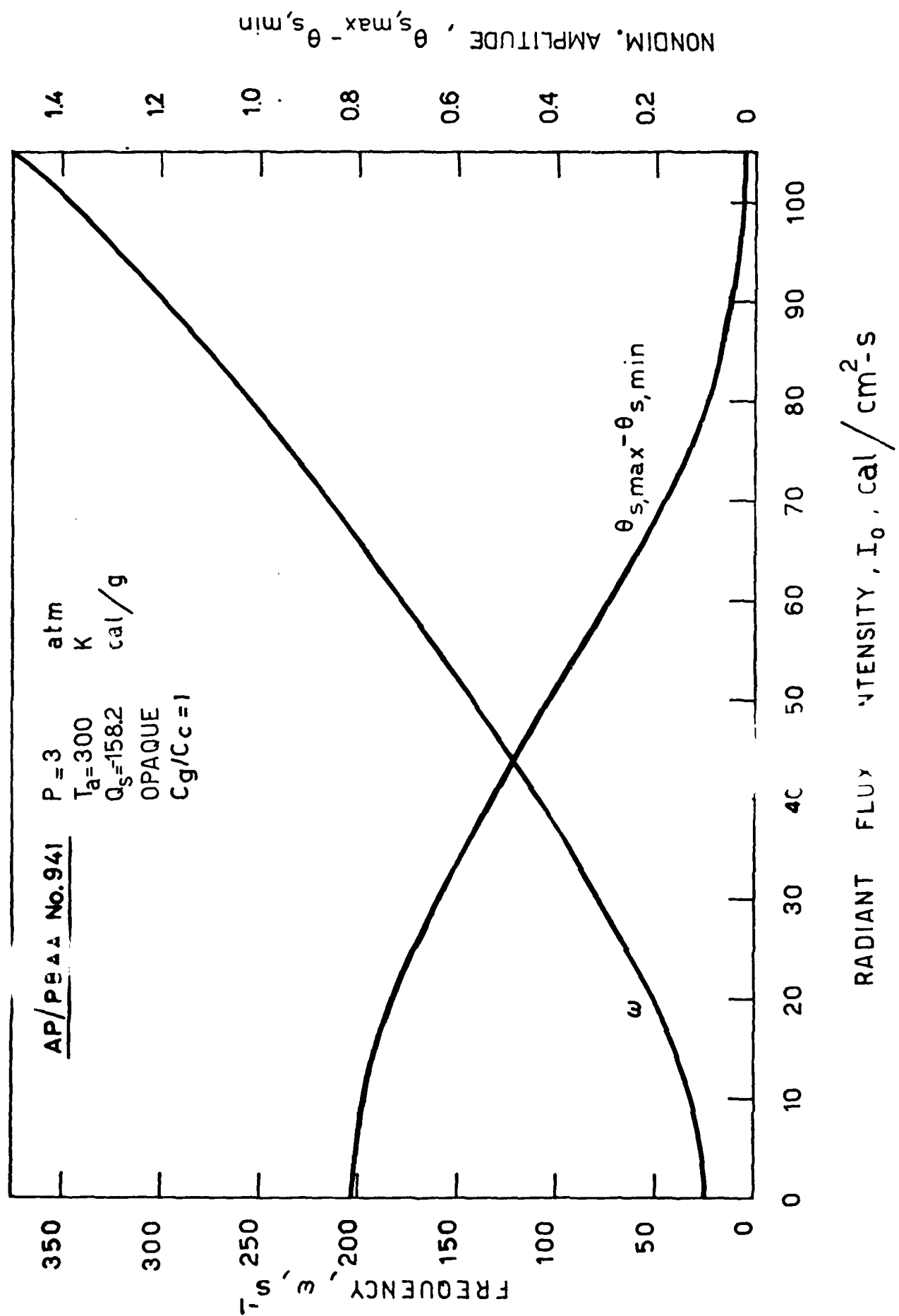


FIG. 70



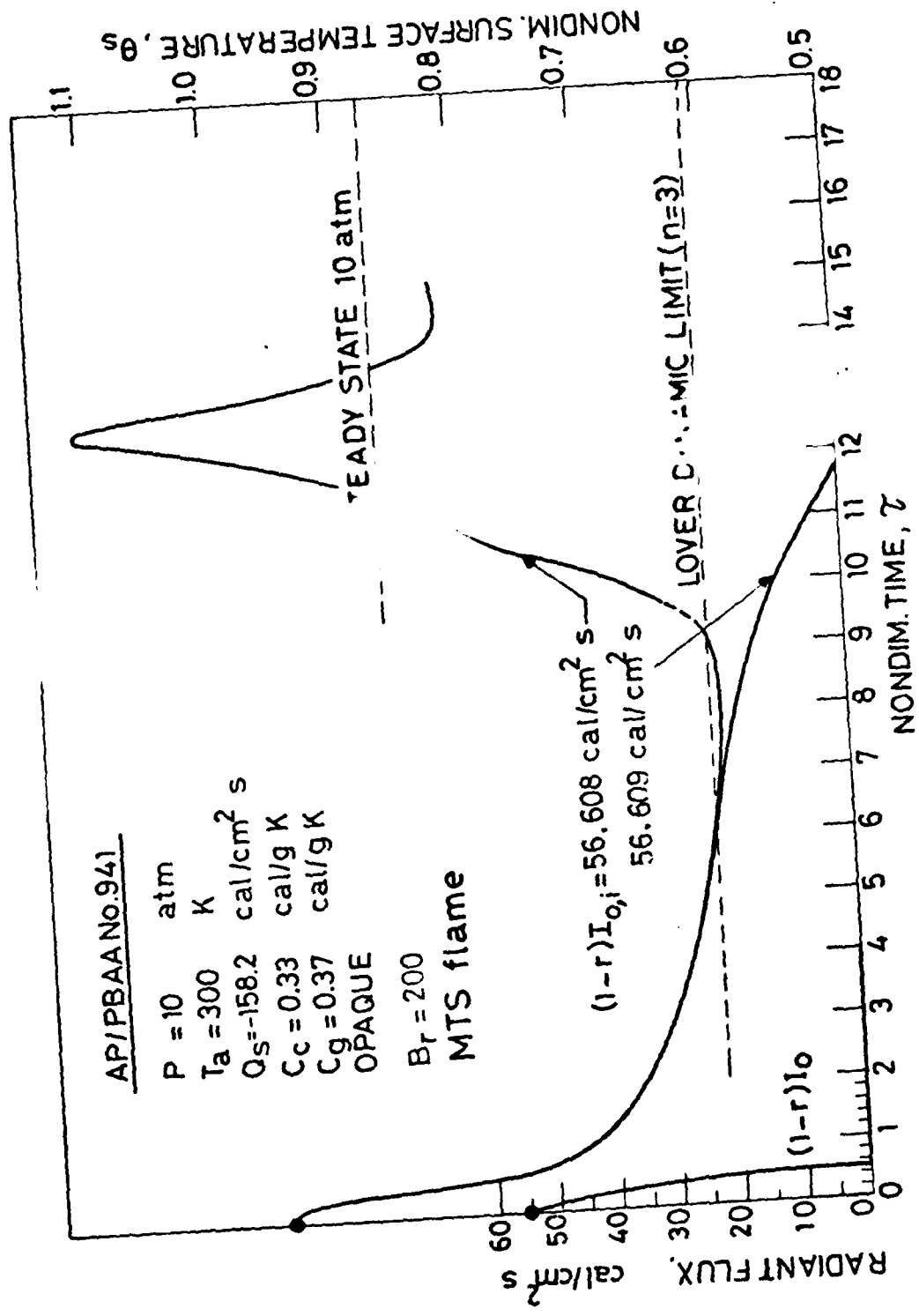


FIG. 72

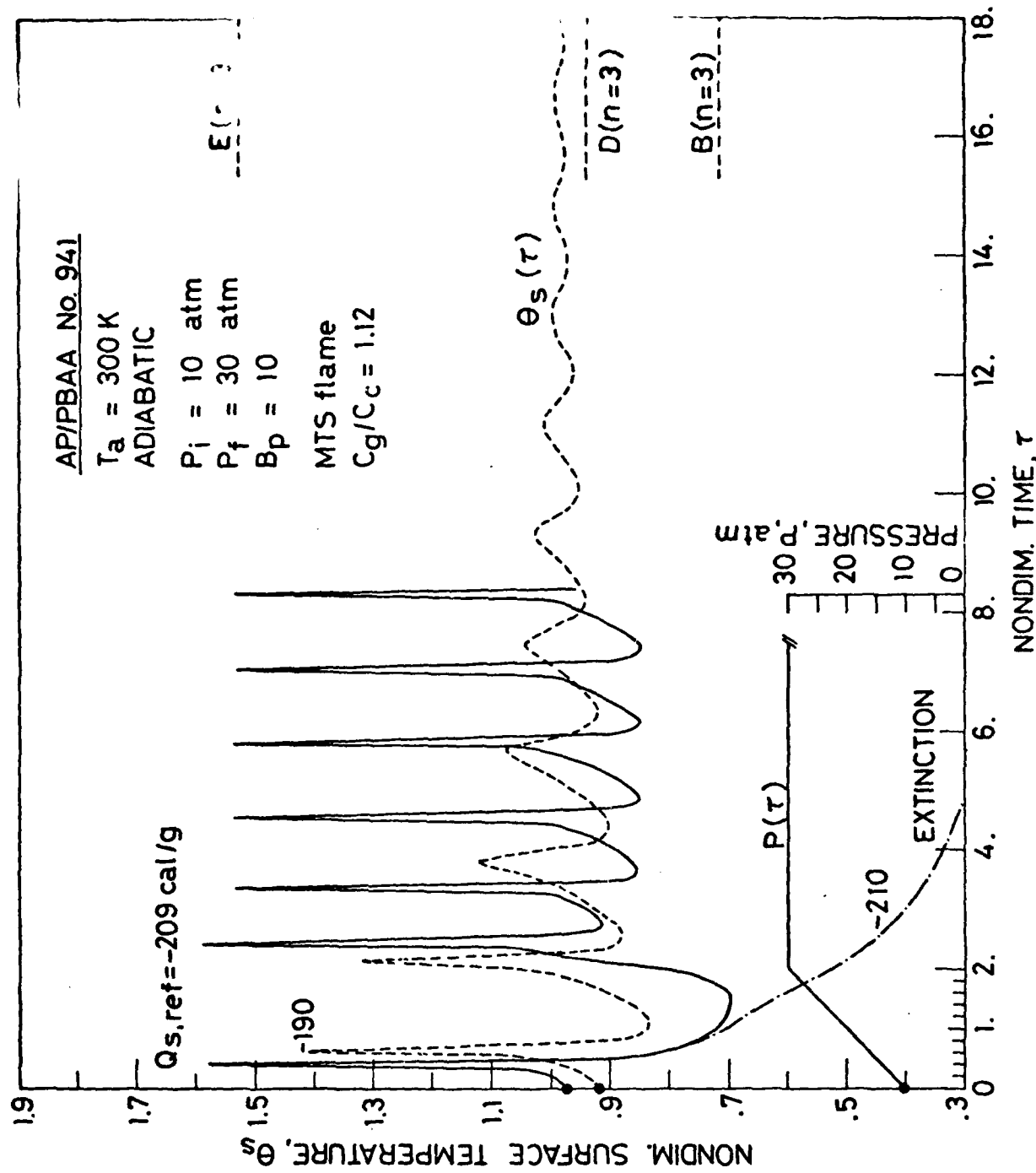


FIG. 73

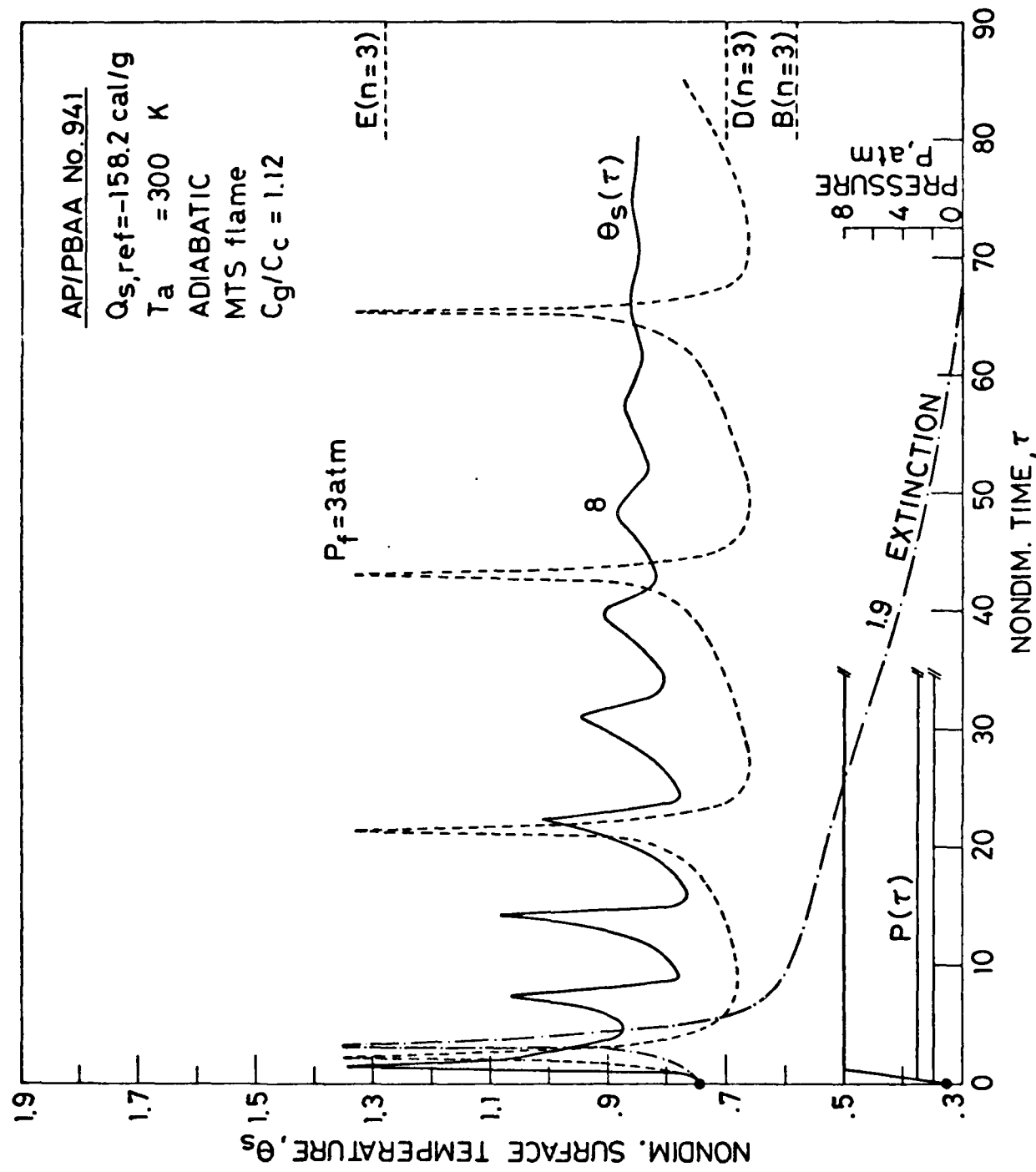


FIG. 44

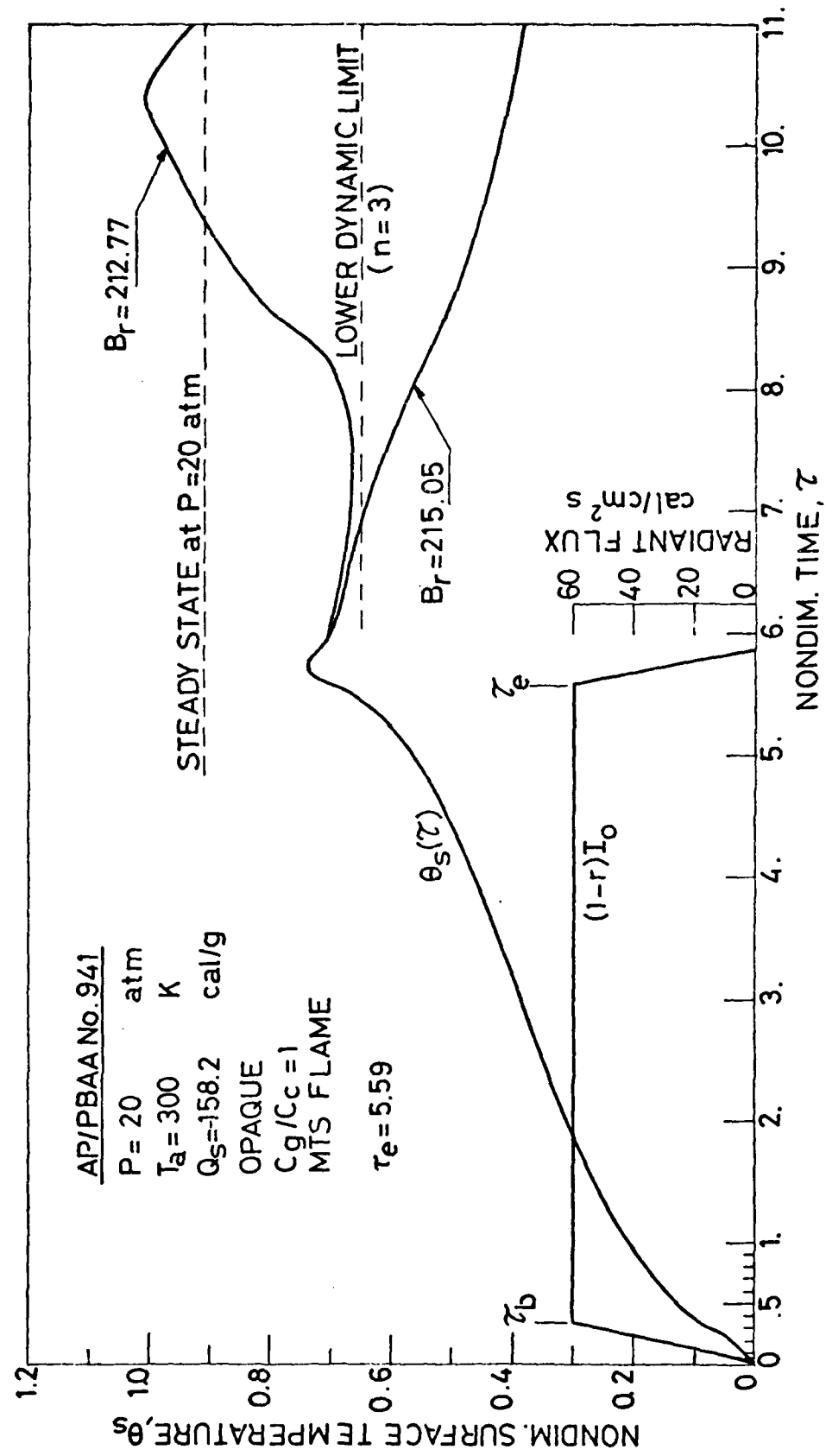


FIG. 75

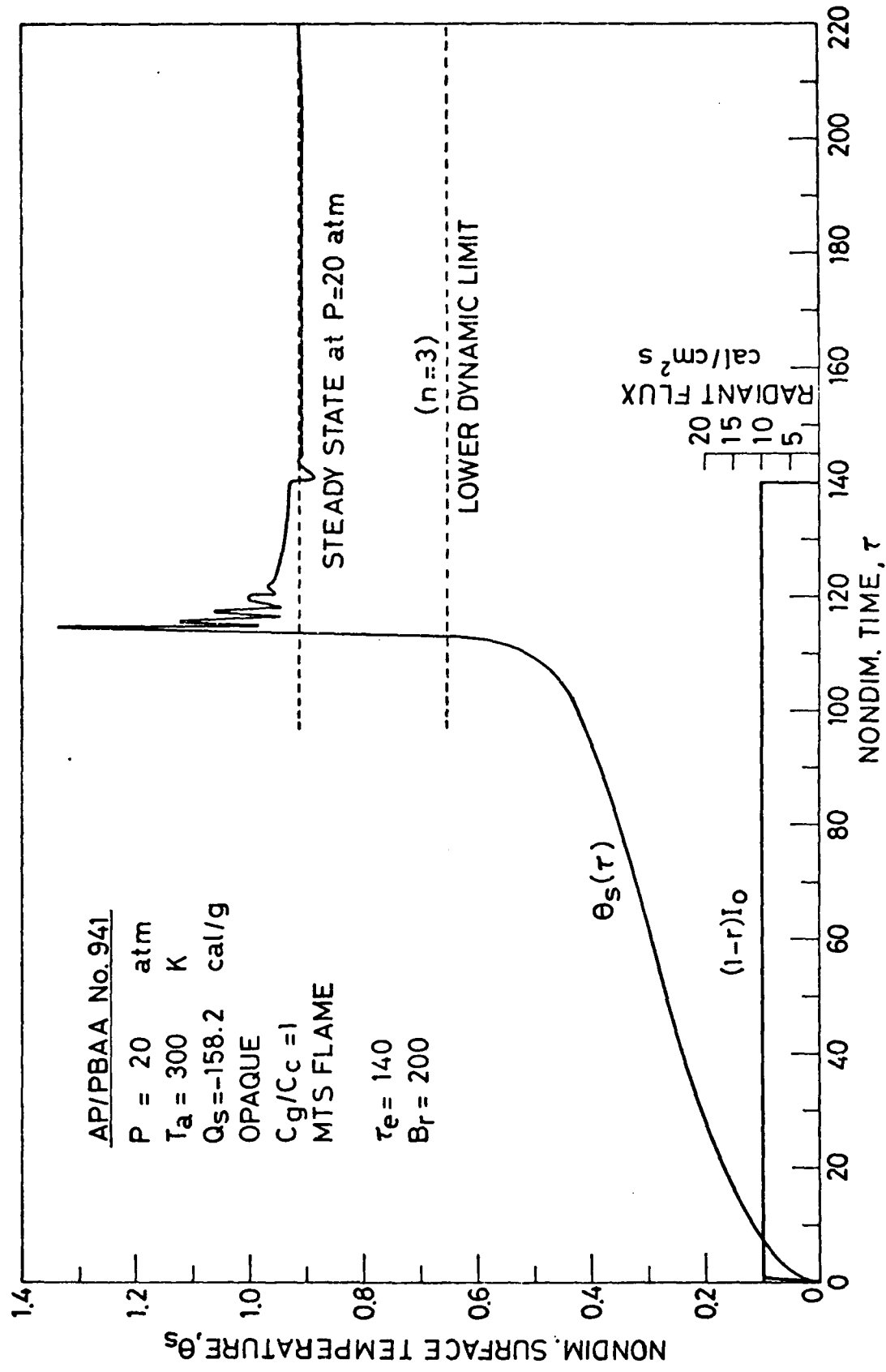


FIG. 75

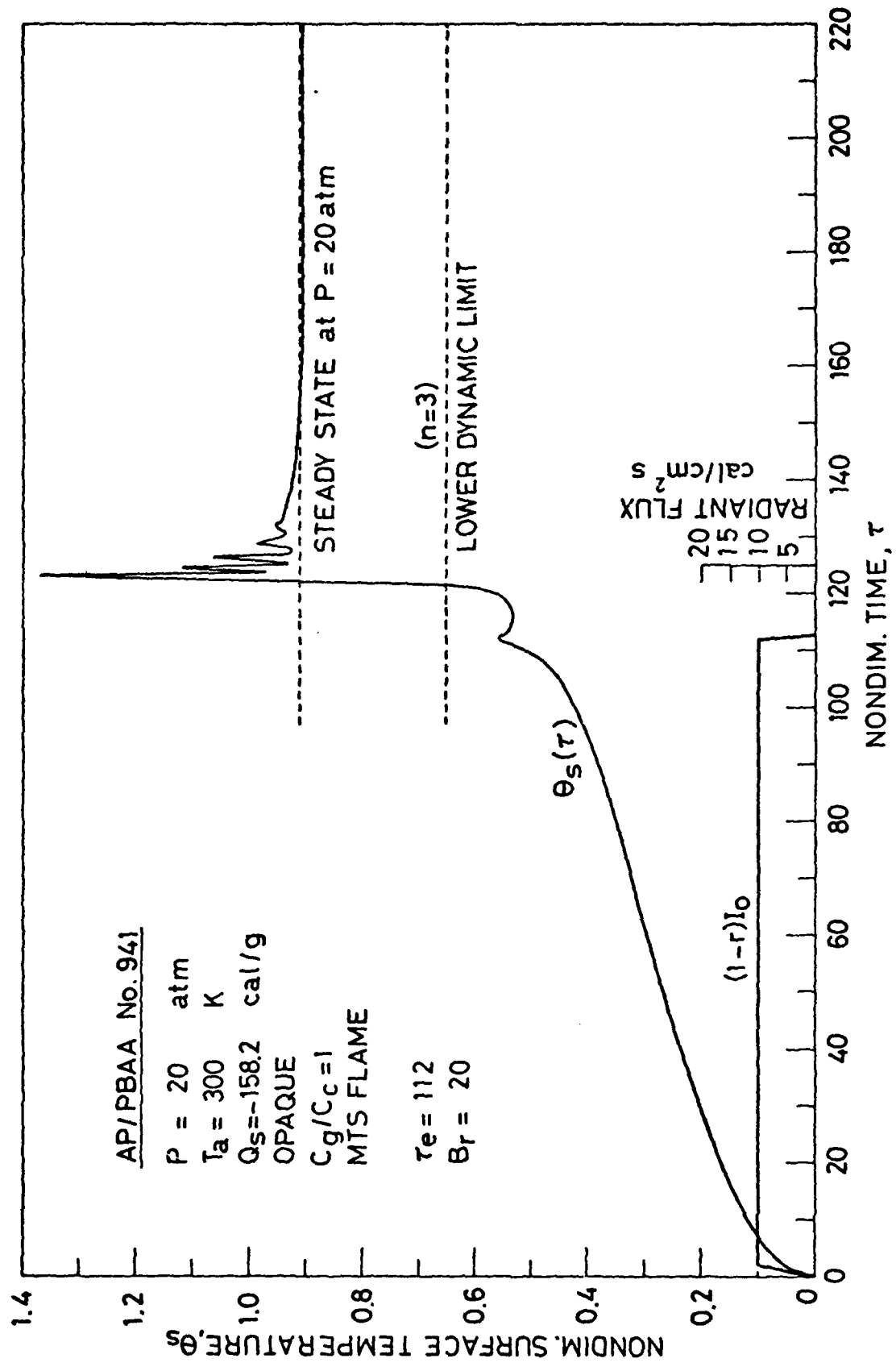


FIG. 77

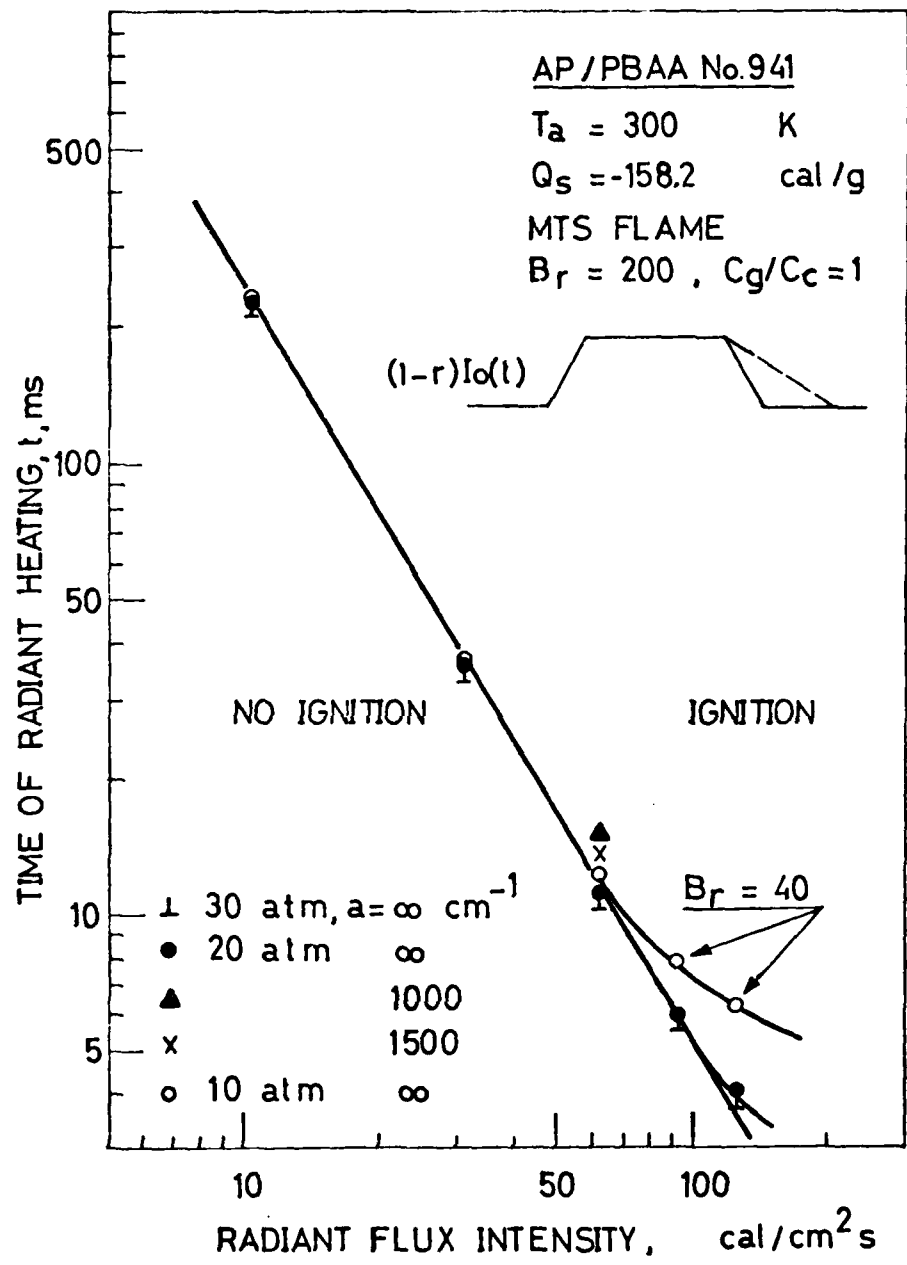


FIG. 78

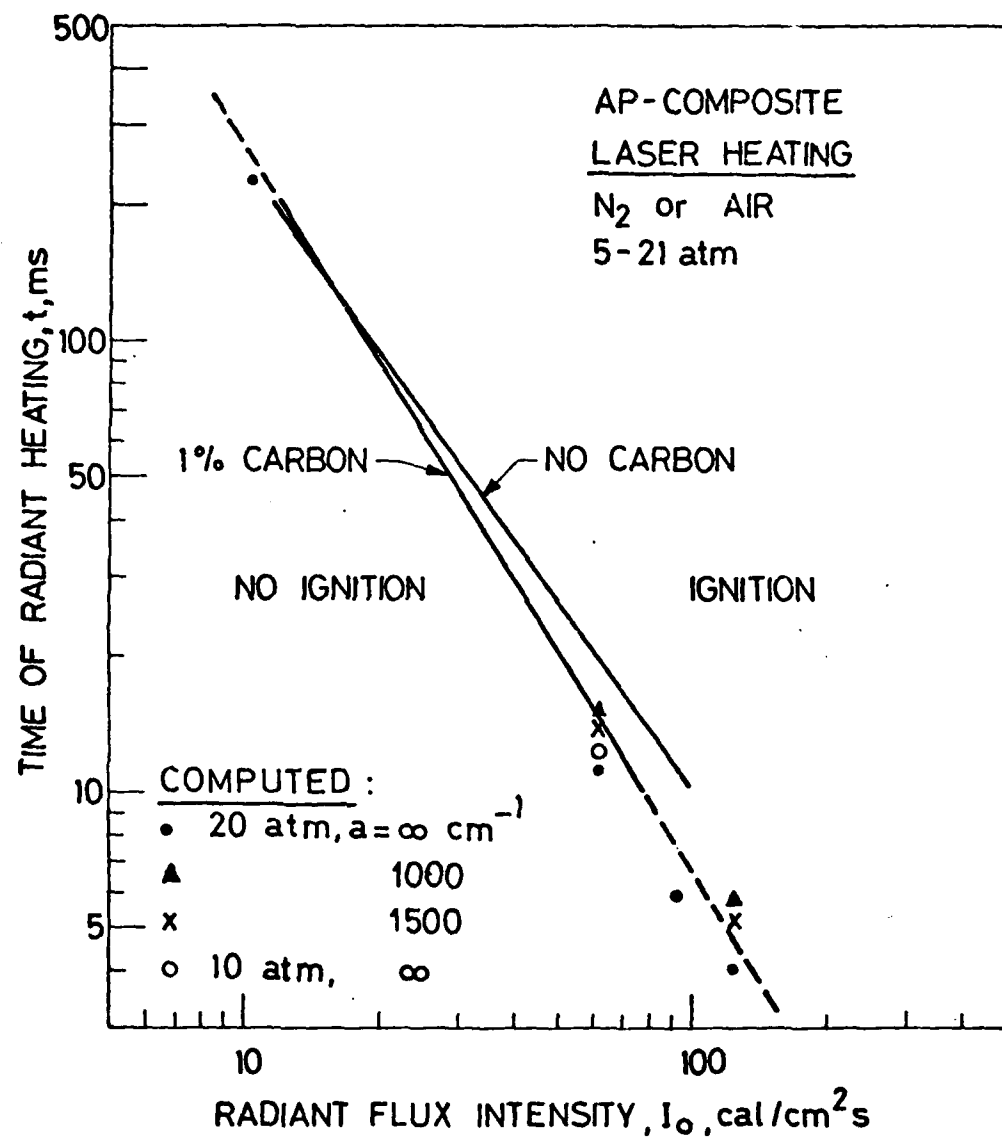


FIG. 79

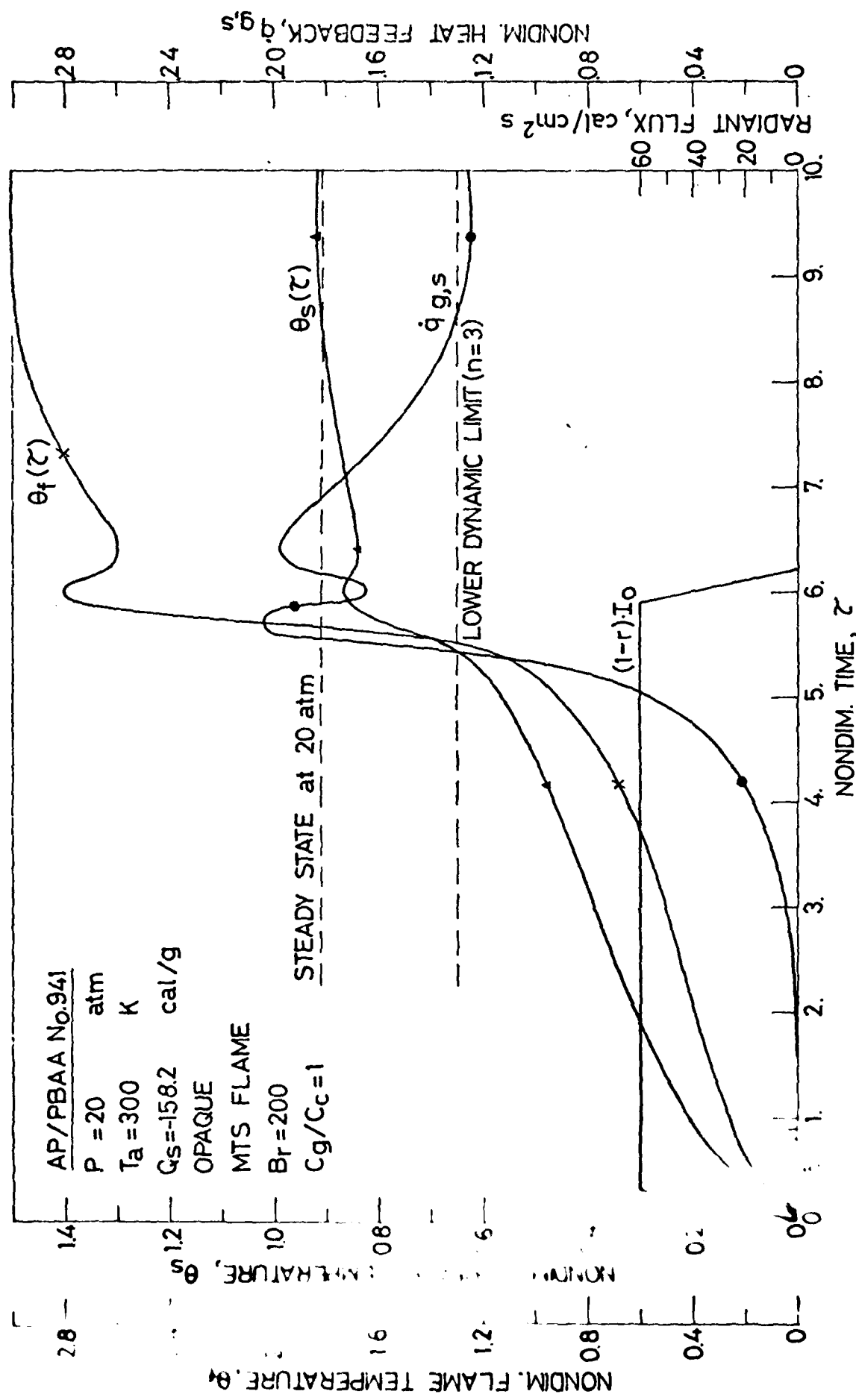


FIG.

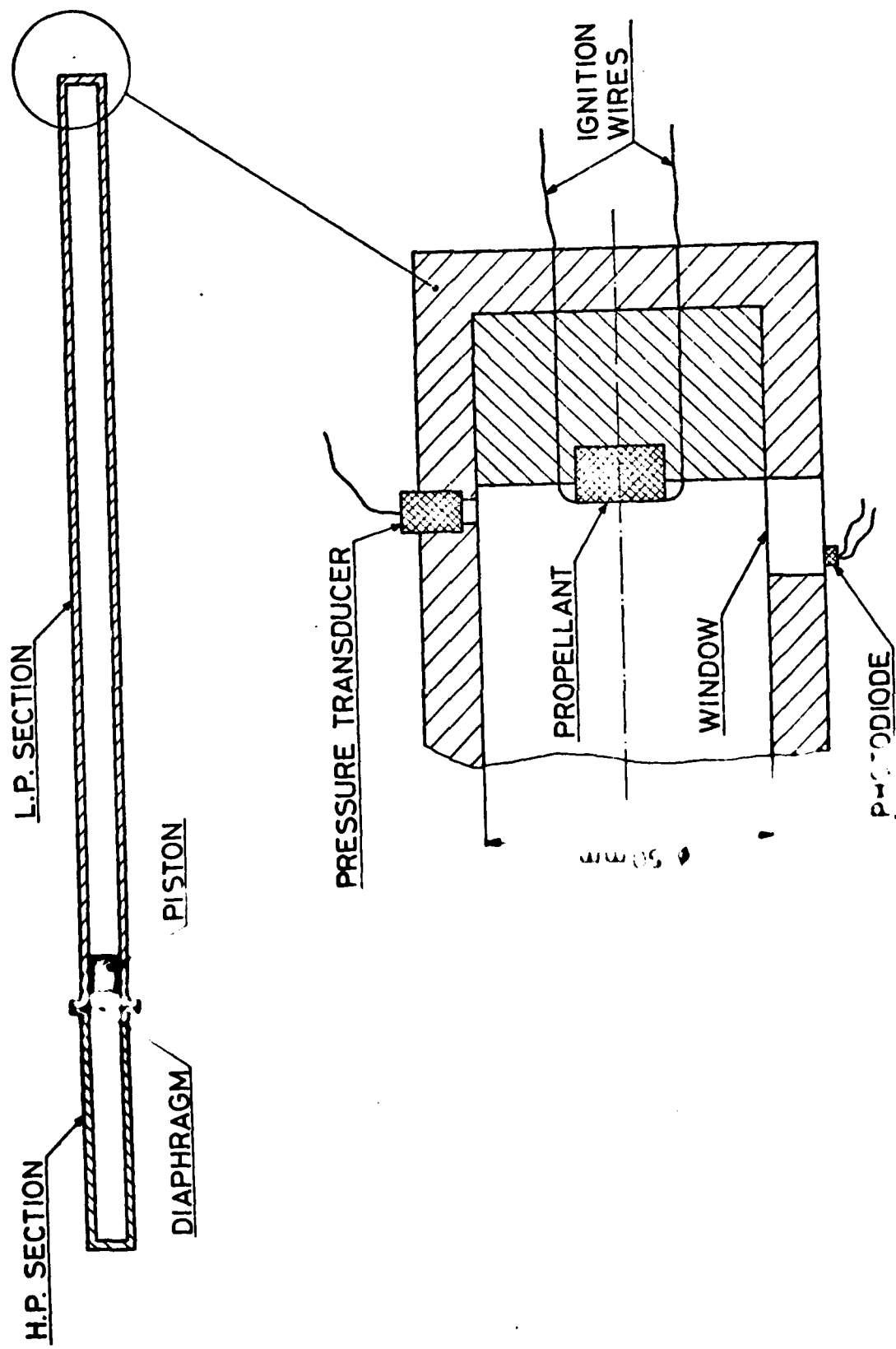


FIG. 81

COMPOSITE  
 $T_2 = 17^\circ\text{C}$

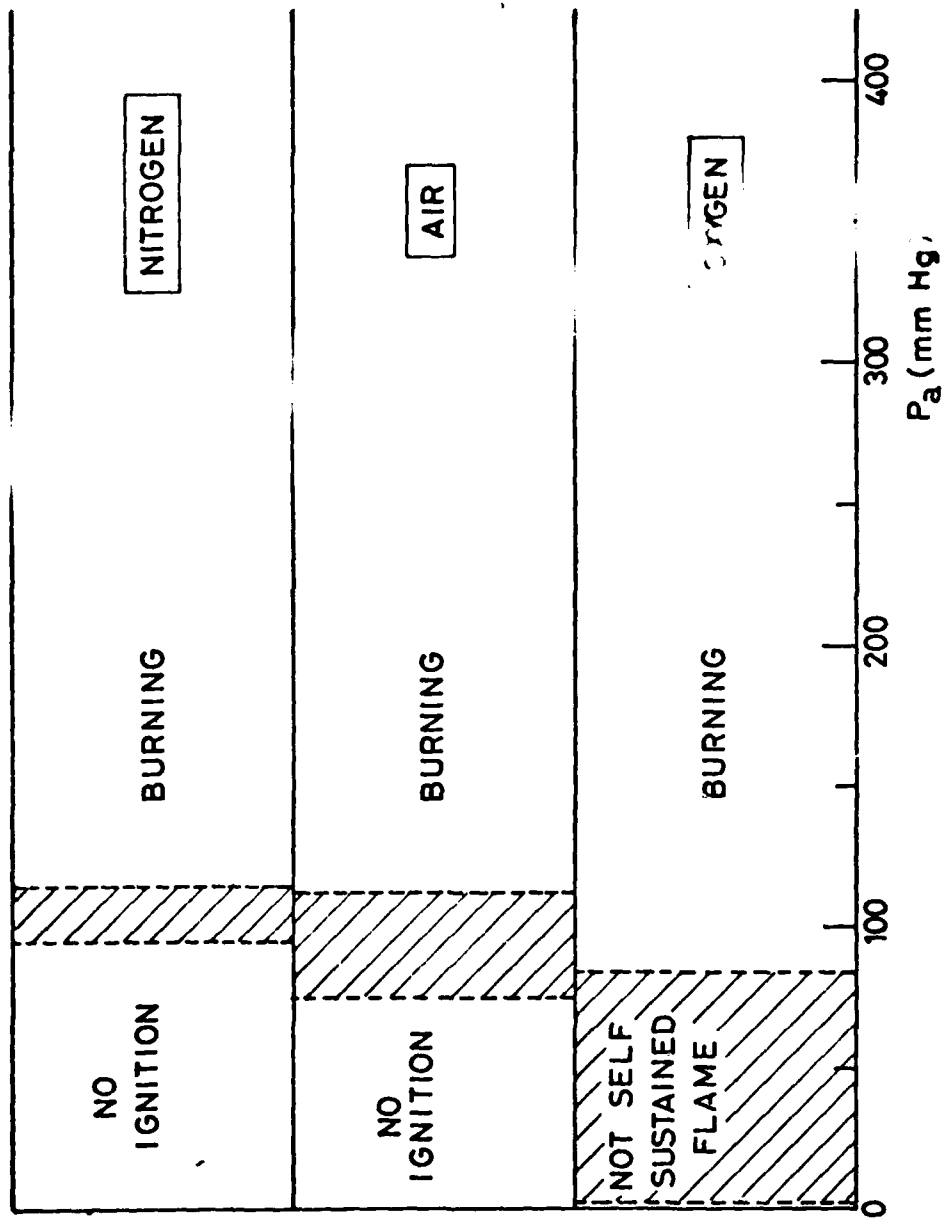


FIG. 82

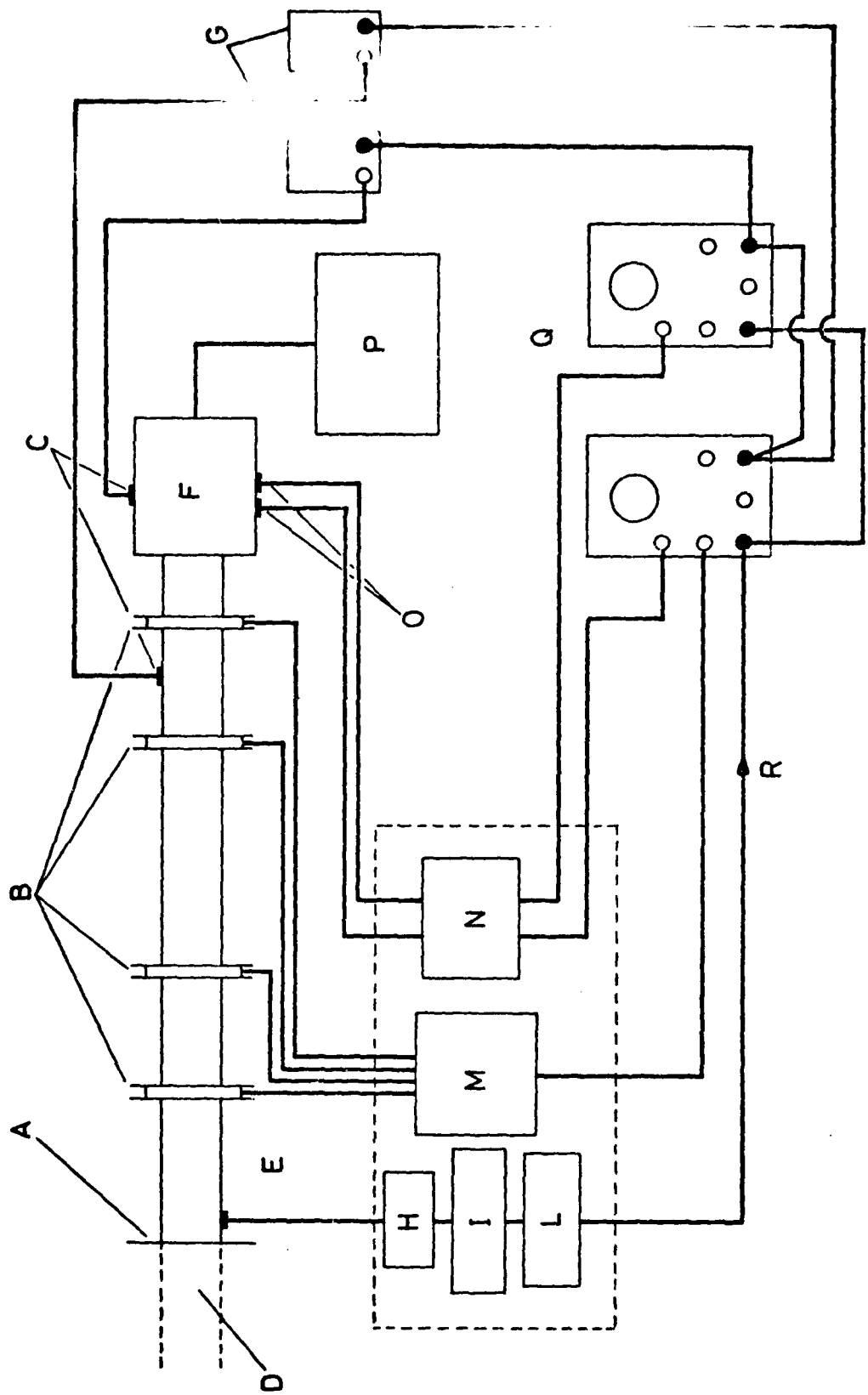


FIG. 83 a

NOMENCLATURE FOR FIG. 83

- A : Diaphragm
- B : Coils
- C : Pressure transducers
- D : Driver section
- E : Pick-up
- F : Test chamber
- G : Charge amplifiers
- H : Amplifier
- I : Smith trigger
- L : Timer
- M : Multiplexer
- N : Resistors
- O : Photodiodes
- P : Igniter
- Q : Oscilloscopes
- R : Trigger

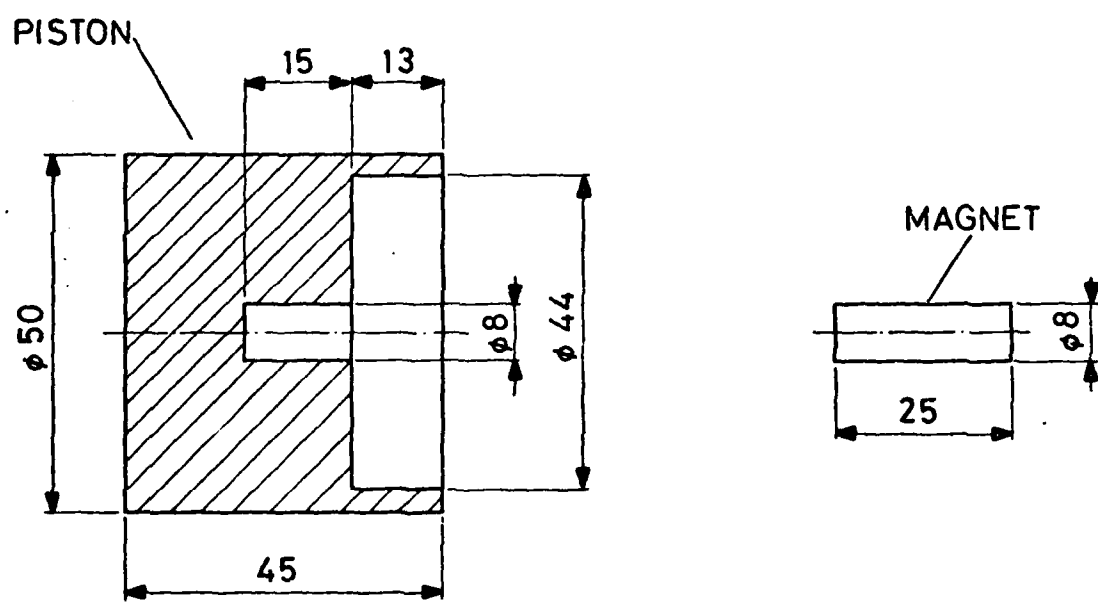


FIG. 84

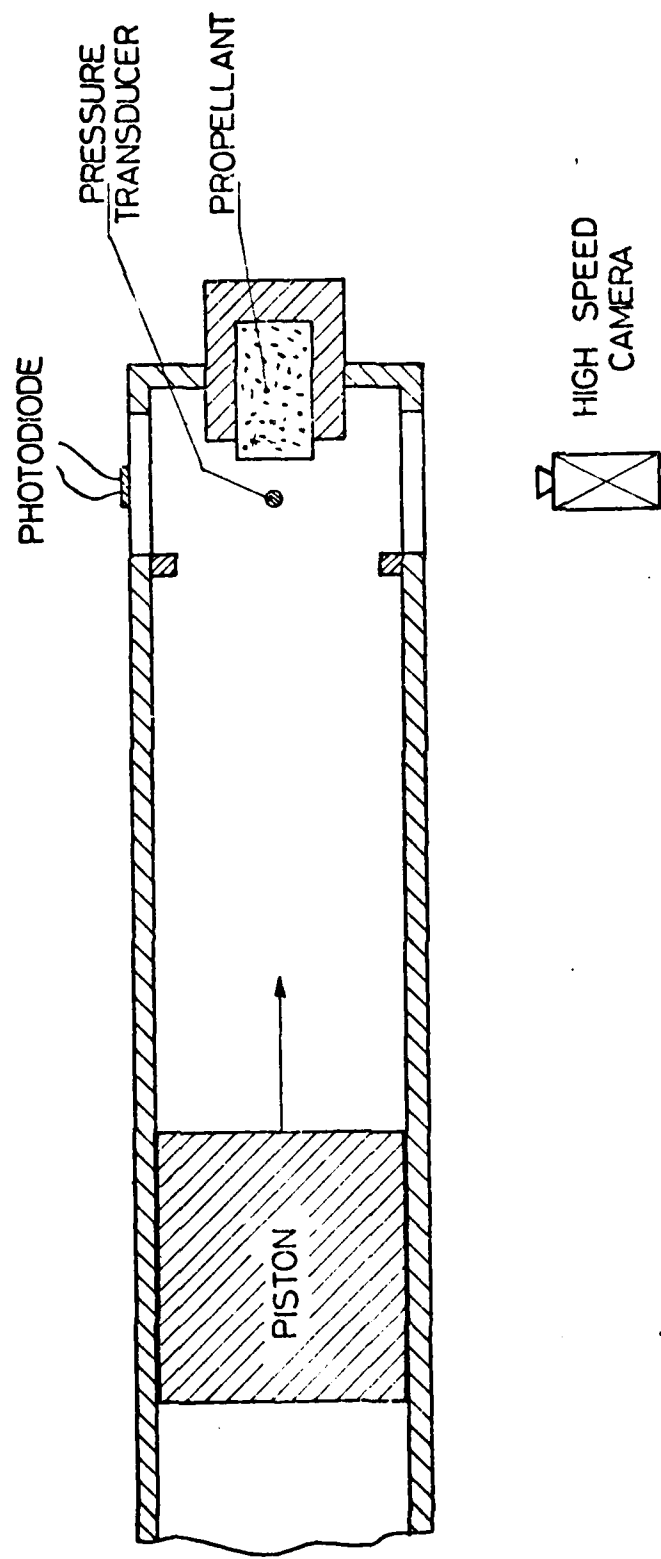
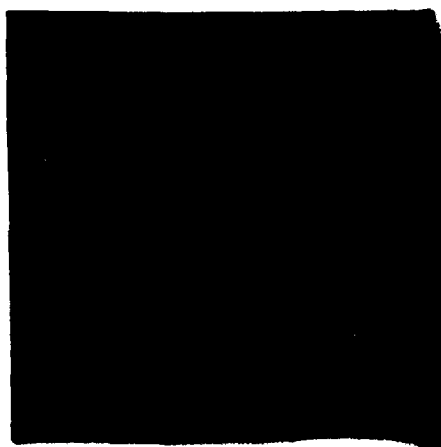
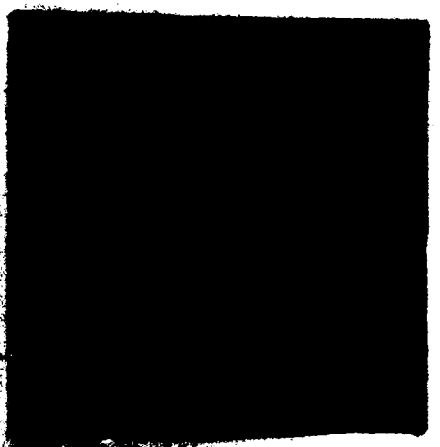


Fig. 85 sketch of the experimental apparatus



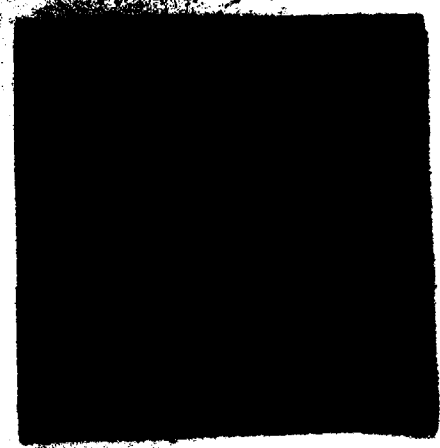
1



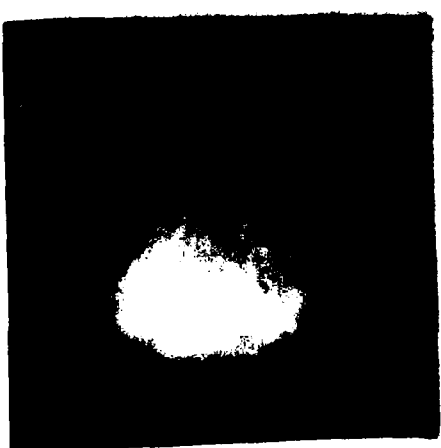
2



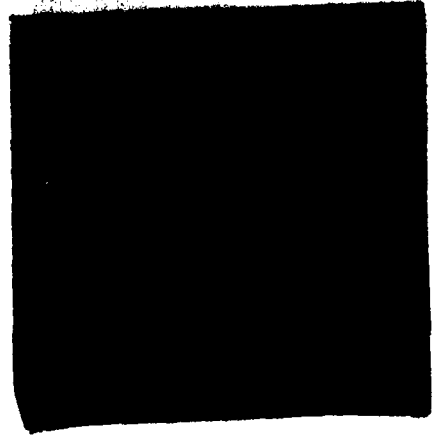
3



4



5



6

FIG. 86a

- 1) - Steady burning in air.  $p \approx 1$  ata.  $t = 0$
- 2) -  $t = 11$  ms.  $p \approx 5$  ata (increasing)
- 3) -  $t = 23$  ms. maximum luminosity.  $p \approx 30$  ata (increasing)
- 4) -  $t = 26$  ms. flame on the propellant surface.  $p \approx 100$  (around maximum)
- 5) -  $t = 29$  ms. flame away from the surface.  $p \approx 2$  ata (decreasing)
- 6) -  $t = 33$  ms. flame out of sight on the left.  $p \approx 1$  ata
- 7) -  $t = 36$  ms. flame extinguished; a small luminous dot is visible near the surface.



Fig. 86 b (end)

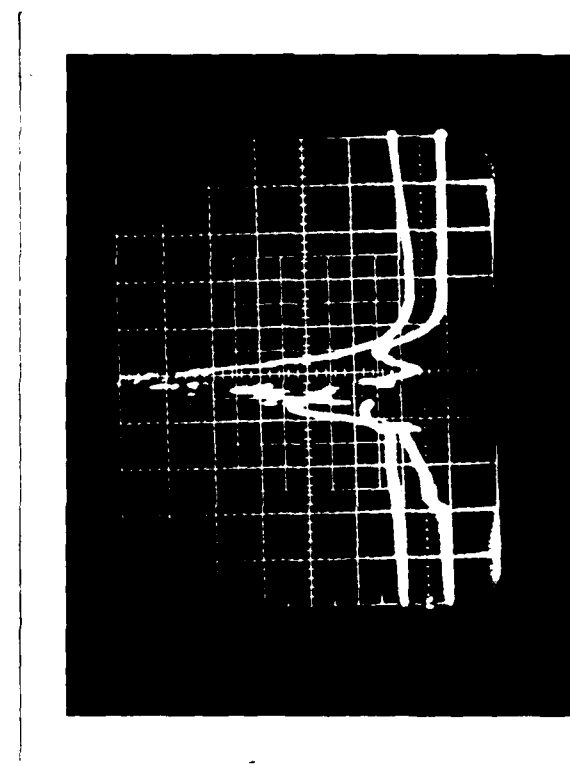
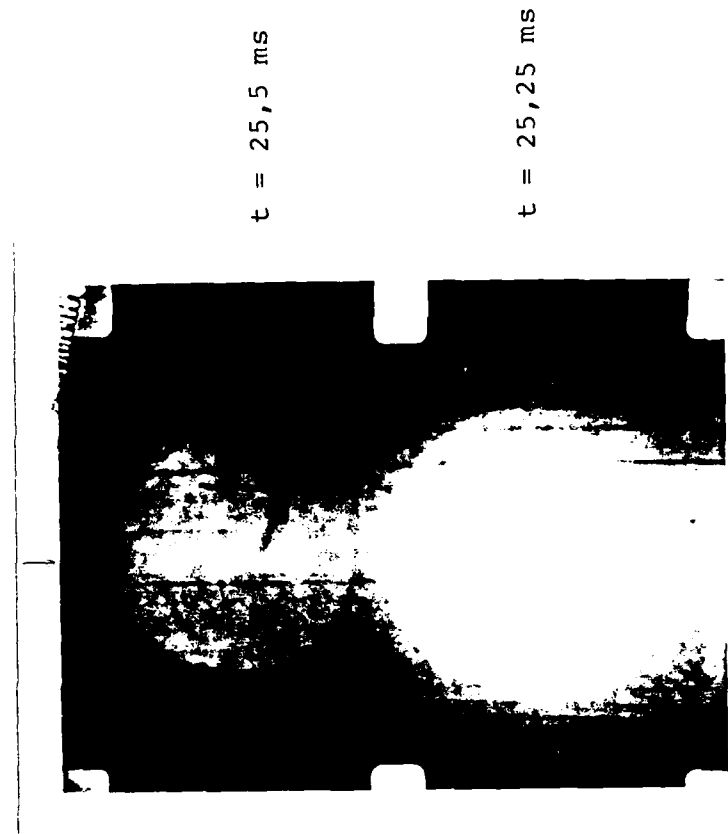


Fig. 87  
Fig. 86

Upper trace: pressure,  $p = 20$  atm/div  
Lower trace: photodiode  
 $t = 5$  ms/div

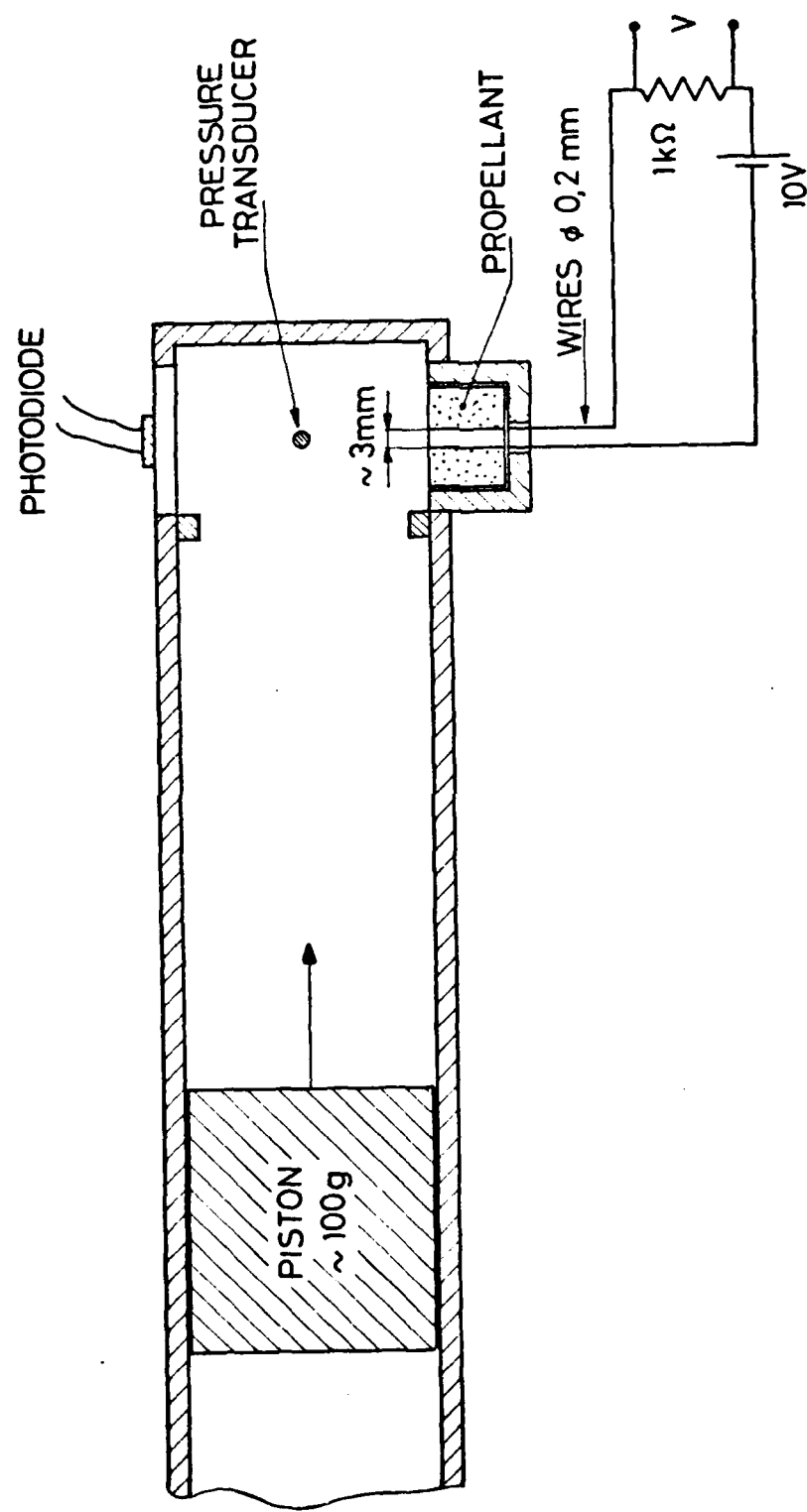


Fig. 89 Experimental setup for the measurement of the ionization at the propellant surface.

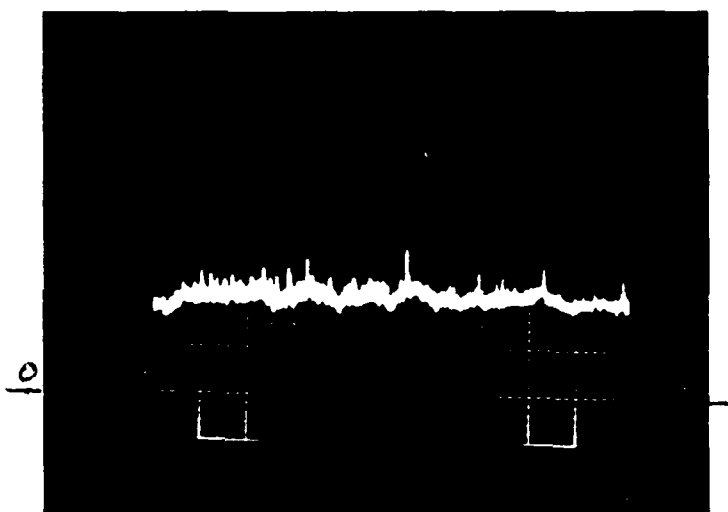


Fig. 90  
Steady burning  
 $t = 5 \text{ ms/div}$

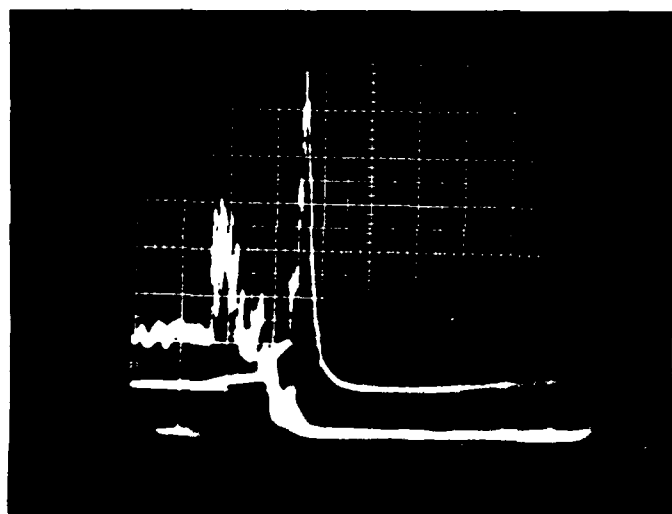


Fig. 91

transient ionization

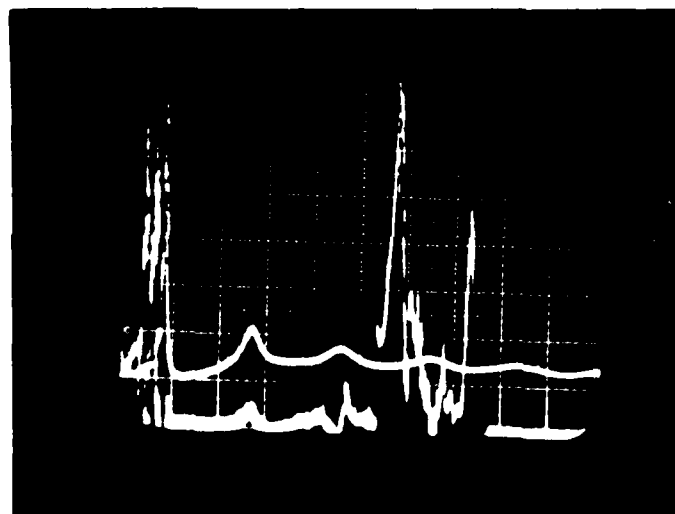


Fig. 92  
 $t = 20 \text{ ms/div}$   
Upper trace: pressure  
 $p = 25 \text{ atm/div}$   
Lower trace: ionization

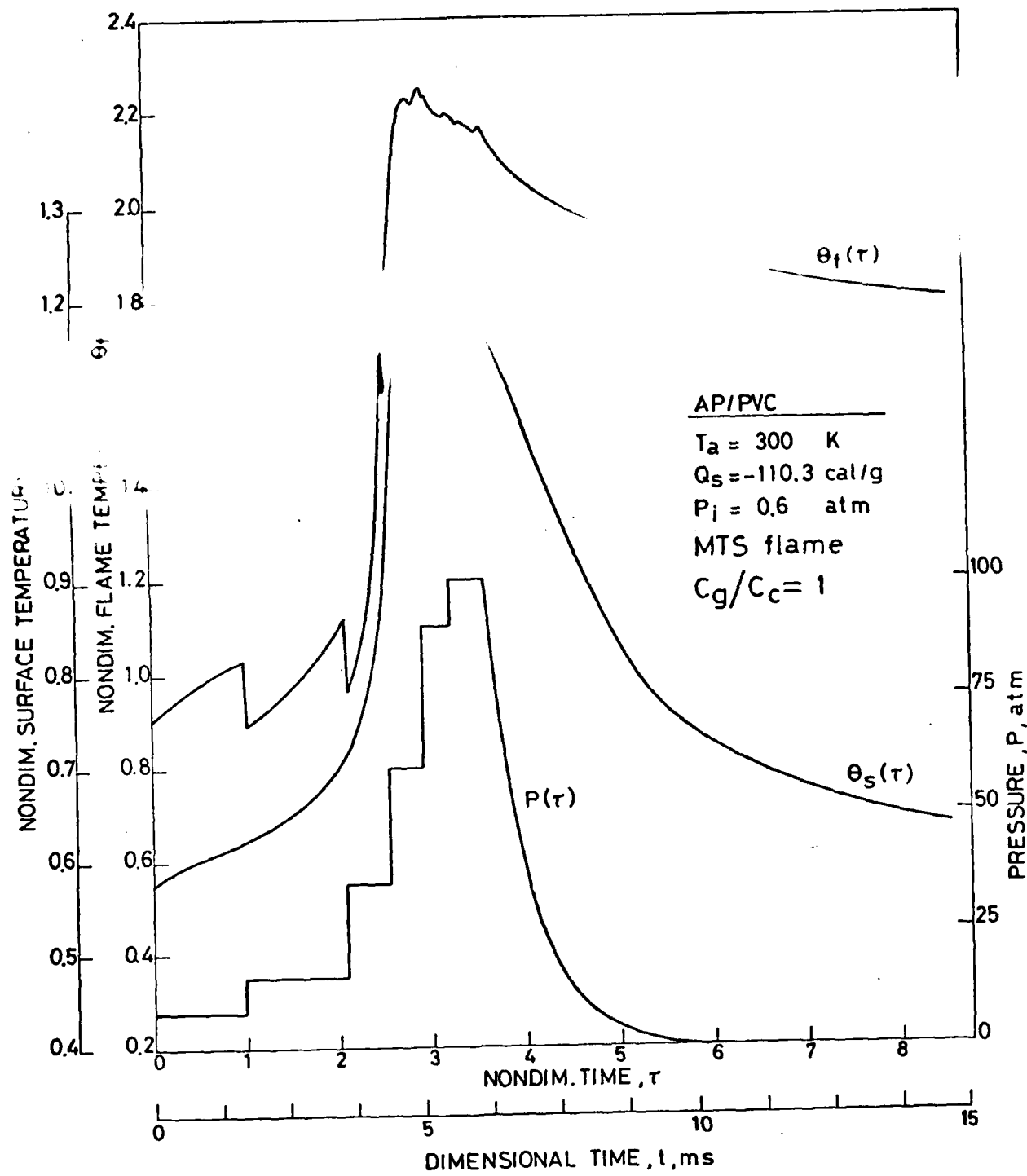


FIG. 93

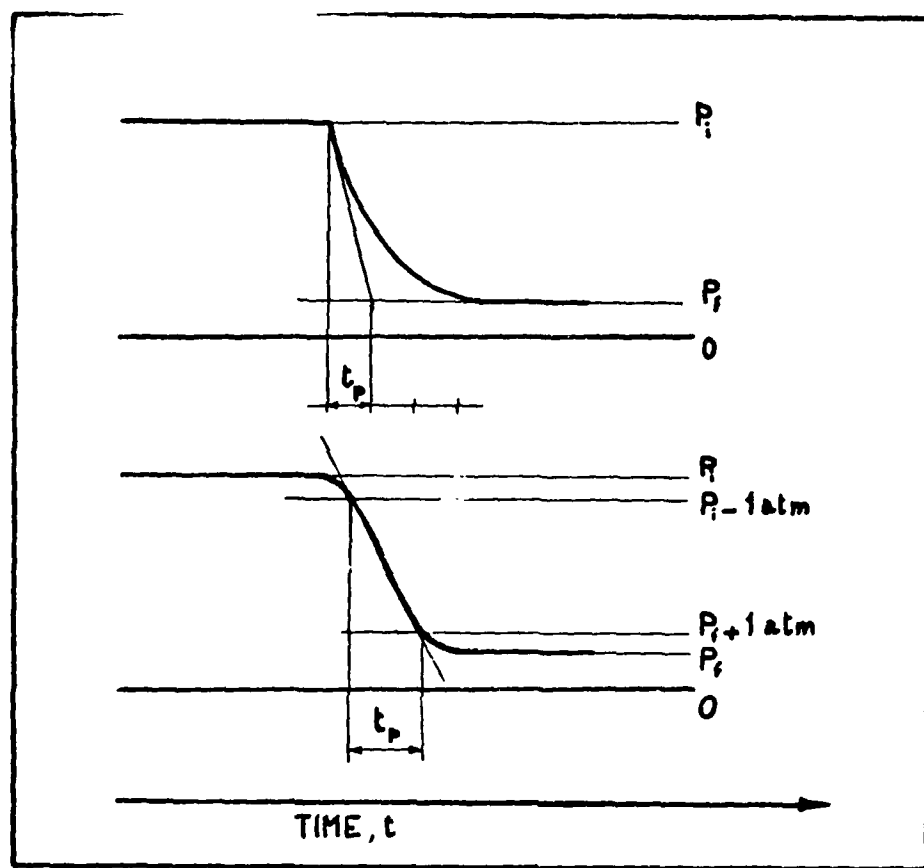


FIG. 94

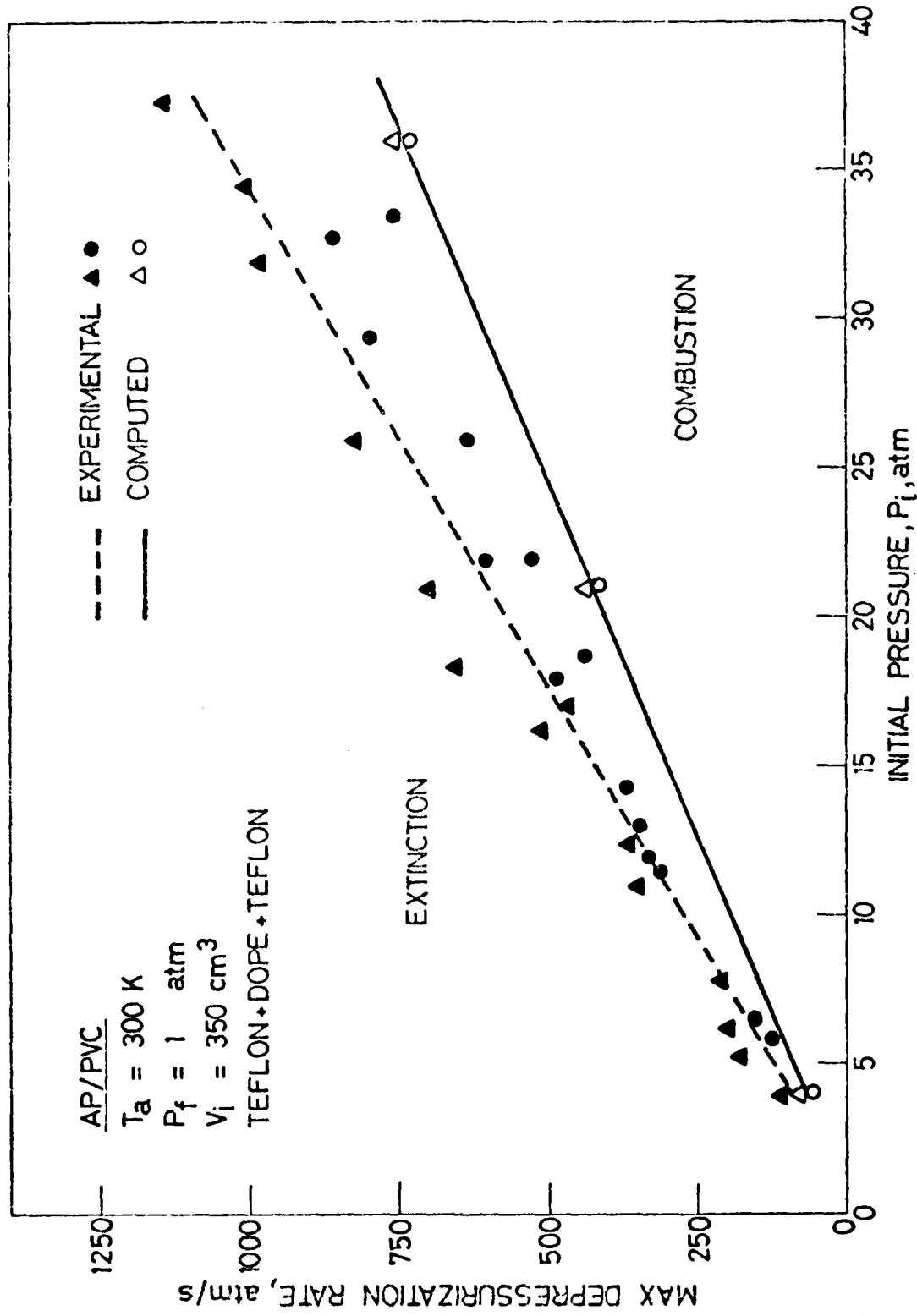


FIG. 35

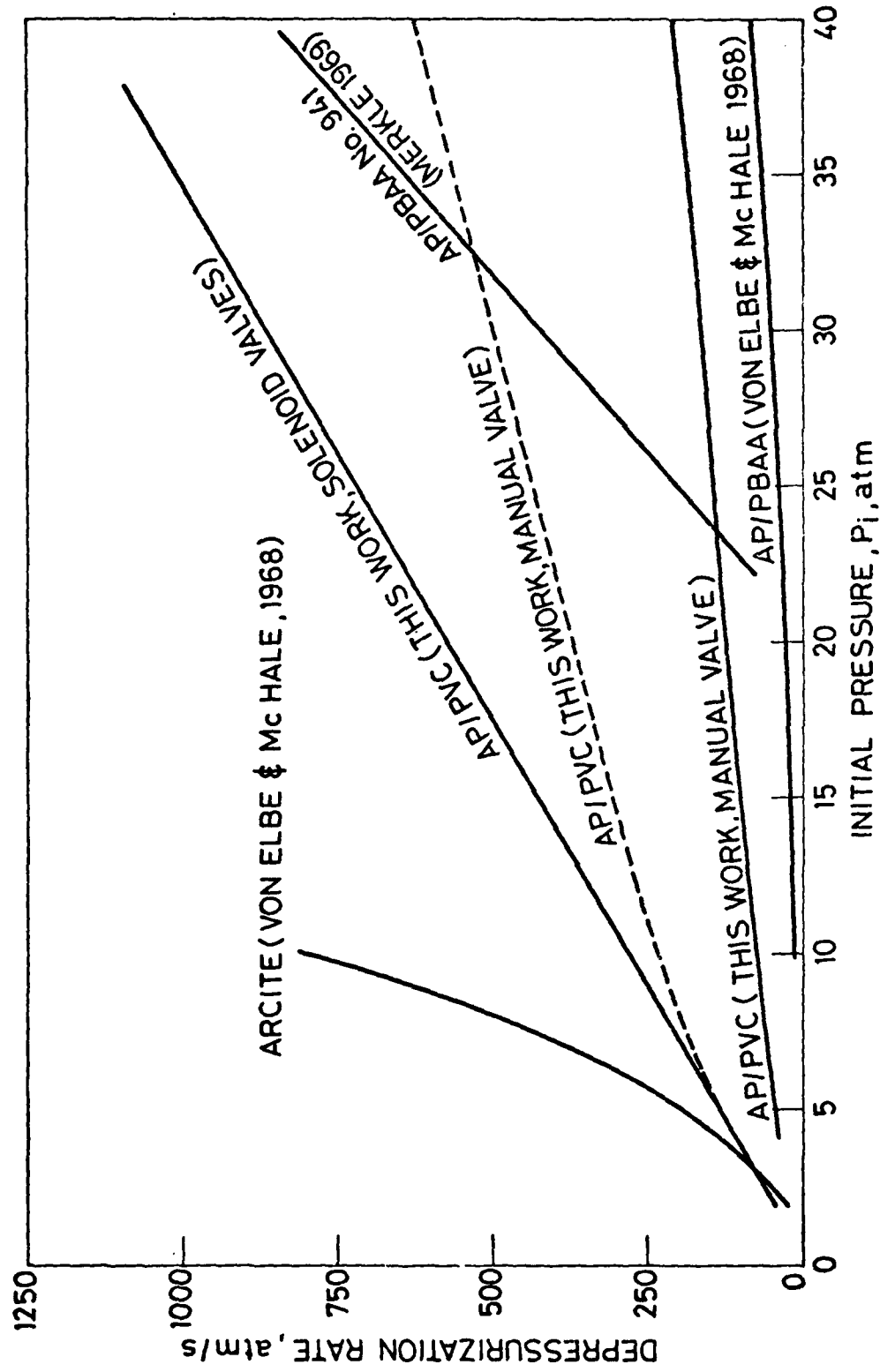


FIG. 96

## CHAPTER 4 - LASER-OPTICAL TECHNIQUES

### Sec. 4.1 - INTRODUCTION

Several nonperturbing laser-based optical techniques were developed to measure the condensed phase burning rate, the velocity profiles in the gaseous region near the combustion surface, and the size of the particles carried away by the gas in the plume of the burning solid propellant.

The Laser Doppler Velocimetry (LDV) was chosen to measure the velocity profiles in the gaseous region near the burning surface of a solid propellant. The main reason of this choice is the fact that the usual intrusive measuring techniques are of little help in a high temperature reactive medium with large thermal gradients.

Flow visualization techniques, like Schlieren optical systems, shadograph and Mach-Zender interferometer methods, give an integrated picture through the flow region. This makes quantitative analysis of results extremely difficult. Hot-wire anemometers and Pitot tubes cannot be applied to reactive media.

It is now well established that LDV technique has important advantages over more conventional techniques both for theoretical and experimental reasons. These fundamental advantages are indicated by the enormous research effort which has gone into their development over the last decade and by the number of commercial systems which have become available. The most important theoretical results required for relating the system outputs to the fluid flow parameters have now been formulated (Refs. 1,2 and 3).

Despite the complexity of a satisfactory theoretical model of the LDV, the output from this instrument is linearly related to the velocity by a simple formula and no problem is concerned with calibration. The major advantage of the LDV is the high spatial and temporal resolution associated with the fact that the instrument measures the component of velocity in a specified direction. Hence this technique can be used in very high turbulence flows and in unsteady situations.

To determine the solid propellant burning rate many laser-based optical techniques were tested in steady state configurations up to 10 atm. Results showed the possibility of accurate measurements of the instantaneous solid propellant burning rate vs time, but some residual problems are to be solved. They are related to the strong background light emission of some propellants and the requirement that the burning surface remains flat and horizontal during the measurement.

### Sec. 4.2 - LASER DOPPLER VELOCIMETRY

The basic principle involved in Laser Doppler Velocimetry is the Doppler frequency shift of a monochromatic and coherent light beam scattered by micrometric particles suspended in a moving medium.

The Doppler frequency shift is normally resolved by heterodyning the scattered light with a reference beam on the surface of a photodetector (reference beam LDV). Alternatively, scattered waves coming from two incident beams can be heterodyned (differential LDV). The resulting light intensity and, hence, the photocurrent will be modulated at the Doppler frequency (Refs. 1-3):

$$(4.2.1) \quad f_D = 2U \sin(\beta/2)/\lambda$$

where  $U$  is the particle velocity component perpendicular to the bisector of the illuminating cross-beams;  $K=2\pi/\lambda$  is the wave vector;  $\lambda$  is the wavelength of the laser beam and  $\beta$  is the angle between the two cross-beams (see Fig. 4.1). The crossing region of the two illuminating beams defines the geometrical probe volume of the LDV system that depends on the cross angle and the focal length of the focusing lens. The effective measuring volume has a more complicate definition, depending on the magnification of the collection optics, its angular position,  $\gamma$ , and aperture,  $\Omega$ . Amplification and triggering level of the electronics have to be also considered.

In all the optical configurations, two laser beams are focused onto a specified point in the flow and light is scattered by small tracer particles, as they pass across this point.

The differential LDV mode is most commonly used because of its higher signal to noise characteristics at moderate particle concentrations. Moreover, this type of LDV system is the best suited for individual realization velocimetry and parallel particle size analysis. It is not difficult to realize the situation in which the Doppler signal, that is available for processing, is produced by no more than one particle in the probe volume at a time. In fact, it is possible to adjust the probe volume dimensions, both in diameter and in length, by selecting the proper cross-beam angle and the magnification of the light collecting system. The main advantage of the differential LDV is that it is quite simple to align and is not sensitive to small vibration. Also, the Doppler frequency is independent of the detection angle and a large collection aperture can be used without a spread of Doppler frequency.

A picture, which is often used to describe this system, is the so called "fringe model" that involves visualising a set of interference fringes produced by two incident laser beams in their cross region. The Doppler signal is produced by light scattered from particles crossing the intersection of the illuminating beams (probe volume), when the scattered light, collected through a receiving lens, reaches a photomultiplier (see Fig. 4.1).

Since the LDV requires the presence in the air flow of microscopic particles, this complicates the use of the technique considerably. In fact, these particles, naturally present or seeded in the flow, should be in size and density such as to follow the flow field. Thus, for accurate measurements of turbulence of unsteady flows, some check of particle dynamics must be made. The capability of particles to follow the gas flow can be roughly estimated from the Bassett's general equation (Refs. 4 and 5). On the assumption that the particle density  $\rho_p$  is larger than the gas density  $\rho_g$ , the Bassett's equation reduces to

$$(4.2.2) \quad \frac{d U_p}{dt} = \frac{1}{\tau} (U_g - U_p)$$

where

$$(4.2.3) \quad \tau = \frac{(2 \rho_p + \rho_g) d^2}{36 \mu}$$

being  $U_p$  and  $U_g$  the particle and gas velocities;  $d$  the particle diameter and  $\mu$  the gas viscosity.

The parameter  $\tau$  has the meaning of a relaxation time for a particle of diameter  $d$  subjected to a spatial velocity gradient. The evaluation of  $\tau$  necessitates the knowledge of the particle density and size distribution.

In unsteady flows the LDV instrument must be treated as a transducer for which the transfer function is determined by the dynamics of tracer particles. This is a disadvantage of considerable importance in air flows where seeding with particles of known size is not likely to be feasible.

The performance of an LDV system strongly depends not only on the size distribution, but also on the concentration of scattering particles. In fact, their number density has to be high enough to obtain good time resolution of the velocity measurement. It must be noted that the time resolution of LDV depends on the particle rate,  $\dot{n}$ , across the measuring volume, hence on the particle concentration,  $N$ , the mean particle velocity  $\bar{U}$  and the effective probe volume cross section,  $S$ :

$$(4.2.4) \quad \dot{n} = \alpha N \bar{U} S$$

where  $\alpha$  is an efficiency factor taking into account amplification and triggering level of the electronics. To obtain a quasi-continuous velocity information, a sufficiently large number of scattering particles ( $\geq 10^8 \text{ m}^{-3}$ ) is required.

In fact, since the particles arrive randomly, the data obtained are randomly collected, with an approximately Poisson distribution of time instants. Time resolution could be limited by the above mentioned characteristics, but it can be good enough if particle number density is high.

In conclusion size distribution and concentration of scattering particles are two important factors in LDV, especially in unsteady flows. For better time resolution and velocity measurement accuracy, we need that particle rate is high and size distribution is within limited bounds.

Our LDV experiments were performed by using as scattering centers the particles present in the plume of the burning solid propellant sample. No external seeding was used in order to avoid any disturbance of the combustion processes. Preliminary experiments showed that, generally, sufficiently high particle rates are found in the region near the burning surface.

The LDV system comprises a 5 mW He-Ne laser and a beam splitter with variable beam separation, which allows continuous variation of the cross-beam angle. The two different parallel laser beams were directed toward the lens  $L_1$ , in such a way that one laser beam was centered on the lens axis. This beam is not diverted from its horizontal direction, but focused on the focal point (on the axis of the strand burner). The second beam is impinging on the lens  $L_1$  at a distance  $h$  from the axis, and is deflected and focused in the same focal point. The crossing region defines the probe volume of the LDV system and the velocity component in the vertical direction can be measured. With the geometry of Fig. 4.2 the measured velocity component is not exactly the axial one; however the difference, of the order of  $\sin(\beta/2)$ , is not significant for small  $\beta$ .

The receiving optics of the LDV system comprises: the lens  $L_2$ , fixed on the burner window, that collects the radiation scattered in the forward direction; the lens  $L_3$  that is movable and focuses the scattered light on a 0.3 mm pinhole in front of a photomultiplier. This is equipped with an interferential optical filter, centered at  $632.8 \pm 1.0$  nm (the laser wave-length), in order to reject flame emission.

The photomultiplier signal is processed by an electronic counter processor (DISA mod. 55L90) that allows working with variable particle concentration and does not have drop-out problems. Moreover, it has a large dynamic range and no slewrate limitations; it accepts individual signals and determine the correct Doppler frequency, hence, the particle velocity. Proper use of this instrument would require rejection of multiple particle signals, because of random phase fluctuations which will lead to incorrect velocity measurements (Ref. 6). This requirement can be generally satisfied by proper reduction of the probe volume dimensions.

#### Sec. 4.3 - PARTICLE SIZING

The feasibility of "in situ" particle sizing in hostile environments by non-intrusive techniques is still questionable. Recently, Farmer et al. (Ref. 7) compared a new particle sizing interferometer and a commercial optical counter in rock-

ket exhaust, but results suggest that no one particle size instrument can give convincing measurement.

Attempts to solve the problem of the determination of particle size distribution have been performed by using many techniques, but their use in hostile environments is generally difficult. Measurement of the light scattered by droplets or solid particles, using a laser source, can be used for "in situ" particle sizing. The angular dissymmetry of the scattered light intensity, the dependence of the scattered intensity on incident light polarization and the light extinction were used in determining small carbon particulate size distribution (Refs. 8 and 9).

A system able to simultaneously determine the size and the velocity of individual fuel droplets is of considerable interest in combustion and thus particular attention was devoted by many research workers to the analysis of the scattering phenomena involved in the LDV system. It was demonstrated that a particle crossing the intersection of two laser beams scatters a modulated light signal containing many informations: a) its modulation frequency is proportional to the particle velocity; b) its signal amplitude and the A.C. amplitude divided by the mean amplitude are related to particle diameter.

A forward scattering LDV system and predictions of mean scattered light power, made by using geometric optics theory, were used to demonstrate that an unambiguous one-to-one relationship can be obtained between signal amplitude and particle diameter for non absorbing particles in the diameter range 30 to 240  $\mu\text{m}$  (Ref. 10). The main disadvantage of this method is the need of a calibration of the signal amplitude vs particle diameter. This is not a problem if the ratio between A.C. and mean amplitudes is considered. This ratio is called visibility

$$(4.3.1) \quad V = \frac{I_{\text{Max}} - I_{\text{min}}}{I_{\text{Max}} + I_{\text{min}}} = \frac{D}{P}$$

where  $I_{\text{Max}}$ ,  $I_{\text{min}}$ ,  $D$ , and  $P$  are defined in Fig. 4.1

The first derivation of the visibility function was made by Farmer (11) under the assumption of paraxial scattering. Robinson and Chu (12) used scalar diffraction theory to determine the forward scattered fields. More recently, Bachalo (13) extended the visibility model to allow off-axis light collection and to cover a wide size range of 5  $\mu\text{m}$  to 5 mm, by using geometric optics theory.

A more rigorous analysis requires the use of the Mie theory for scattering by spherical particles illuminated by two coherent beams (Refs. 14, 15, 16 and 17). In this case any off-axis light collection direction and aperture can be considered, but Mie formula calculations must be performed by large computers which are capable of evaluating the lengthy series of Bessel functions and Legendre polynomials involved.

It is normally accepted (Refs. 14, 15, 16, 17 and 18) that the single particle Doppler signal can be accurately predicted

on the basis of the Mie scattering theory. The general expression of the Doppler photocurrent, produced by a single particle crossing the geometric center of the probe volume, is given by

$$(4.3.2) \quad i(t) = \frac{\eta I_0}{K} \left\{ P(\theta, \phi) + D(\theta, \phi) \cos [\omega_D t - \Psi(\theta, \phi)] \right\}$$

where  $\eta$  is detector sensitivity,  $\omega_D = 2\pi f_D$ , and the two incident beams are assumed to have equal intensities  $I_{01} = I_{02} = I_0$ . The term  $P$  represents the "pedestal" amplitude of the current (Fig. 4.1) while  $D$  represents the Doppler amplitude and  $\Psi$  determines the phase of the scattered intensity.  $P$ ,  $D$ , and  $\Psi$  are integral quantities, integrated over the collecting solid angle,  $\Omega$ , of the receiving optics. They depend on the direction of detection  $(\theta, \phi)$  i.e. the axis of the collecting aperture, and are defined in terms of the complex amplitude functions given by the Mie theory (Refs. 19, 20 and 21).

The quantities  $P$ ,  $D$  and  $\Psi$  depend only on the scattering properties and size of the particle (for a fixed LDV geometry), whereas the photocurrent is a time-varying function of the particle position in the probe volume. Indeed, a moving fringe pattern is seen by the detector due to two beam interference and particle motion.

The fringe contrast or visibility is defined by Eq. 4.3.1; the exact dependence of  $V$  on particle diameter,  $d$ , can be numerically obtained through  $P$  and  $D$  evaluated by a computer code (Ref. 17) based on Mie scattering formula. It is possible to express the visibility in a functional form

$$(4.3.3) \quad V = V\left(\frac{\pi d}{\lambda}, m, \frac{d}{\beta}, \Omega, \gamma, \xi\right)$$

where  $d$  is the diameter of the scattering particle,  $m$  is the complex refractive index of the particle,  $\beta$  is the cross-angle of the two laser beams,  $\lambda$  is the laser wavelength,  $\gamma$  and  $\xi$  are angles defining the position of the axis of the collecting aperture,  $\Omega$  is the collecting solid angle and  $\delta = \lambda / (2 \sin(\beta/2))$ .

It can be noted that visibility depends, among the other parameters, on the diameter of scattering particles. The practical application of the method for particle sizing is based on the hypothesis that in the range of interest visibility is sensitive to particle diameter and an unambiguous one-to-one relation  $V(d)$  can be defined. Because of the large number of possible arrangements of the parameters appearing in Eq. 4.3.3; it is quite impossible to give a complete representation of the visibility behavior. A wide theoretical analysis of the useful range of utilization of the visibility method was performed (Ref. 22) and it was found that in forward scatter, with small cross-beam and collecting angles, the refractive index of the particle has no significant influence and a one-to-one corre-

spondence between visibility and particle diameter can be obtained up to about 80  $\mu\text{m}$ .

Some experimental results reported in the literature showed the possibility of parallel measurements of individual particle velocity and size (Refs. 14,17,18,23,24 and 25). Applications include particle size measurements from calibrated monodisperse aerosols, polydisperse fuel sprays in combustion and dusts in the atmosphere.

Since the first work of Farmer (Ref.11) the particle sizing technique based on visibility received more and more attention by different workers and many comparative tests were performed in order to establish the correct interpretation model of experimental data. Nevertheless, the absolute reliability of this technique is not yet well established. The major problem is related to experimental complexity of real time visibility measurements, but some theoretical uncertainty still remain. The problem is complicated by the absence of alternative reliable techniques for real time *in situ* particle sizing.

At the CNPM we have been involved in preliminary studies on this subject and it was demonstrated (Ref. 23 and 24) that the visibility technique can be also used in flames of liquid sprays with an high background luminosity. But no comparative confirmation can be obtained by other experimental procedures.

A knowledge of particle size distribution will be of fundamental importance for accurately measuring gas phase flow field associated with a burning solid rocket propellant in unsteady conditions, because of the large velocity gradients. In fact, if the natural particles (carried away by the gas in the plume of the burning solid propellant) are used as scatterers it would be necessary to correlate velocity and size of each particle, before validation of the velocity measurement, in order to be sure that the observed particle is adequately following the gas flow.

#### Sec. 4.4 - EXPERIMENTAL APPARATUS

A steady state strand burner, with two symmetrical and opposite optical windows, was specifically designed for LDV experiments. The operating pressure range is 1 to 10 atm. A computerized data acquisition and processing system was also realized. The apparatus has been applied to a steadily burning solid propellant, with the purpose of exploring the possibility of future applications to unsteady situations. Several tests of preliminary nature were performed using double-based(DB) (both catalyzed and noncatalyzed) and ammonium perchlorate(AP) based composite solid propellants. The differential mode of operation was used for the LDV instrument, with observation in the forward direction (Fig.4.2).

The experimental conditions are now schematically described. Initially, the rod of solid propellant, centered on the axis of the burner, shuts out the two incident laser beams. When the rod burns, its surface goes down and at the instant  $t_0$  the horizontal beam is allowed to pass. After a delay  $\Delta t$ , the second beam is also passing and the scattered light with Doppler informations is received by the photomultiplier. A triggering signal, coming out from the photodiode (P.D.) intercepting the horizontal beam, precisely defines the instant  $t_0$ . From this the instantaneous axial position of the LDV probe volume, with respect to the burning surface, can be inferred by comparison of the time delay and the propellant burning rate. The strand burner is also equipped for simultaneous measurements of the propellant burning rate and the instantaneous pressure (Ref. 26).

The delay  $\Delta t$  can be related to a dead zone, above the burning surface, in which LDV measurements cannot be made, as shown in Fig. 4.3. The dead zone thickness  $h$  depends on the cross-beams angle  $\beta$  and on the radius  $r$  of the solid propellant rod:

$$(4.4.1) \quad h \approx r \cdot \operatorname{tg} \beta$$

For example, with  $r=3$  mm and  $\beta=4.7^\circ$  it will result:  $h \approx 0.25$  mm, that is of the order of the probe volume transverse dimension (see Table 4.1). By increasing the  $\beta$  angle the probe volume dimensions are reduced, but the dead zone thickness will be larger.

The burning rate of the solid propellant was initially measured by standard techniques (Ref. 26). Later on, a new technique was developed on the non perturbing laser system shown in Fig. 4.4. The beam of a 5 mW, He-Ne laser was enlarged by a beam expander, passed through a variable diaphragm and directed on the sample of the solid propellants. The beam radius was chosen less than the solid propellant radius, therefore the whole beam is initially stopped. When the burning surface goes down, an increasing portion of the laser beam is transmitted and then collected on a photodiode by means of a focusing lens. A Centronic Quadrant Detector was used, since this kind of photodiode allows a linear relationship between the voltage output and the displacement of the burning surface. A calibration curve referring to an illuminating beam diameter of 3.5 mm is shown in Fig. 4.5. The ordinate is the photodiode voltage output and the abscissa is the solid sample displacement referred to an arbitrary position. The curve was obtained by means of a non burning sample of propellant displaced by a micrometer screw in steps of 0.2 mm. Obviously, accurate measurements of the solid propellant burning rate require that the burning surface remains flat and horizontal. The advantage of this technique is its non perturbing character and continuous output over the fixed spatial range. For example, it points out any change of the burning rate during the LDV measurements.

With propellants characterized by a strong light emission an interferential optical filter was used in front of the photodiode, but when testing AP propellants it was necessary to account for the radiation emitted by the burning propellant also into the bandpass of the optical filter. Therefore, a rotating shutter (chopper) was inserted into the incident laser beam (see Fig. 4.4). In conjunction with a look-in amplifier, it allowed the synchronous subtraction of the background radiation and permitted accurate measurements.

#### Sec. 4.5 - EXPERIMENTAL RESULTS

Many tests were made with the experimental conditions summarized in Table 4.1. If the pass-band filtered Doppler signal, relative to a single scattering particle, satisfies a number of validation conditions, in terms of amplitude level and signal to noise ratio, the counter processor measures the Doppler frequency by means of a zero crossing method.

Four modes of operation of the counter can be selected. In this case, with a relatively poor signal to noise ratio, the best suited mode is characterized by a 2-level validation and 5/8 comparison. When the Doppler burst exceeds a pre-set threshold level, the counter proceeds to measure first 5 and then 8 cycles of the burst and compares the results. If these differ by less than a preset amount, the second count is validated and transferred to a buffer interface (DISA, mod. 57G20). This was required in order to transmit correctly data to the computer. Because the data are coming randomly from the LDV system and very short intervals may occur between samples, which exceeds the data transfer capabilities of the syncroneous transfer of data to the computer, a buffer memory is an integral part of the interface. The DISA buffer interface can be used as a transient recorder. After storage in the buffer, the data in digital form can be read out via the parallel interface under control of the computer.

The DISA counter delivers three words of data:

- the Doppler frequency;
- the time interval between successive samples;
- the number of fringes traversed by the scattering particles.

All this information is of great importance in the further processing, if data have to be corrected for velocity bias errors (Ref. 6) and the timing of input data must be reconstructed.

The data acquisition and processing system was based on a DIGITAL PDP 11/03 minicomputer, equipped with 32 K-words of memory, a dual floppy disc unit, a teletype, a parallel interface board, and a 12 bit A/D converter with a multiplexer that can accomodate up to 16 single-ended inputs and a programmable real time clock.

A special software was used, intended for transfer of data from the buffer interface to the computer and a correct interpretation of results for use in a high level language. A large group of Fortran programs were then used for statical reduction of results and graphical representation.

LDV experiments were preliminarily performed by using as scattering centers the particles present in the plume of the burning solid propellant. These experiments showed that, in general, sufficiently high particle rates are found in the region near the burning surface.

During preliminary experiments, the velocity time history was monitored by a storage oscilloscope, after D/A conversion of the output of the Doppler counter processor. Fig. 4.6 shows a typical oscilloscope record in which each point corresponds to a single particle velocity measurements. Oscilloscope record is triggered by the photodiode signal (upper trace) and the time span corresponds to a displacement of less than 0.5 mm above the burning surface. The propellant is a noncatalyzed Double Base (DB) burning at a pressure of 5 atm.

In Fig. 4.7 is shown the velocity trace of a sample of the same propellant (lower trace), but the record is covering a larger time interval. The upper trace, in this case, refers to the pressure, measured by means of a Kistler quartz transducer mod. 412, equipped with a Kistler Charge Amplifier mod. 5001. The pressure scale is 1 atm/div. It can be noted a slight time variation of the pressure from the initial value of 4 atm to a final value of 4.8 atm. At this point the velocity trace indicates the end of the burning rod of propellant.

Fig. 4.8 refers to a test with an AP based composite propellant at a nearly constant pressure of 7.5 atm.

It can be noted that large variations with sharp gradients characterize the velocity of the DB propellant in conjunction with irregular fluctuations in the particle rate (i.e. the number of points/div. in velocity traces). At exactly the same experimental conditions, higher particle rates and more regular velocity traces were found with the AP propellant.

To quantify velocity results, data reduction was performed by the minicomputer and the data acquisition procedure was activated by a triggering pulse derived by the photodiode signal. Once the velocity data relative to one test (about 500 velocity measurements) have been acquired into computer memory, they were processed to obtain the mean and the r.m.s. values. It should be remembered that we were interested in comparing gas phase velocity and condensed phase burning rate in steady state situation.

The condensed phase burning rate was measured by standard techniques but also by the optical method previously described.

Fig. 4.9 shows an example of the photodiode voltage output (trace 1) that can be related to the relative displacement of the burning surface of the solid propellant by means of the calibration curve of Fig. 4.5. In Fig. 4.9 the abscissa is the time and the mean burning rate can be easily deduced. All test runs were performed with an automatic control system able to keep constant the pressure in the strand burner within some percent. Trace 2 in Fig. 4.9 is the output of the pressure transducer. Fig. 4.9 refers to a test in which the rotating shutter was not used.

Accurate measurements of the solid propellant burning rate were obtained if the burning surface remains flat and horizontal. To verify this condition, that is also important in LDV measurements, the strand burner was equipped with another window to allow high speed cinematography. The camera (Hitachi 16 HD) is switched on manually, but the trigger pulse coming from the photodiode activates an event-marker and a time mark-generator on the film.

Fig. 4.10 shows some frames from one film at 100 fr/s. It can be easily observed the crossing point of the two laser beams of the LDV system and the burning surface displacement.

In all runs the mean gas phase velocity was compared with the corresponding condensed phase burning rate measured by standard fuse wire techniques or optical methods. Results agree satisfactorily on the basis of a steady state mass balance:

$$(4.5.1) \quad \bar{U} = \bar{m}/\rho_g = \bar{R} \rho_c/\rho_g$$

being  $\rho_c$  and  $\rho_g$  the condensed phase and the gas phase densities, and  $\bar{R}$  the condensed phase burning rate. Typical results are summarized in Table 4.2, in which mean values of the measured quantities  $\bar{R}$  and  $\bar{U}$  are reported. For comparison, values of  $\bar{U}$  evaluated from the measured burning rates are also reported. It must be noted that in all runs a large gas velocity dispersion (up to 20%) was observed around the mean value. This is difficult to explain on the basis of fluidynamics considerations, but could be due to a polydisperse particle size distribution and the consequent difficulty for larger particles or agglomerates to follow accurately the gas flow. Another critical parameter in the use of the above equation is the gas temperature; this was not directly measured, but only estimated from available data (Ref. 27).

So far, only tests in a steady state situation at pressure up to 10 atm were performed, but data collected suggest the possibility of reasonable measurements of gas phase velocity also in unsteady conditions. This is demonstrated in Figs. 4.11 and 4.12 in which the velocity profile near the burning surface is well resolved. In abscissa there is time which is proportional to the surface displacement. Mean velocity values were evaluated over about 50 samples and a time window of .25 s. The error bar is defined by  $\pm s$ , the standard deviation. Because the burning rate was about 3 mm/s, the 1 s time interval corresponds to a 4 mm displacement over the burning surface. The propellant is a noncatalyzed Double Base (DB) burning at a pressure of 4 and 7 ata. It is clearly observed the velocity increase near the burning surface up to a steady state situation.

#### Sec. 4.6 - CONCLUSIONS

Data collected up to now suggest the possibility of LDV measurements in the gaseous region above the burning surface of a solid propellant. So far, only tests in a steady state situation at pressure up to 10 atm were performed, but experimental work is in further progress.

Some aspects of LDV results are not completely understood right now. The velocity measurements seem to show more complicated profiles than expected. In fact, comparison with shadograph movies (4000 fr/s) at similar test conditions suggests a quasi-monodimensional laminar gas flow, unless of turbulence time scale well above the movie speed. The discrepancy with the presumed steady state laminar flame conditions is likely due to the polydisperse particle size distribution and the consequent difficulty for larger particles or agglomerates to follow accurately the gas flow.

To overcome these difficulties, special propellants will be tested, seeded with monodisperse alumina particle and with assigned particle concentration. Moreover, some modifications of the strand burner, by inserting new larger windows, will allow a better optical access for shadograph movies.

To improve the LDV instrumentation, the optics will be implemented by an higher power laser and a rotatable beam splitter unit that would allow to measure other velocity components beside the axial.

The possibility of reasonable measurements of gas phase velocity and burning rate by laser techniques has been clearly demonstrated in steady-state conditions. LDV measurements can be extended also to unsteady conditions and this is a very important result because the LDV is the only technique capable of space and time resolved measurements in such hostile environmental.

Sec. 4.7 - REFERENCES

- 1) Durst,F., Melling,A. and Whitelaw,J.H., "Principles and Practice of Laser Doppler Anemometry", Academic Press, 1976.
- 2) Watrasiewicz,B.M. and Rudd,M.J., "Laser Doppler Measurements", Butterworths, 1976.
- 3) Durrani,T.S. and Greated,C.A., "Laser Systems in Flow Measurement", Plenum Press, 1977.
- 4) Soo, S.L., "The Physics of Fluids", 18, 2, 1975.
- 5) Melling,A. and Whitelaw,J.H., Proceedings of the LDA Symposium, pp.382-402, Copenhagen, 1975.
- 6) George,W.K., Proceedings of the LDA Symposium, pp.20-63, Copenhagen, 1975.
- 7) Farmer,W.M., Harwell,K.E., Hornkohl,J.O. and Schwartz,F.A., "Particle Sizing Interferometer Measurements in Rocket exhausts" in: "Laser Velocimetry and Particle Sizing", ed. H.D. Thompson and W.H. Stevenson. Hemisphere Publ. Corp., Washington, 1979.
- 8) D'Alessio,A., Fifteenth Symposium (International) on Combustion, The Combustion Institute, Pittsburgh, 1974, pp.1427-1438.
- 9) Bonczyk,P.A., Combustion and Flame, 35, pp.191-206, 1979.
- 10) Chigier,N.A., Ungut,A. and Yule,A.J., Seventeenth Symposium (International) on Combustion, University of Leeds, 1978.
- 11) Farmer,W.M., Applied Optics, 11, 11, pp.2603-2612, 1972.
- 12) Robinson,D.M. and Chu, W.P., Applied Optics, 14, 9, pp. 2177-2183, 1975.
- 13) Bachalo,W.D., Third International Workshop on Laser Velocimetry, Purdue University, 1978.
- 14) Chu,W.P. and Robinson,D.M., Applied Optics, 16, 3, pp.619-626, 1977.
- 15) Adrian R.J. and Orloff,K.L., Applied Optics, 16, 3, pp. 677-684, 1977.
- 16) Coghe,A., Ghezzi,U. and Pasini,S., XXXIII Congresso Nazionale ATI, Università di Ancona, Italy, 1978.
- 17) Coghe,A. and Ghezzi,U., Proceedings of Dynamic Flow Conference, Marseille, France, 1978, pp.825-849.
- 18) Adrian,R.J. and Earley,W.L., Proceedings of the Minnesota Symposium on Laser Anemometry, Minneapolis, Minnesota, 1976, pp.426-454.
- 19) Kerker,M., "The Scattering of Light", Academic Press, 1969.
- 20) Born,M and Wolf,E., "Principles of Optics", Pergamon Press, 1975.
- 21) Van de Hulst,C.H., "Light Scattering by Small Particles", J.Wiley, 1957.
- 22) Anglesio,P., Coghe,A. and Ghezzi,U., Meeting of the Aerodynamic and Oil Panel of the I.F.R.F., Lyon, France, 1978.
- 23) Ghezzi,U. and Coghe,A., 4th International Symposium on Air Breathing Engines, Florida, USA, 1979.
- 24) Ghezzi,U., Coghe,A. and Gamma,F., Symposium on Laser Probes for Combustion Chemistry, 178th ACS National Meeting, Washington, USA, 1979.

- 220 -

- 25) Farmer,W.M., "Measurement of Particle Size and Concentrations Using LDV Techniques", Dynamic Flow Conference, Baltimora, USA, 1979.
- 26) De Luca,L. and Zanotti,C., "Measurement of Steady Solid Propellant Burning Rate and Data Processing", XXXII Congresso ATI, Roma, 1977.
- 27) Kubota,N., Ohlemiller,T.J., Caveny,L.H. and Summerfield, M., "The Mechanism of Super-rate Burning of Catalyzed Double-base Propellants", Princeton University, AMS Report No.1087, March 1973.

LIST OF TABLES

Tab. 4.1 - Typical optical features of the LDV experimental set-up used in this work.

Tab. 4.2 - Comparison of expected and measured values of the gas phase velocity, based on some typical experimental results. Temperature and density data from Ref. 27.

LIST OF FIGURES

Fig. 4.1 - Schematic representation of the differential LDV system with the enlarged probe volume and a typical single particle Doppler signal.

Fig. 4.2 - Experimental set-up for LDV measurements.

Fig. 4.3 - LDV geometry and definition of the dead zone thickness.

Fig. 4.4 - Optical system for the burning rate measurement of solid propellants.

Fig. 4.5 - Calibration curve of the optical system of Fig. 4.4: the output (Volts) of the photodiode vs the displacement (mm) of the solid propellant surface.

Fig. 4.6 - LDV results for a noncatalyzed DB propellant. Upper trace: photodiode signal vs time (vertical scale: 0.2 V/div; horizontal scale: 20 ms/div). Lower trace: LDV analog output vs time (vert. scale: 1.15 m/s/div).

Fig. 4.7 - LDV results for a noncatalyzed DB propellant. Upper trace: pressure vs time (vert. scale: 2 atm/div; horiz. scale: 0.5 s/div). Lower trace: LDV analog output vs time (vert. scale: 1.15 m/s/div).

Fig. 4.8 - LDV results for an AP-based composite propellant. Upper trace: pressure vs time (vert. scale: 2 atm/div; horiz. scale: 0.5 s/div). Lower trace: LDV analog output vs time (vert. scale: 2.30 m/s/div).

Fig. 4.9 - Example of the photodiode voltage output of Fig. 4.4 (trace 1); output of the pressure transducer (trace 2).

Fig. 4.10 - Six frames from a color movie at 100 fr/s.

Fig. 4.11 - Velocity profile and standard deviation near the combustion surface of a DB propellant burning at 4 atm of pressure. DB noncatalyzed.

Fig. 4.12 - Velocity profile and standard deviation near the combustion surface of a DB propellant burning at 7 atm of pressure. DB noncatalyzed.

TABLE 4.1

Typical optical features of the LDV experimental set-up used in this work

---

Laser wavelength, $\lambda$	632.8 nm
Cross-angle, $\beta$	$4.70^\circ$
Fringe spacing = $\lambda/(2 \sin(\beta/2))$	= 7.7 $\mu\text{m}$
Probe volume dimensions	$3 \times 0.15 \times 0.15 \text{ mm}^3$
Fringe number (effective)	20
Collecting solid angle, $\Omega$	$4^\circ - 6^\circ$
Dead zone thickness ( $h = r \tan \beta$ )	0.25 mm ( $r = 3\text{mm}$ )

---

TABLE 4.2

Comparison of expected and measured values of the gas phase velocity, based on some typical experimental results. Temperature and density data from Ref. 27.

Propellant	Pressure, P, atm	Measured Condensed Density, $\rho_c$ , g/cm <sup>3</sup>	Evaluated Gas Density, $\rho_g$ , g/cm <sup>3</sup>	Gas Phase Velocity, $\bar{U}$ , cm/s.	
				Burning Rate (mean values), $\bar{R}$ , cm/s	Evaluated Measured
DB noncatalyzed	6	—	1.63	$1.27 \times 10^{-3}$	0.28
	8	—	1.63	$1.69 \times 10^{-3}$	0.36
AP composite	10	—	1.63	$2.10 \times 10^{-3}$	0.45
	8	—	1.61	$0.89 \times 10^{-3}$	0.35
				360	$340 \pm 70$

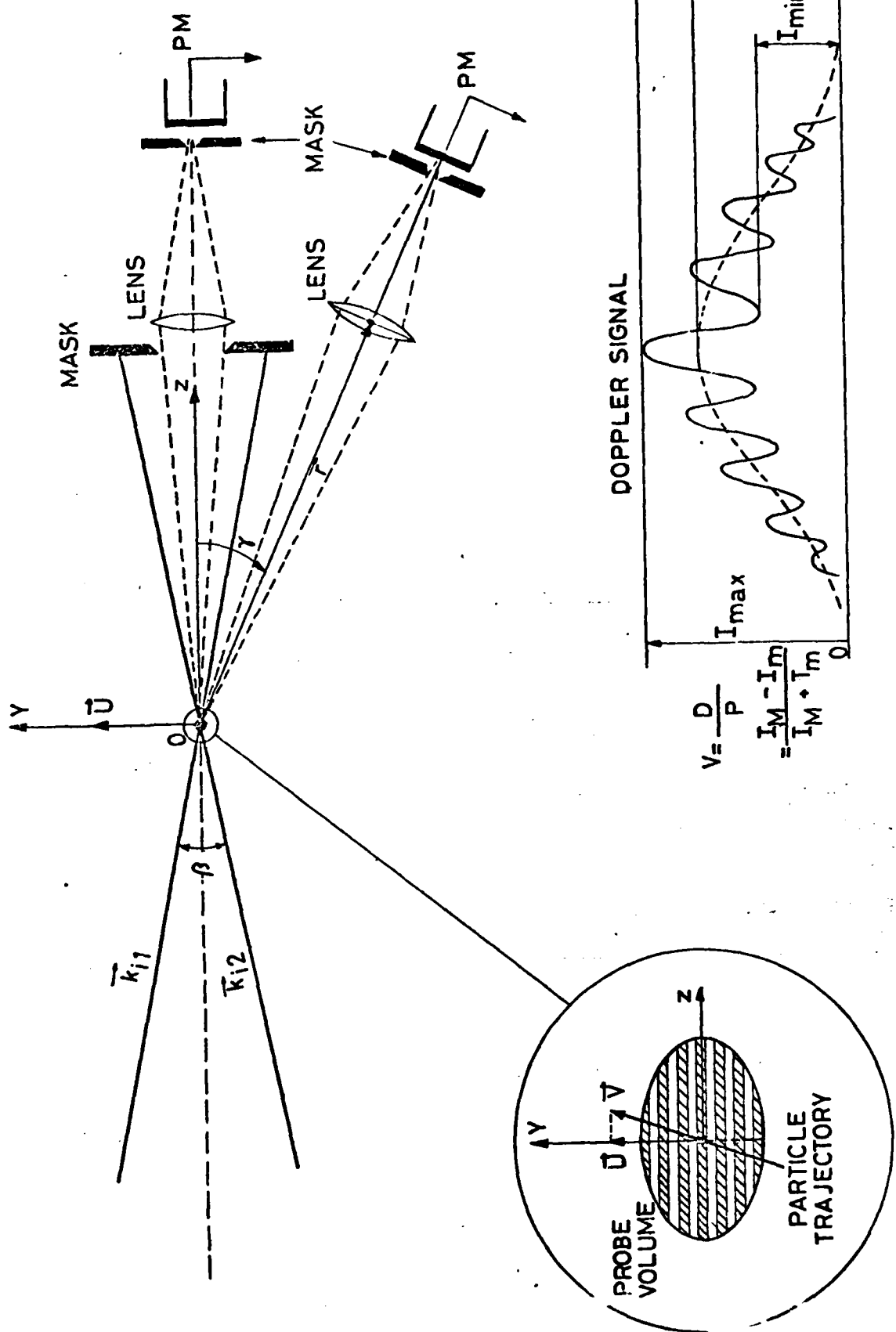


FIG. 4.1

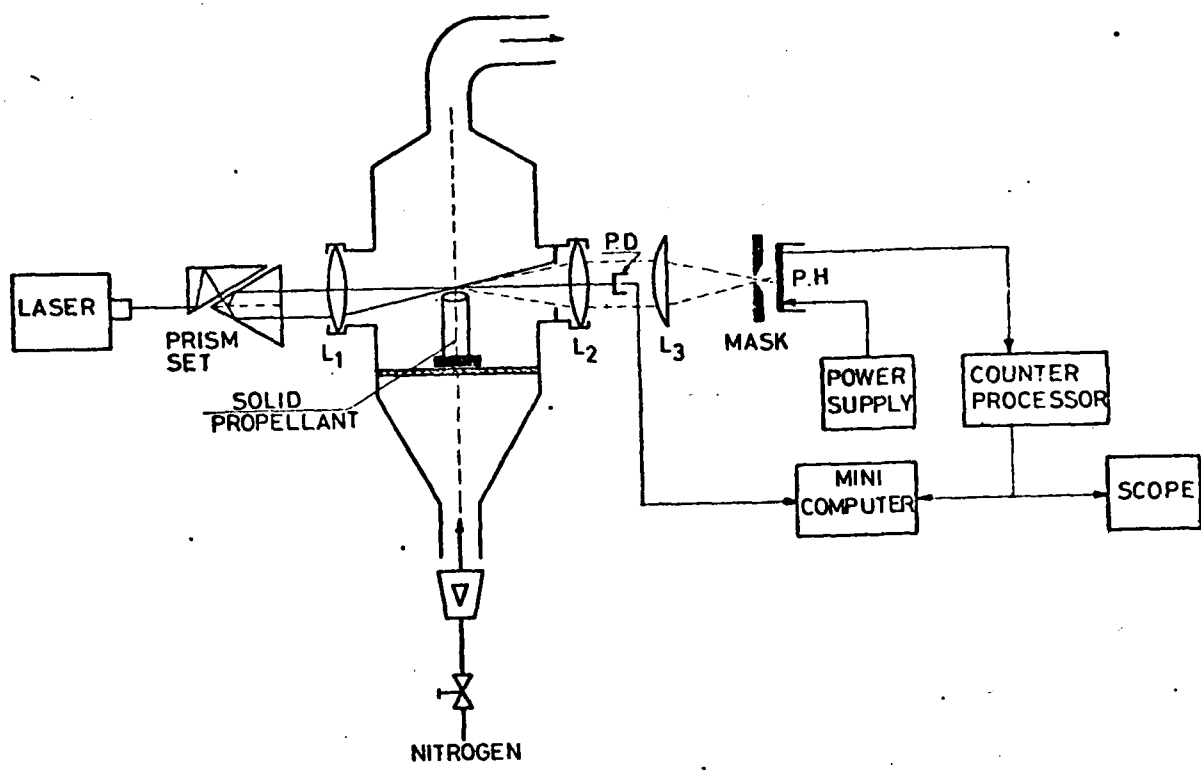


FIG.4.2

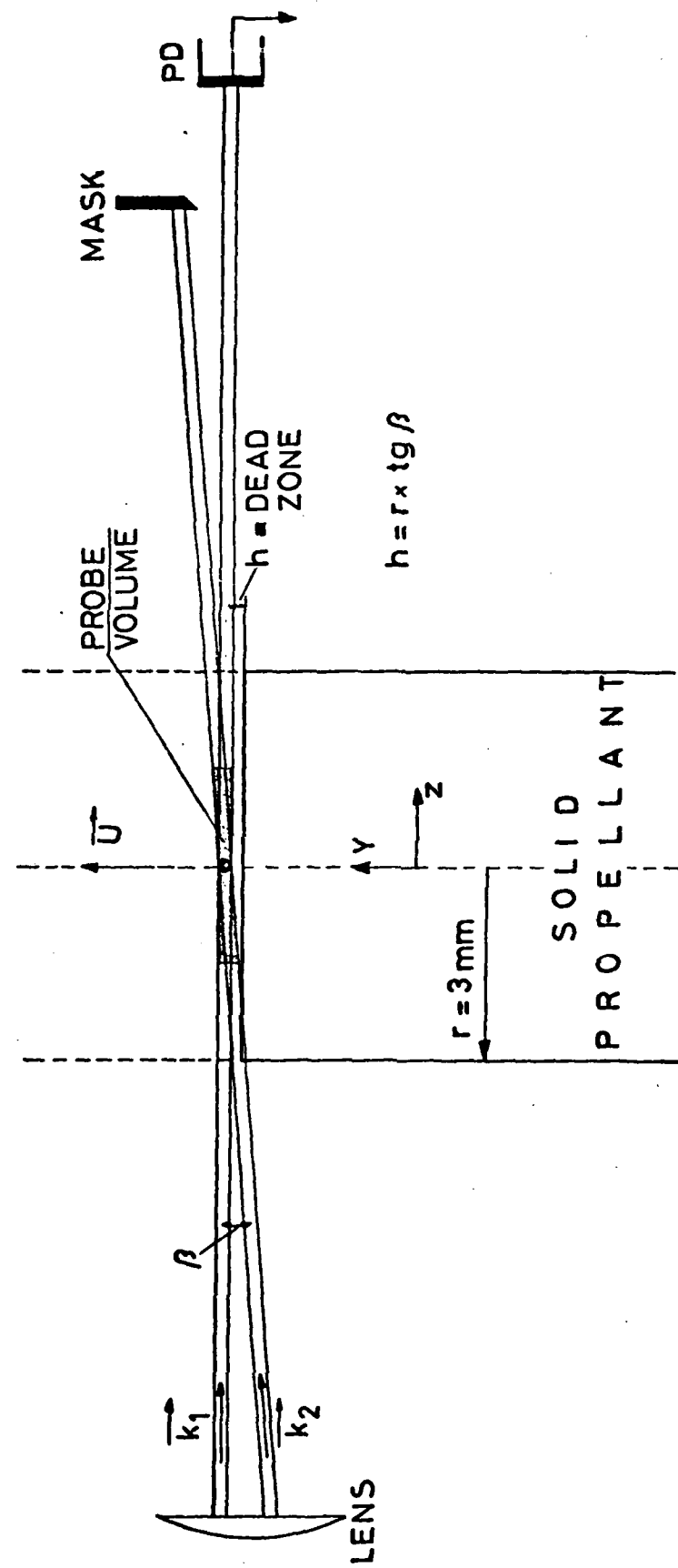


FIG. 4.3

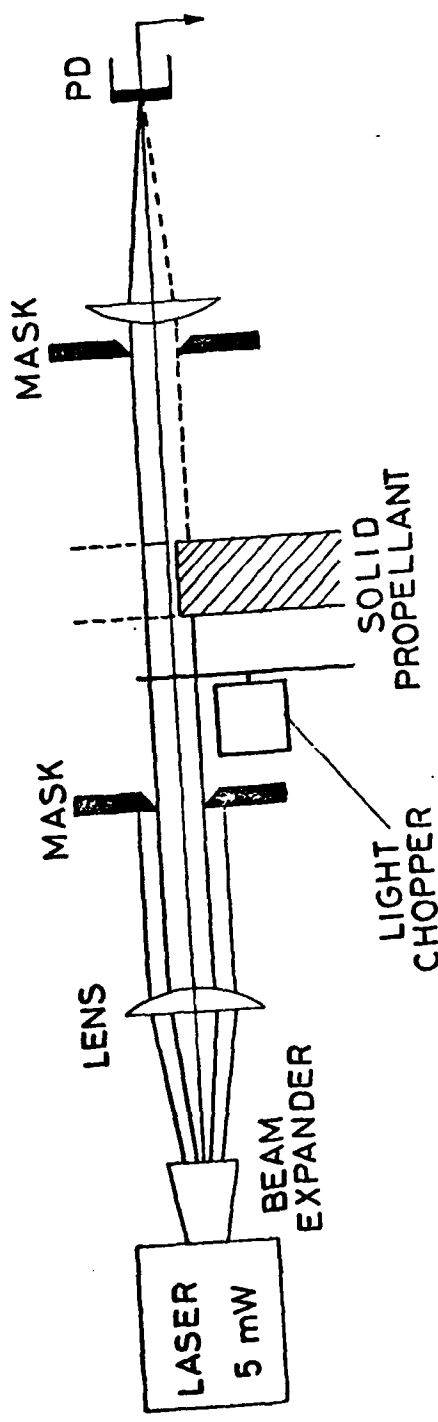


FIG. 4.4

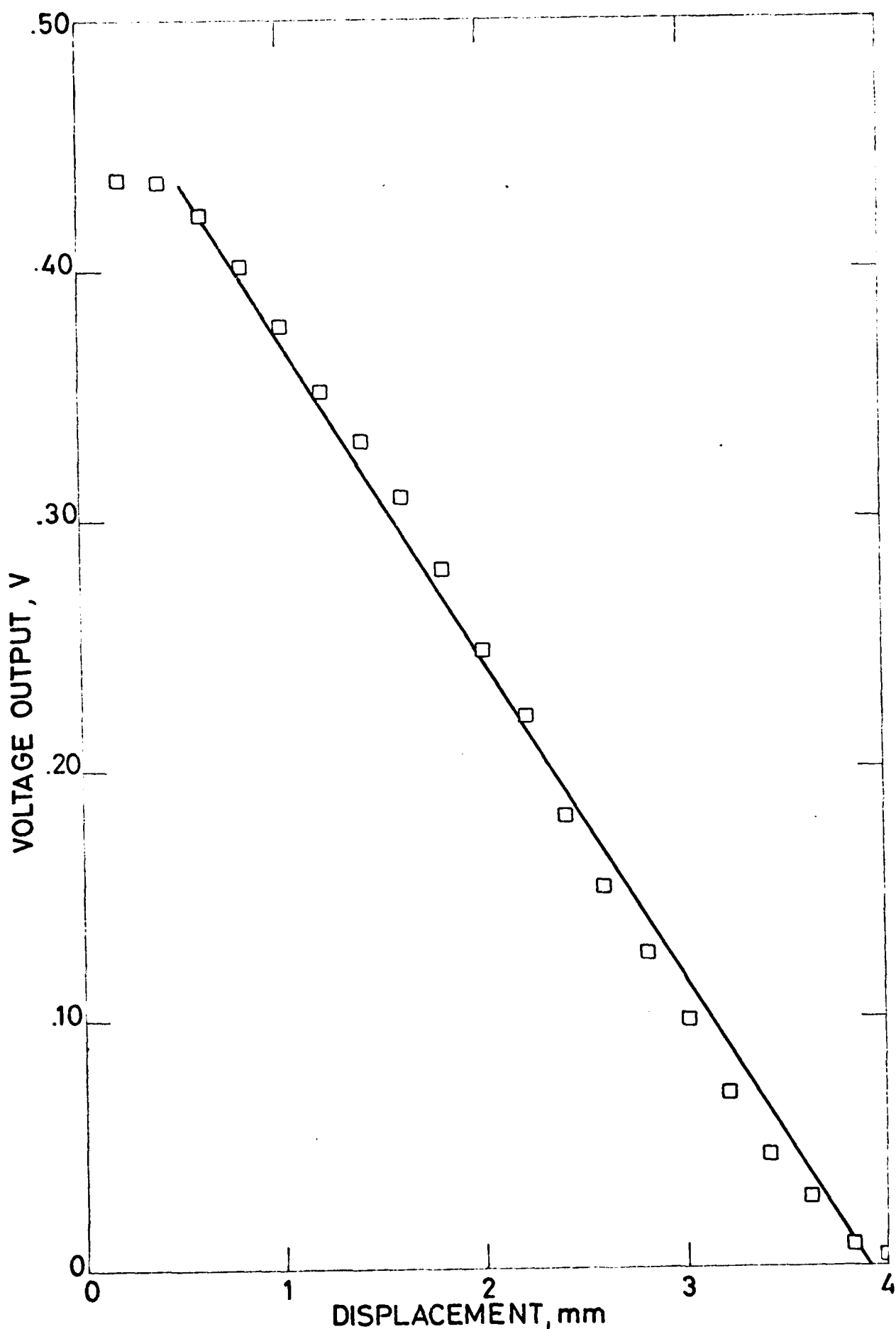


FIG. 4.5

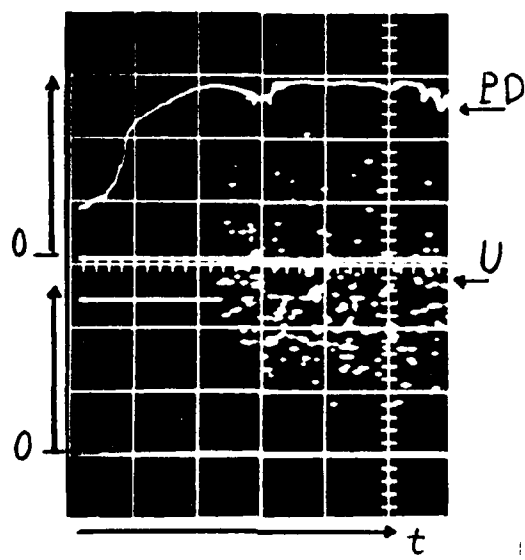


Fig. 4.6

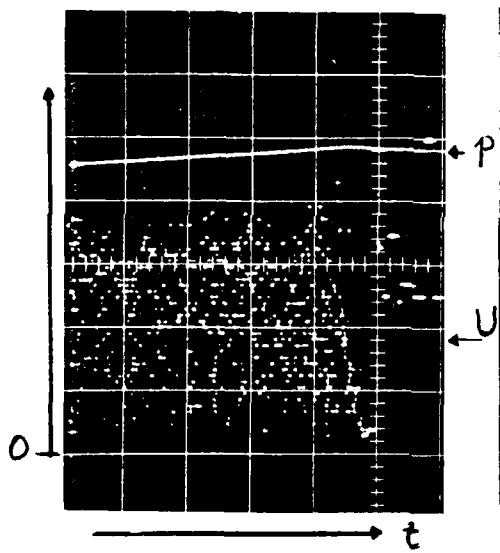


Fig. 4.7

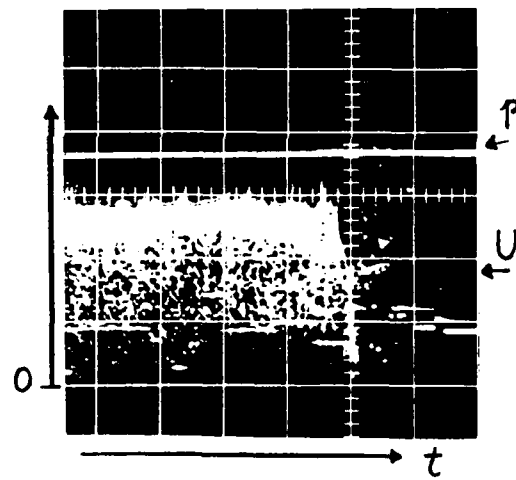


Fig. 4.8

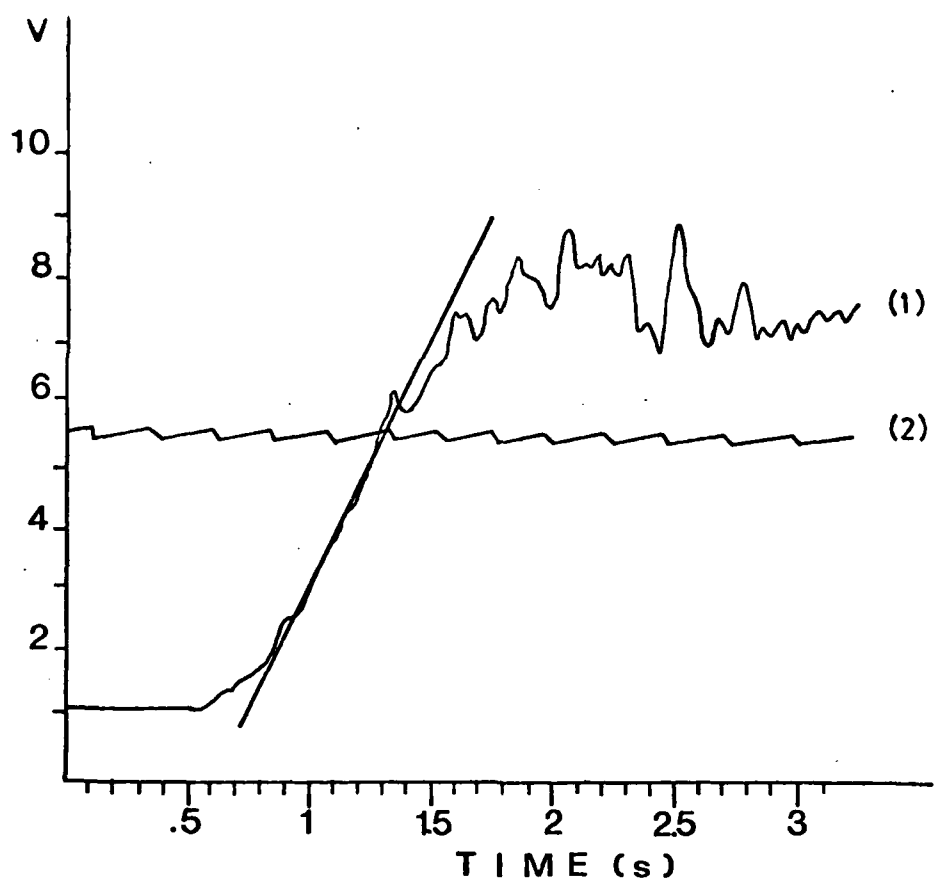
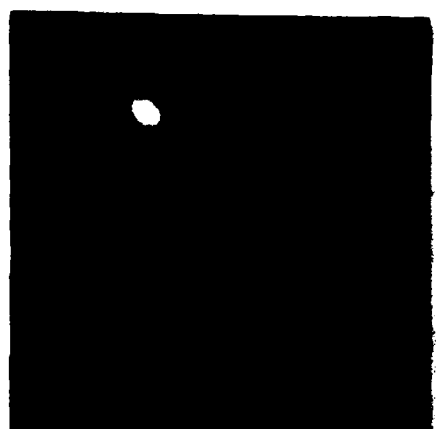
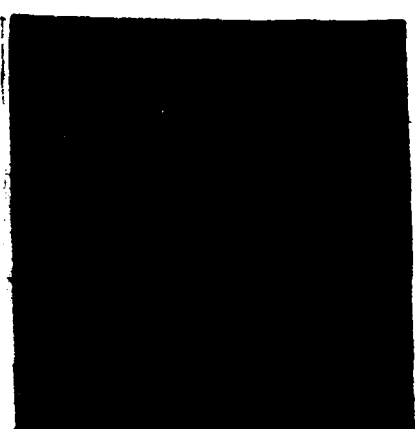


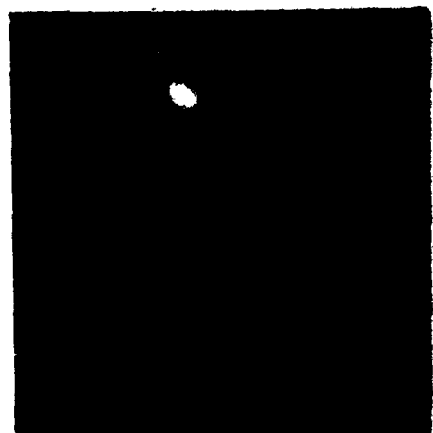
Fig. 4.9



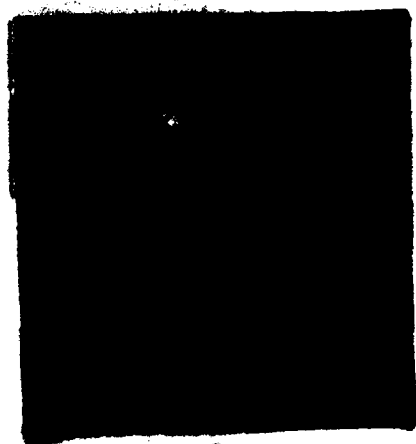
1



2



3



4



5



6

FIG. 4.10

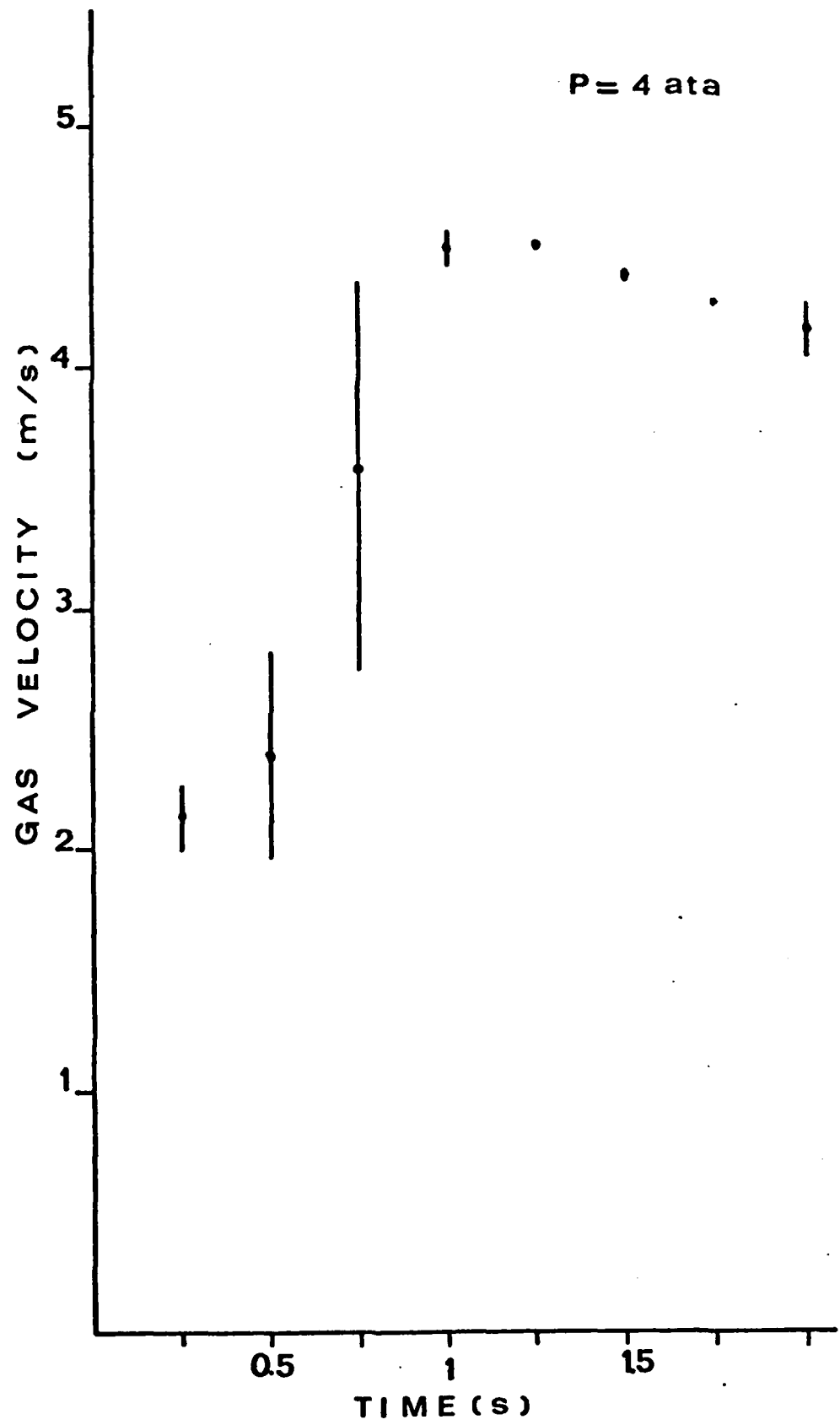


FIG. 4.11

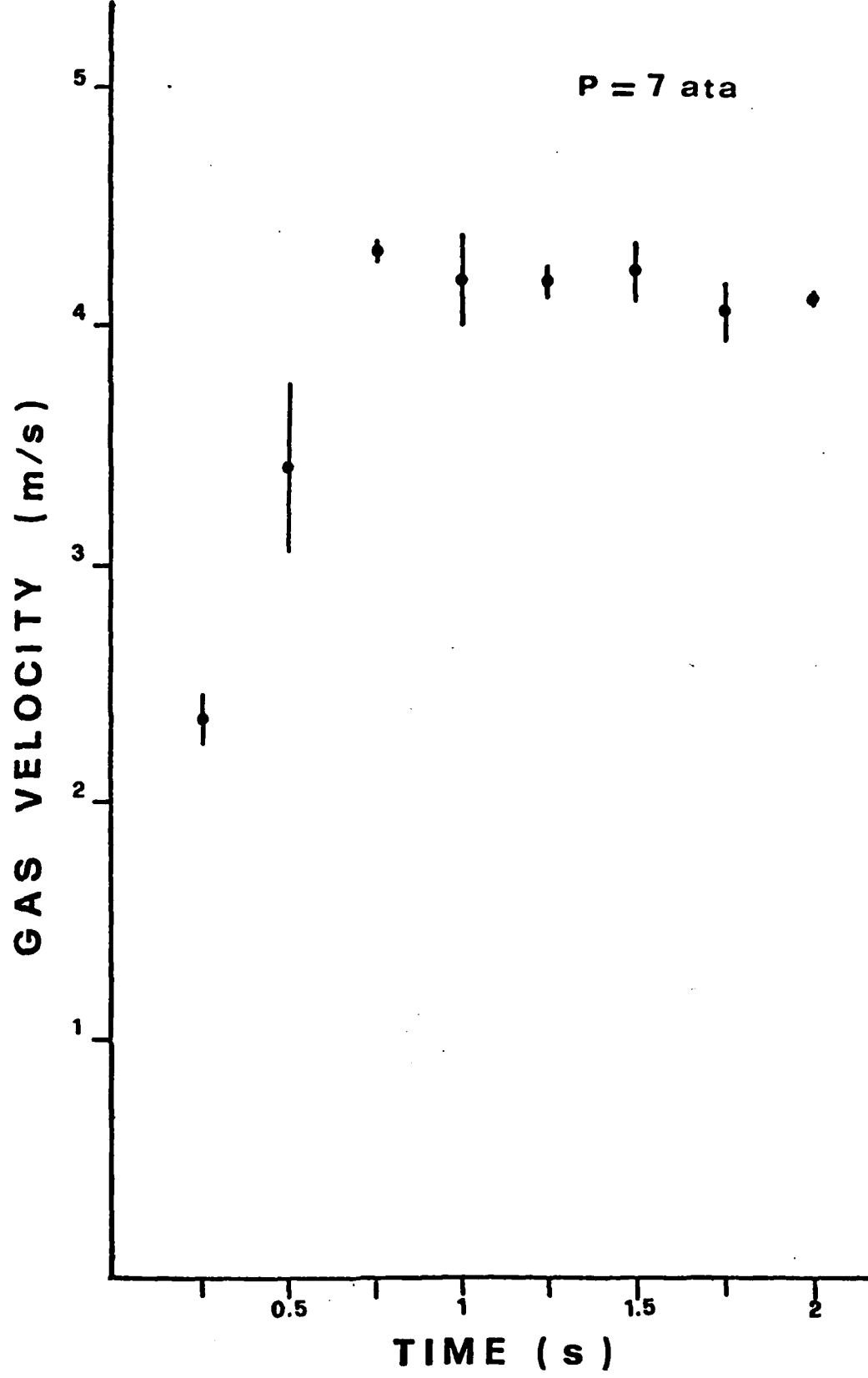


FIG. 4.12

## CHAPTER 5 - CONCLUSIONS AND FUTURE WORK

### Sec. 5.1 - CONCLUSIONS

A nonlinear stability analysis of solid propellant burning was carried out, within the framework of a thermal theory and for quasi-steady gas phase, allowing for finite size disturbances. This required an integral method in reducing the partial differential equation for the condensed phase heat transfer to an approximate ordinary differential equation. It is shown that a nonlinear algebraic function, called restoring function, can be defined that contains all basic properties of equilibrium and stability of burning solid propellants. This function does not depend on time, but only on the nature of the solid propellant (including its flame) and the operating conditions (pressure, ambient temperature, and energy exchange with surrounding). Analysis of the nonlinear algebraic restoring function reveals that two well defined burning regimes exist, each limited by stability boundaries: the static and the dynamic regimes. Of these two, the region of dynamic burning is wider, in that under dynamic conditions propellant may pass through a region which is statically forbidden but dynamically stable.

The static regime can be observed experimentally and therefore can be studied also in the framework of Zeldovich approach. The statically stable steady solution is either stationary or self-sustained oscillating. The static burning boundary is defined as that ultimate burning condition, at constant pressure and for a given set of operating conditions, below which steady solutions are no longer found. Pressure deflagration limit is defined as that minimum pressure, for a given set of operating conditions, below which steady solutions are no longer statically stable. Methods are suggested as to the prediction of both static boundaries.

The dynamic regime cannot be observed experimentally in a stationary mode and can only be studied in the framework of a flame model. In general, a lower (burning rate below the steady value) dynamic stability boundary is always found, except for large enough ambient temperature and/or (external) radiant flux. Moreover, for each propellant an appropriate combination of pressure and surface heat release exists for which lower and upper (burning rate above the steady value) dynamic stability boundaries are found. The lower dynamic stability boundary is defined as that ultimate burning condition beyond which extinction necessarily follows during a burning transient. The upper dynamic stability boundary implies vigorous accelerations of the combustion wave, possibly followed by dynamic extinction.

It is shown that the lower dynamic stability boundary holds true both for deradiation and/or depressurization, for opaque as well as transparent condensed phase, for fast deceleration of the combustion wave (e.g., by depressurization) as well as for fast acceleration (e.g., by pressurization) if

an excessively large burning rate overshoot is attained. The lower dynamic stability boundary was determined as an asymptotic (in time) boundary for arbitrary but levelling off external controlling parameters and instantaneous boundary for monotonically decreasing external controlling parameters. If no change in time of the external controlling parameters occurs, the propellant is only subjected to random intrinsic disturbances and the static stability analysis apply. If the effect of the time change of the external controlling parameters (nonautonomous function) is negligible compared to the restoring function, the lower dynamic stability boundary collapses to the range of influence of the statically stable equilibrium configuration and therefore holds true for any time (even finite) and for any external law (even non monotonic or levelling off).

MTS, KTSS nonlinear, KTSS linearized, KZ, and LC unsteady flame models were implemented in this study. While KTSS linearized, KZ, or LC are of no value for burning rate less than about 90% of the steady state value, very reasonable and similar results are displayed by MTS and KTSS nonlinear. However, MTS flame model is considered superior since it accounts also for chemical kinetics (but it requires two constants to be evaluated).

The order of the polynomial chosen to approximate the disturbance thermal profile in the condensed phase does not affect qualitatively the shape of the restoring function. A cubic law was found to give accurate predictions for pressures up to about 30 atm; a quadratic law may be more appropriate for larger pressures. This point is under investigation.

The validity of this nonlinear stability theory was verified by computer simulated transients. In general, excellent agreement was found between the analytical predictions and the numerical results obtained by integration of the governing partial differential equation. Numerical values are given only for a particular, ammonium perchlorate based, composite propellant. It is felt, however, that all analyses were conducted from a broad point of view and, therefore, the conceptual findings may be extended to other types of solid propellants, provided a proper flame model is employed. The point we wish to make is that the numerical integration of the basic set of equations in terms of the PDE suggests the existence of a no-return point for fast transients and defines its value by a trial and error procedure. The values obtained in several different configurations are in excellent agreement with the predictions made from an analysis of the approximate ODE describing the system. This also confirms that the static stability boundary, as determined for example in the Zeldovich approach, has no relevance in dynamic disturbances of finite size.

The above result of detecting recovery points down to  $\theta_s \leq 0.6$  is important only to the extent to which it illustrates the validity of the analytical developments of this report. Indeed, it is very questionable whether chemical processes are still active at such low surface temperature. Moreover, heat loss mechanisms are very likely not negligible in that surface temperature range. All this implies that more sophisticated flame models have to be considered, if one wishes accurate results in the marginal domains of burning. Incidentally, it was observed that changes in the decay rate are most effective in affecting the overall fate of the dynamic history if realized in the early portion of the transition.

It is felt that conclusive evidence was offered for: (1) the existence of several static burning regimes (stationary burning, damped oscillatory burning, self-sustained oscillatory burning, extinction); (2) the capability of the proposed theory to predict pressure deflagration limit even for adiabatic combustion waves. In conclusion, the nonlinear static restoring function contains all basic properties of equilibrium and asymptotic (both static and dynamic) stability of burning solid propellants, even for finite size disturbances, provided that the external forcing terms are monotonic or level off in time.

Experimental work is in progress. Three different solid propellants are being characterized: an ammonium perchlorate based composite, a catalyzed double - base, and a noncatalyzed double - base. Steady state burning rates are measured in a strand burner; thermal profiles in the condensed phase and radiative emissions are detected; pictures and high speed movies are taken. Depressurization and pressurization tests are conducted respectively in a specifically designed strand burner and piston tube. Laser doppler anemometry is applied to burning propellants to measure the gas velocity in the plume of the sample. Experimental results so far obtained qualitatively agree with the theoretical predictions.

Sec. 5.2 - FUTURE WORK

The delicate assumption of a polynomial space dependence of the disturbance thermal profile has to be further investigated. Other quasi-steady models shall be tested and compared; but the quasi-steady gas phase assumption has to be properly qualified. The Zeldovich approach shall be examined and included in the proposed nonlinear combustion stability theory. Variable thermal properties in the condensed phase shall be accounted for. Considering the importance of the condensed phase heat release, the assumptions of concentrated chemical reactions at the burning surface shall be dropped. Exact predictions of the oscillating burning period have yet to be proposed. Extension of the proposed theory to the ignition problem will be continued. Extension of both, stability theory and computer simulated tests, to high pressure range (above 60 atm) and low pressure range (below 1 atm) will be done. Very likely, the subatmospheric pressure range will require a careful choice of the flame model, including its steady state aspects.

Experimentally, further data on combustion vs extinction will be furnished both from depressurization strand burner and piston tube. This should allow a quantitative comparison between predicted and experimentally observed dynamic stability boundaries. Further data are also expected from the laser doppler velocimetry apparatus. The behavior of the steady deflagration wave at low pressure is of particular interest; more sophisticated diagnostic techniques are planned.

**DATE  
ILME**